LEABHARLANN CHOLÁISTE NA TRÍONÓIDE, BAILE ÁTHA CLIATH | TRINITY COLLEGE LIBRARY DUBLIN
Ollscoil Átha Cliath | The University of Dublin

Terms and Conditions of Use of Digitised Theses from Trinity College Library Dublin

Copyright statement

All material supplied by Trinity College Library is protected by copyright (under the Copyright and Related Rights Act, 2000 as amended) and other relevant Intellectual Property Rights. By accessing and using a Digitised Thesis from Trinity College Library you acknowledge that all Intellectual Property Rights in any Works supplied are the sole and exclusive property of the copyright and/or other IPR holder. Specific copyright holders may not be explicitly identified. Use of materials from other sources within a thesis should not be construed as a claim over them.

A non-exclusive, non-transferable licence is hereby granted to those using or reproducing, in whole or in part, the material for valid purposes, providing the copyright owners are acknowledged using the normal conventions. Where specific permission to use material is required, this is identified and such permission must be sought from the copyright holder or agency cited.

Liability statement

By using a Digitised Thesis, I accept that Trinity College Dublin bears no legal responsibility for the accuracy, legality or comprehensiveness of materials contained within the thesis, and that Trinity College Dublin accepts no liability for indirect, consequential, or incidental, damages or losses arising from use of the thesis for whatever reason. Information located in a thesis may be subject to specific use constraints, details of which may not be explicitly described. It is the responsibility of potential and actual users to be aware of such constraints and to abide by them. By making use of material from a digitised thesis, you accept these copyright and disclaimer provisions. Where it is brought to the attention of Trinity College Library that there may be a breach of copyright or other restraint, it is the policy to withdraw or take down access to a thesis while the issue is being resolved.

Access Agreement

By using a Digitised Thesis from Trinity College Library you are bound by the following Terms & Conditions. Please read them carefully.

I have read and I understand the following statement: All material supplied via a Digitised Thesis from Trinity College Library is protected by copyright and other intellectual property rights, and duplication or sale of all or part of any of a thesis is not permitted, except that material may be duplicated by you for your research use or for educational purposes in electronic or print form providing the copyright owners are acknowledged using the normal conventions. You must obtain permission for any other use. Electronic or print copies may not be offered, whether for sale or otherwise to anyone. This copy has been supplied on the understanding that it is copyright material and that no quotation from the thesis may be published without proper acknowledgement.

TRINITY COLLEGE DUBLIN
08 MAR 2017
ACADEMIC REGISTRY

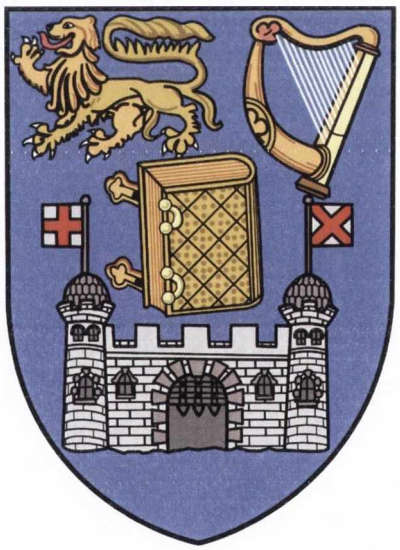
PhD
CHEMISTRY

The Liquid Phase Exfoliation of Transition Metal Oxides for High Energy Li-ion Batteries

Author:
Seán O'Brien

Supervisor:
Prof. Valeria Nicolosi

A thesis presented for the degree of
Doctor of Philosophy



Characterization and Processing of Advanced Materials
Department of Physics
University of Dublin, Trinity College

February 9, 2017

TRINITY LIBRARY
24 OCT 2017
DUBLIN
Thesis 11642

Declaration of Authorship

I, Seán O'BRIEN, declare that this thesis titled, "The Liquid Phase Exfoliation of Transition Metal Oxides for High Energy Li-ion Batteries" and the work presented in it are my own.

I declare that this thesis has not been submitted as an exercise for a degree at this or any other university.

I agree to deposit this thesis in the University's open access institutional repository or allow the library to do so on my behalf, subject to Irish Copyright Legislation and Trinity College Library conditions of use and acknowledgement.

Signed: _____ _____

Date: _____ _____

"You are a failure!"

Mr. Dunne, Physics Teacher, Secondary School.

UNIVERSITY OF DUBLIN, TRINITY COLLEGE

Abstract

The Faculty of Engineering, Mathematics and Science

Department of Physics

Doctor of Philosophy

The Liquid Phase Exfoliation of Transition Metal Oxides for High Energy Li-ion Batteries

by Seán O'BRIEN

Compared to other electrochemical energy sources, lithium ion (Li-ion) batteries represent the choice energy storage device for small hand-held electronics such as power tools or cellphones. This is due mainly to the balance of high energy and power densities present in the devices. It is envisioned that such devices will become major components in the next generation of hybrid electric vehicles (HEV) which may be key in exploitation of alternative energy sources. However, improvements in both the power densities and cycling properties are necessary if applications in HEVs are ever to be realized. Much research has been done on improving these properties with the introduction of nanostructured materials, providing an increase in the overall active surface areas. Recently, two dimensional nanomaterials have shown huge promise in high powered, reusable energy storage devices such as rechargeable batteries and supercapacitors. Specifically, two dimensional transition metal oxide (TMO) materials have shown impressive pseudocapacitive behaviour rivalling that of traditional rechargeable battery systems e.g. $LiCoO_2$ or graphite.

This dissertation focuses on some of the important issues surrounding the facile synthesis of TMO nanomaterials, the subsequent fabrication of high energy electrodes and their electrochemical characterization. A major challenge is to find a facile method to produce a stable, concentrated nanoparticle colloid which can be efficiently used in electrode fabrication. Traditional exfoliation techniques employ the use of toxic chemicals such as formamide or N-Methyl-2-pyrrolidone. A simple and cost effective liquid phase exfoliation (LPE) method is presented in the current

work to provide stable dispersions of TMO nanomaterials without the use of surfactant materials or environmentally hazardous solvents.

Ultrasonic spraying was used to fabricate a series of thin film composite electrodes, pairing TMO materials such as vanadium pentoxide (V_2O_5), titanium dioxide (TiO_2) and molybdenum trioxide (MoO_3) with conductive agents such as single-walled carbon nanotubes (SWCNT) or graphene. The electrochemical performances of these materials were analysed and compared to both unexfoliated powders and previously published reports. In each case the overall storage capacities showed a marked increase relative to that of their unexfoliated counterparts plus a general improvement than that shown in published works. Similarly, the cycling properties of each electrode showed dramatic improvement indicating that a combination of the nanostructuring and addition of conductive additives served to alleviate the semiconducting behaviour commonly exhibited by TMO materials.

In this study, a V_2O_5/SWCNT composite cathode was shown to reach initial storage capacities upwards of 393 $mAh\,g^{-1}$ at current densities of 0.05 C with a 81% retention after 100 cycles. Similarly, a TiO_2/SWCNT anode showed a 716 $mAh\,g^{-1}$ storage capacity at a current density of 0.1 C and a 59% capacity retention after 100 cycles. In the case of MoO_3, a series of nanocomposite layered materials were fabricated by similar ultrasonic methods. Specifically, a MoO_3/V_2O_5 nanocomposite showed an initial discharge capacity or 374 $mAh\,g^{-1}$ at 20 $mA\,g^{-1}$ with an impressive 90% retention after 100 cycles.

Overall, this thesis details the facile, eco-friendly and cost effective synthesis of stable TMO nanoparticle colloids in inert solvents such as H_2O and IPA. It further suggests stabilization mechanisms and then goes on to demonstrate a simple ultrasonic method to produce high energy thin film electrodes. It finally shows how simple nanostructuring coupled with the addition of conductive additives improves the overall energy storage properties of the TMO materials. These methods can easily be extended to a whole range of materials necessary for the future of energy storage devices.

Acknowledgements

First and most importantly, I would like to thank Prof. Valeria Nicolosi for providing me with the opportunity to pursue a PhD. Over the past four years she has shown so much support in furthering my research and providing the necessary means to accomplish this thesis.

I would also like to thanks the other Valerians specifically Dr. John Zhang for drilling how to write a scientific paper into my head and providing me with help to finish my thesis. Other colleges such as Henrik, Clive and Dermot for teaching me the dark and mysterious ways of the microscopes. Also Beatriz for introducing me to the potentiostat and the dreaded spraying tool. Specific thanks should go to Carol who organized so much and sorted out so much administrative nonsense when I was way over my head. The rest of the Valerians also deserve a mention for putting up with me over the past few years including Megan, Andres, Evie, Alexey, Richard, Sonia, Park, Jesus, Agata, Anuj, Lorcan, Hannah, Eva, Cathal, Dileep, Chris, Iftikar, Meiying, Xinhua, Sergio, Arthur Daire, Dahnan, Oskar and Owen. However, Edmund and Joao deserve a special mention as they essentially endured me from day one. Many a night has been spent playing nerdy board games with Edmund and many a day has been spent listening to Joao impersonate a certain Family guy character.

Over the years a range of other people in CRANN have supported my scientific research including Damien, Lily, Ehsan, Riley, Shaun, Maria, Hugo, Arlene, Ivan, Niall, Conor, Sonia and Auren along with various people overseas such as Dr. Neal Fairly, Dr. Holly Warren and Prof. Marc in het Panhius. I would also like to acknowledge my examiners, Professor Colm O'Dwyer and Professor Hongzhou Zhang who took time out to examine my thesis. Thanks should also be directed at John O'Rourke who was the first person who ever believed I could pursue a PhD and the Naughton family who provided me with my first scholarship. Finally to my parents who initially financially supported me through college and provided so much support and Luiza who has had to deal with me writing this thesis.

Contents

Declaration of Authorship iii

Abstract vii

Acknowledgements ix

List of Figures xv

List of Tables xix

List of Abbreviations xxi

Physical Constants xxiii

List of Symbols xxv

1 Introduction and Motivation 1
- 1.1 Motivation . . . 1
- 1.2 Energy Storage . . . 3
- 1.3 Electrochemical Energy Storage . . . 4
  - 1.3.1 Batteries . . . 4
    - 1.3.1.1 Lithium Ion Batteries . . . 8
  - 1.3.2 Supercapacitors . . . 11
- 1.4 Nanoscience . . . 15
  - 1.4.1 Nano-energy Storage . . . 17
  - 1.4.2 Two-dimensional Nanomaterials . . . 18
- 1.5 Scope and Aim . . . 19

2 Theory 21
- 2.1 Electrochemical Power Storage . . . 21
  - 2.1.1 Cell Property Classifications . . . 22
  - 2.1.2 Thermodynamics . . . 25
  - 2.1.3 Kinetics . . . 28
  - 2.1.4 Electrode Processes . . . 31
    - 2.1.4.1 Faradaic Reactions . . . 31
    - 2.1.4.2 The Electrochemical Double Layer . . . 32
    - 2.1.4.3 Pseudocapacitance . . . 35
  - 2.1.5 Diffusion . . . 36
- 2.2 Colloidal Dispersions . . . 39

3 Experimental Methods **45**
3.1 Liquid Phase Exfoliation . . . 45
3.2 Ultrasonic Spraying . . . 47
3.3 Ultraviolet-visible Spectroscopy . . . 48
3.4 Electron Microscopy . . . 49
3.5 Brunauer-Emmet-Teller Surface Area . . . 52
3.6 X-ray Diffraction . . . 53
3.7 X-ray Photoemmision Spectroscopy . . . 55
3.8 Electrochemical Techniques . . . 56
3.8.1 Cyclic Voltammetry . . . 57
3.8.2 Galvanic Cycling . . . 59
3.8.3 Electrochemical Impedance Spectroscopy . . . 60

4 Vanadium Pentoxide Nanosheets **65**
4.1 Introduction . . . 65
4.2 Experimental . . . 68
4.3 Results . . . 70
4.3.1 Synthesis of the Nanosheet Colloid . . . 70
4.3.2 Cathode Fabrication . . . 79
4.3.3 Electrochemical Characterization . . . 81
4.3.3.1 Single Li-Ion Intercalation Mechanism . . . 81
4.3.3.2 Diffusion Studies . . . 83
4.3.3.3 Multi Li-ion Intercalation mechanism . . . 84
4.3.3.4 Electrochemical Impedance Spectroscopy . . . 88
4.3.4 Post Characterization . . . 89
4.4 Conclusion . . . 91

5 Titanium Dioxide Nanoparticles **93**
5.1 Introduction . . . 93
5.2 Experimental . . . 96
5.3 Results and Analysis . . . 98
5.3.1 Synthesis of the Nanoparticle Colloid . . . 98
5.3.2 Anode Fabrication . . . 104
5.3.3 Electrochemical Characterization . . . 105
5.3.4 Post Characterization . . . 110
5.4 Conclusion . . . 112

6 Nanostructured Molybdenum Trioxide Composites **115**
6.1 Introduction . . . 115
6.2 Experimental . . . 118
6.3 Results . . . 120
6.3.1 Molybdenum Trioxide Nanobelts . . . 120
6.3.1.1 Synthesis of the Nanobelt Colloid . . . 120
6.3.1.2 Cathode Fabrication . . . 125
6.3.1.3 Electrochemical Characterization . . . 126
6.3.2 Molybdenum Trioxide/Graphene Nanocakes . . . 129
6.3.2.1 Synthesis of the Nanocake Colloid . . . 129
6.3.2.2 Cathode Fabrication . . . 134

6.3.2.3 Electrochemical Characterization 135
6.3.2.4 Post Characterization 139
6.3.3 Molybdenum trioxide/Vanadium Pentoxide Nanocomposite 140
6.3.3.1 Cathode Fabrication 140
6.3.3.2 Electrochemical Characterization 144
6.3.3.3 Post Characterization 148
6.4 Conclusion 149

7 Conclusion and Future Work **151**
7.1 Outlook 154

Bibliography **157**

List of Figures

1.1 Greenhouse emissions map 2
1.2 Ragone plot 4
1.3 Basic electrochemical cell 5
1.4 Hybrid electric vehicle 6
1.5 The voltaic pile 6
1.6 Different classses of supercapacitor Materials 13
1.7 Examples of nanomaterials 16
1.8 Intercalation mechanism 17

2.1 Gibbs energy profile 25
2.2 Chemical potentials 27
2.3 Electrode kinetics 28
2.4 Redox reaction 32
2.5 Capacitor schematic 33
2.6 Capacitive properties at the electrode surface 35
2.7 Potential distribution of a capacitor 36
2.8 Difussion process 37
2.9 Colloidal coagulation processes 41
2.10 Colloidal potential energy curves 42

3.1 The Sonication Process 45
3.2 The Cavitation Process 46
3.3 The Ultrasonic Spray Head 47
3.4 The electron microscope 50
3.5 The electron beam 51
3.6 Typical adsorption isotherms 53
3.7 XRD apparatus 54
3.8 XPS example 56
3.9 Potentiostat equivalent circuit and schematic of a typical cell 57
3.10 Typical CV profiles 58
3.11 GC Profiles 60
3.12 Typical nyquist plot and randles circuit 62
3.13 Impedance processes 63

4.1 V_2O_5 powder and crystal structure 66
4.2 TEM analysis of the V_2O_5 NS 71
4.3 XPS spectra of V_2O_5 NS 72
4.4 XRD patterns of V_2O_5 NS 74

4.5 The Extinction spectra of V_2O_5 NS . . . 75
4.6 The optimization of V_2O_5 NS in H_2O . . . 77
4.7 V_2O_5 NS particle count . . . 78
4.8 V_2O_5 stability . . . 78
4.9 V_2O_5 NS dispersion and ultrasonically sprayed film . . . 79
4.10 SEM images of V_2O_5 NS cathodes . . . 80
4.11 CV of the of V_2O_5 NS cathodes for a single Li-ion intercalation . . . 81
4.12 Initial GC of the V_2O_5 NS cathodes for a single Li-ion intercalation . . . 83
4.13 GITT profiles of the V_2O_5 NS cathodes . . . 84
4.14 CV curves of both the V_2O_5 NS cathodes for a multi ion intercalation process . . . 85
4.15 GC profiles of both the V_2O_5 NS cathodes for a multi ion intercalation process . . . 86
4.16 Cyclability and rate performance of the V_2O_5 NS cathodes for a multi ion intercalation process . . . 87
4.17 EIS of the V_2O_5 NS cathodes . . . 88
4.18 Post electrochemical TEM and SEM of the V_2O_5 NS/SWCNT cathode 89
4.19 Post electrochemical XPS and XRD patterns of the V_2O_5 NS/SWCNT cathode . . . 90

5.1 Anatase TiO_2 powder and crystal structure . . . 94
5.2 TEM analysis of TiO_2 NP . . . 99
5.3 XRD patterns of the of TiO_2 NP . . . 100
5.4 XPS spectra of the TiO_2 NP . . . 101
5.5 The Extinction spectra of TiO_2 NP . . . 102
5.6 Sonication Parameters of TiO_2 NP dispersion . . . 103
5.7 TiO_2 NP particle count . . . 104
5.8 SEM of TiO_2 nanoparticle electrodes . . . 105
5.9 CV of the TiO_2 NP anodes . . . 106
5.10 GC curves of the of TiO_2 anodes . . . 107
5.11 GC curves of the of TiO_2 NP anodes . . . 108
5.12 Cycleability and rate performance of the of TiO_2 NP anodes . . . 109
5.13 TiO_2 NP EIS spectrum . . . 110
5.14 SEM post cycling of the TiO_2 NP/SWCNT anode . . . 111
5.15 Post electrochemical XPS and XRD patterns of the TiO_2 NP/SWCNT anode . . . 112

6.1 MoO_3 powder and crystal structure . . . 116
6.2 TEM analysis of the MoO_3 NB . . . 121
6.3 XPS spectra of MoO_3 NB . . . 123
6.4 MoO_3 NB particle count . . . 124
6.5 XRD patterns of the MoO_3 NB . . . 124
6.6 SEM of the MoO_3 NB cathode . . . 125
6.7 CV of the of MoO_3 NB cathode . . . 126
6.8 GC curves of the MoO_3 NB cathode . . . 127
6.9 Rate performance and cycleability of the MoO_3 NB cathode . . . 128
6.10 EIS of the MoO_3 NB cathode . . . 129
6.11 TEM analysis of the MoO_3 NC . . . 131

6.12 XPS spectra of the MoO_3 NC 132
6.13 The optimization of the MoO_3 NC 133
6.14 XRD patterns and particle count of the MoO_3 NC 133
6.15 SEM of MoO_3 NC cathodes 134
6.16 CV of the of MoO_3 NC cathode 136
6.17 GC curves of the MoO_3 NC cathodes 137
6.18 Rate performance and cycleability of the MoO_3 NC cathodes 138
6.19 EIS the MoO_3 NC cathodes 138
6.20 Post electrochemistry SEM images of the MoO_3 NC/SWCNT cathodes 139
6.21 Post electrochemical XPS and XRD of the MoO_3 NC cathodes 140
6.22 SEM of MoO_3/V_2O_5 nanocomposite cathodes 141
6.23 XPS of MoO_3/V_2O_5 nanocomposite cathodes 142
6.24 XRD patterns of MoO_3/V_2O_5 nanocomposite cathodes 143
6.25 CV of the MoO_3/V_2O_5 nanocomposite cathodes 144
6.26 GC curves of the MoO_3/V_2O_5 nanocomposite cathodes 145
6.27 GC curves of the MV25 nanocomposite cathode 146
6.28 Rate performance and cycleability of the MV25 nanocomposite cathode147
6.29 EIS of the MV25 nanocomposite cathode 148
6.30 Post electrochemical SEM of the MV25 nanocomposite cathode . . . 148
6.31 Post electrochemical XPS spectrum of the MV25 nanocomposite cathode149
6.32 Post electrochemical XRD pattern of the MV25 nanocomposite cathode 150

7.1 Ragone plot for studied TMO materials 154

List of Tables

2.1 Standard Reduction Potentials 23

6.1 Relative quantities of various V_2O_5 oxidation states for different composite cathodes. 143

List of Abbreviations

2EC	**2** Electrode Cell
3EC	**3** Electrode Cell
AC	Activated Carbon
BET	Brunauer Emmett Teller
BV	Butler Volmer
CE	Counter Electrode
CNT	Carbon Nanotube
CP	Conductive Polymers
CVD	Chemical Vapour Deposition
DFT	Density Functional Theory
EDL	Electrochemical Double Layer
EDX	Electron Dispersive X-ray
EELS	Electron Energy Loss Spectroscopy
EM	Electron Microscopy
EMF	ElectroMotive Force
ESCA	Electron Spectroscopy for Chemical Analysis
FFT	Fast Fourier Transform
GITT	Galvanic Intermittent Titration Technique
HEV	Hybrid Electric Vehicle
HOMO	Highest Occupied Molecular Orbital
IHP	Inner Helmholtz Plane
ITO	Indium Tin Oxide
KE	Kinetic Energy
LIB	Lithium Ion Bbattery
LPE	Liquid Phase Exfoliation
NB	NanoBelt
NC	NanoCake
Ni-CD	Nickel Cadmium
Ni-MH	Nickel Metal-Hydride
OHP	Outer Helmholtz Plane
OPE	Open Circuit Potential
RE	Reference Electrode
SC	SuperCapacitor
SEI	Solid Electrolyte Interface
SEM	Scanning Electron Microscope
SHE	Standard Hydrogen Electrode
STEM	Scanning Transmission Electron Microscope
SWCNT	Single Walled Carbon Nanotube
SWG	Signal Waveform Generator
TEM	Transmission Electron Microscope

TMD	**T**ransition **M**etal **D**ichalchogenide
TMO	**T**ransition **M**etal **O**xide
UV-vis	**U**ltra**V**iolet **S**pectroscopy
WE	**W**orking **E**lectrode
XPS	**X**-ray **P**hotoelectron **S**pectroscopy
XRD	**X**-**R**ay **D**iffraction

Physical Constants

Faraday's constant	$\mathrm{F} = 9.648 \times 10^4\ C\,mol^{-1}$
Avagadro's number	$N_A = 6.022 \times 10^{23}$
Electron charge	$\mathrm{e} = 1.602 \times 10^{-19}\ C$
Universal gas constant	$\mathrm{R} = 8.314\ J\,K^{-1}\,mol^{-1}$
Boltzmann constant	$k_B = 1.381 \times 10^{-23}\ m^2\,kg\,s^{-2}\,K^{-1}$
Permittivity of free space	$\epsilon_0 = 8.854 \times 10^{-12}\ A^2\,s^4\,kg^{-1}\,m^{-3}$
Mass of electron	$m_e = 9.109 \times 10^{-31}\ kg$
Plank's Constant	$\mathrm{h} = 6.626 \times 10^{-34}\ m^2\,kg\,s^{-1}$
Pi	$\pi = 3.14159$

List of Symbols

a_j	Activity of Species j	
${a_R}^r$	Reactant Activity	
${a_P}^p$	Product Activity	
a_0	Lattice Parameter	m
A	Absorbance	
A_{BET}	Specific Surface Area	$m^2\,g^{-1}$
A_{total}	Total Surface Area	m^2
A_c	Pre-exponential Factor	$M^{-(n-1)}\,s^{-1}$
A_s	Surface Area	$m^2\,g^{-1}$
A_H	Hamaker Constant	
BU	Binding Energy	J
c	BET constant	
C	Capacitance	F
C_{DL}	Double Layer Capacitance	F
C_a	Concentration of electrolyte at the anode	$g\,l^{-1}$
C_c	Concentration of electrolyte at the cathode	$g\,l^{-1}$
C_j	Concentration of species j	$g\,l^{-1}$
CPE	Constant Phase Element	F
C_{R_O}	Surface Concentration of the Reactant	$g\,l^{-1}$
d	Distance	m
d_{hkl}	Inter-planer Spacing	m
D	Diffusion Coefficient	$mol\,cm^{-2}\,s^{-1}$
D_∞	Diffusion Coefficient Infinite Temperature	$mol\,cm^{-2}\,s^{-1}$
E	Potential	V
E_{Att}	Attractive Surface Potential	J
E_{Rep}	Repulsive Surface Potential	J
E_T	Total Surface Potential	J
E_a	Anodic Potential	V
E_c	Cathodic Potential	V
E_{cell}	EMF of a Cell	V
${E_{cell}}^o$	Standard Potential of a Cell	V
E_i	Input Potential	V
E^i_{Sur}	Cohesive Energy Density	$J\,m^2$
${E_f}^0$	Formal Potential	V
E_{OCP}	Open Circuit Potential	V
E_O	Output Potential	V
$E(0)$	Applied Potential Amplitude	V
$E(t)$	Time Dependent Potential	V
E_+	Positive Potential	V

E_-	Negative Potential	V
G	Amplifier Gain	
$i(t)$	Time Dependant Current	A
$i(0)$	Current Amplitude	A
I	Current	A
j	Current Density	$A\,m^{-2}$
k_0	Rate Constant	$M^{-(n-1)}\,s^{-1}$
k^0	Frequency factor	$M^{-(n-1)}\,s^{-1}$
k_a	Anodic Rate Constant	$M^{-(n-1)}\,s^{-1}$
k_a^0	Anodic Frequency factor	$M^{-(n-1)}\,s^{-1}$
k_c	Cathodic Rate Constant	$M^{-(n-1)}\,s^{-1}$
k_c^0	Cathodic Frequency factor	$M^{-(n-1)}\,s^{-1}$
k_n	nth Order Rate Constant	$M^{-(n-1)}\,s^{-1}$
KU_{max}	Maximum Kinetic Energy	J
l	length	m
L_D	Length of Diffuse Layer	m
m	mass	g
M_w	Molecular Weight	$g\,mol^{-1}$
n_j	Number of Moles of Species j	mol
n	Number of Particles	
p	Pressure	Pa
p_o	Standard Pressure	Pa
p_i	Molar coefficient of product i	
q	Experimental Capacity	$mAh\,g^{-1}$
Q	Theoretical Capacity	$mAh\,g^{-1}$
Q_i	Charge of Species i	C
r_i	Molar Coefficient of Reactant i	
R	Radius	m
R_{CT}	Charge Transfer Resistance	Ω
R_S	Series Resistance	Ω
t	A Point in Time	s
t_i	Time Length of Event i	s
t_{switch}	Time of Switching	s
T	Absolute Temperature	K
s	Cross Sectional Area	m^2
U	Energy	J
U_{max}	Energy Density	$J\,kg^{-1}$
U_A	Activation Energy	J
U_c	Cohesive Energy Density	$J\,kg^{-1}$
v	Particle Velocity	$m\,s^{-1}$
v_g	Volume of Gas Adsorbed	l
v_m	Volume of One Monolayer	l
V_m	Molar Volume	$l\,mol^{-1}$
z	Particle Charge	
$Z(0)$	Impedance Amplitude	Ω
Z_0	Impedance of an Ideal Capacitor	Ω
Z_i	Impedance of element i	Ω

Z_t	Time Dependant Impedance	Ω
Z_W	Warburg Impedance	Ω
α_a	Transfer Coefficient of anode	
α_c	Transfer Coefficient of cathode	
γ_j	Activity coefficient of Species j	
δ	Phase Angle	$^\circ$
δG	Partial Gibb's Free Energy	J
δ_{n_j}	Partial Mole Fraction of species j	$M\,Pa^{0.5}$
δ_i	Solubility Parameter of component i	$M\,Pa^{0.5}$
δ_H	Hydrogen Bonding Hansen Solubility Parameter	$M\,Pa^{0.5}$
δ_D	Dipole Hansen Solubility Parameter	$M\,Pa^{0.5}$
δ_P	Polar Hansen Solubility Parameter	$M\,Pa^{0.5}$
δ_{NS}	Hildebrand Solubility Parameter of Nanosheet	$M\,Pa^{0.5}$
δ_{Su}	Hildebrand Solubility Parameter of solute	$M\,Pa^{0.5}$
δ_{Sv}	Hildebrand Solubility Parameter of solvent	$M\,Pa^{0.5}$
δ_t	Hildebrand Solubility Parameter	$M\,Pa^{0.5}$
ΔE_S	Potential Window Between Relaxation	V
ΔE_τ	Potential Window Between Pulse	V
ΔE	Potential Window	V
ΔG_{mix}	Gibb's Free Energy of Mixing	$J\,mol^{-1}$
ΔG_P	Gibb's Free Energy of the Products	J
ΔG_R	Gibb's Free Energy of the Reactants	J
ΔG_{sys}	Gibb's Free Energy of a System	J
Δ_{so}	Spin Orbital Splitting	eV
ΔG^+	Gibb's Free Energy at Transition State	J
ΔH_{mix}	Enthalpy of Mixing	$J\,mol^{-1}$
ΔS_{mix}	Entropy of Mixing	$J\,mol^{-1}\,K^{-1}$
ϵ	Extinction Coefficient	$g\,mol^{-1}\,cm^{-1}$
ϵ_r	Relative Permittivity	
ζ	Zeta Potential	V
η	Overpotential	V
η_C	Concentration Overpotential	V
η_{CT}	Charge Transfer Overpotential	V
θ	Angle	$^\circ$
κ^{-1}	Debye Length	m^{-1}
λ	Wavelength	m
μ_j	Chemical potential of species j	$J\,mol^{-1}$
$\mu_j{}^0$	Standard Chemical potential	$J\,mol^{-1}$
ν	Frequency	Hz
ν_{NS}	nanosheet Volume	m^3
τ	Period of a Pulse s	
υ	Scan Rate	$mV\,s^{-1}$
Φ	Work Function	J
ϕ_{El}	Potential on the Electrode	V
ϕ_{IHP}	Potential on the IHP	V
ϕ_{Sol}	Potential on the Solvent	V
ϕ_{OHP}	Potential on the OHP	V

ω	angular frequency	rad

List of Publications

- K. R. Paton, E. Varrla, C. Backes, R. J. Smith, U. Khan, A. O'Neill, C. Boland, M. Lotya, O. M. Istrate, P. King, T. Higgins, S. Barwich, P. May, P. Puczkarski, I. Ahmed, M. Moebius, H. Pettersson, E. Long, J. Coelho, **S. O'Brien**, E. K. McGuire, G. S. Mendoza Sanchez B.and Duesberg, N. McEvoy, T. J. Pennycook, C. Downing, A. Crossley, V. Nicolosi, and J. N. Coleman, "Scalable production of large quantities of defect-free few-layer graphene by shear exfoliation in liquids", Nat. Mater. 13, 624–630 (2014).

- H. Nolan, B. Mendoza-Sanchez, N. A. Kumar, N. McEvoy, **S. O'Brien**, V. Nicolosi, and G. S. Duesberg , "Nitrogen-doped reduced graphene oxide electrodes for electrochemical supercapacitors", Phys. Chem. Chem. Phys., 16, 2280-2284 (2014)

- **S. O'Brien**, H. Petterson, V. Nicolosi, "Liquid Phase Exfoliation of Two Dimensional Transition Metal Oxides for Electrochemical Applications", Flatlands - Beyond Graphene, Bar-Ilan University, Tel Aviv, Israel (2015)

- C. S. Cucinotta, K. Dolui, H. Pettersson, Q. M. Ramasse, E. Long, **S. O'Brien**, V. Nicolosi, and S. Sanvito, Electronic Properties and Chemical Reactivity of TiS2 Nanoflakes", J. Phys. Chem. C, 119 (27), 15707–15715 (2015)

- **S. O'Brien**, C.F. Zhang, V. Nicolosi, "Liquid Phase Exfoliation of Two Dimensional Transition Oxide Metals", 228th ECS Meeting, Phoenix, Arizona, USA (2015)

- B. Mendoza-Sanchez, D. Hanlon, J. Coelho, **S. O' Brien**, H. Pettersson, J. Coleman, V. Nicolosi, "An Investigation of the Energy Storage Properties of a 2D $\alpha - MoO_3$-SWCNTs Composite Films" (2016)

- J. C. F. Zhang, T. M. Higgins, S-H. Park, **S. O'Brien**, D. Long,. J. N. Coleman, "Highly Flexible and Transparent Solid-State Supercapacitors Based on RuO_2/ PEDOT:PSS Conductive Ultrathin Films" Nano Energy (2016) (Pending)

- **S. O'Brien**, C.F. Zhang, V. Nicolosi, "Liquid Phase Exfoliation of Two Dimensional Vanadium Pentoxide", NanoTeC16, Trinity College, Dublin, Ireland (2016)

Chapter 1

Introduction and Motivation

1.1 Motivation

Due to the effects of greenhouse emissions, climate change is becoming major problem throughout both the developed and developing world [1]. This is especially evident in the erratic weather patterns coupled with regional flooding, the melting of the ice caps and of course the smog epidemic in many major cities [2]. These environmental problems have increased the globe's awareness of the necessity to reduce greenhouse emissions. To date, most greenhouse emission stem from the burning of fossil fuels in the production of energy for transport systems, industry and grid electricity. Both historically and in modern times, energy production and dissipation has played a vital role in powering out infrastructure. However, if greenhouse emissions are to be reduced, care must be taken not to damage global economies and energy security. Furthermore, the energy needs of the one billion people currently living off the grid due to poverty needs to be addressed. It is estimated that, due to increases in the global population and the high energy demands of modern electronic devices, the world's energy consumption will grow by more than 50% by 2040. The prospect of using nuclear energy as an alternative to fossil fuels has recently been overshadowed by severe and disastrous events such as the events in Chernobyl, Three Mile Island and Fukushima. The safe and efficient disposal of nuclear waste also provides grave concerns. However, contemporary energy production and dissipation is still largely dependant on the burning of fossil fuels. The depletion of this natural resource forces us to seek viable alternatives.

In December 2015, the 21st Conference of Parties (COP21) met in Paris to discuss greenhouse emissions and climate change [1]. It is their aim to limit the rise in global temperatures due to greenhouse gases to below $2^{\circ}C$ relative to pre-industrial

levels. To achieve this aim, the Emissions Trading Scheme (ETS) was set up to monitor the amount of greenhouse gas pumped into the atmosphere by each region of the world. Figure 1.1 indicates how much CO_2 each region of the world pumps into the atmosphere from fossil fuel consumption each year. According to the ETS, each region has a particular "allowance" of greenhouse emissions it must comply to keep in line with the proposed limit.

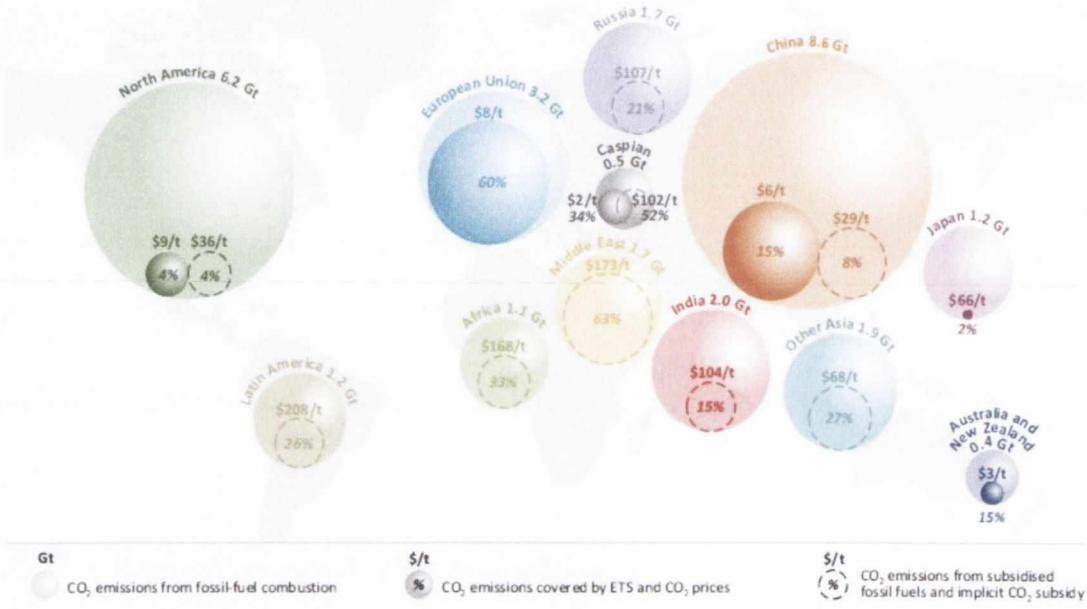


FIGURE 1.1: Map showing relative greenhouse emissions from each part of the world coupled with the average ETS allowance for each area (taken from [1]).

This "allowance" will have many countries pledging to cut greenhouse emissions drastically. For example, by 2025 the United States plans on cutting greenhouse emissions by 28% relative to 2005 while, by 2040 the European Union hopes to reach 40% relative to 1990. This would result in energy related greenhouse gas emissions declining at twice the rate achieved since the beginning of the millennium. Even now, the use of low carbon emitting sources is expanding rapidly. In 2014 alone the world economy grew 3% while global greenhouse emissions stayed relatively flat. This can be heavily attributed to the continuing investment ($270 Billion in 2014) countries such as China, Japan, Germany and The United States are pumping into renewable energies.

As a consequence, significant work is being focused on implementing and expanding renewable energy sources in modern society [3]. While fossil fuels maintain their levels of consumption, low carbon emitting sources of renewable energy

currently account for about 10% of global energy production [1]. Continued implementation of renewable energy sources in transport, industry and grid energy will contribute highly to aims expressed by the COP21. Currently, most renewable energy is sourced from solar, wind and hydrothermal energy, with geothermal and wave energy increasing in popularity. Many high scale renewable energy plants around the world produce vast amounts of energy such as the Charanka Solar Park in India (600 MW) and the London Array Offshore Wind farm in the United Kingdom (630 MW). However, in cases such as that in transport systems, efficient and environmentally friendly methods of storing this energy are required as the production of energy is only a precursor stage. Similarly, portable electronics such as laptops, cellphones and power tools will require a direct flow of energy off the grid. Therefore, it is necessary that reliable and sustainable energy storage devices are available [4].

1.2 Energy Storage

Energy storage devices have been a major milestone in the efficient distribution of energy ever since the advent of the technological revolution [5, 6]. From large scale transport vehicles to hand-held devices, much of modern life relies heavily on the direct access to electricity. However, not all devices can be directly connected to power grids.

Over the last two centuries, the development of energy storage has provided us with a wide range of devices with various energy and power densities [7]. The interplay between energy and power for a selection of devices is illustrated by the typical Ragone plot shown in Figure 1.2. Ideally, energy storage devices should exhibit both high energy and power densities such as that exhibited by a typical combustion engine. The burning of fossil fuels provides a large amount of energy while providing a large power needed short time-scale applications (e.g. acceleration) [8]. However, combustion engines are a heavy contributor to greenhouse emissions. They also have low output efficiencies as they are limited by the Carnot cycle [9]. Devices with higher efficiencies and lower output emissions, such as that of electrochemical devices, tend to favour a high energy or power density while keeping the other low.

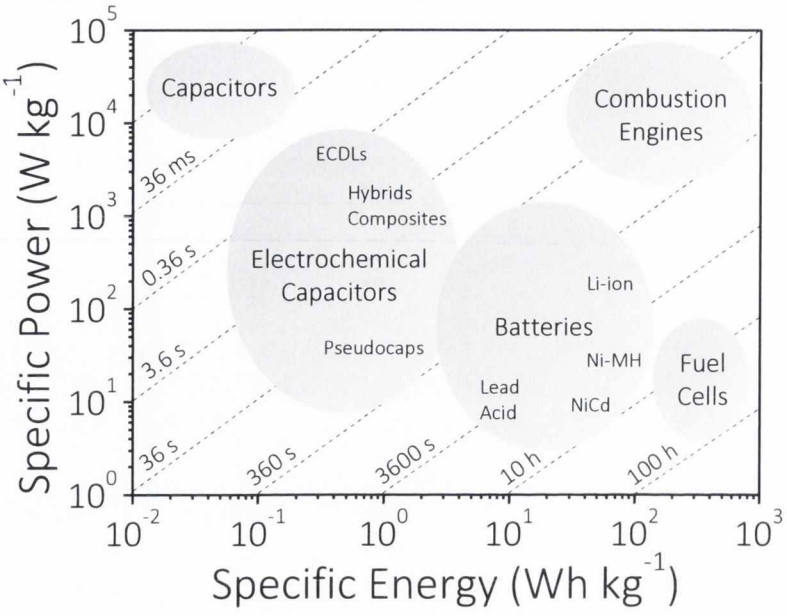


FIGURE 1.2: Ragone plot

1.3 Electrochemical Energy Storage

For portable electronics and HEVs, electrochemical storage devices are in widespread use. The three most common types of electrochemical storage device are the fuel cell, the supercapacitor and the battery [10]. Currently, rechargeable batteries are dominating the energy storage markets with niche positions available for supercapacitors and fuels cells. Rechargeable batteries are common power sources for items such as laptops, cell phones and in the ignition of engines in automobiles [4]. The energy storage mechanisms for each system are relatively unique, however, they retain a general similarity. The basic operation of an electrochemical device is the transfer or storage of charge at an electrode/electrolyte interface. For example, a typical Zn-Cu system is illustrated in Figure 1.3. Electron transfer reactions occur at the interfaces between the Cu cathode, Zn anode and the ionically conductive electrolyte.

Here follows a brief description of both batteries and supercapacitors.

1.3.1 Batteries

Almost all modern portable electronic devices are powered by either single use or rechargeable batteries. Currently, batteries are being developed to meet an increasing diverse range of applications. Unlike other electrochemical devices, batteries

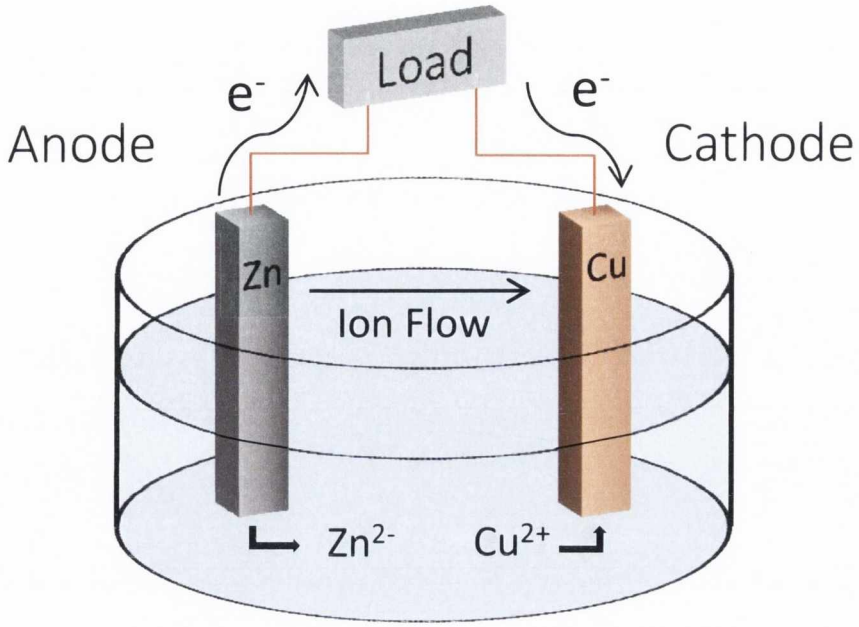


FIGURE 1.3: Basic schematic of an electrochemical cell

have the advantage of intense decades of research coupled with many commercially available types such as the alkaline, the metal hydride, the lead acid and, the possibly better known, Li-ion battery (LIB) [11].

Although batteries are already used in the ignition of automobile engines, they may in the future find a position in vehicular energy storage. Coupled with other devices such as supercapacitors, they will provide the energy needed to operate a vehicle as the burning of fossil fuels may become obsolete [12]. It is likely the batteries will store energy from renewable sources such as wind or solar energy. Already, contemporary HEVs couple a high energy Li-ion or Li-MH battery with a combustion engine to reduce greenhouse emissions, see Figure 1.4 [13]. In the above example, the Li-ion batteries act to provide constant energy to keep the car moving while acceleration is achieved by the combustion engine. However, as fossil fuels become obsolete, supercapacitors may have to provide the necessary power normally provided by the combustion engine [14]. It is estimated that, due to future demands for batteries in HEVs, the battery market is expected to grow to $190 billion by the year 2019 with China being the largest producer of batteries [1]. Much work is being done to improve modern battery systems to meet the needs of the future.

Before the inventions of electronic grids, fuel cells or electronic generators, batteries played the leading role in energy dissipation in the late 19th century. Initially, all batteries were what are called a "primary cell". A primary cell is a battery that,



FIGURE 1.4: Hybrid electric vehicle with rows of Li-ion batteries(taken from[15]).

once they were discharged they could no longer be used due to the inherent irreversible chemical processes. As such all batteries were assembled in a charged state and disposed of after a full discharge.

In 1800, Alessandro Volta invented the first true functioning battery, which comprised of a series of Cu and Zi electrodes separated by layers of cloth soaked in salt water [16]. This became known as the Voltaic Pile (see Figure 1.5). The Voltaic pile was the first device to provide a constant electric current to an external circuit contrary to previously discovered devices such as the Leyden jar [17]. The Voltaic pile was paramount in the discovery of such elements as sodium and calcium by Humphrey Davy as it worked to isolate these elements [18].

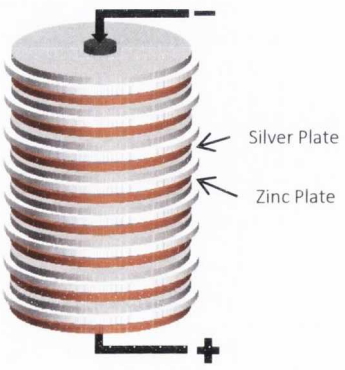


FIGURE 1.5: The Voltaic Pile

Similar to other electrochemical devices, batteries contain a pair of electrodes separated by an ionically conducting electrolyte. Energy is provided to or dissipated through an external load by means of slow Faradiac chemical reaction on the surfaces of the electrodes. Depending on the electrode materials, these reactions may be reversible or irreversible. Typically batteries can be classified as either primary batteries, as mentioned earlier, or secondary batteries. Secondary batteries generally exhibit highly reversible reactions on the electrode surfaces allowing the devices to be recharged and used again. As such, they are also termed rechargeable batteries.

The work of Volta inspired many other researchers in the 19th and 20th century to design new and improved primary battery systems. In 1836 the invention of the Daniel cell prompted the first use of the both Cu and Zi based electrodes and electrolytes [19]. This cell was commonly used as the source for power in the contemporary industries and actually became the standard to which the volt was defined [20]. The rest of the 19th century seen improvements and variations in this technology, for example, Bird's cell, the gravity cell, the Grove and Dun cells [21–24]. Progress in battery research advanced significantly in the 20th century with improvements in both battery safety and storage capability. Primary batteries have seen many technological advances over the past century, from the invention of the Leclanchè cell to the modern day use of the disposable alkaline MnO_2 batteries [25–27]. The alkaline MnO_2 cell accounts for nearly 80% of manufacturing and sales of primary batteries today. While having a low nominal potential of 1.5 V, the alkaline MnO_2 cell displays an energy density reaching upwards of 80 $Wh\,kg^{-1}$ making it attractive for long term use in small portable devices. They also exhibit an impressive shelf life. The overall reaction present in an alkaline MnO_2 cell is:

$$Zn + 2MnO_2 \rightleftharpoons ZnO + Mn_2O_3 \tag{1.1}$$

While primary batteries such as the alkaline MnO_2 system provides a large energy density needed for modern electronic devices, they are single use devices which make them both inefficient and hazardous to the environment if not recycled properly.

Secondary batteries - In 1859, Gaston Plantè discovered the first rechargeable lead-acid battery [28, 29]. Currently, most of the worlds lead acid batteries are employed in the ignition of vehicular engines [30]. However, they have also found

application as large backup power supplies for housing and industry. Despite being a popular choice for rechargeable device, lead-acid batteries exhibit a low energy density reaching no higher than 50 $Wh\,kg^{-1}$ coupled with a low cycle life time. Compared to the alkaline MnO_2 battery, this energy density is relatively low. Despite this, the lead acid battery does exhibit a nominal potential of 2 V and can demonstrate power densities upwards of 180 $Wh\,kg^{-1}$ due to large surge currents. Lead acid batteries exploit the reversibility of lead metal in a lead sulphate electrolyte.

$$Pb + PbO_2 + 2H_2SO_4 \rightleftharpoons 2PbSO_4 + 2H_2O \tag{1.2}$$

The first major competitor of the lead acid battery was the Ni-Cd battery discovered by Jungner in 1899 [31]. The energy density exhibited by the Ni-Cd system was compatible to that of the alkaline MnO_2 battery while still maintaining high reversibility. The device is known to exceed 1500 cycles far outreaching that of the lead acid battery, although it exhibits a lower nominal potential of 1.2 V. The chemical process can be described as,

$$2Ni(OH) + Cd + 2H_2O(l) \rightleftharpoons 2Ni(OH)_2 + Cd(OH)_2 \tag{1.3}$$

The Ni-Cd system was widely used in power tools and portable electronics until the invention of higher energy rechargeable batteries in the 1990s such as the Ni-MH or the Li ion batteries. Ever since then the Ni-Cd batteries have dropped in sales by 80%.

The first Ni metal hydride (Ni-MH) batteries came on the scene in the late 1960s and early 1970s [32]. Although it averaged an energy density of about 120 $Wh\,kg^{-1}$, it sometimes exceeded 1000 $Wh\,kg^{-1}$. As a result, it quickly replaced the Ni-Cd device in portable consumer electronics despite having a much lower cycle life (<500 cycles) [33]. Currently, the Ni-MH system batteries account for over 2 million HEVs. Despite their popularity, the Ni-MH system is in high competition with modern Li-ion intercalation systems.

1.3.1.1 Lithium Ion Batteries

Lithium ion batteries (LIB) are a highly promising candidate for high energy density applications, specifically in the areas or portable electronics and HEVs [34, 35].

Currently, LIBs are present in most hand-held electronic devices from laptops and cellphones to cordless power tools. Lithium ions (Li-ions) possess a range of attractive properties such as low atomic radius and a relatively high electronegativity, making them idea candidates for intercalation based energy storage devices.

In the early 1970s it was discovered that Li-ions could intercalate into a series of layered dichalcogenides [36]. Specifically, TiS_2 was most appealing due to the formation of a single phase through the intercalation mechanism [37]. This allowed for more reversible intercalation and deintercalation processes. Also, as TiS_2 is known to be a semi-metal, there is no need for the addition of conductive diluent However, TiS_2 is known to pose safely concerns as well as being highly oxidizable. Similarly, the use of pure Li metal as the counter electrode for consumer energy storage devices poses serious safety concerns.

The work of Goodenough in the early 1980s showed how Li-ions could be electrochemically extracted from materials such as $LiCoO_2$ [38]. This lead SONY to produce the first commercial Li-ion battery in the early 1900s which, to this day, dominates the Li-ion market [39]. This device utilized $LiCoO_2$ as the cathode material, graphite as the anode material with propylene carbonate (PC) as the electrolyte. Unlike Li metal, graphite is a much safer material forming only Li_xC_6 upon Li-ion intercalation when the cell is in a charged state [40]. Discharging the cell will cause the Li-ions to deintercalation from the graphite matrix and intercalate back into the CoO_2 structure according to the following equations,

$$Li_{1-x}CoO_2 + xLi^+ \rightleftharpoons LiCoO_2 \quad (Cathode) \tag{1.4}$$

$$6C + xLi \rightleftharpoons Li_xC_6 \quad (anode) \tag{1.5}$$

Although the theoretical charge storage capacity of $LiCoO_2$ is 272 $mAh\,g^{-1}$, experimentally and practical values reach no higher than 140 $mAh\,g^{-1}$ in a potential window of 3 V – 4.2 V [41]. This is due to $LiCoO_2$ only being able to accommodate 0.5 Li/Co safely and still remain partially reversible [34]. Despite this, $LiCoO_2$ is known to exhibit energy densities upwards of 180 $Wh\,kg^{-1}$ which provides a satisfactory runtime for such devices as cell phones or laptops, however, inefficient for large scale devices such as automobiles. Having a nominal potential of 3.7 V, there is much scope for a much higher energy density device provided work is done on reducing the irreversibility of the $LiCoO_2$ electrode. The low storage capacities

and cycling performances of $LiCoO_2$ based cathodes coupled with its limited applications and the scarcity of Co prompted the investigation into a series of other Li based oxide materials.

When researching LIB materials, is it desirable to design a material with a high energy density, long life cycle with minimal reduction in capacity retention. Similarly a material that delivers a high power density is desirable. An efficient rechargeable battery system should be able to run for 2000 cycles while still retaining 80% of its initial capacity. Therefore, it is advantageous to optimize the system's cathode, anode and electrolyte performances. It has been widely shown that the overall capacity of a cell is greatly limited by the capacity of the cathode.

Cathode materials - With the exception of materials such as carbon and TiS_2, most prospective cathode materials are semiconducting in nature and require conductive diluent to optimize their performance [42, 43]. In general materials such as carbon nanotubes (CNT) and activated carbons (AC) are added to decrease the inherent charge transfer resistances of these cathodes. Similarly, polymer binders are commonly added to improve the structural integrity.

Olivine $LiFePO_4$ has recently been gaining popularity as a LIB cathode material ever since it was first discovered it could intercalate Li-ion in 1996 [44, 45]. Although having a lower specific energy (110 $Wh\,kg^{-1}$) than $LiCoO_2$, $LiFePO_4$ offers a longer life time coupled with a high power density (>2000 $W\,kg^{-1}$). $LiFePO_4$ also shows improved safety considerations as well as commercially abundant materials. However, high self-discharge problems are common compared to that of other Li-ion cathode materials which leads to poor ageing. Despite this, $LiFePO_4$ is showing promise as an efficient LIB cathode material for wide spread applications including in automobiles and backup power systems.

The insertion of Li-ions into manganese oxides was first realized in 1983. It was not until 1996 that the first $LiMn_2O_4$ LIB was commercialized [46]. The relatively high power densities exhibited by this material can be attributed to the efficient diffusion of Li-ions down its spinel structure. Despite having a theoretical capacity of 148 $mAh\,g^{-1}$, $LiMn_2O_4$ experimentally exhibits a capacity no higher than 125 $mAh\,g^{-1}$. A energy density of 110 $Wh\,kg^{-1}$, a nominal potential of 3.8 V and a good thermal stability makes $LiMn_2O_4$ competitive with $LiFePO_4$ and it is commonly used in power tools and medical instruments.

Many other Li-based metal oxides are showing promise as efficient LIB cathode materials including $LiNiMnCoO_2$ (220 $Wh\,kg^{-1}$) and $LiNiCoAlO_2$ (260 $Wh\,kg^{-1}$)

although improvements in cycle behaviour and life time are paramount in the utilization of these materials in consumer products [34]. A wide range of other metal oxides and metal chalcogonides are also being investigated as suitable cathode materials for the next generation of LIBs [47].

Anode materials – Anode materials have been widely researched and generally show much larger storage capacities than that of their corresponding cathode materials [48–50]. Traditionally, anode materials revolve around the use of carbon materials such as graphite [51]. Graphite exhibits both a high theoretical capacity of 372 $mAh\,g^{-1}$ and a superior energy density of 1500 $Whkg^{-1}$ making it a common anode material found in modern energy storage devices. However, graphite is known to have some serious safety concerns specifically with the formation of SEI layers and dendrites [52–55].

More recently, research into a wider array of potential anode materials is being carried out, with anodes such as $Li_4Ti_5O_{12}$ already in commercial use. Nanostructured materials such as graphene (960 $mAh\,g^{-1}$) [56], CNTs (1100 $mAh\,g^{-1}$), Si (4200 $mAh\,g^{-1}$) [57] and its oxides (1600 $mAh\,g^{-1}$) [58], Sn (994 $mAh\,g^{-1}$) [53] and the titanates (300 $mAh\,g^{-1}$) [59] are promising materials competitive with that of graphite for the next generation of Li-ion battery anodes.

1.3.2 Supercapacitors

Recently, supercapacitors (SC) have attracted a significant amount of research attention due to their inherent high power densities, reversibilities, long life cycles and shelf life [60–62]. Like batteries, SCs are electrochemical energy storage devices, however, charge storage is mainly based on the adsorption of ions at the electrode/electrolyte interface of a high surface area material [10, 63]. The surface areas of SC exceed even that of conventional capacitors and as a result can store upwards of 100 times more charge. The characteristic physical adsorption of SC materials allows for a more rapid transfer of charge than that commonly exhibited by conventional battery materials. As such, SC enjoy a much higher power density which can even rival that of combustion engines. This method of adsorption also facilitates longer life cycles (> 100,000 cycles) and faster charging time periods (< 5 minutes) compared to contemporary devices. However, the amount of energy a SC can store is relatively low compared to that of combustion engines or batteries. Similarly, if left for a prolonged time in a state of charge a SC will slowly discharge itself. SCs

have found application in photographic flashes in digital cameras, portable speakers, energy harvesting and HEVs [60, 62]. It is envisioned that SCs will act as a complimentary device to a battery in the next generation of HEVs completely phasing out the need for combustion engines. While batteries will provide the energy to keep the car running, SCs will act as source for high power applications such as accelerations.

The SC was first patented in 1957 when The General Electric Company designed the first porous carbon electrolytic capacitor using an aqueous electrolyte [64]. The underlying physics of the SC charge storage mechanisms remained a mystery until in 1966 when the Standard Oil Company of Ohio determined the charge was stored electrostatically. This was based on previous research on the electrochemical double layer by von Helmholtz the previous century [65]. However, the SC remained relatively low key until in the early 1990s. It was about then it was first realized that the SC could be a possible hybrid device in HEVs [66, 67]. Currently the global supercapacitor market is estimated at $1.8 billion while it is expected to rise to $2 billion by 2020 [68].

SCs generally exhibit two different types of charge storage mechanisms [69–72]. The storage properties of both mechanisms heavily depend on the surface area and chemical properties of the electrode materials as well as the conductive properties of the electrolyte. However, both mechanisms differ in that charge can either be stored *via* the formation of capacitive double layer along the electrode/electrolyte interface or by the occurrence of pseudocapacitive charge transfer reactions on the electrode surface. Both of these processes happen at much faster rates than that of the Faradiac reactions evident in most battery materials. As such, SCs are known for their superiority power densities and low internal resistances. SCs can be classified into three main types based on the properties of their electrode materials as shown in Figure 1.6.

Initially, research focused on the capacitive properties of certain carbon based compounds [73, 74]. The formation of a highly capacitive electrochemical double layer along the surface of the carbon, such as AC, provided researchers with a new way to store charge. These carbons also benefited from high conductivities and chemical stabilities as well as utilizing low cost and wide spread availability. As a result, not only is carbon the most common materiel found in commercial SCs, it also is widespread in battery devices. Depending on their properties, carbons can be classed as either ACs, nanomaterials or aerogels [75, 76]. These various forms of carbons are quite structurally diverse and exhibit a wide range of properties. Carbon

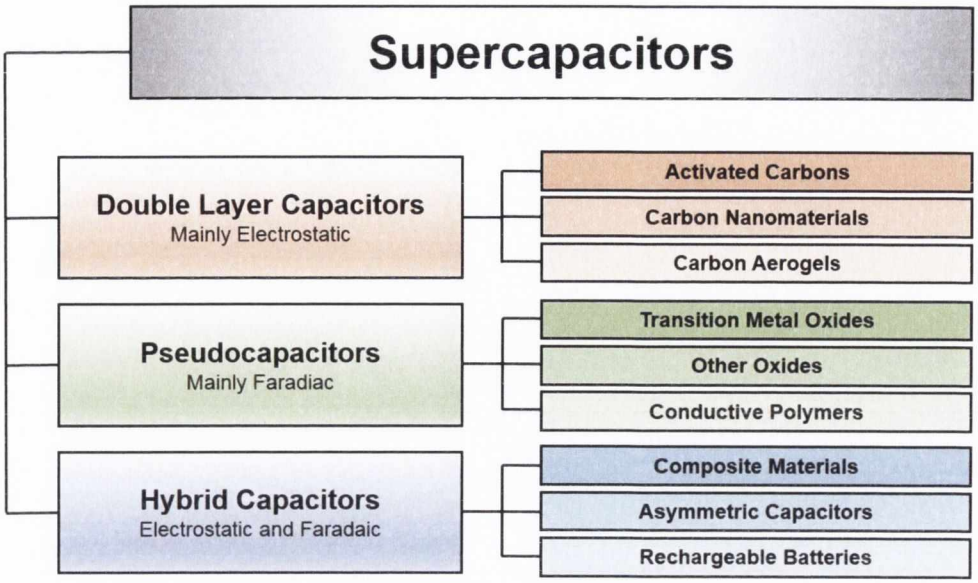


FIGURE 1.6: Different classes of supercapacitor materials.

itself is known to have four ordered allotropes based on various bonding mechanisms. Two of these allotropes are naturally occurring, namely graphite (sp^2) and diamond (sp^3), while the other two, carbine (sp^1) and fullerenes (distorted sp^2), are synthetic [77, 78].

Currently, the majority of commercially sold SCs are in the form of activated carbons (AC) [79]. ACs are a synthetic form of carbon, widely available and processable from carbonaceous materials such as coal or pitch. They are highly porous and can have a surface area that can reach upwards of 3000 $m^2\,g^{-1}$ depending on methods of fabrication. AC electrodes have been shown to exhibit capacities in the regions of 100 $F\,g^{-1}$ in aqueous electrolytes [73]. Carbon nanomaterials are another synthetic class of carbon materials [80]. While many different structural forms of nanostructured carbon exist, a vast majority of research is focused on both graphene and the CNT. Various methods have been used to synthesize graphene either by chemical synthesis or by the mechanical cleaving of individual sheets of graphite. Graphene has been shown to have very impressive structural and conductive properties making it an ideal candidate for the intercalation of Li-ions. Graphene suffers from a relatively low volume expansion and phase change upon ion intercalation commonly exhibited by in bulk electrode materials. This can be directly related to the layered structure of the material. Electrodes fabricated from graphene have been shown to exhibited capacitances upwards of 205 $F\,g^{-1}$ exceeding that of ACs [81]. Structurally similar to graphene, CNTs are a type of fullerene which consists of a rolled up graphene sheet. They show similar properties to graphene such as high

conductivities and surface areas but only reach capacitances upwards of 80 $F\,g^{-1}$ [76]. The last main group of carbons are the aerogels [82]. What make aerogels unique is the controllable mesoporous structure. They shows surface areas of about 1000 $m^2\,g^{-1}$ with capacitances reaching 220 $F\,g^{-1}$.

The second class of SC have a dominant pseudocapacitive charge storage mechanism on the electrode surfaces. They generally comprise of the transition metal oxides (TMO) or a range of conductive polymers [83, 84]. Similar to other layered materials, such as graphene or boron nitride, the TMOs are widely researched due to their layered structure. However, they possess a large range of oxidation states and facilitate highly reversible Faradaic reactions on the surface. The presence of these fast faradaic reactions are responsible for the pseudocapacitive behaviour which in the capacitances generally exceeds that exhibited by the carbons. Much research is being focused on the capacitive properties of RuO_2, MnO_2, MoO_3 and V_2O_5 [83]. Alone RuO_2 has been shown to reach capacitances upwards of 900 Fg^{-1}, however, the relative cost and scarcity of this material makes it unsuitable [85, 86]. Conversely, MnO_2 is a much more affordable material but its capacitance values are generally limited to 220 $F\,g^{-1}$ [87, 88]. As the TMOs charge storage mechanisms are similar to that of batteries they suffer from poor stabilities and cycle lifetimes. Also, their semiconducting nature severely limits their ability to transfer charge. Like the TMOs, Conductive polymers (CP) exhibit pseudocapacitive behaviour. CPs are a range of organic polymers which, through doping, can conduct electricity [89]. This is due to a conjugated π-bonding system due to overlapping p_z orbitals. The dopant acts to delocalize the π electrons hence making electrical conductivity possible. CPs are both lightweight and flexible and have the advantage of storing charge throughout the material itself as opposed to just on the surface. Various different conductive polymers are currently being researched such as polyaniline (C = 1500 $F\,g^{-1}$) [90, 91], polypyrole (C = 100 - 500 $F\,g^{-1}$) [92], polythiophene and its derivatives such as PEDOT (C = 1500 $F\,g^{-1}$) [93].

The last class of SC consist of a series of hybrid capacitors. Composites of two or more capacitive materials are synthesized in order to exploit the advantages of both [9]. For example, a graphene - TMO composite exploits the pseudocapacitive properties of the TMO material while using graphene as a highly conductive and capacitive additive alleviating the semiconducting behaviour and providing sites for improved storage of charge.

1.4 Nanoscience

The concept exploiting material properties on the atomic scale was first popularized in 1959 when Richard Feynman expressed his belief in the possibility of "manoeuvring things atom by atom" [94]. What makes the concept of the nanoscale so attractive is how the laws of physics vary between a bulk material and its nano equivalent. It is not uncommon for the well-established properties of a material to break down on the nanoscale such as thermal properties, surface properties and most notably, the dominance of quantum effects [95, 96]. Traditionally, the nanoscale has been associated with polymers, colloids, biological sub-cellular structures and even the concept of large individual molecules, see Figure 1.7. However, the recent discoveries of fabricated structures, such as that of two dimensional layered materials [97–99], zero dimensional quantum dots or buckyballs [100–103], and one dimensional nanotubes and nanowires [104–106], has open up doors into a wide variety of materials with diverse properties, see Figure 1.7. In 2014 it was estimated that $26 billion was invested in nanotechnology while this is expected to rise to $64.2 billion by 2020 [107].

The nanoscale has shown a diverse range of applications specifically in the fields of medicine [116, 117], biology [117, 118], energy storage [119, 120] and the semiconductor industry [100, 121]. One of the main driving forces for research on the nanoscale is the implementation of Moore's law [122]. According to Moore's law the amount of power a computer chip can process doubles every 18 months. Therefore, newer and more complex methods of synthesis on the nanoscale are being developed over time to keep up with this trend in computing. Further research is also required to consider the breakdown of well established properties on the mesoscale, as quantum effects tend to dominate on the nanoscale. However, the effect of nanomaterials on human health and the environment need to be considered [123, 124].

This emerging field of nanoscience can be loosely defined as the study and manipulation of nanoscale materials with focus on the breakdown of bulk properties. The implementation of these "nanomaterials" in industry and consumer electronics can be classified under nanotechnology. As a general rule, nanomaterials are defined by having one of more dimension less that 100 nm in length. More accurately these materials can be defined as pseudo-dimensional. For example, a zero-dimensional nanomaterial has all three lateral dimensions below 100 nm, one dimensional materials have two and two dimensional materials have three.

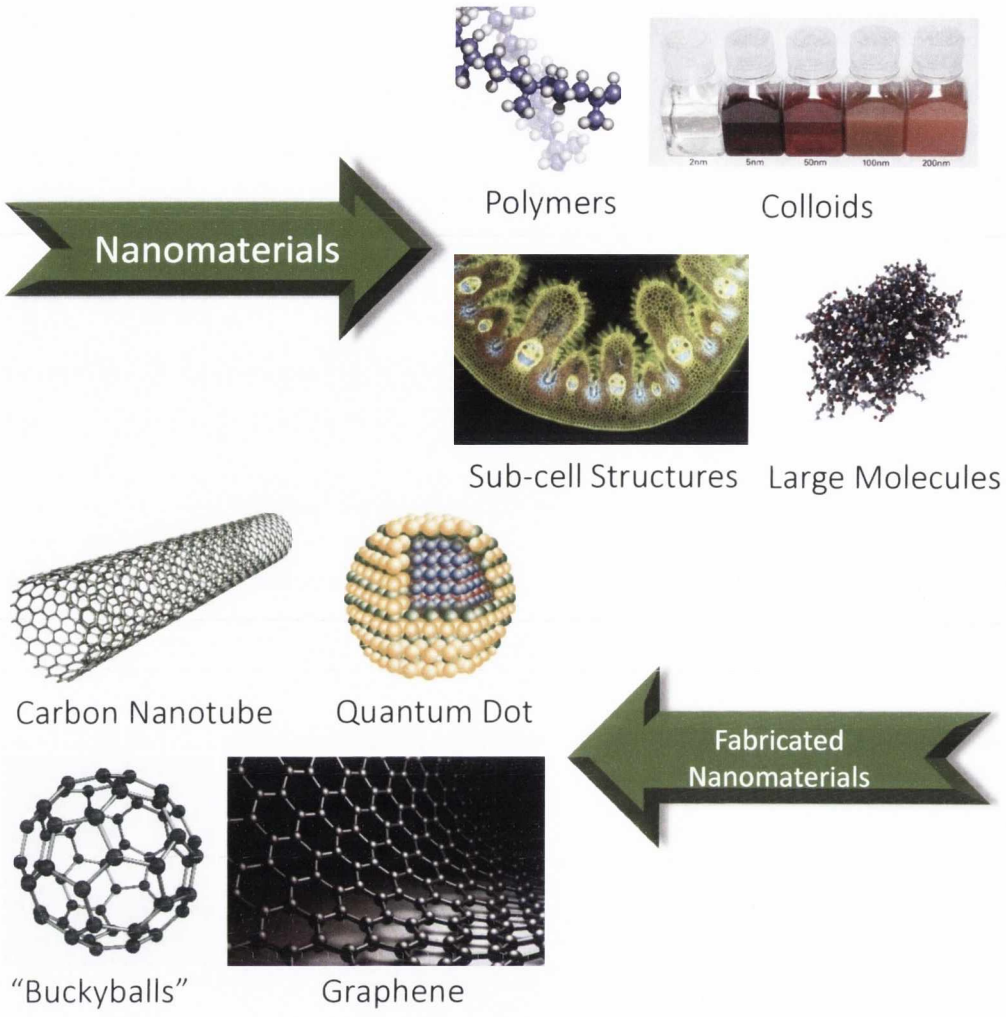


FIGURE 1.7: Examples of both naturally occurring and fabricated nanomaterials (taken from [108–115].)

Both naturally occurring and artificial nanomaterials have existed for a long time. The artificial implementation of nanomaterials has stretches even as far back as the 4th century when the Romans used gold nanoparticles to change the optical properties of the Lycurgus Cup [125, 126]. The fields of biology and medicine commonly deal with naturally occurring nanoscale structures, such as DNA or cell components, while modern advances in medicine have engineered nanoscale drug delivery systems and future prospects suggest the use of nanoscale robots capable of performing surgury [116, 117, 127]. Even naturally occurring inorganic matter such as sea water, volcanic ash and the atmosphere consist of various particles on the nanoscale [128]. Recent research in synthetic fabrication methods have opened up a world of artificial nanostructured particles and devices which are finding many real world applications due to their unique structures and desirable properties.

1.4.1 Nano-energy Storage

The incentive for designing energy storage devices based on nanomaterials would derive a significant improvement in both the energy and power properties [119, 120]. As exemplified earlier, intercalation based materials, such as $LiCoO_2$, possess a high theoretical capacity for a single Li-ion intercalation mechanism [34]. However, in cases such as in $LiCoO_2$, a fraction of the amount of Li-ions are intercalated per unit formula. Therefore, it is desirable to design new materials which can easily accommodate multiple Li-ions. By implementing nanostructured materials as active electrodes a series of significantly enhanced properties are evident. The vastly increased surface area of the electrodes act to provide more sites for ion intercalation and subsequent storage. Similarly, there are increased pathways conducive to ionic transport increasing the over all diffusion coefficients. This may also facilitate access to more material in thicker electrodes. These processes are illustrated in Figure 1.8. Materials such as bulk $LiCoO_2$ suffer from volume constraints upon ion intercalation and in some cases undergo irreversible phase changes. As such, this severely limits the amount of intercalation ions. Nanostructured materials would allow for better tolerance to volume change allowing for increased storage capacities and a reduction in phase changes.

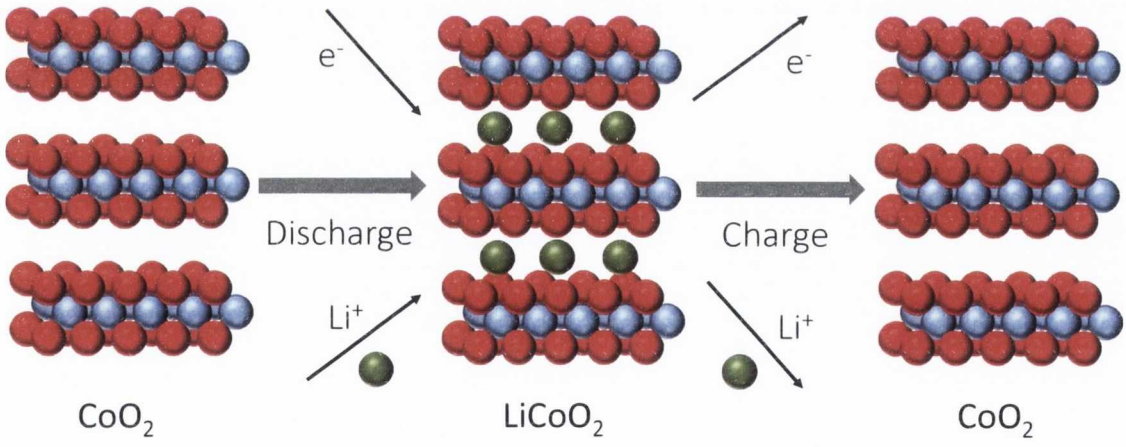


FIGURE 1.8: The general intercalation mechanism of nanostructured $LiCoO_2$.

To date, nanomaterials have been used to fabricate flexible thin film electrodes for use in low profile components such as flexible electronics [129], medical devices [130], bio-sensors [131] and energy storage devices. The fabrication of thin film electrodes has seen significant advances in the past few years ranging from simple filtration methods to highly sophisticated ultrasonic or deposition techniques [132]. High precision methods such as inkjet printing have also shown application in the

fabrication of high powered supercapacitor materials [133]. It is envisioned that nanomaterials will become the materials of choice for high energy Li-ion storage devices. This may range from low-level electronics, such as cellphones and laptops, to high level devices such as HEVs.

1.4.2 Two-dimensional Nanomaterials

A relativity new fields of nanoparticle research focuses on the application of a series of layered two dimensional materials. Layered materials possess a unique array of exotic electronic, thermal and mechanical properties while exhibiting a high degree of surface area important for catalysis, sensing and energy storage application [97, 134, 135]. The first artificially synthesized layered material was discovered by Novosolov and Geim in 2004 when they mechanically exfoliated graphite to produce graphene monolayers [136]. This anatomically thin allotrope of carbon possesses a unique honeycomb structure which exhibits a wide range of superior properties. Its large surface area (2630 $m^2\,g^{-1}$) [137], high carrier mobility ($\approx$ 15,000 $cm^2\,V^{-1}\,s^{-1}$) [138], Young's modulus ($\approx 1\ TPa$) [139] and thermal conductivity (upwards of 5000 $W\,m^{-1}\,K^{-1}$) [140] makes it an attractive material for a wide range of applications [141].

The work with graphene led many researchers to discover a whole zoo of two dimensional layered materials ranging from Boron Nitride, to a range of TMOs, TMDs, TMTs, MXenes and layered hydroxides [97, 98]. However, the synthesis and development of these materials have been held back due to the lack of facile methods to exfoliate large quantities of mono- of few-layers materials. To date, methods such as mechanical cleaving [142], ion intercalation [143], chemical vapour deposition (CVD) [144] and chemical synthesis [145] have all shown to produce reasonable yields of layered materials. However, the recent the work of Coleman and Paton has shown how simple liquid phase techniques can be employed to produce large quantities of nanosheets in stable dispersions [135, 146, 147].

The potential application of layered materials as electrochemically active electrodes for both SCs and LIBs has been extensively researched over the past decade [48, 119, 148]. Layered materials promote large surface areas coupled with marked reductions in ion diffusion coefficients [135]. Because of these advantageous, layered materials tend to exhibit much larger storage capacities than that of their bulk counterparts. Specifically, work on a series of pseudocapacitive TMO materials, such as MnO_2, V_2O_5, MoO_3 and RuO_2, have shown applications in a wide variety of

SC and LIB devices, despite their inherent semiconducting nature [149, 150]. Much work is being done to improve the long term cycling properties of these materials for the next generation of energy storage devices.

1.5 Scope and Aim

In this work, the aim is to implement ultrasonically synthesized nanomaterials to improve the electrochemical performances of a series of TMO materials and investigate their eligibility as electrodes Li-ion energy storage devices. The process of this investigation is outlines as follows: (a) A range of high capacity TMO materials were chosen, namely V_2O_5, TiO_2 and MoO_3, reflecting their ability to form nanostructures, coupled with high theoretical storage capacities [59, 151, 152]. (b) The nanostructured TMO particles were synthesized by liquid phase exfoliation techniques. (c) A series of microscopic and X-ray based physical characterization techniques were carried out to determine structural form. (d) The electrochemical properties of these materials were characterized by employing cyclic voltammetry (CV), galvanic discharging (GD) and electrochemical impedance spectroscopy (EIS).

Chapter 2 will provide a concise overview of basic electrochemical theory as well as a description of both the Faradiac and electrochemical double layer charge storage mechanisms commonly found at electrode/electrolyte interfaces. It will provide a general description of the relative thermodynamic, kinetic and diffusive considerations of these mechanisms. It will also provide a basic thermodynamic description on the formation of colloidal dispersions with a focus on two dimensional layered materials. Chapter 3 will introduce the reader to the basic concepts behind the series of experimental techniques covered in this project. I will give brief descriptions of the ultrasonic methods used to synthesize the nanomaterials and fabricate highly uniform thin film electrodes. This will be followed by brief introductions to the microscopic and x-ray based characterization methods as well as the electrochemical techniques used.

Chapter 4 will report on the synthesis of V_2O_5 nanosheets by liquid phase exfoliation in H_2O and the subsequent ultrasonic fabrication of thin film V_2O_5 cathodes. It will further investigate the effect of varying exfoliation parameters resultant yields of V_2O_5 nanosheets. The charge storage properties of V_2O_5 nanosheet cathodes will be assessed with focus in single and multi Li-ion intercalation processes. This chapter proposes that the exfoliation of V_2O_5 produces high surface area

nanosheets providing access to more charge storage sites coupled with increased Li-ion diffusion pathways. It also proposes that the exfoliation in H_2O causes swelling of the nanosheets. This new "Xerogel structure is characterized by a general increase in the overall interlayer spacing. Such processes are analysed by a mix of diffraction and electrochemical diffusion methods. As V_2O_5 is a well established semiconducting materials, an investigation into the addition of single walled carbon nanotubes (SWCNT) as a conductive additive was also carried out. The SWCNTs acted to decrease any charge transfer resistance and the tendency to cause phase change.

Chapter 5 reports of the synthesis of a stable TiO_2 colloid and the fabrication of a thin film TiO_2 anode similarly to that described previously for V_2O_5. However, as opposed to the formation of a nanosheets colloid, the TiO_2 formed a stable dispersions of zero dimensional particles in H_2O. As before, the optimizations were investigated and the electrochemical properties of both a TiO_2 and a TiO_2/SWCNT anode were characterized as efficient Li-ion anodic hosts. This chapter proposes that an anode fabricated from a TiO_2 colloid may provide a safe and effective anode material competitive to that used in contemporary graphite based anodes.

Chapter 6 introduced the concept of two dimensional composite materials. Previously, the TMOs in question were combined with one dimensional SWCNTs providing extra conductive states. This chapter proposes that the fabrication of high capacity composite electrodes can be achieved by the formation of stable colloids of multiple layered materials. Herein, composite cathodes of commonly semiconducting MoO_3 will be fabricated with the addition of either graphene or V_2O_5 nanosheets. The electrochemical properties of these materials will be assessed with particular focus on the long term cycling properties. Due to its semiconducting behaviour, MoO_3 tends to exhibit poor cyclability despite having a large theoretical capacity of 1117 $mAh\,g^{-1}$.

Chapter 7 gives a brief conclusion of the full thesis and possible future work.

Chapter 2

Theory

2.1 Electrochemical Power Storage

Electrochemical power is usually stored in devices called electrochemical cells [153–156]. Electrochemical cells are devices that convert stored or supplied chemical energy to electrical energy. These conversions happen by either slow redox or fast capacitive processes. Typically, electrochemical reaction occur by various charge transfer mechanisms across a phase boundary, usually an electrode/electrolyte interface. Despite terms such as "battery", "fuel cell" or supercapacitor" being used, a basic electrochemical unit is called a cell. For example, a 9 V battery may be a series combination of three individual cells each with a nominal potential of 3 V. Unlike contemporary combustion engines, most electrochemical devices are not subject to the strict limitation imposed by Carnot law. As such, electrochemical devices make more efficient energy conversions [157].

Based on the direction of charge migration of an electrochemical cell, a cell may be either classed as a galvanic or an electrolytic cell [158]. Typically, a galvanic mechanism comprises of a series of spontaneous chemical reactions providing a potential driven current to an external load. An electrolytic mechanism, on the other hand, required energy from an external device to facilitate electrochemical reaction. In effect, an electrochemical device may be viewed as a galvanic cell when providing current to an external load and an electrolytic cell when being recharged. The basic layout of a cell comprises of three main components: (i) the anode, or the negative electrode, (ii) the cathode, or positive electrode and (iii) the electrolyte, which provides a medium for charge transfer between the two electrodes. For a galvanic cell, the anode oxidizes the electrolyte ions in a spontaneous reaction while the cathode reduces the ions, and *vice versa* in an electrolytic cell. A typical example is shown in Figure 1.3 in Chapter 1 for a typical Zn-Cu based cell [16]. In this system, a Zn

anode and Cu cathode are immersed in an electrolyte containing both $CuSO_4$ and $ZnSO_4$ electrolyte salts. A spontaneous reaction at the Zn anode oxidizes the $ZnSO_4$ according to equation (2.1) and sends electrons through the external circuit which facilitate the reduction of the $CuSO_4$ electrolyte at the Cu cathode as in equation (2.2). As such the Zn anode depletes while the Cu cathode increases in mass. These processes occur until chemical equilibrium is achieved.

$$Cu \rightleftharpoons Cu^{2-} + 2e^{-} \tag{2.1}$$

$$Zn \rightleftharpoons Zn^{2+} + 2e^{-} \tag{2.2}$$

When designing an electrochemical cell, materials demonstrating high energy and power densities while minimizing the relative mass or volumes are of extreme importance [11]. Such a combination is necessary for today's growing demand for portable electronic and transport systems. However, various other material characteristics should be considered such as cost, scarcity, chemical reactivity and environmental friendliness. Similarly, facile and cost effective methods of synthesis and fabrication are important [35].

2.1.1 Cell Property Classifications

The Standard Potential - An electrochemical cell's standard potential, E^0_{cell}, is determined by considering the individual reduction potentials of each electrode at a standard state [159, 160]. For a general pair of electrodes, if $E^0_{cell} > 0$ the cell is considered spontaneous and the cell delivers energy to an external load. However, if $E^0_{cell} < 0$ the cell is considered non-spontaneous and is taking energy from an external load. By considering the standard reduction potentials of each electrode, E^0_{cell} can be calculated,

$$E^0_{cell} = E_c - E_a \tag{2.3}$$

where E_c and E_a are the standard reduction potentials of the cathode and anode respectively. When considering the Zn - Cu system described earlier the E^0_{cell} can be calculated from the values expressed in table 2.1 [161].

TABLE 2.1: Standard Reduction Potentials

Electrode	Potential	Material	Value
Cathode	E_c	Cu	0.34 V
Anode	E_a	Zn	-0.76 V

The standard potential of the overall cell can be determined from equation 2.3.

$$E^0_{cell} = 0.34\,V - (-0.76V) = 1.10\,V \tag{2.4}$$

However, realistic values do not match the ideal case, as effects such as polarization losses and internal resistances alter the value [162]. The experimental standard potential is determined by measuring the potential difference across the two electrodes in a case where the current is negligible. This is called the open circuit potential, E_{OCP} and is heavily dependant on factors such as cell design, current state of charge and internal resistances.

Storage Capacity - Before the storage capacity of a cell's electrode is determined, the value is compared to a calculated theoretical capacity, Q. Q is a value determined by considering both the molecular weight of the host material and the amount of ions it can store per unit formula. For convenience, Q, is usually quoted in how many mA needed to fully charge or discharge a cell per unit hour [156].

$$Q = \frac{n\,x\,F}{3.6\,x\,M_w\,x\,m} \tag{2.5}$$

where n is the number of charge ions stored per unit formula of the host lattice, F is Faraday's constant and M_w is the molecular weight of the host lattice. The units of theoretical capacity are $mAh\,g^{-1}$.

Experimentally, the storage capacity, q, is determined by applying a constant current between a pre-determined potential window and measuring the resultant change in charge capacity. When charging a cell the current maintains a positive value, while discharging the cell the current remains negative.

$$q = \frac{I\,\Delta t_i}{m} \tag{2.6}$$

where I is the current (mA), Δt_i is the time interval and m is the mass.

Consider a $LiFePO_4$ based cathode material in a fully charged state in a half cell configuration vs. Li/Li^+ weighing 1 mg [44]. If it takes 10 hr to fully discharge the cell at a constant potential of -17 mA, then q = 170.16 $mAh\,g^{-1}$. Comparing this to the theoretical capacity determined from equation 2.5 where M_w = 157.76 $g\,mol^{-1}$, the values match. However, depending on the methods of synthesis, the diffusion coefficients and the quality of the material, these values rarely coincide.

For comparative purposes, both theoretical and storage capacities are quoted in terms of half-cell capacities. In general, the working electrode of a half cell consists of the active material while the counter electrode is generally a material to compliment the reaction such as pure Li metal or an inactive platinum electrode. A third high impedance electrode is also present which consists of a standard material of a well established reduction potential. This reference electrode provides a potential to which the output potential of the working electrode is compared to. For example, most organic based systems use either pure Li metal as a counter electrode while aqueous systems favour the standard calomel electrode ot the standard hydrogen electrode (SHE) [163, 164].

Cell Capacitance - Similar to a cell's storage capacity, the cell's capacitance is another way to determined the quantity of stored charge [158]. However, as LIB material's are usually quoted in terms of capacity, devices such as SC are quoted in capacitance. The capacitance of a cell's electrode can be determined as follows,

$$C = \frac{Q_i}{E} \tag{2.7}$$

where Q_i is the charge of species i and E is the potential across the device.

Specific Energy - The specific energy of an electrode is defined as the quantity of usable energy possessed by unit kg of the active material [7]. It is usually quantified by considering the potential window of the material coupled with the q of a full discharge. The large specific energies of Li-ion batteries can be attributed to the large stable potential window of the electrolyte and the high output capacities of the electrode materials.

$$U_{max} = \frac{\Delta E\, x\, q}{m} \tag{2.8}$$

In general the q is given in Ah and the mass in kg. The Ragone plot presented in Figure 1.2, Chapter 1 plots the specific energy of a range of energy storage devices against the corresponding specific powers.

Specific Power - The specific power of an electrode material can be defined as the amount of energy the material can release per unit hr [7]. Similar to specific energy it is quoted per unit kg and is expressed on Ragone plots.

$$P_{max} = \frac{U_{max}}{t_i} = \frac{(\Delta E)^2}{4R_S m} \tag{2.9}$$

where t_i is the time, E is the potential, R_S is the internal resistance and m is the mass.

2.1.2 Thermodynamics

This section deals with the fundamentals of chemical equilibria and the Nernst equation [165, 166]. Generally, thermodynamics predicts the direction of chemical reactions (although not the rate, which is determined by kinetics). Consider the general chemical reaction,

$$\Sigma rR = \Sigma pP \tag{2.10}$$

where R and P are the sum of the reactants and products respectively, and r and p are their molar coefficients. According to thermodynamics, this system will reach equilibrium when the Gibbs free energy, ΔG_{sys} is minimized, see Figure 2.1.

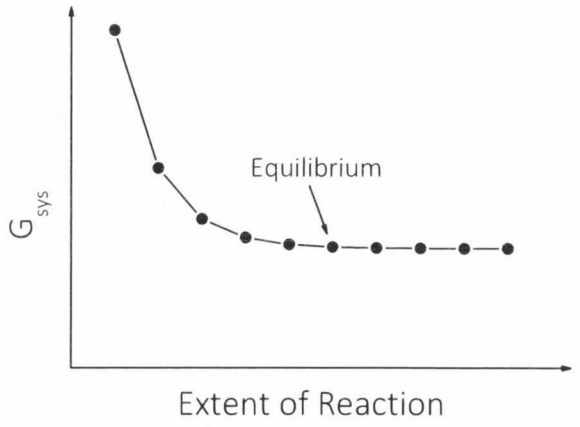


FIGURE 2.1: Typical Gibb's energy profile as a function of extent of reaction (e.g. time).

The total Gibb's free energy of the system is the difference between that of the products and reactant,

$$\Delta G_{sys} = \Delta G_P - \Delta G_R \tag{2.11}$$

ΔG_{sys} is a measure of the total work that can be extracted from an electrochemical system. If no current is being applied to the system the total potential of a cell may be determined. This potential is directly related to the free energy of the system,

$$\Delta G_{sys} = -nFE_{cell} \tag{2.12}$$

where n is the number of electrons transferred, F is the Faraday constant (F = eN_A), e is the charge of an electron and N_A is the amount of charged particles in 1 mole. The term E_{cell} is the electromotive force (EMF) or the potential difference between the two electrodes at zero current. Spontaneous reactions occur when ΔG_{sys} of the system is negative while E_{cell} is positive (galvanic reactions). Although, when ΔG_{sys} is positive and E_{cell} is negative, energy needs to be supplied to the system for reaction to occur (a non-spontaneous or electrolytic reaction).

Chemical equilibrium of a system is heavily dependant on the sum of the chemical and electrical potentials. In cases where current is negligible, chemical potential is dominant and depends on the individual chemical potentials of the reactants and products [167, 168]. The chemical potential, μ_j, is defined as,

$$\mu_j = (\frac{\delta G}{\delta n_j})_{T,n_i \neq n_j} \tag{2.13}$$

where n_j is the number of moles of species j, and T is the absolute temperature. Figure 2.2 demonstrates a typical situation whereby a metal cathode is immersed in a conductive electrolyte. The chemical potential of the metal is the energy at the Fermi level i.e. the highest band of electrons, while the chemical potential of the electrolyte is the energy at the highest occupied molecular orbital (HOMO). Completing the circuit causes a current flow, as dissimilar chemical potentials are the driving force behind electron transfer. As the Fermi level is higher, electrons will transfer to the HOMO continuously until both levels coincide and the relative chemical potentials match. At this point no more current flows and the system has reached thermodynamic equilibrium.

The general equation of the chemical potential of a phase at any point in time can be expressed in terms of the concentration at the phase boundary,

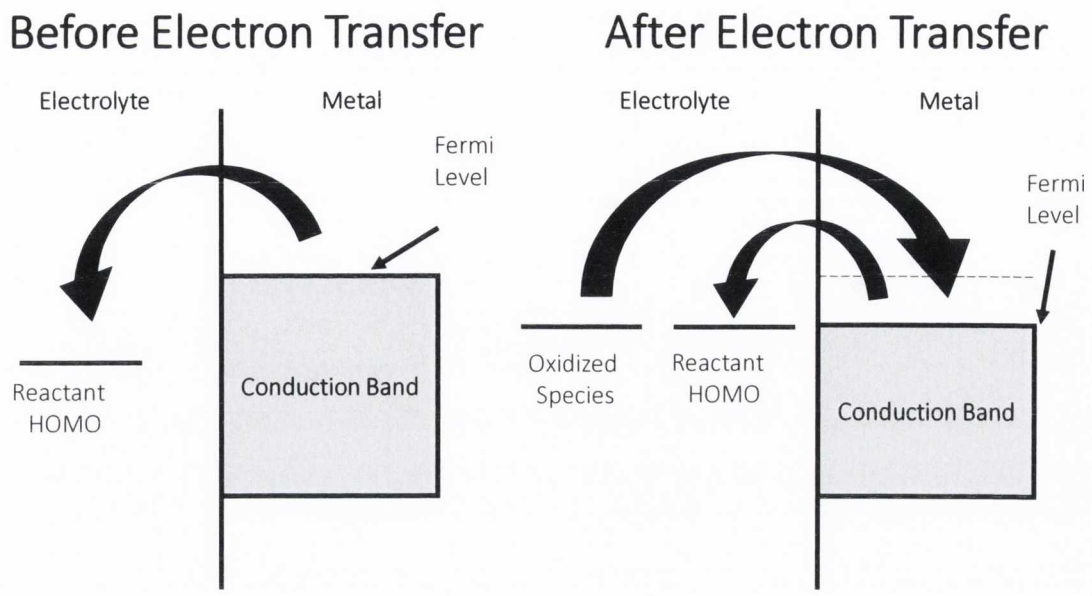


FIGURE 2.2: The chemical potentials of the electrons in the electrolyte and metal cathode

$$\mu_j = \mu_j^0 + RT\, Ln[C_j] \tag{2.14}$$

where μ_j^0 is the standard chemical potential, R is the universal gas constant and C_j is the concentration of species j. Combining equations (2.12), (2.13) and (2.14) an expression for E_{cell} in terms of reactant and product concentrations is formed,

$$E_{cell} = E_{cell}^0 - \frac{RT}{nF} Ln \frac{a_P^p}{a_R^r} \tag{2.15}$$

where E_{cell}^0 is the difference in the Standard Potential of the Cell, and a is the chemical activity of the products and reactants. The chemical activity of species j is defined as,

$$a_j = \gamma_j C_j \tag{2.16}$$

where γ_j is the activity coefficient of species j. The activity coefficient is a measure of how susceptible an individual ion or atom of species j is to reaction ($0 < \gamma_j < 1$).

Equation (2.15) is termed the Nernst equation and is the general equation which relates the potential difference of the cell to the standard cell potentials and the activities of the reactants and products [169]. Once the cell reaches thermodynamic

equilibrium the Gibbs energy is minimized and as a result E_{cell} is zero.

2.1.3 Kinetics

As the previous section explained the thermodynamics of the electrochemical cells, this section will demonstrate the kinetic operations evident in electrochemically active species [170, 171]. Kinetics deals with quantifying the electric currents in cells as well as particle reaction fluxes. The rate of electron transfer is a major limiting factor in the operation of electrochemical cells. Electron transfer occurs *via* quantum mechanical tunnelling across the electrode/electrolyte interface [172]. As a consequence, the reactant electrolyte ions only undergo electron transfer within 2 nm of the electrode surface. This is due to the rapid decrease in tunnelling rate with distance. Therefore, fresh electrolyte ions from the bulk must diffuse to the electrode surface for further transfer reactions to take place, see Figure 2.3.

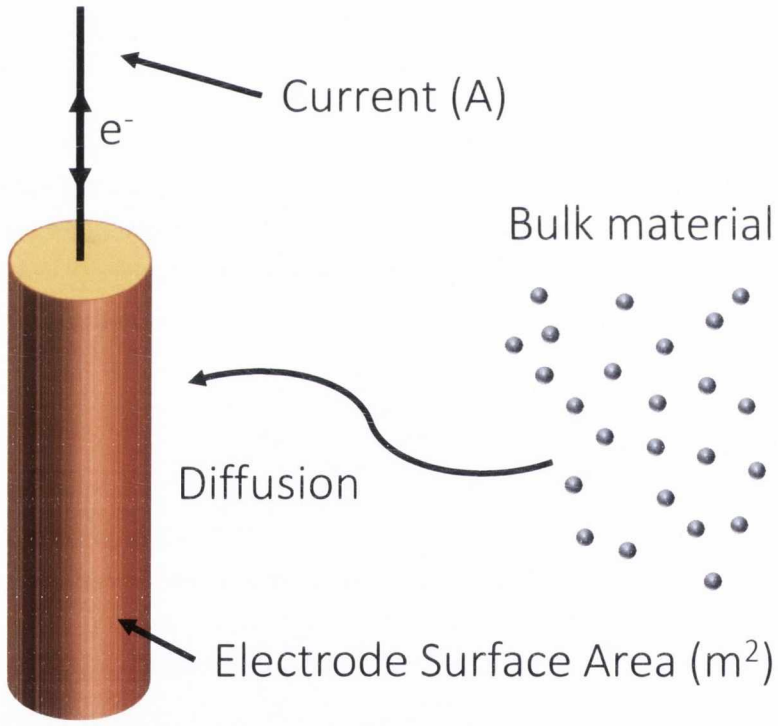


FIGURE 2.3: The diffusion process between electrode and electrolyte.

The electrons which cross the phase boundary cause currents to flow throughout the circuit. This current is directly proportional to the flux of reactant that comes in contact with the electrode surface,

$$I = FA_s j \tag{2.17}$$

where A_s is the active surface area of the electrode and j is the flux of reactant ($mol^{-1}\, cm^{-2}\, s^{-1}$). Subsequently, the reactant flux is directly proportional to the concentration of reactant at the surface,

$$j = k(n)C_{[R]_0^n} \tag{2.18}$$

where $k(n)$ is the nth order rate constant and $C_{[R]_0^n}$ is the concentration of the reactant directly at the surface. It is important to highlight the difference between the concentration of the reactant at the electrode surface and in the bulk electrolyte. Charge transfer reactions deplete the useful electrolyte ions directly at the surface. Therefore, a concentration gradient exists in which there is an uneven concentration between the surface and bulk. As a result fresh electrolyte diffuses from the bulk to the surface.

The rate constant, $k(n)$, describes the probability a given reaction will occur. It is heavily dependant on the spontaneous Gibbs free energy and the local temperature of the reaction. $k(n)$ can be described by the Arrhenius equation [173],

$$k(n) = k^0 e^{\frac{-\Delta G}{k_b T}} \tag{2.19}$$

where k^0 is denoted as the frequency factor and k_b is the Boltzmann constant. The frequency factor describes the frequency at which a reactant molecule will come into contact with an active site on the electrode surface.

As described earlier, an electrochemical cell consists of two electrodes, a cathode which supplies electrons, and an anode which removes electrons. Therefore the total flux of cell is dependant on the combination of each individual electrodes flux. The total flux of a cell is given by,

$$j = k_c[C_c]_0 - k_a[C_a]_0 \tag{2.20}$$

where k_c and k_a are the cathodic and anodic rate constants. Equation 2.17 described how the flux was directly proportional to the current. Therefore, is it possible to

express the reactant fluxes in terms of the electrochemical potential. Initially focusing on the cathode, applying (2.19) will relate the rate constant to the cathodic free energy,

$$k_c = A_c e^{\frac{-\Delta G_c^+}{RT}} \tag{2.21}$$

where A_c is a pre exponential factor and G_c^+ is the cathodic free energy at the transition state. Further manipulation, while taking equation (2.12) into account, leads to an expression relating the rate constant to the cathodic potential,

$$k_c = k_c^0 e^{[\frac{-\alpha_c F \eta}{RT}]} \tag{2.22}$$

where k_c^0 is the cathodic frequency factor, α_c is the transfer coefficient, η is the overpotential ($\eta = E - E_f^0$) and E_f^0 is the formal potential of the redox couple. The transfer coefficient lays in the range of $0 \leq \alpha_c \leq 1$ although quite commonly $\alpha_c = 0.5$.

The overpotential is an important quantity as it gives a realistic value of the potential of the electrode [162]. It was described earlier, that the maximum amount of energy deliverable by a cell is given by the ΔG_{sys}. In the ideal case, 100% of this energy would be converted into useful electrical energy. However, three main components contribute to the apparent energy losses. Firstly, the polarization losses due to the energy required in charge transfer processes at the electrode/electrolyte interface. This is the energy required to overcome the potential barrier and drive the electrochemical reaction. Secondly, the polarization losses arising due to the concentration gradient of the electrolyte. This is the energy requires to maintain a balanced reactant flux from diffusion to the electrode surface. Finally, the losses due to the inherent resistance of the electrolyte. As electrolytes are not perfect conductors, a natural resistance to ion flow exists in the cell. This also takes into account resistance contributions from mechanical separators and electrical contacts. The total over potential experienced by a cell is given by,

$$\eta = [(\eta_{ct})_c + (\eta_C)_c] + [(\eta_{ct})_a + (\eta_C)_a] + IR_S \tag{2.23}$$

where η_{ct} is the charge transfer or activation polarization, η_C is the concentration polarization, I is the current and R_S is the total series resistance of the cell.

Similar kinetic derivation can be applied to the anode. Letting $k_c^0 = k_a^0 = k^0$ and taking Equation (2.17) into account an general equation can be derived for the over all potential dependant current of a cell,

$$I = FAk^0([e^{\frac{\alpha_c F\eta}{RT}}][C_c]_0 - [e^{\frac{-\alpha_a F\eta}{RT}}][C_a]_0) \tag{2.24}$$

where α_a is the transfer coefficient of the anode. This is termed the Butler-Volmer equation and is valid only in situations where electron transfer is dominant over mass transfer [174, 175]. Current may also be limited by diffusion processes and will be described in section 2.1.5. This relation highlights the exponential dependence of the current on the applied potential. At relatively negative potentials, the cathodic term may dominates the expression while at relatively positive potentials the anodic term dominates.

2.1.4 Electrode Processes

2.1.4.1 Faradaic Reactions

The most commonly exhibited storage mechanisms in battery electrodes are Faradaic reactions [158, 170]. This type of reaction involves the transfer of electrons from one phase to another across a well defined boundary. In the case of battery materials, this boundary is the electrode/electrolyte interface. This type of mechanism can also be termed a redox reaction as it involves the coupling of both an oxidation of the electrolyte at the anode and a reduction of the electrolyte at the cathode. As such, the oxidation states of each material in question alter by the gain or loss of electrons. Despite their commonality in battery materials, Faradaic reactions are vital to many basic functions of nature, such as corrosion [176], combustion [8], respiration [177] and photosynthesis [178].

Consider the Zn - Cu system described in Chapter 1 earlier (Figure 1.3). Zn - Cu have been the basis for wide range of historical battery discovered such as those covered in section 1.3.1. This system represents the most basic example of a primary battery as it exhibits irreversible Faradaic reactions at the electrodes. When a Zn - Cu system is not at equilibrium, a net chemical driving force causes a series of redox processes to occur on the electrode surfaces. At the anode, the Zn atoms are oxidized according to equation 2.2. This liberates electrons which flow through the external circuit to facilitate the reduction of Cu^{2+} ions in the electrolyte at the surface of the

cathode according to equation 2.1. The cathodic reduction process is illustrated in Figure 2.4.

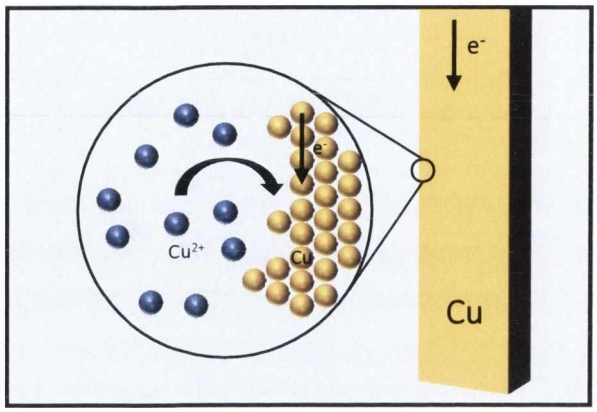


FIGURE 2.4: Typical redox reaction at a copper electrode.

2.1.4.2 The Electrochemical Double Layer

Capacitors have long existed as temporary charge storage devices and have found applications in a wide range of electronic devices such as camera flashes and computers [158, 179]. The traditional electrolytic capacitor consists of a pair of oppositely charged metallic plates separated by in insulating dielectric layer such as mica or glass. Charge storage exists by the formation of sheet of counter charge along the plate/dielectric interface relative to the charge of the plate itself, see Figure 2.5. As such, certain similarities can be drawn between standard electrochemical storage devices and electrolytic capacitors. However, the charge storage mechanism on the surface is purely electrostatic as opposed to Faradaic, giving the capacitor advantageous in fast discharging and lifetime. Due to the relatively low surface area of a capacitor, the high specific energies exhibited by batteries are not achieved.

A fully charged capacitor acts as a temporary power source in an electrical system and provides short bursts of energy for local applications. The amount of charge stored on a capacitor is heavily dependant on the surface area of the metallic plates and the relative potential applied to the system. Similarly, permittivity and the thickness of the dielectric contribute to the over all capacitance, C.

$$C = \frac{q_i}{E} = \frac{\epsilon_0 \epsilon_r A_s}{d} \tag{2.25}$$

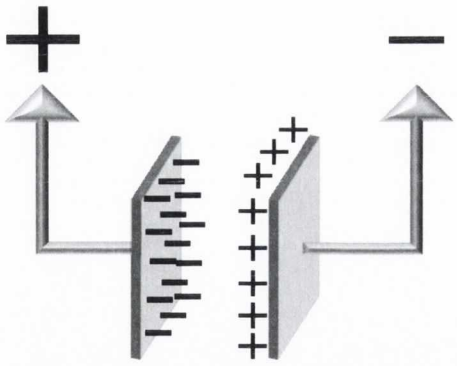


FIGURE 2.5: Typical schematic of a capacitor.

where q_i is the amount of charge stored, E is the applied potential, A_s is the surface area of the metallic electrode, d is the distance between the two plates, ϵ_0 is the permittivity of free space and ϵ_r is the relative permittivity of the dielectric. The unit of capacitance is the Farad (F).

As mentioned earlier, traditional electrolytic capacitors are assembled using flat metallic electrodes. However, more recently it was realized that certain high surface area materials, such as AC, could be employed to increase the relative surface areas of these devices [180, 181]. This increase in surface area will increase the over all energy of the device allowing for more large scale application. These new forms of capacitors were named "supercapacitors" due to their enhanced charge storage properties. The term SC is also synonymous with the term "electrochemical capacitor" as a series of electrochemical reaction occur on the phase boundaries. As such, SCs are manufactured replacing the dielectric materials with typical battery based organic or aqueous electrolytes. Similarly, the conductive plates can be viewed as electrodes immersed in this electrolyte.

Charge storage at the electrode/electrolyte interface of a SC occurs with the formation on an electrochemical double layer (EDL) [182]. Relative to conventional capacitor or battery materials, SCs are more suited to rapid storage and release of energy while maintaining an appreciable specific energy.

The EDL was was first investigated by von Helmholtz in the 19th century with his work on colloidal suspensions [183, 184]. According to this theory, a layer of counter charge is formed along the surface of a charged particle as shown in Figure 2.6. As such, a negative electrode will attract a series of positive counter ions. However, an inherent separation between the electrode surface and the counter ions exists measuring about one ion thick. This combination of oppositely charged layers

coupled with the inherent separation can be viewed as an effective double layer capacitor. Furthermore, this theory predicts that there is a linear relationship between the applied potential and the resultant capacitance according to equation 2.25. Experimentally this relationship did not hold up.

This discrepancy was investigated in the 1910s when Gouy and Chapman discovered that, not only is the capacitance dependant on the potential applied, but also the concentration of the ionic electrolyte [185, 186]. The distribution of the ions throughout the electrolyte is governed by the minimization of G_{sys}.

$$\Delta G_{sys} = \Delta H_{sys} - T\Delta S_{sys} \tag{2.26}$$

The G_{sys} is dependant on the enthalpy, H_{sys}, induced by charge interactions couple with the entropy, S_{sys}, based on the random distribution of the ions. However, the presence of the electrode severely alters the H_{sys} of the system and hence changes the over all distribution of ions. Gouy and Chapman suggested an exponential decrease in counter ion concentration as the system approaches the bulk electrolyte and hence a similar variation in potential. This region of interrupted ionic concentration near the electrode is termed the "diffuse layer" and it is calculated as follows,

$$L_D = (\frac{\epsilon\epsilon_0 k_b T}{2nz^2e^2})^{\frac{1}{2}} \tag{2.27}$$

where k_b is the Boltzmann constant, T is the absolute temperature, n is the number density of ions in the electrolyte, z is the ionic charge and e is the charge of the electron. This model results in a parabolic dependence of the capacitance on potential, however it was not enough to describe the apparent experimental behaviour.

In 1924 Stern decided to combine both the Helmholtz and Gouy-Chapman models [187]. In this model, both a compact Helmholtz layer", called the outer Helmholtz plane (OHP), at the electrode and a diffuse layer exists trailing off into the bulk electrolyte. Grahame furthered this model in 1947 with proposing that certain ionic species and solvent molecules can penetrate the Helmholtz layer [188]. The most commonly used model today is the Bockris, Devanthan, and Muller model [189]. This model combines the Grahame model with a series of solvent dynamics at the electrode. As mentioned earlier, electrochemical electrolytes usually consist of a a ionizable salt dispersed in an solvent. The solvent acts to stabilize the ions by the formation of a solvent sheath. For example, in an aqueous electrolyte the highly

polar H_2O molecules orient themselves in such a way that the oppositely charged end is in contact with the ion. In general, all other orientations would be considered unstable. As such, this sheath prevents direct contact of the ion at the OHP with the electrode surface, hence forming charge separation". However, as H_2O molecules are locked in place between these layers, the permittivity of this capacitive system is much lower than that of what would be exhibited for an electrolytic counterpart ($\epsilon = 78.3$ in capacitors, $\epsilon \approx 10$ between the electrode and OHP) [190].

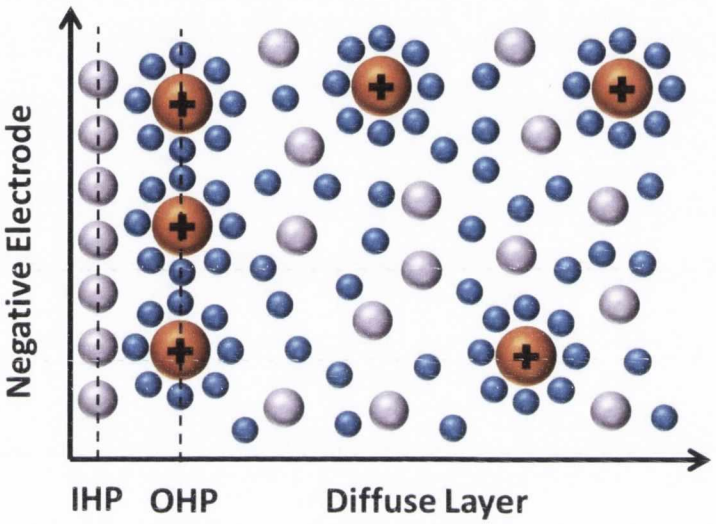


FIGURE 2.6: Capacitive properties at the electrode surface.

Figure 2.7 (a) shows how the the distributions of (i) Charge, (ii) charge density, (iii) electric field and (iv) potential difference varies across a full SC. The electric field across the capacitor exists as a result of charge separation across the electrolyte. Therefore, a potential difference exists across the device when fully charged. Figure 2.7 (b) shows a detailed map of the potential difference between a typical electrode and the bulk electrolyte. The OHP consists of a compact layer of counter ions demonstrating a linear decrease in potential from ϕ_{met} to ϕ_{OHP}. However, as the net concentration of counter ions decreases towards the bulk the potential decreases exponentialy.

2.1.4.3 Pseudocapacitance

For many capacitive materials, such as that of the TMOs or TMDs, a secondary charge storage process is evident along the electrode surfaces [71, 72, 191]. While

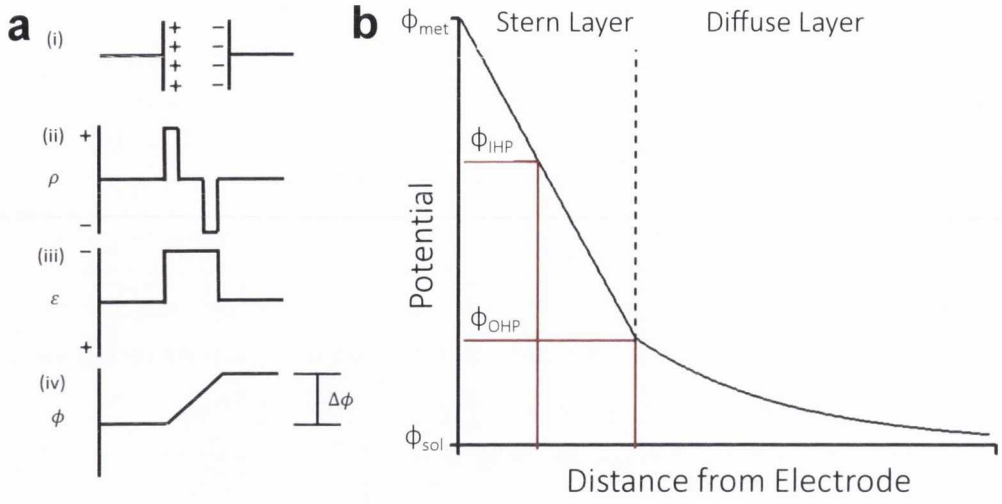


FIGURE 2.7: (a) (i) Charge, (ii) charge density, (iii) electric field and (iv) potential difference distribution across a full capacitor. (b) Potential difference distribution at the surface of a capacitor electrode.

counter ions form a well defined EDL along the electrodes surface, a series of oppositely charged ions are known to leave their hydration sheaths and adsorb directly onto the surface of the electrode. As such these ions undergo rapid redox reactions contributing to the over all capacitance of the material. This is characterized by the inner Helmholtz plane exhibited in Figure 2.6. These charge transfer processes are pseudocapacitive and bridge the gap between capacitive and Faradaic reactions. Much like charge storage at the EDL, pseudocapacitive processes are highly reversible and share many of the same advantageous as conventional EDL capacitance. It is estimated that these pseudocapacitive processes can contribute upwards of 100 times more capacitance than that of EDL processes to the overall capacitance of the material.

2.1.5 Diffusion

In chemistry, diffusion is a commonly observed process [192, 193]. The need to reduce the overall energy of a typical system is the driving force behind the diffusion of any mixture. In electrochemical systems diffusion plays an important role in the management of diffusion and activation controlled reactions [162]. As described in section 2.1.3, the operation of many battery system requires efficient diffusion of the electrolyte species. Diffusion was first described mathematically by Adolf Fick in the 1860 [194]. In a system where there is an unbalanced concentration regime,

materials tend to diffuse from regions of high concentration to regions of low concentration. According to Fick's first law,

$$j = -D\frac{\delta C}{\delta x} \tag{2.28}$$

where j is the flux ($mol\, cm^{-2}\, s^{-1}$), D is the diffusion coefficient ($cm^2\, s^{-1}$) and $\delta C/\delta x$ is the concentration gradient. The negative sign is attributed to the direction of flow down the gradient. Diffusion coefficients are heavily dependant on factors such as the mobility and the size of the diffusion species as well as the volume of space the diffusion species can move. For example, a Li-ion travelling through a host matrix would have a easier time diffusing than that of a Na-ion due to the decreases ionic radius. Similarly, if the host matrix consisted of larger channels, diffusion of the Li-ion would be much simpler. The diffusion coefficient, D, can be quantified as,

$$D = D_\infty e^{(\frac{-U_a}{RT})} \tag{2.29}$$

where D_∞ is the hypothetical value at infinite temperature and U_a is the activation energy for diffusion.

Fick went on to investigate the time dependence of diffusion at a certain point. Consider a slab of area A_s and a thickness δx. The amount of material that passes this point per unit time can be visualized in Figure 2.8.

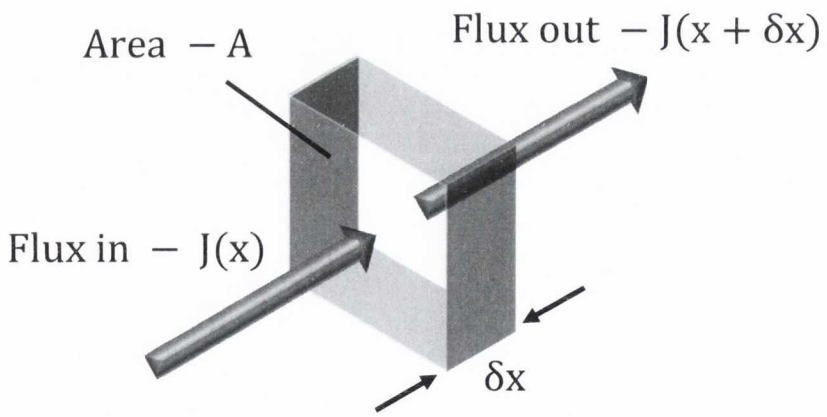


FIGURE 2.8: Diffusion process

At point x, the flux is given by J while the flux at point x + δx is given by J'. The change in concentration, ΔC_j, over this slab can be expressed by,

$$\Delta C = C'_x - C_x l \frac{\delta C_j}{\delta x} \tag{2.30}$$

where C_x is the concentration at point x, C'_x is the concentration at point x + δx and l is the total length of the slab. Applying this to Fick's first law gives and expression for Fick's second law for a one dimensional diffusion process.

$$\frac{\delta C_j}{\delta t} = D \frac{\delta^2 C_j}{\delta x^2} \tag{2.31}$$

Much like Fick's first law, this is dependant both on the diffusion coefficient and the concentration gradient. Manipulation of Fick's law can provide a useful expression to relate the time to the distance diffused.

$$\sqrt{(x^2)} = \sqrt{2Dt} \tag{2.32}$$

The above equation suggests the tendency of diffusion to decrease rapidly over large distances. As such, it is recommended that modern energy storage devices consist of thin electrolyte layers to overcome this issue [195]. As mentioned earlier, the diffusion of the electrolyte is important particularly in mass transfer controlled devices. In the Zn - Cu example from Chapter 1, the Cu^{2+} become reduced at the cathode, depleting the local region of Cu^{2+}. If this process was activation controlled, the rate of reaction dominates the charge transfer process while the electrode remains fully stocked with electrolyte. However, a mass transfer controlled reaction requires the efficient diffusion of electrolyte ions to the surface to accommodate the continuous reactions. Nevertheless, in most electrochemical systems this depletion is a common occurrence and can be easily observed in many electrochemical characterization methods such as cyclic voltammetry.

In the early 1900s, Cottrell derived and equation to describe this depletion process based off Fick's seconds law [196].

$$I = \frac{nF\sqrt{D}C_j}{\sqrt{\pi t}} \tag{2.33}$$

This equation relates the change in the resultant electrochemical currents with time in a controlled potential experiment. Intuitively speaking, both D and C_j would naturally increase the resultant current. However, as time progresses the resultant current decreases in a manner proportional to the square root of time. This can be

directly related to the depletion of electrolyte ions near the surface of electrodes. As such, the overall resulting current has contribution from both the BV equation mention in section 2.1.3 and the Cottrell equation above.

2.2 Colloidal Dispersions

Solid/liquid mixtures come in three forms, namely a solution, a suspension and a colloid. A colloid, or colloidal dispersion, is a evenly distributed mixture of nanoparticles in a suitable solvent [197]. The nanoparticles themselves are not actually dissolved in the dispersion, rather they are stabilized with solvent sheaths. If the particles are smaller than 1 nm it is considered a solution (i.e. individual molecules) or if the particles are larger than 1 μm the system is considered a suspension. The nanoparticle colloid itself can be defined as meta-stable i.e. it is not at thermodynamic equilibrium although the particles can remain dispersed for a long period of time.

Typically, depending on the stability of the system, the nanoparticles in dispersion may undergo aggregation or sedimentation. There are a wide range of methods to ensure a meta-stable colloidal dispersion is achieved. For a stable dispersion the dispersing solvent should minimize the interfacial tension between the nanoparticle and the solvent itself [147]. Similar to that expressed for a stable electrolyte mixture, the Gibbs free energy of mixing, ΔG_{mix}, for a stable colloid must be minimized according to equation 2.26. The ΔH_{mix} can be defined as the net energy of a system when two or more substance are mixed together. It results from the balance between both attractive and repulsive forces in the dispersion. The relationship between the ΔH_{mix} of a system and the degree of miscibility was first determined by the Hildebrand [198, 199]. The Hildebrand solubility parameter, δ_t, give a numerical estimate as to the degree of interaction between the materials.

$$\Delta H_{mix} \propto (\delta_{Su} - \delta_{Sv}) \tag{2.34}$$

where δ_{Su} and δ_{Sv} are the Hildebrand solubility parameters of the solute and solvent respectively. The solubility parameters themselves have a direct relationship to the square root of the components surface energies, E^i_{Sur}.

$$\delta_i \propto \sqrt{E^i_{Sur}} \tag{2.35}$$

Equation 2.34 suggests that a solute and solvent with similar solubility parameters tend to interact in a positive manner. Theoretically, if both the solute and solvent have similar parameter a stable solution should form. This may be considered as the individual components surface tensions matching based on equation (2.35). As surface interactions consist of a series of different components, the work of Hanson suggested that the Hildebrand solubility Parameters could be deconvoluted into separate parameters [200, 201]. These parameters account for the individual dispersion, polar and hydrogen bonding forces. The dispersion forces account for the local changes in atomic charge densities forming temporary dipoles. The polar forces account for the permanent dipoles existing in polar molecules. Lastly, the hydrogen bonding forces account for the attractive forces between hydrogen and highly electronegative atoms. The Hildebrand solubility parameter can be expressed in terms of the Hansen solubility parameters.

$$\delta_t^2 = \delta_D^2 + \delta_P^2 + \delta_H^2 \tag{2.36}$$

where δ_t is the Hildebrand solubility parameter and, δ_D, δ_P and δ_H and the Hansen solubility parameters for the dispersion, polar and H-bonding forces. Applying equation (2.36) to equation (2.34) an overall expression for the enthalpy of mixing can be determined,

$$\Delta H_{mix} \propto [(\delta_{D,Su} - \delta_{D,Sv})^2 + (\delta_{P,Su} - \delta_{P,Sv})^2 + (\delta_{H,Su} - \delta_{H,Sv})^2] \tag{2.37}$$

Similar to that suggested by Hildebrand, the individual Hansen parameters for each component should match for efficient mixing. Although this relationship was originally derived for basic solutions it has been shown to extent to the areas of nanoparticle dispersions. Coleman *et al.* showed how the concentration of a layered nanosheet dispersions in a range of different solvents exhibited Gaussian distribution consistent with the following equation [135].

$$C_j \propto exp[-\frac{\nu_{NS}}{3k_BT}(\delta_{sol} - \delta_{NS})] \tag{2.38}$$

where ν_{NS} is the average nanosheet volume, k_B is the Boltzmann constant and δ_{NS} is the solubility parameter of the nanosheets material.

For a stable colloid the ΔS_{mix} of the system also needs to be maximized. This is a naturally occurring process driven by the tendency of a system to disorder itself.

There are many cases in which solvent is not enough to keep the dispersion stable. Inter-atomic forces along the particle surfaces tend to attract other particles causing aggregation [202]. A typical sedimentation process is illustrated in Figure 2.9. Initially particles become loosely bound in a process called flocculation. However, this process is easily reversible. As time progresses these flocculated particles start to irreversibly aggregate forming larger particles. As the particles aggregate further, gravity takes over and the particles form a sediment on the bottom of the vessel. The addition of surface active agents (surfactants) forms a repulsive shell around the particles cancelling any attractive interactions and forming a stable dispersion [203].

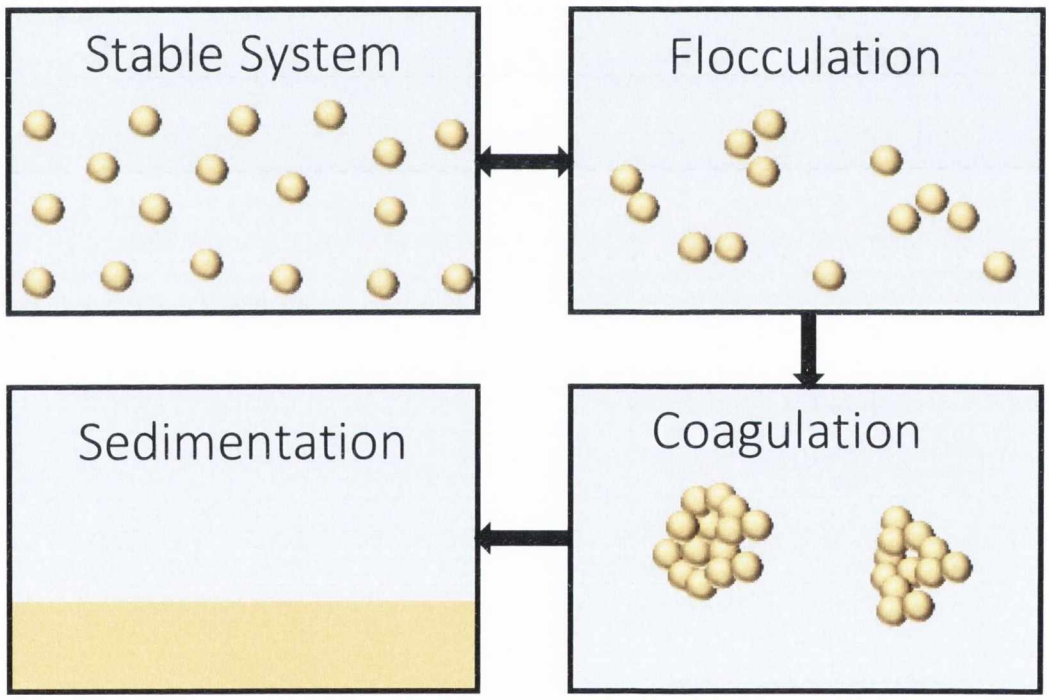


FIGURE 2.9: The coagulation process exhibited by unstable colloidal dispersions.

The formation of a repulsive shell follows the same general principals as the formation of an EDL. This EDL can be used to quantify the stability of the system. The interaction between the attractive van der Waal forces and repulsive forces from the surfactant can be described with DLVO theory [204, 205]. The total potential experienced by a typical spherical nanoparticle, V_T, can be given by,

$$E_T = E_{Rep} - E_{Att} = 2\pi\epsilon_0\epsilon_r R\zeta^2 e^{-L_D d} - \frac{A_H R}{12D} \tag{2.39}$$

where R is the radius of the particle, ζ is the zeta potential, L_D is the diffuse length given by equation 2.27, d is the distance from the centre of the nanoparticle and A_H is the Hamaker constant. The Hamaker constant described the contribution of the geometry of the nanoparticles to the over all potential [206]. Figure 2.10 (a) shows how the attractive element, V_{Att}, and the repulsive element, V_{Rep} combine to form an overall potential profile of a stable dispersion. It is clear that the repulsive double layer causes a potential barrier to the attractive van der Waal forces in the nanoparticles preventing aggregation. However, if the potential barrier is overcome the nanoparticles irreversibly coagulate.

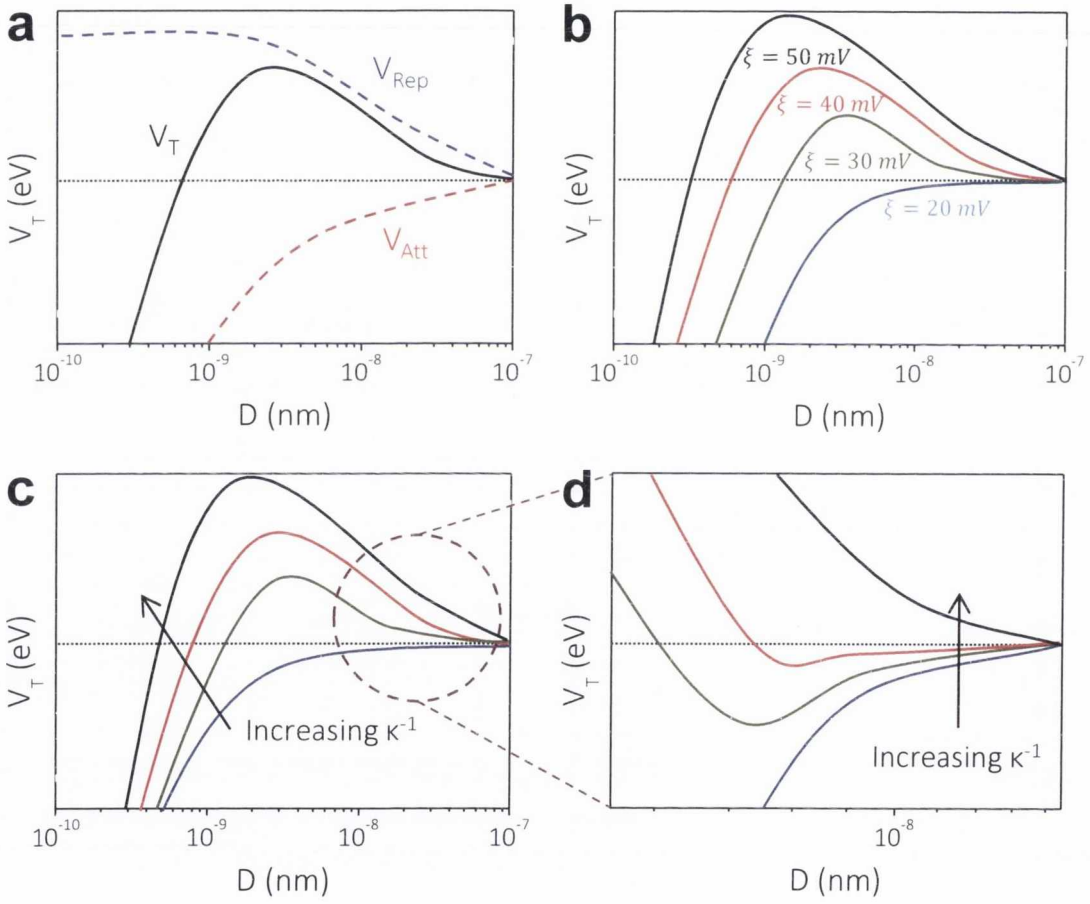


FIGURE 2.10: Potential energy curves describing (a) V_T as a combination of V_{Att} and V_{Rep}, (b) V_T's dependence on ζ potential, (c) V_T's dependence on κ^{-1} and (d) V_T's flocculation profile.

In colloidal dispersions ζ is commonly used to determine how stable the dispersion is. It is generally accepted that particles with $|\zeta| > 30$ mV are stable against aggregation. Figure 2.10 (b) shows how the potential barrier decreases as the ζ potential decreases. The ζ potential derives from the inherent electric field present from the double layer. Figure 2.10 (c) shows how potential barrier is dependent on the screening diffuse layer of the ions. As κ^{-1} decreases the barrier also decreases in height. This is due to the solvent ions being closer to the nanoparticle. Figure 2.10 (d) shows how changing κ^{-1} also effects the small potential well present before the large potential barrier. This potential well is the cause of the nanoparticles flocculating.

Chapter 3

Experimental Methods

3.1 Liquid Phase Exfoliation

Section 1.4.2 in Chapter 1 presented a few common techniques to synthesize high quality nanomaterials. For a wide range of applications, it is desirable for the synthesized nanomaterials to exist as a colloid. Liquid phase exfoliation (LPE) represents a facile and cost effective method to produce a high quality nanomaterial dispersion[97, 135, 147, 207]. This time efficient method is highly scalable and environmentally friendly, provided a suitable solvent medium is used. LPE involves dispersing a 2D layered material in a solvent and applying high powered sonic energy. This process, also called sonication, is illustrated in Figure 3.1. The term "exfoliation" only applies to 2D layered materials, therefore when referring to 1D materials or nanoparticles clusters, the term "sonication" is just used.

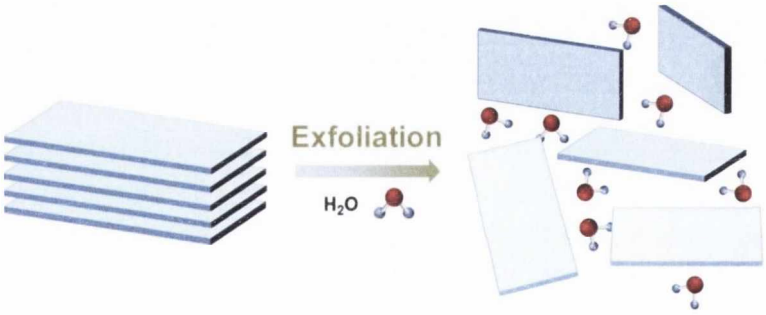


FIGURE 3.1: Schematic of the sonication process.

The ultrasonic energy is generated from the vibrations of a piezoelectric crystal when a current is passed though it. It is believed that ultrasonic waves throughout the solvent/solute mixture cause areas of compression and rarefaction. This process is illustrated in Figure 3.2. The frequency of these pressure changes is proportional

to the frequency of the ultrasonic waves themselves. During rarefaction, the sonic waves create extremely high-temperature vacuum bubbles which collapse violently during compression in a process called cavitation [208]. For a typical layered material in dispersion, the cavitations act to disrupt the weak van der Waal interactions between individual the sheets causing them to delaminate. After the solvent forms a stable sheath around the delaminated particles, an exfoliated colloid is formed.

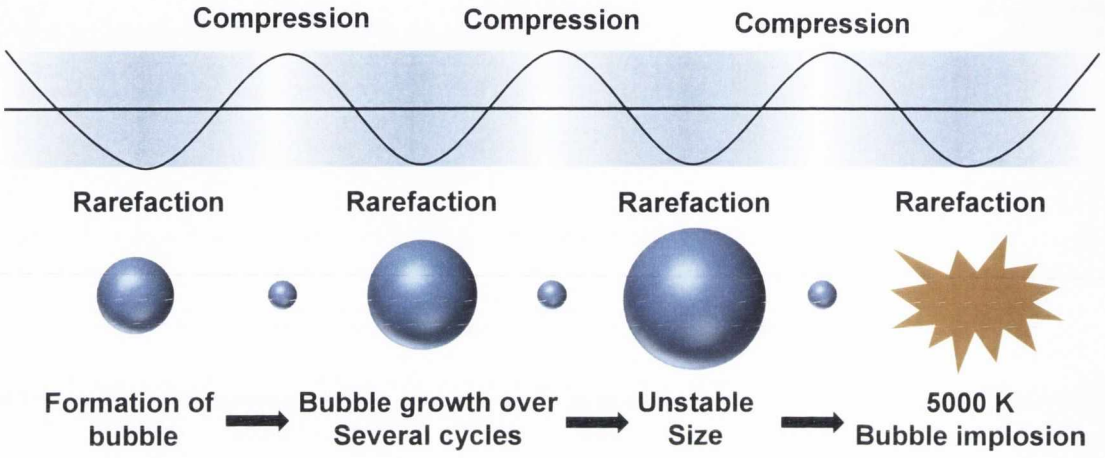


FIGURE 3.2: Schematic of the cavitation process.

In general, sonication devices allow for a series of variable experimental parameters. For examples, the relative powers, frequencies and sonication times can be adjusted while it is also common to vary the initial unexfoliated powder concentration. Changing these experimental parameters can have a direct effect on the resultant colloid's concentration or nanoparticle morphology. Similar consideration must be taken into account when choosing an appropriate solvent medium. However, a certain critical concentration is often achieved whereby continued sonication will not increase the resultant yield. This is directly due to the formation of stabilizing solvent sheaths surrounding each nanoparticle. Above this critical concentration, there is no available solvent molecules for further stabilization The critical concentration must be considered when choosing an appropriate dispersing solvent.

Post sonication processing involves the high speed centrifugation of the resultant dispersions [209, 210]. In most cases a majority of the material remains unexfoliated due to an inefficient quantity of solvent molecules forming sheaths or unoptimized experimental parameters. The centrifugal force applied to the dispersion causes a concentration gradient, separating the particles according to mass. If an appropriate centrifugation speed is chosen, the unexfoliated particles will sediment at

the bottom of the container while the nanoparticles will remain in dispersion. However, if the centrifugation rate is changed, a size selected dispersion of particles can be achieved.

3.2 Ultrasonic Spraying

The fabrication of uniform thin film electrodes was carried out by ultrasonic spraying [211–213]. Similar to the colloid synthesis in section 3.1, ultrasonic spraying relies on the use of ultrasonic waves greater than 20 kHz. This method of fabrication if highly repeatable, scalable and can produce large area, thin film electrodes in a short time period. Figure 3.3 illustrated the general operating principle of the ultrasonic spray head. The nanoparticle dispersion is stored in a external liquid applicator (syringe) which is connected to an ultrasonic spray head through the precision liquid delivery system.

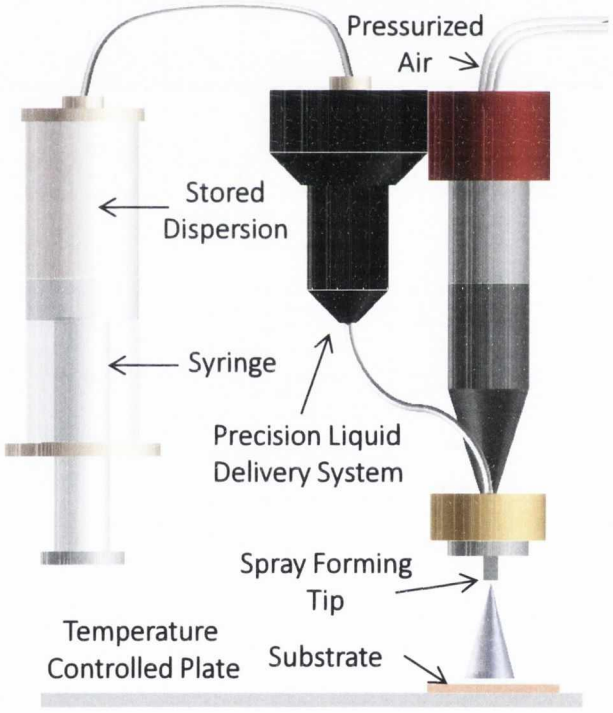


FIGURE 3.3: The ultrasonic spray head.

Pressurized air forces the dispersion out of the spray forming tip which consists of an ultrasonic transducer. Utilizing the piezoelectric effect, the transducer acts to

atomize the dispersion, producing a uniform cone which is directed towards a temperature controlled substrate. The substrate generally consists of a electrochemical current collector material such as Cu, Al or ITO coated glass.

As a controlled amount of dispersion is pumped through the spray tip, the piezoelectric transducer applies high frequency sonic waves. The sonic energy will cause large capillary waves to form in the dispersion and, when they reach a critical amplitude, the dispersion separates into a series of atomized droplets. This process is termed "atomization". Experimental parameters such as flow rate and atomization frequency can tune droplet sizes. While choice of dispersing solvent is important in the stabilization of the nanoparticle colloids, the relative effect on both the spray cone the ultrasonic spraying equipment must also be considered. Different surface tensions and viscosities have a direct effect on the flow rate and droplet size while more reactive solvents may have an adverse effect on the sprayer itself.

3.3 Ultraviolet-visible Spectroscopy

Ultraviolet-visible (UV-vis) spectroscopy is a method to determine the relative optical transitions of a material [214]. UV-vis spectroscopy works on the principle that, both π bonding and non bonding electrons can absorb either visible or UV light. The absorbed energy excites these electrons to higher anti-bonding orbitals. The transitional wavelength is highly dependant on the relative band gap of the material. Uv-vis spectroscopy is a useful method in determining optical transitions, extinction coefficients and concentrations of a material.

A suspended material, such as a colloid or a solution, is subject to both visible (400 - 800 nm) and UV light (< 400 nm). The material works to either absorb or transmit this electromagnetic radiation. The absorption spectrum is determined by subtracting the transmitted radiation from the incident beams and plotting the resultant absorbance against the wavelength. As a control, the spectrum of the pure dispersion solvent is subtracted from the resultant absorption spectrum. Peaks in the adsorption spectrum correspond to particular electron transitional events in the material. Commonly, as reflected light is not absorbed, the dominant absorption peak occurs at a wavelength corresponding to the complementary colour of the material itself.

The absorbance, A of a materiel is governed by the Beer-Lambert law [215–217],

$$A = \epsilon l C_j \tag{3.1}$$

where ϵ is the extinction coefficient ($g^{-1}cm^{-1}$), l is the path length in cm and C_j is the concentration of the species j. ϵ defines how strongly a material absorbs light at a given wavelength and can be determined by a linear plot A vs. C_j.

3.4 Electron Microscopy

Electron Microscopy (EM) is a high end characterization method which exploits the interaction between electrons with the features of highly crystalline nanomaterials [218, 219]. It is applicable in the areas of morphological characterization, elemental and crystalline analysis. EM was first developed in the early 1930s as a way to overcome the optical limitation of light set by Rayleigh's criterion [220]. This limit determined that the maximum resolution of light waves was about half the wavelength (i.e. $R \sim \lambda/2 \sim 200\ nm$) however, this limit is rarely experimentally observed.

Due to the work in quantum theory, it was determined that electrons exhibit wavelengths 100,000 shorter than standard light waves [221]. Electrons had previously shown to interact with atomic core levels in various X-ray characterization techniques. As such, their application in high end microscopy was envisioned. The first truly functioning EM was built in Germany in 1931 by Ernst Ruska and Max Knoll and has become the basis of the modern day scanning EM [222]. Over the past 8 decades, EM power and resolution has increased drastically to the point where atomic resolution is possible [223]. More recently, inventions such as the aberration corrected EM have shown that objects at about 50 pm in dimension can be resolved [224]. EMs have shown application in a wide variety of scientific disciplines such as materials science, biology and medicine [219].

In 1924, the wave particle duality of subatomic particles was initially suggested by de Broglie. As such, particles that possess wavelike properties also possess a characteristic wavelength. According to de Broglie, the wavelength of a particles can be connected to its relative momentum,

$$\lambda = \frac{h}{mv} \tag{3.2}$$

where h is Plank's constant, m is the particle's mass and v is the particle's velocity. If a potential is applied to one of these particles, The kinetic energy of the particle travelling in the resultant electric field is given by,

$$\frac{1}{2}mv^2 = q_i E \tag{3.3}$$

where q_i is the charge of the particle and E is the potential. Applying equation 3.3 to equation 3.2 gives an expression relating the wavelength of the particles to the potential applied.

$$\lambda = \frac{h}{\sqrt{2m_e eE}} \tag{3.4}$$

where e is the charge of an electron. As resolution is directly proportional to the wavelength, increasing the applied potential should theoretically increase the resolution. This is the basic operational principle behind EM and the reason some EMs have operational potentials upwards of 300 kV. This potential is applied to an electron producing source situated at the top of an EM column. Contemporary EMs consist of either a field effect gun or a high boiling point metal tip, designed to produce a coherent beam of electrons. As such, EM columns are in a state of very high vacuum to allow an unimpeded flow of electrons as it reaches the sample.

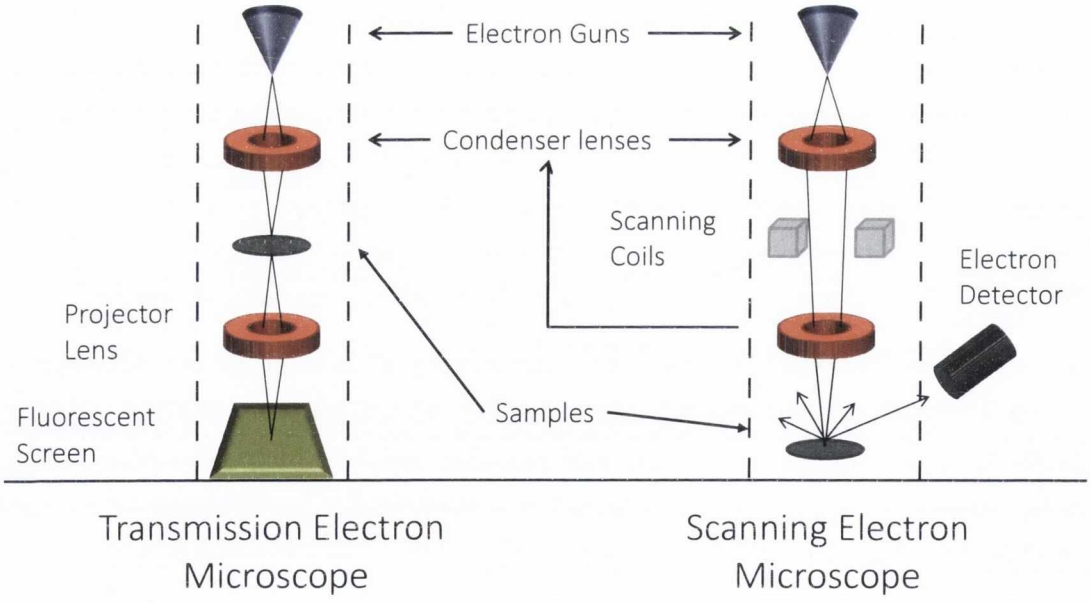


FIGURE 3.4: Schematic of a typical TEM and SEM.

EMs are split into two two broad categories based on their interaction principles as illustrated in Figure 3.4. Both the transmission electron microscope (TEM) and the scanning electron microscope (SEM) operate by focussing the coherent beam of electrons directly onto a sample using a series of condenser and objective lenses. These lenses are manufactured from sources of copper and magnetic iron and subject the electron beam to the basic Newtonian laws of optics.

However, while TEMs detect electrons that pass through relatively thin samples, SEMs operate by detecting back scattered and secondary electrons. In TEM, the beam interacts with a series of crystalline planes in the nanoparticle and an image is formed from the the resultant diffracted electrons. On the other hand, the scattered and secondary electrons emanating from a nanoparticle in SEM analysis are a result of the surface features of the particle. Figure 3.5 shows a series of interactions commonly exhibited when an electron beam interacts with a sample.

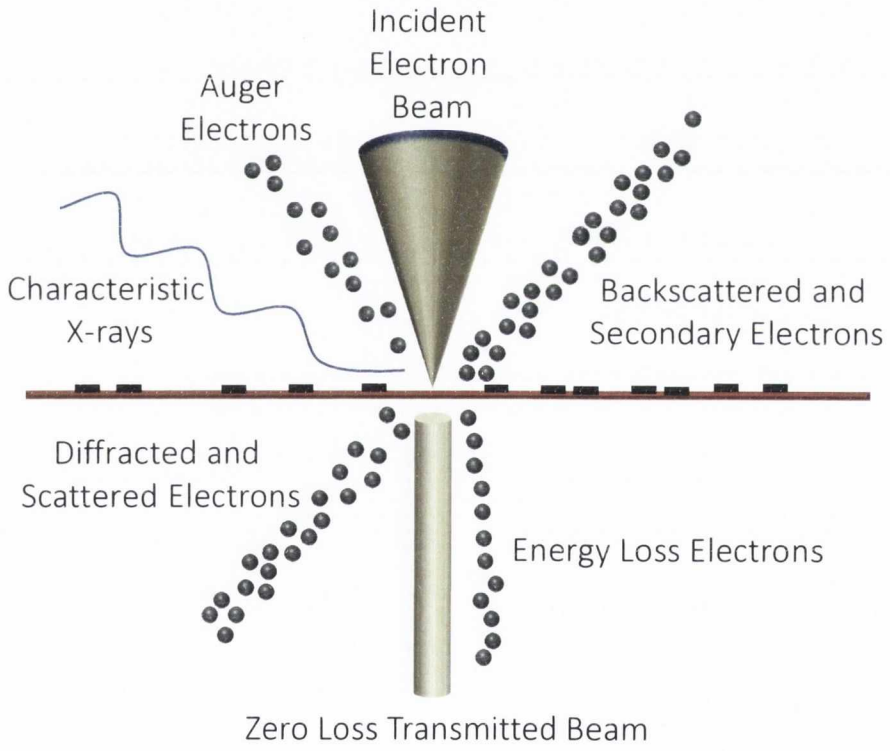


FIGURE 3.5: Common signals resulting from the electron beam's interaction with the sample.

For sufficiently thin samples, such as that exhibited by 2D materials, the electron beam passes through the sample causing a series of scatterings. In a TEM, a small portion of the electrons pass through uninhibited, however, some interact elastically with the nucleus or inelastically with the electron cloud. When focused,

the elastically scattered electrons contribute to the formation of an image. However, focusing the back focal plan of the objective lens allows the viewer to witness the corresponding diffraction pattern. Inelastically scattered electrons scatter at very low angles and, due to interactions with the electron cloud, can be used for elemental analysis in a process called electron energy loss spectroscopy (EELS) [225]. Electrons which scatter backwards in processes such as Rutherford scattering are mainly detected by a series of detectors above the nanoparticle in SEM analysis. Resultant Auger electrons and X-ray can be used for elemental analysis (EDX) [226].

3.5 Brunauer-Emmet-Teller Surface Area

Nanostructured materials tend to exhibit a larger surface area than their bulk counterparts. The relative quantity of absorption sites can be easily determined by nitrogen absorption techniques. Various methods of analysing nitrogen absorption exist, however, Brunauer-Emmett-Teller (BET) analysis is in widespread use due to its accuracy [227]. Surface adsorption can either be classed as chemisorption and physisorption [228]. When a particle is chemisorbed onto a surface an overall change in electron density occurs and the particle is chemically bound. However, if the particle is physisorbed, it exhibits a weak physical bond to the surface with no overall change in electron density. BET theory aims to explain the physical adsorption of gas molecules on the surface of a solid material.

In the 1930s Brunauer, Emmett and Teller derived a relation from gas kinetics relating the partial pressure of an adsorbate to the multi-layer build up on the surface of the dry powder. Initially, surface adsorption was described by Langmuir who studied the formation of a monolayer on the surface of a solid [229]. Figure 3.6 (a) shows the relative surface coverage of a single layer as time progresses. BET theory extended this theory to include the formation of further layers above the initial layer. Figure 3.6 (b) illustrates and example of this. As the surface is partially covered, a second layer grows on top of the first layer, often before the first layer reaches 100% coverage. In both cases, however, the coverage is heavily dependant on the partial pressure (or concentration) of the Nitrogen.

Brunauer, Emmett and Teller derived an equation to show the linear relationship between the surface coverage and the partial pressure of the gas.

$$\frac{1}{v_g[(\frac{p_0}{p}) - 1]} = \frac{c-1}{v_m c}\frac{p}{p_0} + \frac{1}{v_m c} \tag{3.5}$$

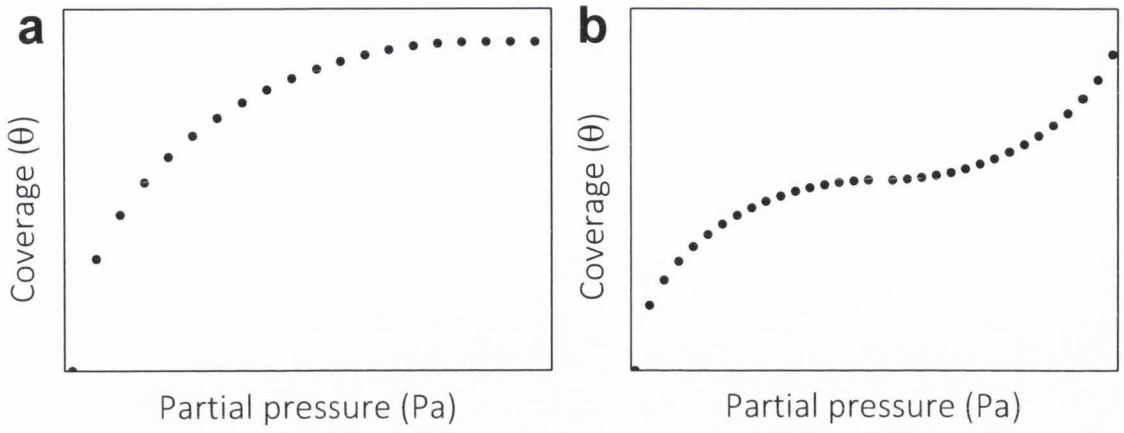


FIGURE 3.6: (a) Langmuir and (b) BET isotherms.

where p and p_o are the partial and saturation pressures of the adsorbate, v_g is the volume of gas adsorbed, v_m is the volume of one monolayer and c is the BET constant. From v_m, calculated in equation 3.5, the surface area of the material can be calculated from the following two equations.

$$A_{total} = \frac{v_m N_A s}{V_m} \tag{3.6}$$

$$A_{BET} = \frac{A_{total}}{m} \tag{3.7}$$

where N_A is Avegadro's number, s and V_m are the cross sectional area and molar volume of the adsorbate, and m is the total mass of the sample.

3.6 X-ray Diffraction

X-ray diffraction (XRD) is a spectroscopic method used to determine the crystalline structure of a material's surface [230]. In a typical XRD set-up illustrated in Figure 3.7, high energy electromagnetic X-rays are generated from the interaction of high energy electrons with a metal target. The X-rays are then directed towards a crystalline sample at a particular angle, θ, in which they diffract at characteristic angles. The diffracted beams undergo constructive and destructive interference in which the constructive components are analysed. The detector is placed at an angle

2θ from the X-ray source and the sample is aligned so the normal angle is half way between the source and detector.

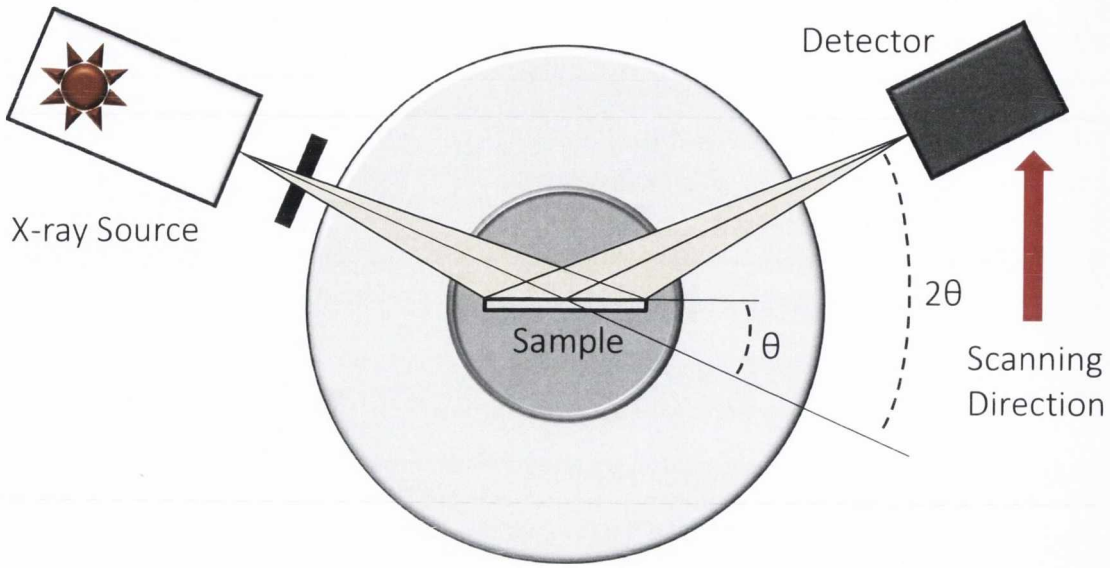


FIGURE 3.7: A typical XRD apparatus.

The constructively interfered beams are received by a detector and the relative intensities are plotted against their corresponding values for 2θ. A general XRD spectrum is represented by a set of peaks characteristic to the material in question. Each individual set of planes diffracts X-rays at set angles which are represented in the spectrum. In 1913, William Lawrence Bragg and his father William Henry Bragg proposed that the diffraction angle of a set of planes can be related to the inter planer spacing [231].

$$\lambda = 2d\,sin(\theta), \quad n = 0, 1, 2, ... \tag{3.8}$$

where λ is the X-ray wavelength, d is the inter-planer spacing and θ is half the angle of the peak determined from the XRD spectrum. Special fitting methods can be used to determine both the Miller indices of the plane in question and the relative lattice constants. For example, in a simple cubic system the lattice constant, a_0 has equal lengths in all three dimensions with the corresponding angles between them being 90°. Applying least square fitting methods can be used to determine the quantities from the following equation,

$$d_{hkl} = \frac{a_0}{\sqrt{h^2 + k^2 + l^2}} \tag{3.9}$$

In general, crystalline structures adopt more complex structures, such as the orthorhombic or triclinic systems. A whole series of equations exist to quantify these patterns and are presented elsewhere [232].

3.7 X-ray Photoemmision Spectroscopy

X-ray photoelectron spectroscopy (XPS) is a surface sensitive method used to probe the core ion levels of surface atoms [233]. Not only can XPS analysis be used to determine the elemental composition of a material, it can also elucidate the electronic states of the components of a chemical in a process called electron spectroscopy chemical analysis (ESCA) [234]. This is advantageous in confirming the chemical composition of material.

X-rays sources from targets such as Al or Mg interact with the core levels of an atom resulting in ejections of electrons as illustrated in Figure 3.8 (a). These "photoelectrons" are analysed by a detector and the signal intensity is presented as a function of the kinetic energy (KU_{max}) of the photoelectrons. The KU_{max} is characterized by the binding energy of a core level electron as determined by Einstein's photoelectric equation [235].

$$KU_{max} = h\upsilon - \Phi - BU \tag{3.10}$$

where KU_{max} is the maximum kinetic energy detected, $h\upsilon$ is the incident X-ray energy, Φ is the work function of the atom and BU is the binding energy holding the electron to its core level. The Φ of the atom describes the energy needed to remove an electron completely from the atom while the BE describes the characteristic energy binding the electron to a core level. In general, spectra are obtained from the photoelectrons which have escaped from the top $\sim 10nm$ layers of the material.

Figure 3.8 (b) shows the typical plot of the core level BU plotted against the resulting intensities. At low BUs the loosely bound valence electrons are evident. However, at higher BUs both core lines and secondary peaks are apparent representing the principal core levels of the atom. Various other signals are present referring to the presence of Auger electrons which are described elsewhere [236].

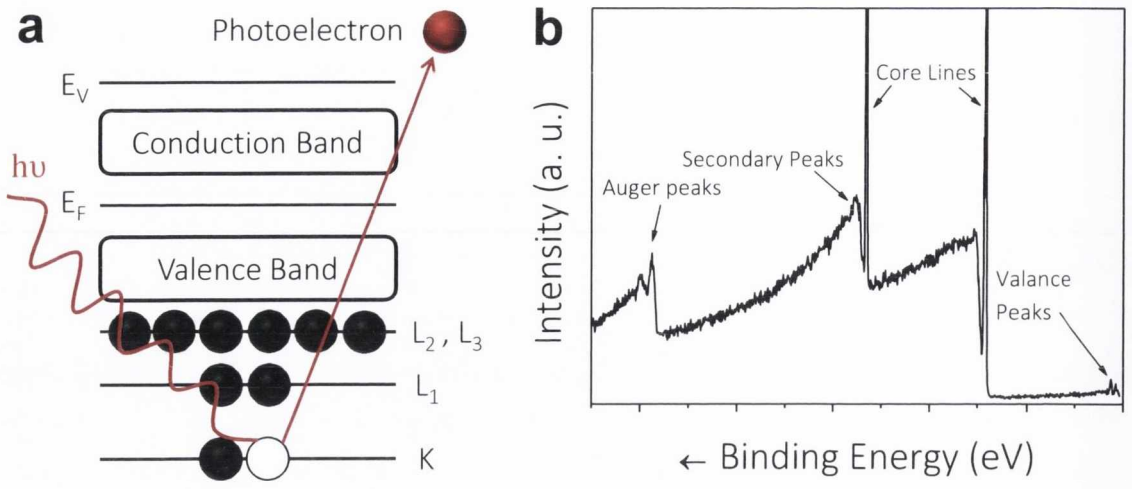


FIGURE 3.8: (a) Band structure and (b) general photoemission spectrum showing the main signals produced in XPS.

3.8 Electrochemical Techniques

Modern electrochemical workstations are generally composed of three main components: a potentiostat, a signal waveform generator (SWG) (which is commonly housed with the potentiostat) and a computer [155, 158, 237]. Experimental parameters are entered into a user interface which controls the operation of the potentiostat. Electrochemical methods can either be defined as transient (cyclic voltammetry or galvanic discharging) or stationary (electrochemical Impedance spectroscopy) based on the waveform applied to the cell from the SWG. A general electrochemical channel on a potentiostat has three ports which connect to an electrochemical cell. The ports are connected to the working electrode (WE), the counter electrode (CE) and the reference electrode (RE) electrodes of a triple electrode cell. Figure 3.9 show simplified schematics of both the potentiostat and cell respectively.

In Figure 3.9 (a), the operation of the potentiostat can be approximated as that of an operational amplifier. It is paramount that the potential across the cell needs to be controlled accurately and, as such, the impedance of the RE electrode is set very high (>15 $k\Omega$). This is to ensure a negligible current flows through it the allows accurate measurements of potential between the WE and RE. The RE is connected to the negative terminal of the "amplifier", in which the initial driving potential, V_i, is applied to the positive terminal ($E_i = E+$). Therefore the output potential, E_O, experienced by the working electrode is given by,

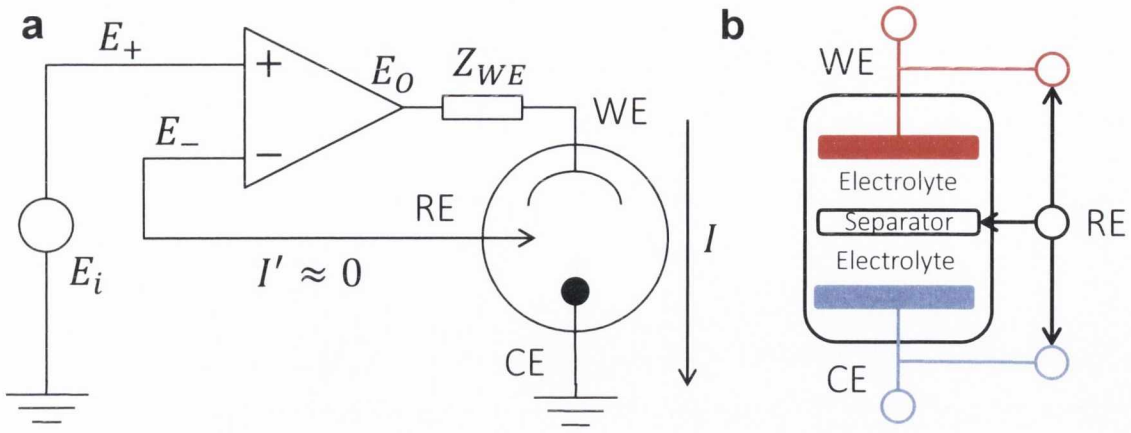


FIGURE 3.9: (a) The potentiostat equivalent circuit and (b) schematic of a typical cell.

$$E_O = G(E_+ - E_-) \tag{3.11}$$

where G is the amplifier gain, and $E+$ and $E-$ are the input potentials.

Figure 3.9 (b) shows the general set up of a triple electrode cell (3EC). To provide mechanical support and to prevent short circuiting, an ionically permeable separator is places in between the WE and CE and soaked with a suitable electrolyte [238]. The WE is described as the electrochemically active material being studied while the CE is a suitable material used to provide a counter reaction such as pure Li or an inactive Pt electrode. The RE consists of a standard reference material such as that mentioned in section 2.1.1. As such, 3EC cells can also be termed "half cells" as they are compared to a standard reference material

When determined the electrochemical properties of a full cell, i.e. when not compared to a standard reference cell a two electrode cell (2EC) set up is used. This cell does not contain an individual RE, hence any potential measurements are determined at the CE. Herein is a description of the three most common electrochemical characterization methods operated by a potentiostat.

3.8.1 Cyclic Voltammetry

Cyclic voltammetry (CV) is one of the most widely employed methods in the study of electrochemistry [166, 239]. The main principle of this technique is to apply a

linear potential ramp to a cell between two potential limits and to measure the generated current. The experiment commences at a potential E_1 at $t = 0$ and a constant increasing linear potential is applied at a scan rate, υ, given in units of $mV\ s^{-1}$, see Figure 3.10 (a).

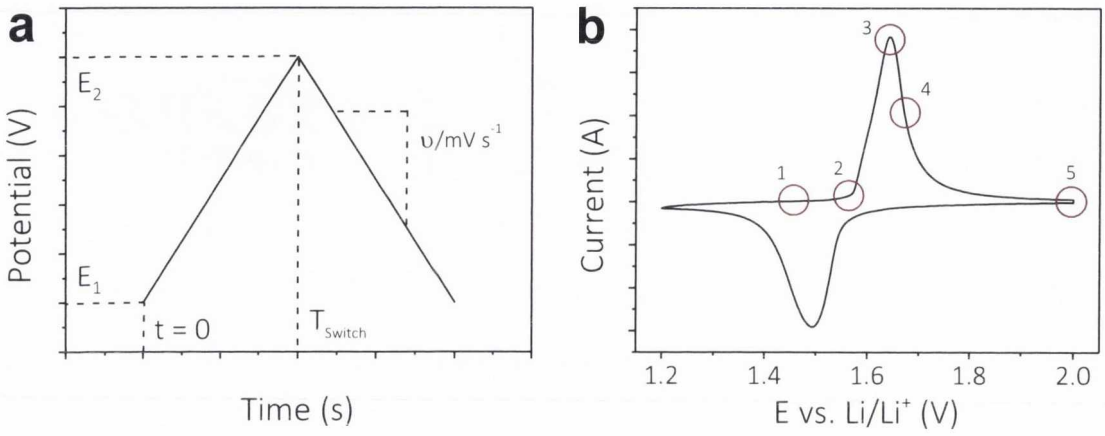


FIGURE 3.10: Potential-time dependence for a CV and (B) typical CV of $Li_4Ti_5O_{12}$ anode cycled between 1.2 and 2 V at a scan rate of $0.1mV s^{-1}$.

Once the potential reaches E_2 at t = t_{switch} the scan rate is reversed. The interval $E_2 - E_1$ is termed the potential window and is heavily dependent on the stability of the electrolyte and, in some cases, the potential range in which resides the electrochemical process of interest. The experiment is generally started at a potential inside the potential window where negligible current flows i.e. the E_{OCP}. This started potential is selected so that the electrode being investigated is not initially oxidized or reduced.

Depending on the electrochemical processes being studies CVs can have varying shapes. Slower, faradaic reactions tend to exhibit large redox peaks, while small peaks or rectangular CVs tend to indicate more pseudocapacitive or capacitive responses. CVs can be used to map out other such processes as intercalations or phase changes. Figure 3.10 (b) shows a typical example of a CV in which the intercalation and deintercalation processes are pointed out in the electrochemical cycling of $Li_4Ti_5O_{12}$, a commonly studies anode material for Li-ion batteries. As the potential increases from its initial value it remains at negligible current though the E_{OCP} at point 1. When sufficient potential is applied to overcome the activation polarization, the current increases rapidly as shown at point 2. This process is an example of an activation controlled process as the concentration of electrolyte at the interface is plentiful (see BV kinetics in section 2.1.3). At point 3 the current has reached maximum as the electrolyte ions near the surface of the electrode have sufficiently

depleted. As more electrolyte ions need to diffuse from the bulk to the surface the electrochemistry is mass transfer controlled. At point 4 the current is decreasing as a result of the mass transfer having a slower rate than the rate of reaction at the electrode as governed by the Cottrell equation as described in section 2.1.5. At point 5 the upper potential window is reached and the potential reverses direction.

The capacitance of a device can be directly inferred from the CV by plotting the local charge, Q_i, as a function of potential, E. It is well established that,

$$Q_i = |\int i(t)dt|_E \tag{3.12}$$

where $i(t)$ is the time dependant current, t is the time and E is the potential. In terms of quick electrochemical processes, a plot of Q_i against E is linear. The capacitance can be thus determined from the slope of the graph (See equation 2.25). However, in slower redox process this plot can be non-linear resulting in the use of the following equation to determine capacitance.

$$C = \frac{\int_{E_2}^{E_1} i(t)\,dt}{\int_{E_2}^{E_1} i(t)\,dt} \tag{3.13}$$

3.8.2 Galvanic Cycling

Another commonly used transient technique used in electrochemical analysis is galvanic cycling (GC). GC differs from CV in that as opposed to applying a constant potential over a set potential range, a constant current is applied and the potential is measured as a function of time. This method is very useful in determining such properties as storage capacity, cyclability and rate capability. GC is commonly used in battery research as it can be applied to large scale power storage.

Figure 3.11 shows the typical GC plots exhibited by both capacitive and redox electrodes. As the charging starts at E_1 the potential increases as a function of time. Once it reaches E_2 the direction of the current changes and the potential is measured until it reaches its initial value E_1. As charge is a product of current and time, the amount of charge acquired during charging and lost during discharge can be calculated. Similar to CV, both fast capacitive and slow redox processes can be easily determined. As shown in Figure 3.11 the solid line represents capacitive charging evident in an ECDL capacitor while the dashed line represents a redox process evident in a battery.

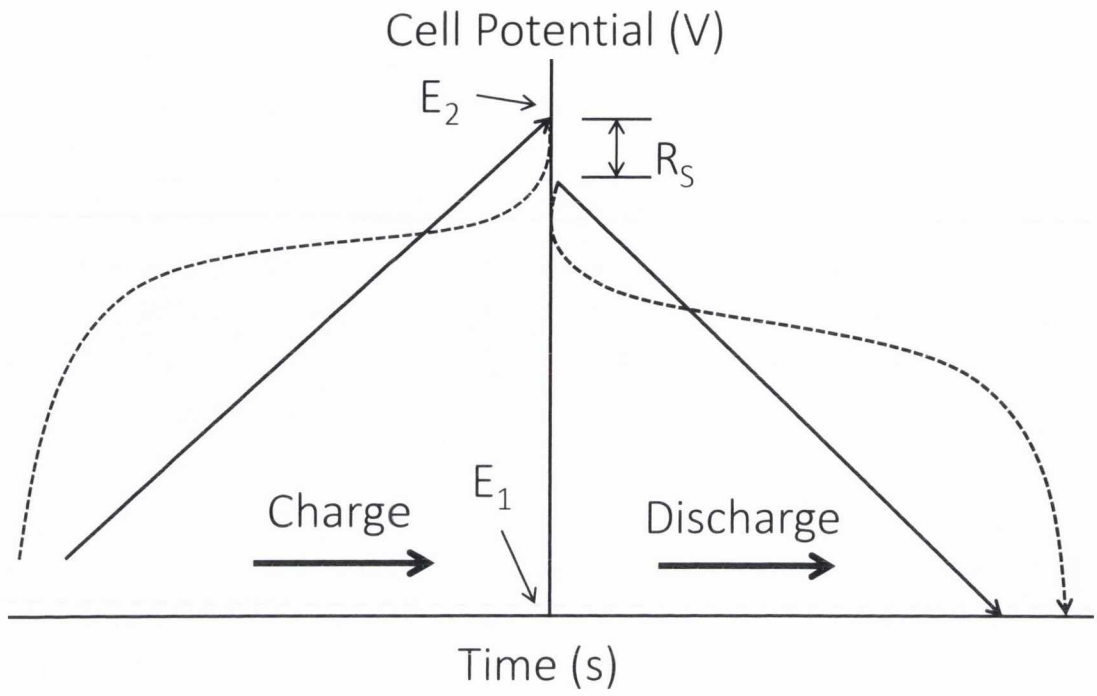


FIGURE 3.11: Typical galvanic charge/discharge profiles for both batteries and supercapacitors

GC tests can be further employed to determine the diffusion coefficient of Li-ions in certain materials [240]. Applying a series of constant current pulses between a defined potential window separated by a controlled rest period the diffusion coefficient can be determined by analysis of the following equation,

$$D = \frac{4}{\pi\tau}\left(\frac{mV_m}{M_W S_A}\right)^2\left(\frac{\Delta E_S}{\Delta E_\tau}\right)^2 \tag{3.14}$$

where τ is the period of the pulse, m is the mass and, V_m is the molar volume, M_B is the molecular weight and S_A is the active surface area of the host lattice. ΔE_S and ΔE_τ define the potential difference between subsequent relaxations and potential difference spanned over the range of the current pulse. This method is directly known as Galvanic intermittent titration technique (GITT).

3.8.3 Electrochemical Impedance Spectroscopy

Electrochemical impedance spectroscopy (EIS) is a stationary technique used to determine the impedance and phase properties of an electrochemically active material

as a function of frequency [241]. It can be used to elucidate charge transfer processes at electrode/electrolyte interface

A circuit element's resistance is defined as the ability of the element to resist the flow of electric current. Mathematically this is given by Ohm's law,

$$R_S = \frac{E}{I} \tag{3.15}$$

where R_S is the resistance, E is the potential and I is the current. This simple relationship is limited to an ideal resistor. Ideal resistors obey Ohm's law in all situations, have a frequency independent resistance and have an "in phase" relationship between the applied potential and the resulting current. However, most real world elements deviate majorly from this ideal situation and require a more general circuit parameter. This is how the concept of impedance came into existence. Much like resistance, impedance is measure of the ability of the circuit element to resist the flow of current, however, the resulting impedance is heavily frequency dependent and an apparent phase difference exists between the potential and the current.

EIS works by applying an alternating sinusoidal potential, $E(t)$, to an electrochemical cell and measuring the resultant current over a range of frequencies. The resulting current will also be sinusoidal in nature. In order to measure a more linear response, a small excitation potential is applied as to approximate the potential as pseudo-linear. The potential applied is given by,

$$E(t) = E(0)sin(\omega t) \tag{3.16}$$

where $E(0)$ is the applied potential amplitude and ω is the radial frequency which equals $2\pi\nu$. In this pseudo linear system, the current response, $i(t)$, to the applied potential will possess the same frequency, however there will be an inherent phase change based on the properties of the circuit element. The current response is given by,

$$i(t) = i(0)sin(\omega t + \delta) \tag{3.17}$$

where $i(0)$ is the peak current and δ is the phase difference. Similarly to Ohm's law the impedance can be given as,

$$Z(t) = \frac{E(t)}{i(t)} = \frac{E(0)sin(\omega t)}{i(0)sin(\omega t + \delta)} = Z(0)\frac{sin(\omega t)}{sin(\omega t + \delta)} \tag{3.18}$$

where Z(0) is the impedance amplitude. This expression is commonly expressed as a complex function using Euler's formula,

$$Z(t) = Z(0)(cos(\delta) + isin(\delta)) \tag{3.19}$$

As shown in Figure 3.12 (a), plotting the real part of equation on the x-axis and the imaginary part on the y-axis, a Nyquist plot is formed. This particular Nyquist plot is characteristic of a Randles circuit, shown in Figure 3.12 (b), and demonstrates the common parameters in a a typical electrochemical cell [242]. Each electrochemical process can be approximated as an individual circuit component. The impedances of the most common circuit elements are shown in Figure 3.13. It is clear that the Nyquist plot has very different responses for different circuit components.

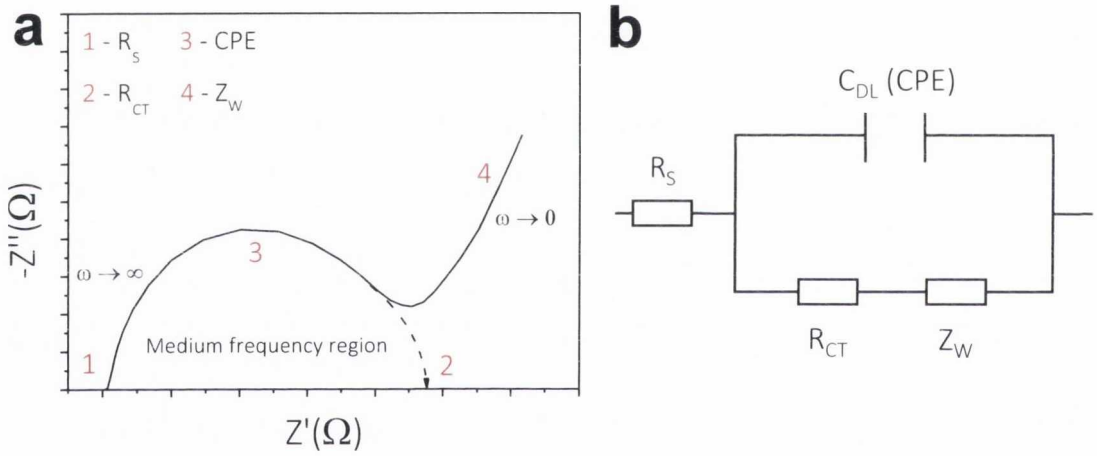


FIGURE 3.12: (a) A typical Nyquist plot and (b) Randles circuit

At AC potentials with high frequencies (as $\omega \longrightarrow \infty$) kinetically controlled processes are dominant. In Figure 3.12 (a), the resistance of the electrolyte, R_S, can be seen at the extreme high frequency region. As there is no capacitive build up of ions in the bulk electrolyte, this is a purely resistive process and happens on the μs scale. When the frequency decreases, a wide semicircle is observed corresponding to the charge transfer and double layer processes exhibited at the electrode/electrolyte phase boundary. These slower process refer to the charge transfer resistances exhibited by faradaic and pseudocapacitive processes, R_{CT}, and the capacitive build

up of ions at the double layer, C_{DL}. For ideal capacitive behaviour the centre of the circle resides on the x-axis, however, as no capacitor is ever ideal the centre tends to lie below. This is represented by the constant phase element, CPE [243, 244]. The CPE is given by the following equation,

$$CPE = \frac{Z_0}{\omega^f} e^{-\frac{\pi}{2} fi} \tag{3.20}$$

where Z_0 is the impedance of a ideal capacitor and f is a constant. The value of f depends on the properties of the material. For an ideal capacitor $f = 1$ and the value decreases for less ideal capacitors. Finally, for low frequency processes on the order of 1 s, such as that of the diffusion of ions though the active material matrix, a straight line 45° is observed. This corresponds to the Warburg impedance, Z_W of the material [245]. This is an important concept for layered materials as it quantifies the electrolyte ions travelling through the host material.

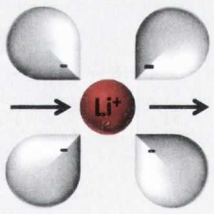
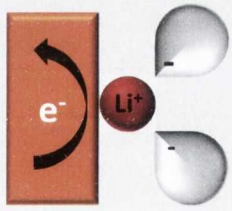
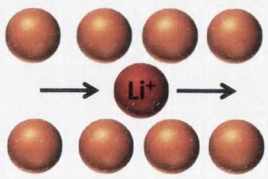
Frequency Region	High	Medium	Low
Physical Phenomenon	Diffusion within Electrolyte	Charge-transfer and capacitive processes	Solid-state Diffusion
Time Scale	< 10 µs	10 µs – 1 s	1 s
Schematic			

FIGURE 3.13: The basic processes associated with EIS.

Chapter 4

Vanadium Pentoxide Nanosheets

4.1 Introduction

The intercalation of Li-ion into layered dichalcogenides was first realized in the early 1970s with such examples as TiS_2 and TaS_2 [10]. It was not until a few years later that Li-ion intercalation was realized for a series of multivalent metal oxide materials. It was demonstrated that these metal oxide compounds could exhibit high experimental capacities and often large open circuit potentials (upwards of 3 V) [150]. In particular, vanadium pentoxide (V_2O_5) has received significant attention due to its layered structure and relatively high theoretical capacity (294 $mAh\,g^{-1}$ for a 2 Li-ion insertion) [246]. Both abundant and cost-effective, V_2O_5 has been heavily studied over the past 40 years and is a major contender as a high energy LIB or SC cathode material yielding energy densities up to 250 $Wh\,kg^{-1}$ and power densities of 200 $W\,kg^{-1}$ [84, 150, 247–249]. However, recent work has also shown V_2O_5 as a potential cathode material for Na-ion based devices [250–252]. It is projected that V_2O_5 will become a widely used material for the next generation of energy storage devices with vanadium flow batteries already hold a niche position in the energy storage industry [253, 254]. Applications in fields such as sensing [255–257] and catalysis [258, 259] indicates how wide the potential for V_2O_5 will be.

A yellowy-orange compound, see Figure 4.1 (a), V_2O_5 is commonly used as an industrial catalyst specifically in the production of sulphuric acid [261]. Unfortunately, naturally occurring V_2O_5 only exists as the mineral shcherbinaite, which is rare and specifically found in fumaroles (the opening of volcanoes) [262]. As a result, various industrial methods for the production of V_2O_5 have been utilized, most notably the heating of vanadium metal in excess oxygen and the decomposition of ammonia metavanadate [263].

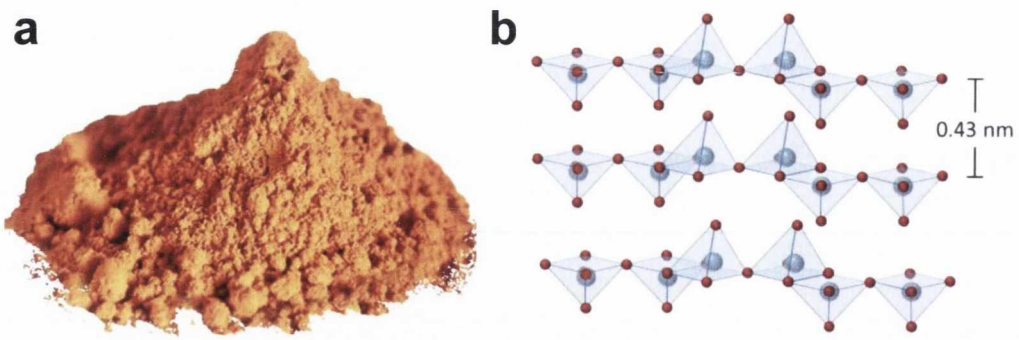


FIGURE 4.1: (a) Optical image showing unexfoliated V_2O_5 powder (taken from [260]) and (b) schematic showing the corresponding crystal structure.

$$2NH_4VO_3 \rightleftharpoons V_2O_5 + 2NH_3 + H_2O \tag{4.1}$$

Commercial V_2O_5 powder exhibits a specific layered orthorhombic arrangement [264–266]. Each individual layer consists of series of bonded VO_5 square pyramids sharing both edges and corners as demonstrated in Figure. 4.1 (b). Alternatively, it can be viewed as a series of distorted VO_6 octahedrons. The sixth atom corresponds to a weakly bonded O atom from an adjacent layer. The anisotropic layered structure crystallizes in the *Pmmn* space group and is known to exhibit an inter-layer spacing of 0.43 nm [267].

The accommodation of Li-ions between adjacent layers of V_2O_5 was first demonstrated by Whittingham *et al.* in 1976 [268]. It has since been demonstrated that the intercalation of Li-ions into V_2O_5 is a complex process [269]. The Li^+ intercalation and deintercalation process can be expressed by,

$$V_2O_5 + xLi^+ + xe^- \rightleftharpoons Li_xV_2O_5 \tag{4.2}$$

The lithiated V_2O_5 exhibits five different phases depending on the intercalated Li content, namely, $\alpha - V_2O_5$ (x < 0.01), $\beta - Li_xV_2O_5$ (0 < x < 1), $\delta - Li_xV_2O_5$ (1 < x < 2), $\gamma - Li_xV_2O_5$ (x = 2) and $\omega - Li_xV_2O_5$ (x > 2). It was realized that Li-ion insertion into the V_2O_5 lattice was completely reversible between the α and β phases, however, due to structural deformations the intercalation process became irreversible once x > 1 [270, 271]. As such, the potential to decrease structural deformation of the host lattice has prompted an exploration of synthesis of nanostructured V_2O_5. Nanostructuring V_2O_5 will also aid in increasing surface area of the cathode and

reducing the Li-ion diffusion lengths as described in section 1.4.2. To date V_2O_5 nanostructures have shown to exhibit a wide variety of morphologies, for example, one dimensional nanorods [256, 272–275], nanotubes [276–280], nanoribbons [269, 281], nanobelts [282–285], amorphous xerogels [286–291] as well as two dimensional nanosheets [292–297]. A wide range of methods have been employed to synthesize nanostructured V_2O_5 including electrodepostion [298–301] hydrothermal sol-gel techniques [285, 302–305], precipitation [306, 307], CVD [308–310] and sputtering [311, 312].

To date, V_2O_5 nanosheets have exhibited relatively high capacities exceeding that of its theoretical capacity. For example, Wang *et al.* demonstrated a low cost and facile precipitation method to synthesize V_2O_5 nanosheets with discharge capacities of 294 $mAh\,g^{-1}$ at 50 $mA\,g^{-1}$ with a 60% retention in capacity after 50 cycles [313]. Similarly, Li *et al.* showed how a facile and green hydrothermal method to fabricate a high energy V_2O_5 nanosheet cathodes with capacities reaching 303 $mAh\,g^{-1}$ at 100 $mA\,g^{-1}$ with an 82% retention in capacity after 100 cycles [314]. The work of Coustier *et al.* demonstrated that sol-gel techniques may be used to fabricate xerogel V_2O_5 cathodes with capacities reaching upwards of 400 $mAh\,g^{-1}$ [315]. This superior value demonstrates how simple techniques may be used to fabricate high energy cathodes. However, the methods are complex and require the use of hazardous chemicals. The work of Rui *et al.* proposed employing the sonication method described in section 3.1 to exfoliate ultra-thin V_2O_5 nanosheets in formamide [151]. This works suggests the exfoliated nanosheets exhibit similar large storage capacities with excellent cycling performance. However, similar to the methods proposed by Coustier *et al.*, formamide is a relatively hazardous and reactive precursor material and potentially harmful to the environment making it unsuitable for large scale fabrication. Traditionally, V_2O_5 is known to form stable xerogels from hydothermal synthesis methods with H_2O. As such, H_2O may represent an alternative sonication medium providing an environmentally friendly and facile method to produce high quality nanosheets.

Herein, a V_2O_5 nanosheet colloid is produced *via* the sonication of commercial powder in pure H_2O. Various exfoliation conditions such as sonication time, power and frequency were also studied. Further investigations were carried out into the stabilization mechanisms over a wider range of solvent mediums. Ultrasonic spraying of both pure V_2O_5 and a V_2O_5/SWCNT blend was carried out to fabricate a large area, flexible, binder free cathode which display high storage capacities and impressive rate capabilities.

4.2 Experimental

Synthesis - The V_2O_5 nanosheets were obtained *via* the LPE of V_2O_5 powder (99.99%, American Elements) in deionized H_2O. The dispersions ($0.1\,mg\,ml^{-1}$) were placed in a 50 ml centrifuge tube and sonicated for 5 h at 182 W, 80 kHz and kept at a temperature of $20°C$ by periodically changing the bath water (Fisherbrand P120 H, 240W). The resultant dispersion was centrifuged at a rate of 1000 rpm for 1 hr (Heraeus Multifuge X1 centrifuge) and the top 20 ml of supernatant was collected and kept in a 200 ml bottle for storage. The LPE process was repeated several times to provide adequate quantities for the succeeding experiments. The concentrations of the V_2O_5 nanosheet dispersions were determined by vacuum filtration through an alumina filter membrane (Whatman, 0.02 μm pore diameter). The effects the sonication time (1 - 10 hr), power (72 - 240 W) and frequency (20 - 80 kHz), and the initial powder concentration (1 - 5 $mg\,ml^{-1}$) on the resultant V_2O_5 nanosheet concentration were determined. In addition, the LPE of V_2O_5 powder in a range of different solvents such as N-methyl-2-pyrrolidone (NMP), benzyl alcohol, benzyl benzoate (BB), ethanol, cyclohexanone, butyl acetate (BA), methanol, dibutyl ether, acetone, 2-propanol (IPA), formaldehyde and dimethylformamide (DMF) were also conducted. A separate dispersion of SWCNT was prepared by mixing 0.1 $mg\,ml^{-1}$ of P3-SWCNTs (99.99%, Carbon Solutions Inc.) with 50 ml water and sonicated at 20 kHz for 1 hr.

Characterization - Scanning electron microscopy (SEM) was performed using a Zeiss Ultra Plus (Carl Zeiss, Germany). Transition electron microscopy (TEM), scanning transition electron microscopy (STEM) and energy dispersive x-ray spectroscopy (EDX) were performed using a Titan high-resolution TEM (HRTEM) at 300 kV (FEI, USA). The nanosheet dispersion was drop-casted onto holey carbon grids (Agar Scientific, UK) and allowed to dry overnight. The nanosheet dimensions were statistically analysed on TEM by measuring the longest axis of the nanosheet and assigning it as the length followed by measuring an axis perpendicular to this at its widest point and assigning it as the width. Optical spectroscopy was done using a Cary 6000i UV-Vis absorbance spectroscopy (Agilent, USA). Each dispersion was diluted by a factor of ten with respect to the dispersing solvent to prevent over-scattering of the incident light beams. To further clarify the chemical compositions of the as-prepared V_2O_5 nanosheets, X-ray photoelectron spectroscopy (XPS) (CLAM 4 MCD, VG Microtech, UK) was employed using a 200 W unmonochromated Mg X-ray excitation source (1253.6 eV) with samples supported on Si substrates. All binding energies were referenced to that of aliphatic carbon at 284.8 eV. Crystal structures

were studied using X-ray diffraction (XRD) spectra (D8 Advance in Bragg–Brentano theta-theta configuration, Bruker, USA) with a monochromatic Mo Kα radiation source (λ = 0.07107 nm) and LynxEye-XE energy dispersive Si strip detector with samples supported on borosilicate glass slides. Brunauer-Emmett-Teller (BET) analysis was done using a Nova 4200e surface area analyser (Quantichrome, USA).

Electrode Preparation - V_2O_5 thin film electrodes were fabricated by the ultrasonic spraying of the dispersed V_2O_5 nanosheets on aluminium foil ($20\,\mu m$ thickness, 18 mm diameter) pre-treated with an adhesive polyethyleneimine (PEI) layer (30%, Alfa Aesar). Typically, the V_2O_5 nanosheet dispersion was diluted down by a factor of two to allow for better flow and 30 ml of the diluted dispersion was placed in the syringe (100 ml) of the ultrasonic sprayer. During the spraying, the aluminium substrate was heated to $100°C$ to allow for H_2O evaporation. The resultant electrodes were then transferred to an argon filled glove box after drying overnight at $100°C$. The mass of the active material was determined by weighing the substrate before and after spraying. For the V_2O_5/SWCNT composite electrode, the V_2O_5 nanosheet dispersion was mixed with 0.1 $mg\,ml^{-1}$ of P3-SWCNT in a mass ratio of 95:5. The blended dispersion was then diluted down by a factor of two and allowed to mix for 1 hr using a magnetic stirring bar. The resulting electrodes were then transferred to the argon glove box after subsequent drying and mass determination. As a control, a separate electrode was fabricated from a slurry comprised of 80% unsonicated V_2O_5 powder, 10% conductive Super C65 and 10% PVDF as a polymer binder.

Electrochemical Characterization - The electrochemical behaviour of the cathodes was evaluated using the half-cell configuration with the active material as the working electrode, Li foil as the counter and reference electrodes, and 1 M lithium perchlorate ($LiClO_4$) dissolved in propylene carbonate (PC) (1 M $LiClO_4$/PC) as the electrolyte. Cyclic voltammetry (CV), galvanostatic cycling (GC), and electrochemical impedance spectroscopy (EIS) measurements were performed on a VMP-300 potentiostat (Bio-Logic, France). CVs was recorded at 0.05 $mV\,s^{-1}$ with a potential range 2.5 V - 3.8 V (vs. Li/Li^+). GC were performed at different C-rates from 0.05 to 10 C with a potential range 2.5 V - 3.8 V (vs. Li/Li^+). Both CV and GC were repeated at a potential window of 1 V - 4 V to represent a multi ion intercalation. The cycling performance was conducted at 1 C for 100 cycles. EIS was measured at open-circuit potential (E_{OCP}) with a 10 mV amplitude and a frequency range of 1 mHz - 1 MHz. GITT measurements were carried out by applying a periodic constant current pulse of 10 mA on the cell for a period of 10 min followed by a rest period of 40 min. The measurements were carried out between a potential window of 1 - 4 V.

4.3 Results

4.3.1 Synthesis of the Nanosheet Colloid

As mentioned earlier, V_2O_5 particles exhibit a two dimensional layered structure. Therefore, the application of ultrasonic energy should theoretically cause the individual layers to delaminate forming a series of nanosheets. Commercial V_2O_5 powder (as can be seen in Figure 4.2 (a)) was added to deionized H_2O in a centrifuge tube and underwent LPE at 80 kHz for 5 hr. The V_2O_5 powder consists of relatively thick particles on the order of 1 μm in size. The LPE cavitation processes should act to weaken the van der Waal interactions between the layers producing thin V_2O_5 nanosheets in a manner similar to that reported elsewhere for graphene or MoS_2 [135, 316]. After the subsequent centrifugation, the supernatant was decanted and the resultant dispersion was herein labelled as "V_2O_5 NS".

The V_2O_5 NS dispersion was dropcast onto a holey carbon grid and allowed to dry overnight at 100 °C. Figure 4.2 (b) shows a representative example of a typical V_2O_5 NS. A relatively thin NS consisting of a few layers is present with a lateral dimension of about 500 nm. The corresponding HRTEM image of the V_2O_5 NS shown in Figure 4.2 (c) indicates the principal crystal planes. Subsequent analysis determined an inter-layer spacing of 0.57 nm which can be indexed to the {002} set of planes [269]. Furthermore, a smaller set of planes is present exhibiting an inter-layer spacing of 0.34 nm which can be indexed to the {110} set of planes. The corresponding FFT pattern shown in Figure 4.2 (d) further shows the presence of both the {002} and {110} set of peaks. These planes are consistent with that of orthorhombic V_2O_5 phase. A third point evident labelled BL corresponds to an inter-planer spacing of 0.28 nm. The implications of this plane will be discussed later. Figure 4.2 (e) shows a typical EDX spectrum of the V_2O_5 NS. The peak at 4.95 keV (and it satellite peak at 5.41 keV) correspond to the $K\alpha$ transition exhibited by the V atoms [317]. Similarly the peak at 0.52 eV corresponds to the $K\alpha$ in O. Quantification of peak areas determined that the atomic percentage ratio of V to O was 2 : 5 which is expected for V_2O_5. The remaining peaks can be attributed to the C and Cu present in the holey carbon grids. Figure 4.2 (f) shows a typical HAADF STEM image of a V_2O_5 NS. It is clear from the image that the NS varies in thickness from one end to the other by the change in intensity of the image. This is desirable as it provides more channels conducive to solid state Li-ion diffusion It should also be noted that V_2O_5 is quite an electron sensitive material in which small areas of damage can be observed in the STEM image [318].

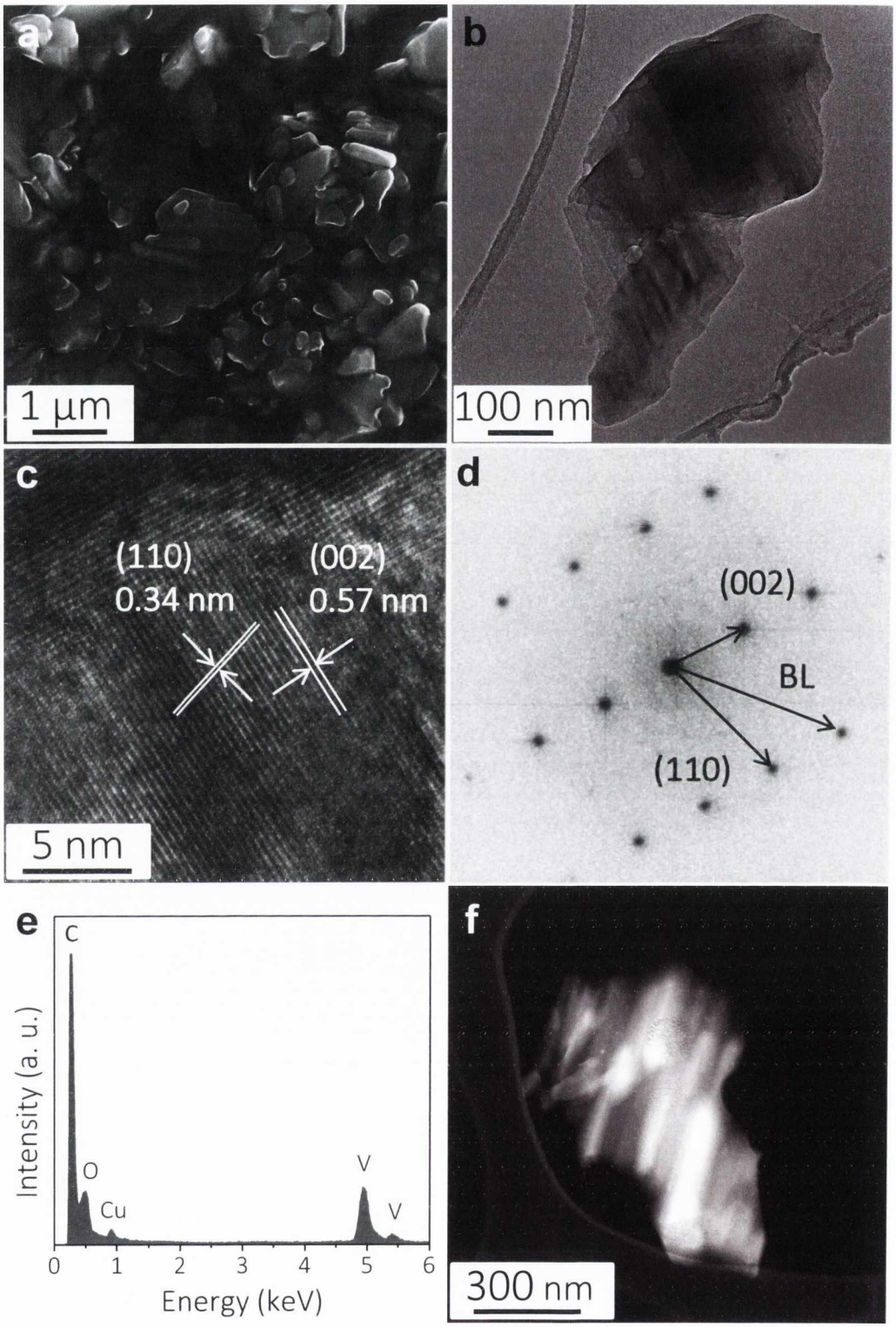


FIGURE 4.2: (a) TEM image of the V_2O_5 powder; (b) Representative TEM image and (c) HRTEM image of a the V_2O_5 NS with (d) the corresponding FFT and (e) EDX spectrum. (f) Representative HAADF STEM image of a V_2O_5 NS.

XPS was used to further understand the chemical composition and morphology of the as-prepared material. The samples were prepared by ultrasonically spraying the V_2O_5 NS dispersion onto Si substrates. The spectrum shown in Figure 4.3 indicates both the V 2p and O 1s core levels associated with V_2O_5. The two peaks at 517.2 eV and 524.2 eV correspond to the binding energies of the V 2p 3/2 and 1/2 states respectively [319, 320]. The relative peak intensities of the V 2p 3/2 and 1/2 states are 2 : 1 corresponding to the degeneracies of a typical atomic p-orbital with a spin orbital splitting energy of $\Delta_{so} = 7.4eV$ [321]. The deconvoluted V 2p core level peaks reveal the presence of a majority V (+5) component and a minority V (+4) component situated at 517.2 and 515.9 eV respectively. The V (+5) peak can be attributed to the V oxidation state found in V_2O_5. The V (+4) minority (4.76%) indicates that the exfoliated NS contains O deficiencies [320]. The presence of O deficiencies require the V to increase in oxidation number in order to keep charge neutrality. However, due to the majority presence of the V (+5) oxidation state, the characteristic blue colour of the V (+4) oxidation state is not evident (see inset).

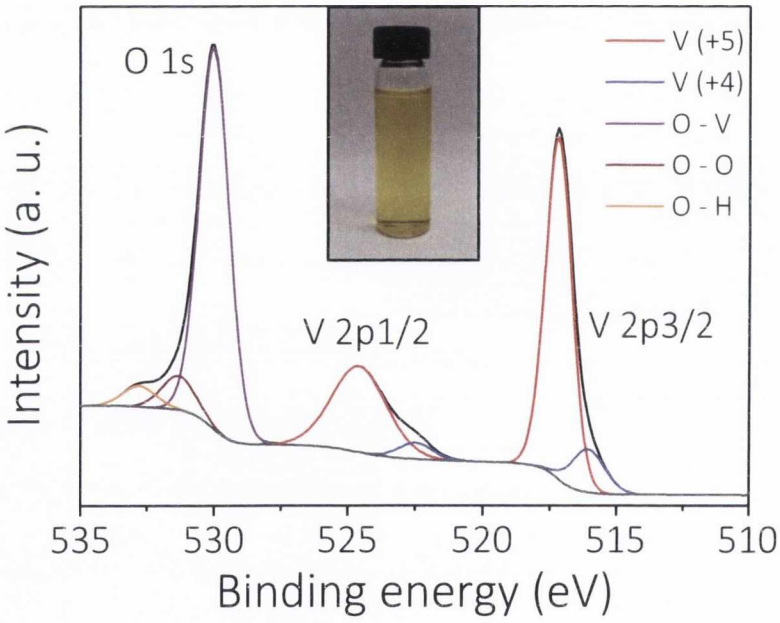


FIGURE 4.3: Deconvoluted XPS spectrum of V_2O_5 NS showing both the major V and O oxidation states.

The O 1s peak situated between 528.0 and 532.0 eV can be deconvoluted into three different peaks representing the three different oxidation states present [322]. The strong intensity peak at 530.00 eV can be attributed to the bond between the O and V in the metal oxide. The remaining smaller peaks at 531.3 eV and 532.8 eV can be attributed to the bonding of the TMO with H_2O molecules and the presence of

possible hydroxyl groups on the surfaces. The relative intensity of the metal oxide peak compared to that of hydroxyl peak indicates the high purity of the V_2O_5 in the cathode.

Even though the sample was thoroughly dried before XPS analysis, the O - O peak evident suggests the presence of water of crystallization in the nanostructured material. V_2O_5 has been commonly observed to dissolve in water, however, several methods describe the formation of nanostructured V_2O_5 based xerogels such as ion exchange chemistry and the addition of molten V_2O_5 to H_2O [323, 324]. A xerogel is defined as a solid that forms from a gel after drying. Typically, the xerogel retains its structure after drying resulting in properties such as increased surface area and diffusion pathways. In the case of V_2O_5, the water molecules are known to bond to the terminal O atoms between the layers of the V_2O_5 by means of hydrogen bonds.

To provide further evidence of this xerogel structure, the ultrasonically sprayed V_2O_5 NS were subject to XRD analysis. For comparative purposes, the XRD pattern of the unexfoliated V_2O_5 powder was also taken. Figure 4.4 (a) shows the relative XRD patterns for each sample. The pattern exhibited by unexfoliated V_2O_5 powder shows a series of peaks consistent with the naturally occurring form of V_2O_5, shcherbinaite (JCPDF No. 01- 0359) [262, 325]. It is clear from the patterns that LPE in H_2O has a dramatic effect on the relative structure of the V_2O_5. Four peaks are observed for the V_2O_5 NS cathode centring at 3.5°, 10.6°, 14.0° and 17.7° with gradual decreasing intensities (JCPDS No. 40-1296). These peaks correspond to the {001}, {003}, {004} and {005} set of planes commonly associated with the hydrated xerogel structure of V_2O_5 [326, 327]. However, the preferential {00l} set of peaks is characteristic of the turbostratic stacking of the V_2O_5 layers parallel to the substrate. The apparent wide "peak" situated between 4° and 7° refers to the amorphous structure of the glass substrate.

All subsequent cell parameters were calculated from the {001} set of planes. Bragg analysis of the {001} peak centred at 9.3° for the unexfoliated powder shows an inter-layer spacing of 0.43 nm consistent with that of shcherbinaite. However, the {001} peak centred at 3.5° for the V_2O_5 NS sample indicates an increase in inter-layer spacing to 1.15 nm. It has been proposed that as the H_2O molecules intercalate and form hydrogen bonds with the terminal Os, the individual V_2O_5 layers expand as illustrated in Figure 4.4 (b), similar to that exhibited by xerogels or clays [328]. The resultant change in inter-layer spacing reflects the change in diffraction angles of the {001} set of planes. Subsequent drying removes the intercalated H_2O molecules not bound to the V_2O_5 leaving a stable nanoporous layered structure conducive to

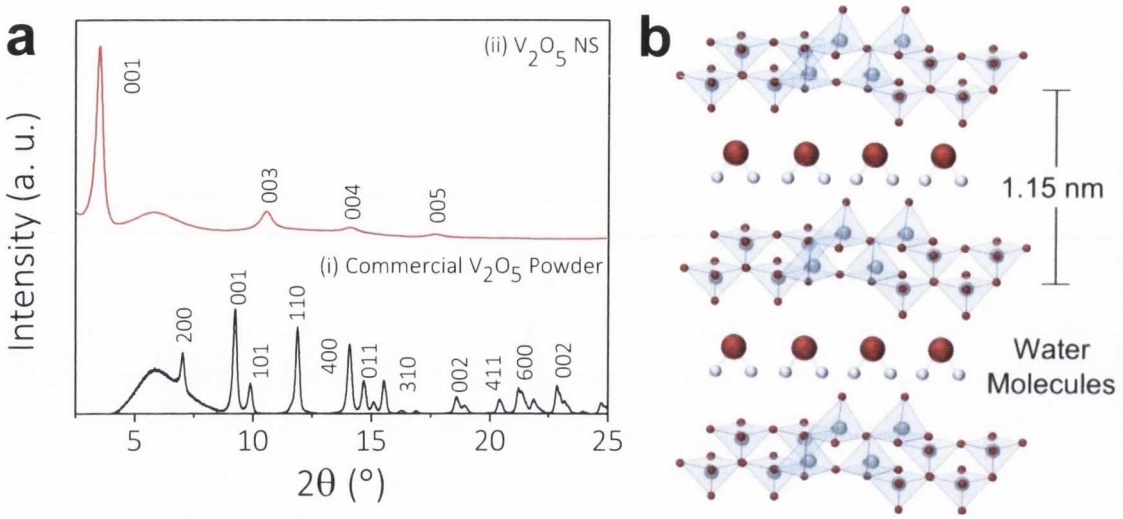


FIGURE 4.4: (a) XRD patterns and (b) schematic of V_2O_5 NS xerogel bilayered structure.

the intercalation of charged ions. Various reports indicate the formation of a bilayered structure in the xerogels. The work of Giorgetti demonstrated how polarized X-ray absorption techniques can be used to prove the existence of these bilayers [290]. This work, along with others indicated an inter-bilayer spacing of 0.28 nm [329] as illustrated in Figure 4.4 (b). It is interesting to note that the third diffraction peak (labelled BL) demonstrated in Figure 4.2 (d) showed a inter-layer spacing of 0.28 nm coinciding with that of the bilayer structure. It can be also observed that, in Figure 4.4, the absence of a well defined {002} peak further indicates the formation of the bi-layered structure [330]. As explained earlier, the formation of V_2O_5 xerogels proceeds by certain high temperature sol-gel techniques or driven ion exchange mechanisms. However, the high temperature cavitation processes inherent in sonication techniques may provide the necessary energy to cause the intercalation of H_2O molecules and the subsequent swelling processes. Essentially LPE provides a similar mechanisms to the formation of a xerogel than those previously reported.

The specific surface area of the V_2O_5 NS xerogel like structure was determined. A 50 ml sample of the dispersion was filtered and the sediment underwent N absorption analysis. From the BET isotherm shown in Figure 4.4 (b), the active surface area was determined to be 25 m^2g^{-1}.

LPE in a wide range of solvents can be used to assess the stability requirements of the resulting V_2O_5 NS dispersions [135]. Similarly, different solvents can provide larger concentrations of stable V_2O_5 NS. Initially a series of solvents were chosen

representing a wide range of Hildebrand solubility parameters. Each experiment underwent a basic sonication recipe of 80 kHz, 182 W with 1 $mg\,ml^{-1}$ initial powder concentration for 5 hr. The resultant dispersion then underwent centrifugation at 1000 rpm for 1 hr and the optical absorption spectra were then measured using UV-vis spectroscopy. The relative extinctions determined at a fixed wavelength can be used to compare the resultant concentrations. Figure 4.5 (a) shows the absorption spectra for a selected range of solvents with a select few dispersion examples in the inset. In the case of V_2O_5, the optical transition evident between 400 and 450 nm refers to the transition of electrons from the oxygen 2p state in the ligand to the vanadium 3d state. This corresponds to a band gap of 2.75 - 3.1 eV which is agreement with literature values [331, 332]. For more aggressive solvents, such as NMP and BB, a large extinction is observable with a well defined peak. However, in cases such as that for BA, a relatively negligible spectrum is observed. No immediate peak is observed for H_2O in the visible range suggesting a shift in the binding energy relative to that of dehydrated V_2O_5. The transparent colour as indicated by the dispersion in the inset could be a direct result of this shift into the UV region [333].

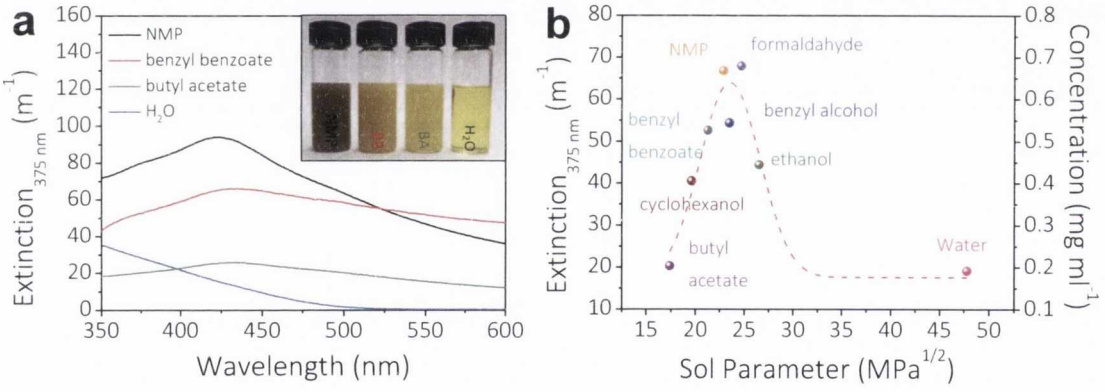


FIGURE 4.5: (a) Extinction spectra of V_2O_5 NS in a selected range of solvents and (b) A plot of the extinction at 375's dependence on each solvents Hildebrand parameters.

Analysis of each dispersion solvent's concentration as a function of the Hildebrand parameters (δ_t) can give information into the relative stabilities of the V_2O_5 NS dispersions. Figure 4.5 (b) shows the normalized extinction intensity at 375 nm plotted as a function of the δ_t for each solvent. The extinction of each solvent exhibited a Gaussian distribution relative to δ_t (see equation (2.38)) in agreement with classical solubility theory. Solvents with a δ_t between 22 - 25 $MPa^{0.5}$ form the most stable and concentrated V_2O_5 NS dispersions such as that observed with formaldehyde or NMP. It was determined that V_2O_5 itself has a δ_t = 23.4 $MPa^{0.5}$ which is in the

range common among two dimensional materials (graphene, MoO_3 *etc.* [210, 334]). Other solvents slightly outside this range, such as BB, cyclohexanol or ethanol, form less concentrated dispersions and tend to be positioned on the lower edges of the Gaussian peak. Solvents which do not produce a stable dispersion, such as that of toluene, do not appear in the Gaussian peak. In the formation of a stable colloid, the energies of both the solvents and particles must match [335]. It has been shown that V_2O_5 has a surface tension of 40.0 $mN\,m^{-1}$ [336]. At room temperature NMP possess surface energies of 40.3 $mN\,m^{-1}$ which explains why it produces such a stable colloid with V_2O_5. As expected solvents with low resultant concentrations have surface energies which differ greatly, such as 23 $mN\,m^{-1}$ for IPA.

However, despite V_2O_5 NS forming a relatively stable dispersion in H_2O, the Hildebrand solubility parameter falls outside the predicted region ($\delta_t = 47.8\ MPa^{0.5}$). Similarly, the surface tension of H_2O is 72.0 $mN\,m^{-1}$. It is possible the formation of a stable dispersion is due to the formation of strong hydrogen bonds suggested earlier. However, the large difference in surface tension may limit the concentration. In general, there is a balance between the attractive hydrogen bonding and the repulsive difference in surface tensions. A model proposed by Kristoffersen *et al.* suggested that the bilayer structure of the gel itself is stabilized by the reactions between water molecules and the oxide surface [327]. In the absence of H_2O, the bilayer structure has a higher energy than the double-layer, therefore it is energetically favourable for the V_2O_5 layers to interact with the H_2O.

Continuing the investigation on the LPE of V_2O_5 in H_2O, various exfoliation parameters can have an effect on the resulting yield of V_2O_5 NS. By measuring the extinctions at 375 nm for each parameter the most favourable condition for the LPE of V_2O_5 NS in H_2O was determined, see Figure 4.6.

Figure 4.6 (a) shows the dependence of the resultant extinctions of the NS after centrifugation as a function of sonication frequency. LPE at 37 kHz and 80 kHz were carried out in a water filled sonic bath while LPE done at 20 kHz were carried out in a sonic horn. Care was taken to keep all other parameters consistent. No immediate trend is evident in the figure although lower frequencies tend to produce a slightly higher concentration. It was determined that sonication frequency has no noticeable effect on the resultant NS concentration. Figure 4.6 (b) shows the dependence of the resultant extinction on the sonication power. Similar to the Hildebrand dependence mentioned above, there is a clear Gaussian distribution with the highest concentration being acquired between 125 - 165 W. It can be assumed that below these power values, insufficient energy is being provided to produce a high concentration. However, above these values the extinction decreases rapidly. It is assumed too much

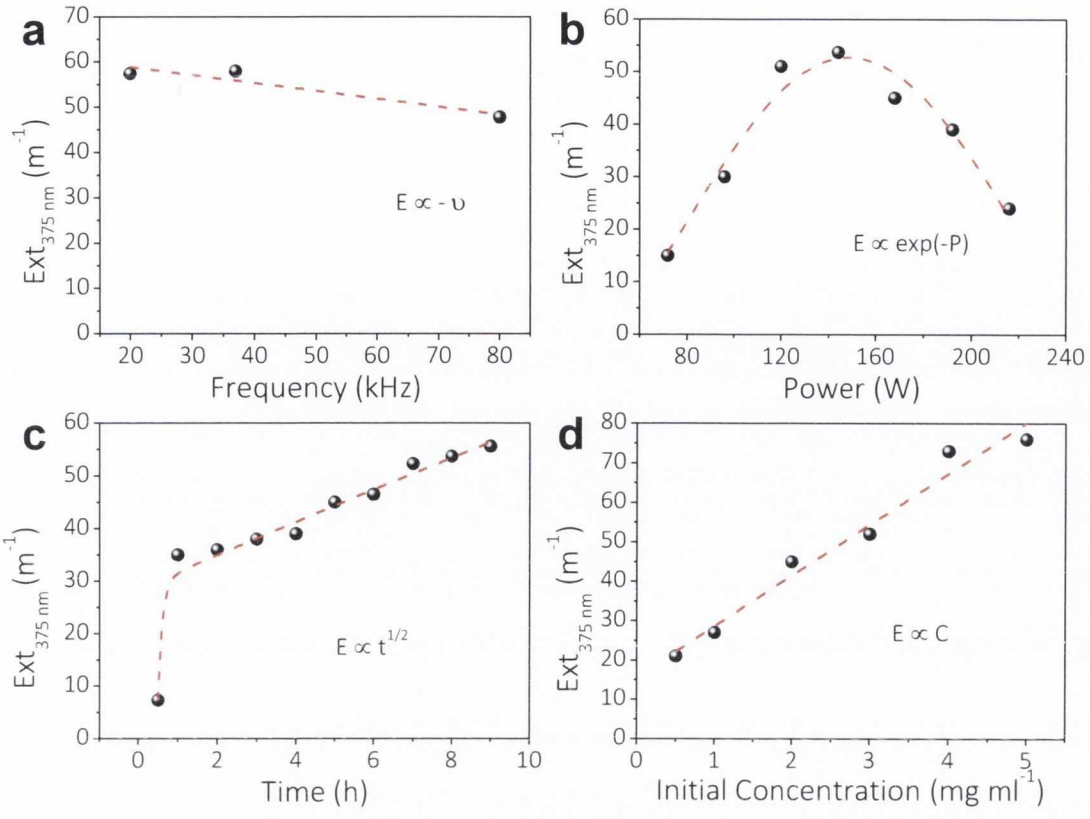


FIGURE 4.6: Plots of the relative extinctions of V_2O_5 NS in H_2O as a function of (a) sonication frequency, (b) sonication power, (c) time and (d) initial concentration.

energy is being supplied causing the breakdown of the gel structure. Figure 4.6 (c) shows the dependence of extinction on the sonication time. There is a clear exponential increase as shown by the trend line, indicating the resultant concentration increases rapidly in the early stages of exfoliation and decreases in rate after time. Finally, Figure 4.6 (d) shows the dependence of extinction on the concentration of the initial V_2O_5 powder. There is a clear linear relationship as the extinction increases rapidly as the initial concentration is increased.

Generally after exfoliation it is desirable to separate the NS from the unexfoliated powder. This is done *via* centrifugation of the sonicated dispersion. As higher centrifugation speeds cause smaller particles to sediment it is necessary to find an optimum centrifugation speed to provide adequate NS concentration and to sediment the unexfoliated powder. Figure 4.7 (a) shows the relative extinctions as a function of centrifugation speed. A general decrease in the resultant concentration is observed however not by an appreciable amount. A separate sample was drop-cast onto a holey carbon grid and statistically analysed using TEM. A representative

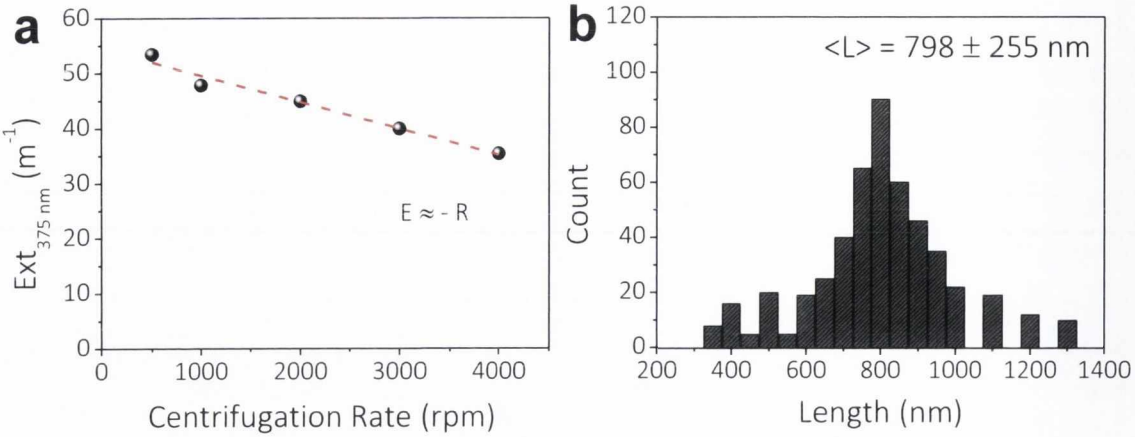


FIGURE 4.7: (a) Relative extinctions of the V_2O_5 NS' dependence on centrifugation rate and (b) particle count histogram.

particle count histogram is shown in Figure 4.7 (b). Most NS present have a lateral dimension between the range of 600 nm to 1000 nm. The average sheet length being 798 $\pm$ 255 nm. From the optimizations above all future sonications were done at 37 kHz, 144 W, with 1 $mg\,ml^{-1}$ initial powder concentration for 5 hr. Centrifugation was done at 1000 rpm.

It has been commonly observed that V_2O_5 dissolves in H_2O. The concern arose as to the stability of the V_2O_5 colloid. A separate sample of 1 $mg\,ml^{-1}$ V_2O_5 was prepared. However, as opposed to direct sonication, the sample was left to mix using a magnetic stirrer bar for 5 hr.

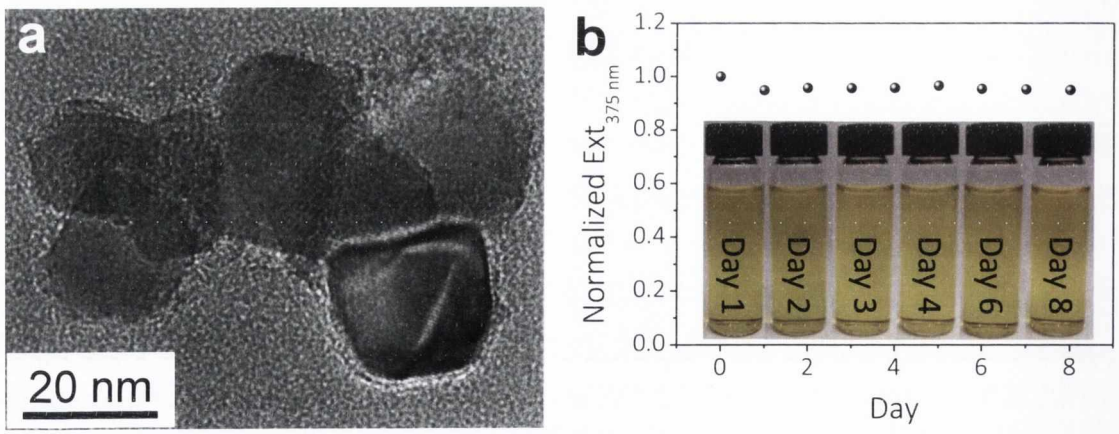


FIGURE 4.8: (a) TEM image indicating typical dissolved V_2O_5 particles and (b) Plot indicating the relative stability of the V_2O_5 NS colloid over a period of eight days with the insets being the corresponding optical images.

The resultant dispersion was centrifuged at 1000 rpm and dropcast onto a holey carbon grid. Figure 4.8 (a) demonstrates an aggregation of dissolved particles with lateral dimensions on the order of 20 nm. As the particles tend to aggregate, UV-vis spectroscopy was carried out to assess the relative stability of the V_2O_5 NS colloid over a period of time. After a period of eight days, the dispersions retains 95% its initial extinction indicating a relatively high stability. However, further processing was done almost immediately after LPE to benefit fully from the process.

4.3.2 Cathode Fabrication

A series of V_2O_5 NS based cathodes were fabricated by the ultrasonic spraying method described in section 3.2. Several hundred ml of V_2O_5 dispersion was synthesized under optimized condition and stored in a series of large bottles, see Figure 4.9 (a). The V_2O_5 NS enriched dispersion showed a deep gold like colour. After being further diluted, the dispersion was placed inside the syringe of the ultrasonic sprayer and sprayed onto a temperature controlled Al substrate pretreated with PEI adhesive [337]. To show how scalable the process is, Figure 4.9 (b) shows a typical large surface area sprayed sample. Several cathodes can be punched from a sample of this size. The xerogel film itself has a thickness on the order of 1 μm.

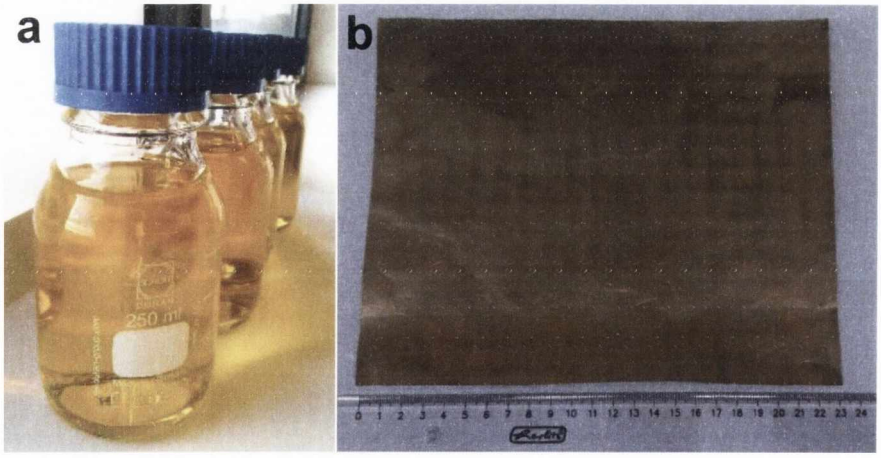


FIGURE 4.9: V_2O_5 (a) large scale NS dispersions and (b) ultrasonically sprayed film.

The structure and morphology of the ultrasonically sprayed V_2O_5 NS cathodes were characterized by SEM. Samples of both the V_2O_5 NS dispersion and V_2O_5 NS/SWCNT were sprayed onto clean Si substrates and allowed to dry over night at 100 °C. Figure 4.10 (a) shows a SEM image of a typical V_2O_5 NS cathode surface. After

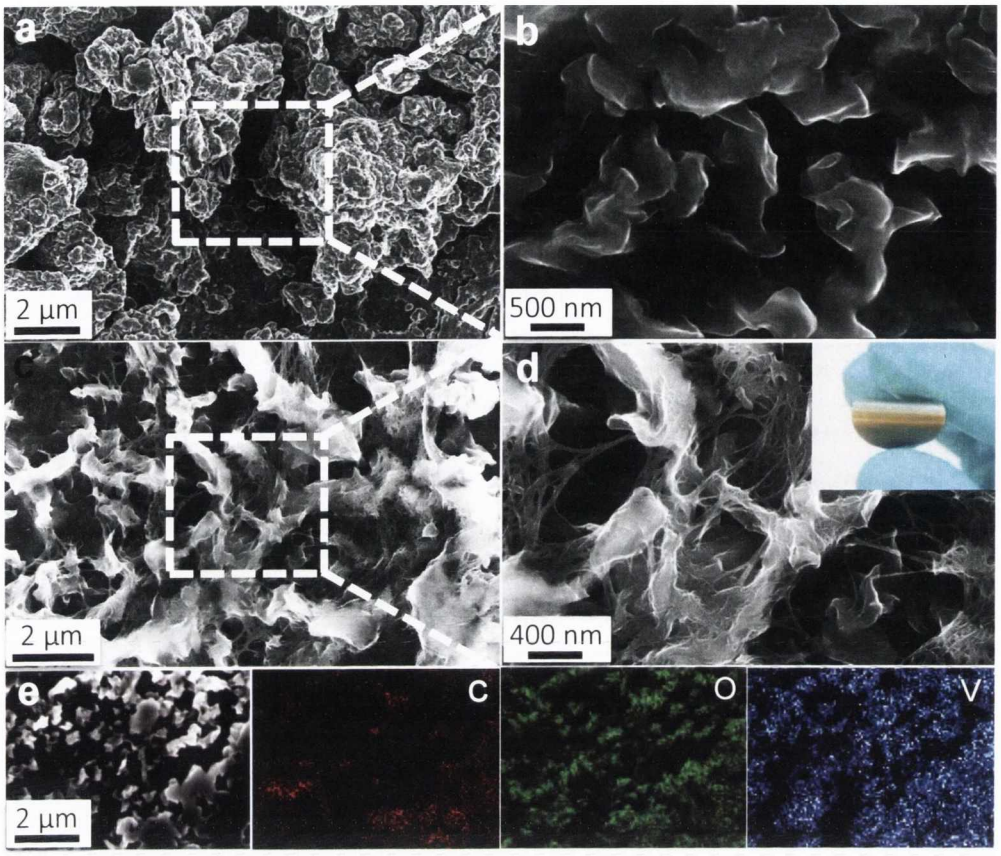


FIGURE 4.10: (a) Low and (b) High magnification SEM images of the V_2O_5 NS cathode. (c) Low and (d) High magnification SEM images of the V_2O_5 NS/SWCNT cathode with the inset showing the flexible cathode. (e)The corresponding surface EDX map.

spraying, the V_2O_5 NS reassemble into an array of fluffy particles with a structure rich in large voids. The high magnification SEM image in Figure 4.10 (b) shows how these voids can reach dimensions higher than 500 nm. These voids may act to reduce the structural integrity of the cathode. Conversely, the V_2O_5 NS/SWCNT cathode, as seen in Figures 4.10 (c) shows a structure in which large scale voids are absent. The high magnification image in Figures 4.10 (c) shows the extensive network SWCNT among the V_2O_5 NS matrix. The overall structure of the V_2O_5 NS/SWCNT cathode represents a highly porous and electronically conducting system. The flexibility and integrity of the V_2O_5 NS/SWCNT cathode is further demonstrated by the example shown in the inset. The surface EDX map of the V_2O_5 NS/SWCNT cathode is shown in Figure 4.10 (e). From the deconvoluted images it can be determined that each of the SWCNTs are efficiently dispersed through out the NS matrix.

4.3.3 Electrochemical Characterization

4.3.3.1 Single Li-Ion Intercalation Mechanism

Initially, investigations into the single Li-ion intercalation mechanism on the V_2O_5 NS cathode were carried out. The mechanism is characterized by the phase transition between $\alpha - V_2O_5$ and $\delta - V_2O_5$. Traditionally, this employs a potential window between 2.5 V to 3.8 V vs. Li/Li^+ and possesses a theoretical charge storage capacity of $147mAh\,g^{-1}$ [338]. Initial electrochemical characterization was carried out using CV at a scan rate of 0.05 $mV\,s^{-1}$ for both the V_2O_5 NS and V_2O_5 NS/SWCNT cathodes as demonstrated by Figure 4.11.

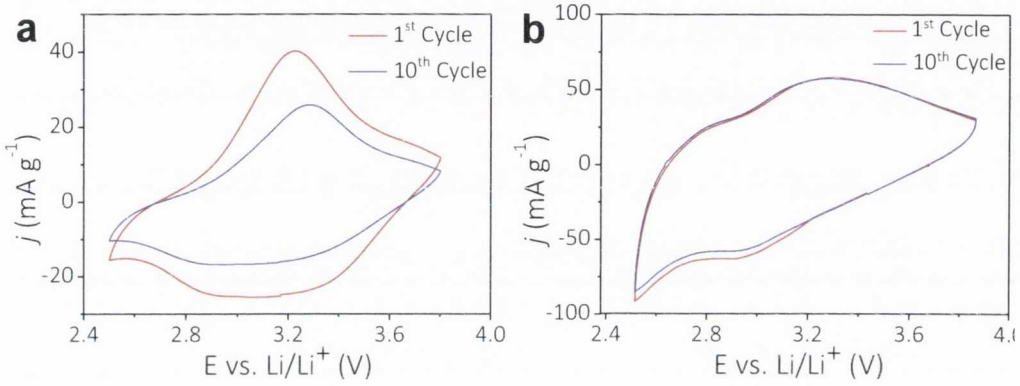


FIGURE 4.11: CVs of both the (a) V_2O_5 NS electrode and (b) the V_2O_5 NS/SWCNT composite electrode at a scan rate of 0.05 mV s^{-1} for a single Li-ion intercalation mechanism.

The V_2O_5 NS cathode in Figure. 4.11 (a) shows broad deintercalation peak for the first cycle at potentials between 3.1 V and 3.4 V. However, the corresponding intercalation "peak" demonstrates a very broad range of energies suggesting the nanostructured material has a wider range intercalation energies. The resultant deintercalation may only stem from stem from a particular set of intercalation sites causing an irreversibility. The apparent reversibility is demonstrated by the tenth cycle also shown in this Figure. As mentioned earlier nanostructured materials have larger surface to volume rations which in turn increase the surface areas and reduce the energy required for adsorption of the Li ion. This may results in a wider range of site energies. The presence of these singular peak corresponds to the relative phase transition between $\alpha - V_2O_5$ and $\delta - V_2O_5$ [338]. However, the V_2O_5 NS/SWCNT cathode shown in Figure 4.11 (b) exhibits a stronger pseudocapacitive behaviour than that of the V_2O_5 NS cathode. As illustrated in the SEM images in Figure 4.10, the SWCNTs act to increase the relative porosity of the cathode. The SWCNTs also act

to decrease the charge transfer resistance by providing electronic conductive states to normally semiconducting V_2O_5 [339, 340]. The apparent improvement in short term cycling can be directly associated with the increased porosity the SWCNTs provide. The SWCNTs act to increase the volume expansion tolerance of the cathode while providing easier routes for Li-ion diffusion in both the access to the micro and nanopore structure and subsequent deintercalation processes. XPS analysis shown previously in Figure 4.3 indicated that even after thorough drying, the xerogel structure of the cathode still retains inherent H_2O molecules. These molecules may react irreversibly with intercalated Li-ions, forming $LiOH$, contributing to the overall diminishing in performance.

$$2Li + 2H_2O \rightleftharpoons 2LiOH + H_2 \tag{4.3}$$

The charge storage properties of the V_2O_5 NS and V_2O_5 NS/SWCNT cathodes were further investigated by GC analysis at current density of 0.05C. For comparative purposes, a cathode fabricated from a V_2O_5 slurry (80% V_2O_5, 10% conductive Super C65 and 10% PVDF) was also measured. Figure 4.12 shows the typical GC curves for all three V_2O_5 based cathodes. The V_2O_5 slurry cathode showed well defined behaviour consistent with the phase changes between $\alpha - V_2O_5$ and $\delta - V_2O_5$ [338]. The discharge plateaus centred at potentials of 3.4 V and 3.2 V correspond to the intercalative phase changes from $\alpha - V_2O_5$ to $\beta - V_2O_5$ and $\beta - V_2O_5$ to $\delta - V_2O_5$ respectively. The corresponding charge plateaus evident at 3.3 V and 3.4 V refer to the respective deintercalation process. The presence of well defined plateaus reflects the 0.43 nm inter-layer spacing of the V_2O_5 powder. The initial discharge capacity reaches 123 $mAh\,g^{-1}$ falling short of the theoretical capacity by 24 $mAh\,g^{-1}$.

The pseudocapacitive response of the xerogel structure of the V_2O_5 NS cathode is evident with the lack of well defined plateaus and potential drops. The increased surface areas and inter-layer spacing caused by swelling allows for more efficient intercalation processes and reduced diffusion coefficients. DFT calculations by Wang *et al.* suggests a 2.5 fold decrease in diffusion barrier of nanostructured V_2O_5 compared to that of the bulk [341]. As a result the initial discharge capacity increases to 159.5 $mAh\,g^{-1}$, a marked increase compared to the V_2O_5 slurry. Similarly addition of the conductive SWCNTS further increases the discharge initial capacity to 185.9 $mAh\,g^{-1}$.

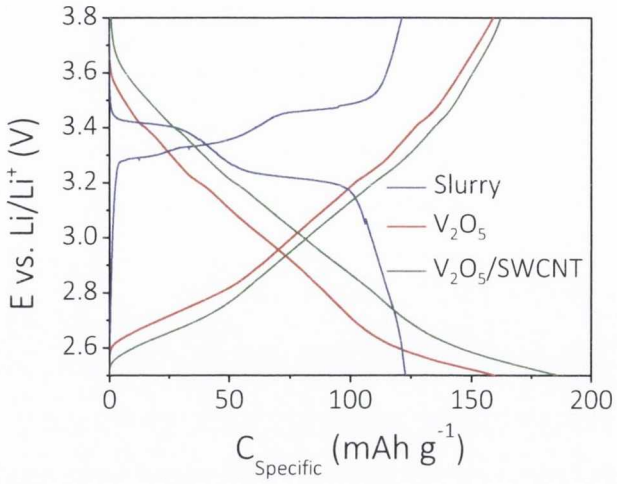


FIGURE 4.12: Initial GC curves of the of the V_2O_5 slurry, NS and NS/SWCNT cathodes.

4.3.3.2 Diffusion Studies

The effect of nanostructuring and subsequent addition of SWCNTs' effects on the solid state diffusion properties was investigated. A series of Galvanic intermittent titration techniques (GITT) were carried out on the V_2O_5 slurry, NS and NS/SWCNT cathode materials [240]. Each cathode was subject to a constant current of 0.1 mA for 10 min before being allowed to reach equilibrium for 40 mins. The experiment was repeated for both the discharge and charge processes between the potential windows of 1 - 4 V. Figure 4.13 (a) and (b) shows representative GITT profiles for both the V_2O_5 slurry and V_2O_5 NS/SWCNT cathodes.

The relative discharge profiles (shown in blue) demonstrate how the solid state diffusion process is more efficient for the V_2O_5 NS/SWCNT cathode. After a similar time period the V_2O_5 slurry exhibits a slow decrease in potential compared to that of the V_2O_5 NS/SWCNT cathode. The subsequent charge profiles (shown in red) indicate a similar result. However, severely diminished profile for the V_2O_5 slurry indicates the the resultant trapping of ions after intercalation as shown previously. A detailed example of the fifth current discharge cycle for the V_2O_5 NS/SWCNT cathode shown in Figure 4.13 (c) indicates the relevant experimental quantities used to determine the diffusion coefficients as described by equation (3.14). Figure 4.13 (d) compares the calculated diffusion coefficients of the V_2O_5 slurry, NS and NS/SWCNT cathode materials. The values determined were 6.2 x 10^{-13} cm^2 s^{-1}, 9.0 x 10^{-12} cm^2 s^{-1} and 1.6 x 10^{-11} cm^2 s^{-1} respectively. It can be concluded that nanostructuring the

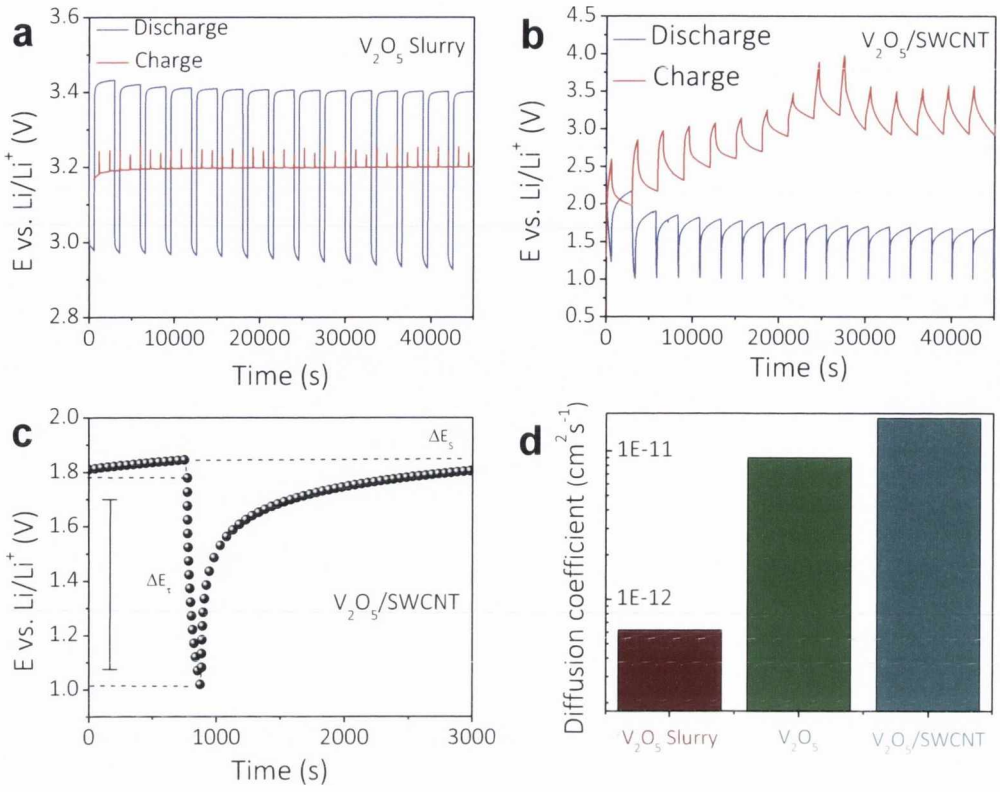


FIGURE 4.13: GITT profiles of both the V_2O_5 (a) slurry and (b) NS/SWCNT cathodes. (c) The fifth current discharge cycle for the V_2O_5 NS/SWCNT cathode. (d) histogram comparing the relative diffusion coefficients of all three V_2O_5 cathodes.

material contributed more to the diffusion increase than that of the SWCNTs. Nanostructuring alone increases the diffusion coefficient by a factor of 14.5.

4.3.3.3 Multi Li-ion Intercalation mechanism

While the V_2O_5 NS/SWCNT cathode shown remarkable cyclability for a single Li-ion intercalation, it is desirable to improve the relatively low storage capacities. Like many other TMO materials V_2O_5 can accommodate multiple ions per unit formula [191]. It has been shown that V_2O_5 can intercalate between two or three Li-ion per unit formula expressing theoretical capacities of 294 $mAh\,g^{-1}$ and 441 $mAh\,g^{-1}$ respectively [313–315]. However, the phase change associated with the $\delta - Li_xV_2O_5$ (x > 1) transition to $\gamma - Li_xV_2O_5$ (x = 2) is known to be irreversible. As a result, the phase change between $\beta - Li_xV_2O_5$ to $\alpha - Li_xV_2O_5$ ceases to happen [270, 271]. However, experimental storage capacities can exhibit values of 300 $mAh\,g^{-1}$ [313,

314] with some reporting capacities of 400 $mAh\,g^{-1}$ [315]. Extending the potential window to cover 1 V to 4 V allows for this increased ion intercalation.

Similar to that shown for the single Li-ion intercalation investigation, the multiple Li-ion process was initially investigated using CV. Figure 4.14 (a) shows the first and tenth CV cycles for the V_2O_5 NS cathode at a scan rate of 0.05 $mV\,s^{-1}$. Two well defined intercalation peaks can be observed at potentials of 2.7 V and 2.4 V with a much larger deintercalation peak at 3.3 V. The diminishing of the peaks after successive cycles may be attributed to trapped Li-ions and interactions with residual H_2O molecules in the xerogel matrix similar to that of the single ion intercalation mechanism. However, the rapid diminishing of the intercalation peak at 2.7 V within the first ten cycles may be reasonably attributed to the irreversible phase transition between $\alpha - Li_xV_2O_5$ and $\beta - Li_xV_2O_5$ as it is assumed the $\gamma - Li_xV_2O_5$ phase is achieved. The increase in negative current density as potentials reaching 1 V could be attributed to the formation of passivation layers along the surface. The presence of relatively broad peaks indicates the cell shows pseudocapacitive behaviour as expected for a TMO material. The CV profiles shown in Figure 4.14 (b) correspond to the first and tenth cycles of the V_2O_5 NS/SWCNT cathode. The general rectangular shape of the CV can be attributed to the improved pseudocapacitive behaviour of the V_2O_5 and the contribution of the SWCNTs to the capacity at low potentials. As the potential approaches 4 V the pseudocapacitive response of the V_2O_5 material dominates the capacity from the SWCNTs. However, as the SWCNTs improve the conductivities of the V_2O_5, the cell retains the rectangular shape.

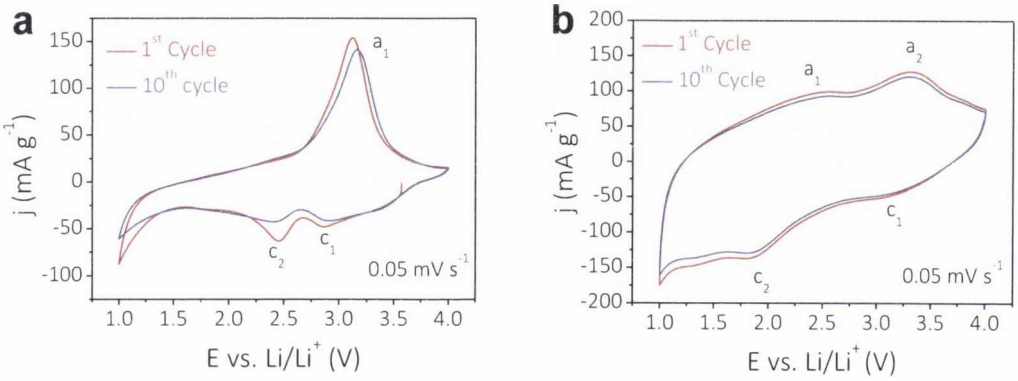


FIGURE 4.14: CV curves of the (a) V_2O_5 NS and (b) V_2O_5 NS/SWCNT cathodes for a multi ion intercalation.

A series of GC measurements were carried out on the V_2O_5 NS cathodes to determine the relative storage capacities of the multi Li-ion ion intercalation process. Figures 4.15 (a) and (b) shows the first, second and tenth GC profiles for both the

V_2O_5 NS and V_2O_5 NS/SWCNT cathodes at a current density of 0.05 C. For both cathodes, no obvious potential plateaus are evident indicating an overall pseudocapacitive response. Similarly, the lack of large potential drops further indicate pseudocapacitive processes. Initial discharge capacities for the V_2O_5 NS and V_2O_5 NS/SWCNT cathodes are 273.4 $mAh\,g^{-1}$ and 393.4 $mAh\,g^{-1}$ respectively consistent with literature values mentioned earlier. After a full intercalation process the V_2O_5 NS, the empirical formula can be expressed as $Li_{1.86}V_2O_5$ corresponding to the δ phase of V_2O_5. Similarly the empirical formula for the V_2O_5 NS/SWCNT can be expressed as $Li_{2.67}V_2O_5$ corresponding to the ω phase of V_2O_5. As the SWCNTs facilitate a larger tolerance to volume change, other phases can be easily achieved. It is worth mentioning that the expanded inter-layer spacing of the V_2O_5 xerogel structure would facilitate the Li-ion diffusion and thus reach a higher capacity compared to a more compacted V_2O_5 structure.

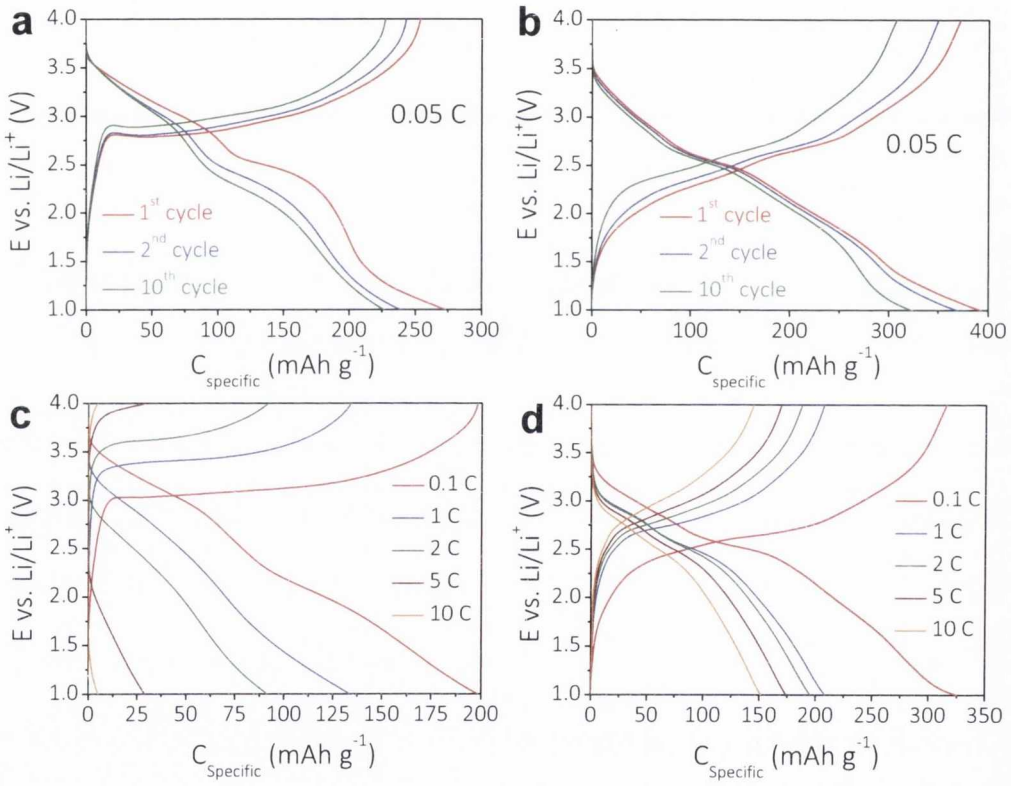


FIGURE 4.15: GC profiles of the (a) V_2O_5 NS and (b) V_2O_5 NS/SWCNT cathodes and (c) - (d) their respective current density ranges for a multi ion intercalation process.

The second cycle of each cathode shows the discharge capacities reducing to 239.5 $mAh\,g^{-1}$ and 370.1 $mAh\,g^{-1}$ respectively. These reduced capacities can be attributed to the irreversible phase change explained earlier. However, as V_2O_5

NS/SWCNT cathode contains SWCNTs, the reduced capacity may be attributed to the formation of an SEI layer as opposed to the irreversible phase change as the potential reaches 4 V [342]. After the tenth cycle, both cathodes stabilize at storage capacities of 226.7 $mAh\,g^{-1}$ and 320 $mAhg^{-1}$ respectively. There correspond to the formation of $Li_{1.54}V_2O_5$ and $Li_{2.17}V_2O_5$.

Figures 4.15 (c) and (d) shows the relative capacities for a range of current densities between 0.1 C and 10 C for both the V_2O_5 NS and V_2O_5 NS/SWCNT cathodes. At higher current densities the V_2O_5 NS cathode exhibits discharge capacities of 198.5 $mAh\,g^{-1}$ at 0.1 C, 133.7 $mAh\,g^{-1}$ at 1 C, 91.6 $mAh\,g^{-1}$ at 2 C, 28.9 $mAh\,g^{-1}$ at 5 C and 5.1 $mAh\,g^{-1}$ at 10 C. The V_2O_5 NS/SWCNT cathode exhibits discharge capacities of 317.2 $mAh\,g^{-1}$ at 0.1 C, 207.1 $mAh\,g^{-1}$ at 1 C, 193.8 $mAh\,g^{-1}$ at 2 C, 158.6 $mAh\,g^{-1}$ at 5 C and 127.7 $mAh\,g^{-1}$ at 10 C. The relatively high discharge capacity at 10 C for the V_2O_5 NS/SWCNT cathode is comparable to that of $LiCoO_2$ used in modern Li-ion batteries despite having a much quicker charge/discharge time of 6 min [41]. Therefore it is envisioned that the nanostructured V_2O_5 NS/SWCNT material has potential as a high powered supercapacitor cathode material.

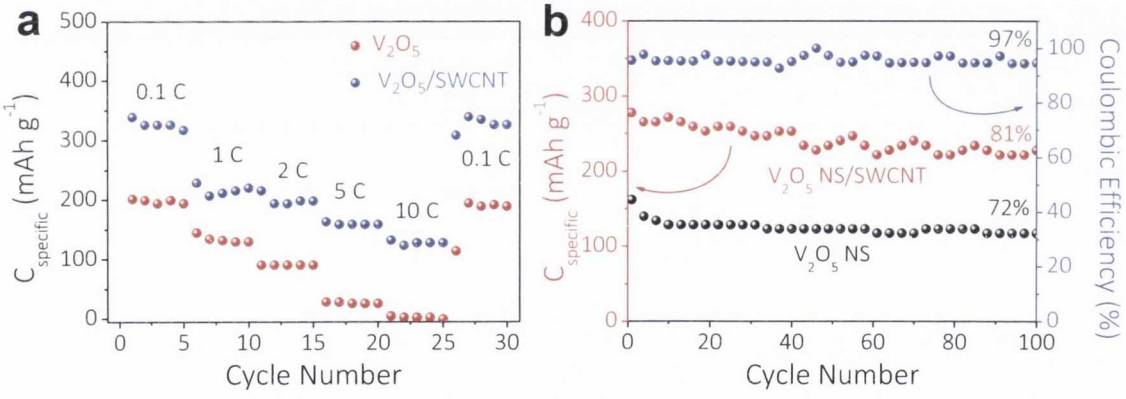


FIGURE 4.16: (a) The cyclability and (b) rate performance of both the V_2O_5 NS cathodes.

The rate performance and long term cyclability properties for the multiple ion mechanism were investigated for the V_2O_5 NS and V_2O_5 NS/SWCNT cathodes. The rate performance was done between a current density range of 0.1 to 10 C and then switched back to 0.1 C. Figure 4.16 (a) shows the rate performances for both the V_2O_5 NS and V_2O_5 NS/SWCNT cathodes. In both cases the cathodes retain their initial capacities when switched back to 0.1 C. The almost constant capacity gap between the pure V_2O_5 NS and V_2O_5/SWCNT composite indicates that the extra contribution to the capacity may be attributed to the capacitive response of the SWCNTs. The relative cyclabilities and Coulombic efficiencies were determined for 100 cycles at 1

C as illustrated in Figure 4.16 (b). While the V_2O_5 NS cathode retains 72% of its initial capacity, the V_2O_5 NS/SWCNT cathode retains 81% while showing a Coulombic efficiency of 97% comparable with literature examples mentioned earlier. The apparent wave like behaviour of the V_2O_5 NS/SWCNT has been exhibited by other such composite TMO materials [343, 344]. This could be associated with a long term activation process. During initial cycling, the V_2O_5's crystallinity may degrade to a disordered or amorphous-like structure. Therefore, more sites for Li-ion adsorption may be available, however, as such sites are not stable there is a further capacity decrease as expected.

4.3.3.4 Electrochemical Impedance Spectroscopy

Both the V_2O_5 NS and V_2O_5 NS/SWCNT cathodes were subjected to EIS at a potential of 10 mV within a frequency range of 1 mHz to 1 MHz. The corresponding Nyquist plots of both cathodes are shown in Figure 4.17. Both cathodes exhibited behaviour common to that of the Randles equivalent circuit as illustrated in the inset [242]. For both cathodes, the semicircle intercepts the x-axis at 11 Ω corresponding to the R_S of the $LiClO_4$ electrolyte. The subsequent intercept suggests a decrease from 1100 Ω to Ω 110 in R_{CT} across the electrode/electrolyte interface. This tenfold decrease may be attributed to the presence of SWCNT and agrees with previously acquired electrochemical results. The reduced shape of each semicircle suggests a general decrease in the exponent value of the C_{CPE}.

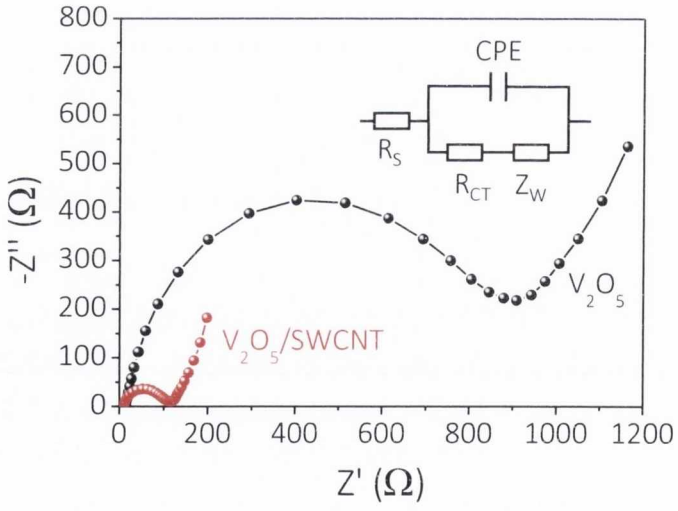


FIGURE 4.17: EIS of the V_2O_5 NS cathodes

The V_2O_5 NS and V_2O_5 NS/SWCNT cathodes exhibit values of a = 0.7 and a = 0.8 respectively indicating the uneven surface which may be reasonably attributed to the porous structure. The larger value for the V_2O_5 NS/SWCNT may represent the increased capacitive properties of the cathode.

4.3.4 Post Characterization

The structure of the V_2O_5 NS/SWCNT cathode was was investigated after it underwent five CV cycles at 0.05 C between a potential window of 1 - 4 V. After cycling, the two cathodes were carefully removed from their respective cells and cleaned with IPA to remove unwanted residual electrolyte.

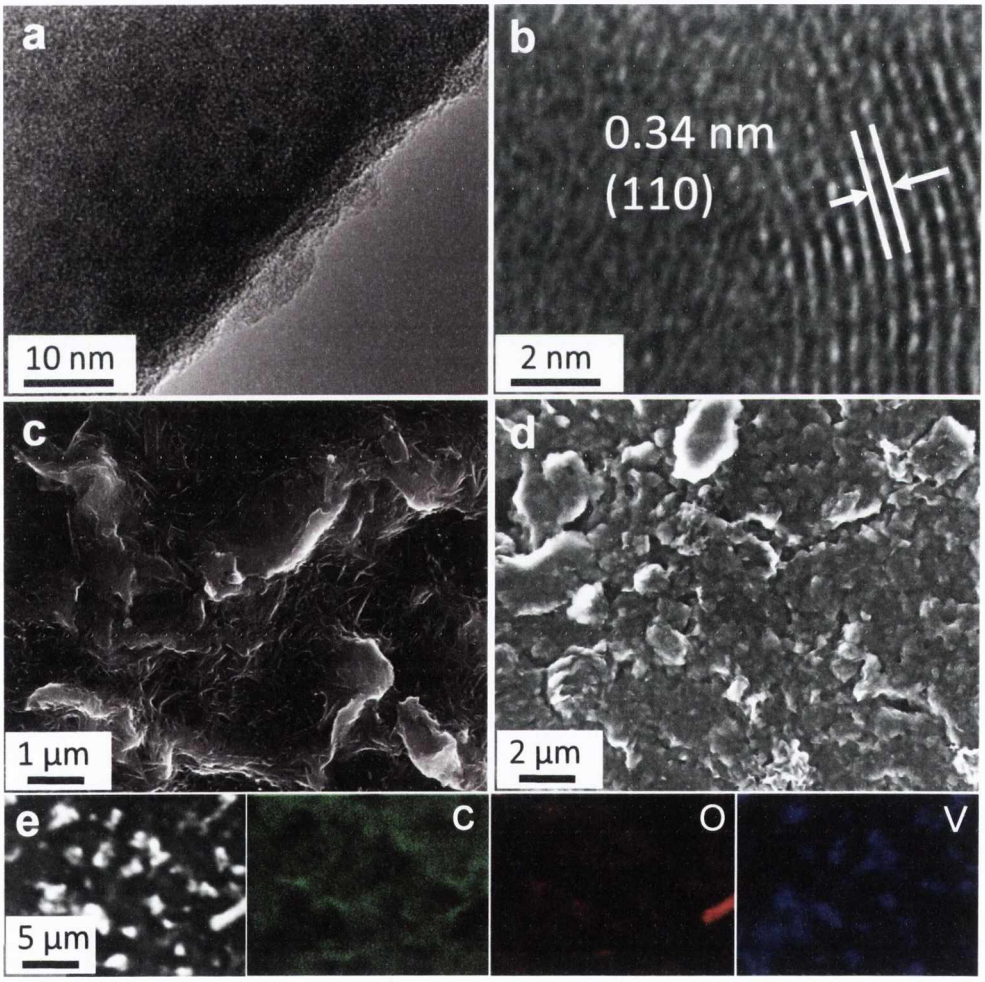


FIGURE 4.18: (a)TEM and (b) HRTEM images of the V_2O_5 NS/SWCNT cathode. SEM images of the (c) V_2O_5 NS/SWCNT and (d) V_2O_5 NS cathodes and (e) the corresponding V_2O_5 NS/SWCNT EDX maps.

Then the cathodes underwent a series of TEM, SEM, EDX, XPS and XRD and experiments and the results were analysed. Initially one cathode was placed inside a centrifuge tube along with 15 ml of H_2O. The cathode underwent sonication to remove and re-disperse the V_2O_5 NS. The sample was then dropcast onto a holey carbon grid for TEM analysis. Figure 4.18 (a) shows the TEM image of the edge of a flake demonstrating the retention of thin flakes. Figure 4.18 (b) shows a HRTEM image indicating the presence of the {110} set of planes. After electrochemical cycling, the individual V_2O_5 NS are shown to retain their crystalline structure. An SEM image of a second electrochemically cycled V_2O_5 NS/SWCNT cathode is shown in Figure 4.18 (c). The cathode itself retains its structural intensity even after undergoing repeated phase changes. In comparison, the V_2O_5 NS cathode shows a series of cracks along the surface as demonstrated in Figure 4.18 (d). It can be assumed the SWCNTs strengthen the structural integrity of the whole cathode reducing any apparent pulverisation. The EDX patterns shown in Figure 4.18 (d) indicates that the distribution of SWCNTs and V_2O_5 NS remains relatively dispersed throughout the cathodic system.

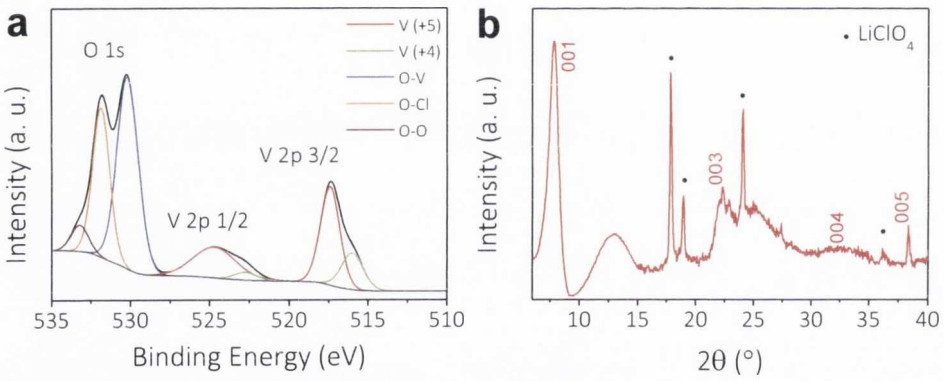


FIGURE 4.19: (a) XPS spectrum showing the deconvoluted O1s and V2p peak, and (b) the XRD pattern of the the V_2O_5 NS/SWCNT cathodes post electrochemical cycling

After the V_2O_5 NS/SWCNT cathode was removed from the SEM, it was subjected to XPS analysis. The major V 2p and O 1s core levels are shown in Figure 4.19 (a). The relative binding energies of the V 2p 3/2 and 5/2 peaks remain relatively unchanged compared to that of the fresh cathode. However, the intensities of each deconvoluted peak change dramatically. The V(+4) shows a marked increase from 4.8 wt% before cycling to 29.3 wt % after. As a result, the relative ratio of V(+5) to V(+4) increases from 1 : 0.05 to 1 : 0.41. Despite the SWCNTs alleviating the phase change consequences as exhibited earlier, a residual effect is still observed. Traditionally, the V(+4) is associated with the formation of O vacancies as described

earlier. There is also a drop in the % O - V peak intensity relative to that of the whole O peak. The drop from 57% to 38% is can be attributed to the increased presence of extra O deficiencies coupled with any residual $LiClO_4$ electrolyte. The crystal structure of the V_2O_5 NS/SWCNT shows similar orientation along the {001}) direction as that of the fresh cathode as demonstrated by the XRD pattern in Figure 4.19 (b). However, a series of extra peaks are present which can be attributed to the presence of residual $LiClO_4$ in the lattice.

4.4 Conclusion

To conclude, a facile method was presented to exfoliate large quantities of 2D V_2O_5 NS from commercially acquired V_2O_5 powder in environmentally green solvents. These V_2O_5 NS adopted a specific xerogel structure similar to that acquired from certain sol-gel and ion exchange techniques found in literature. However, the LPE method provides a simpler single step process without the formation of by products or the use of hazardous materials. We propose that LPE provides similar energies required to intercalate H_2O molecules into the V_2O_5 layers and cause swelling similar to that exhibited in xerogels. This swelling causes the V_2O_5 to form a bilayered structure with an inter-layer spacing increase from 0.43 nm to 1.15 nm as confirmed by TEM and XRD analysis. Furthermore, TEM, XPS and XRD analysis shows that the as-prepared V_2O_5 NS possesses a high degree of purity and the desired crystal structure consistent with that of orthorhombic phase of V_2O_5. To demonstrate the charge storage properties of the xerogel structured V_2O_5 NS a series of single and multi Li-ion intercalation mechanisms were examined. A series of highly flexible, thin film V_2O_5 NS cathodes were fabricated using a facile ultrasonic spraying method. As V_2O_5 xerogels demonstrate semiconducting behaviour, conductive SWCNTs were dispersed throughout the V_2O_5 to reduce the charge transfer resistance across the electrode/electrolyte interface as confirmed by EIS analysis. As predicted, the intercalation of a single Li-ion per unit formula of V_2O_5 showed high reversibility and a storage capacity vs. Li/Li^+ with the addition of SWCNTs coherent with the calculated theoretical capacity. The charge transfer mechanisms exhibited a highly pseudocapacitive response commonly associated with TMO materials as confirmed by the lack of well defined CV peaks. Similarly, electrochemical analysis was carried out on multi-ion intercalation mechanisms. The reversible behaviour associated with a single Li-ion intercalation was not repeated for the multi Li-ion mechanism as the V_2O_5/SWCNT cathode showed an 81% capacity retention and a Coulombic efficiency of 97% after 100 cycles. However, these values exceed many examples found

in literature, showing how this nanostructuring method acts to increase tolerance to volume expansion and reduces the diffusion coefficient similar to the effect of the SWCNTs. Analysis of the diffusion processes indicated that the diffusion coefficient increased by a factor of 14.5 after nanostructuring and by a further factor of 2 after addition of conducting SWCNTs. The initial discharge capacity determined for the V_2O_5/SWCNT cathodes was 393.4 $mAh\,g^{-1}$ at a current density of 0.05 C vs. Li/Li^+, a value vastly exceeding that of a 2 Li-ion intercalation mechanism (294 $mAh\,g^{-1}$). At a current density of 10 C, the cathode exhibited discharge capacity of 140 $mAh\,g^{-1}$ (corresponding to a 6 min discharge). Analysis of the V_2O_5 NS/SWCNT cathode after electrochemical testing demonstrated lack of pulverization of the cathode surface and a retention in crystal structure of the V_2O_5 NS. Comparison with a used V_2O_5 NS indicated that the SWCNTs also act as a structural support to the V_2O_5 NS matrix as the used V_2O_5 NS cathode possessed a series of cracks along its surface. Furthermore a series of LPE tests were carried out in a wide range of solvents to ascertain colloid stabilization information. It was determined that solvents with Hildebrand solubility parameters between 21 and 25 $MPa^{0.5}$ (NMP, formaldehyde *etc.*) produced the most stable and concentrated V_2O_5 dispersion. However, as H_2O has a solubility parameter of 48 $MPa^{0.5}$, it was assumed that stabilization occurs from the formation of a xerogel structure. Further experiments provided a series of optimized exfoliation parameters for the maximization of the V_2O_5 NS in H_2O

Chapter 5

Titanium Dioxide Nanoparticles

5.1 Introduction

Certain TMOs have recently found application as high energy anode materials for LIBs [48–50]. Currently, graphite holds the dominant position as the anode material of choice as highlighted in section 1.3.1.1. However, due to a variety of safety concerns, a range of alternative materials are being researched [52–55]. It is desirable to find a suitable replacement material possessing both high rate performance coupled with improved safety. Titanium based TMOs are highly attractive materials with potential scope to replace graphite as the anodic material due to their unique chemical and structural properties [345–348]. Although various forms of titanate exist, the electrochemically active titanates comprise of both $Li_4Ti_5O_{12}$ and TiO_2. Currently, spinel $Li_4Ti_5O_{12}$ has a niche position as an anode material in commercial electrochemical cells due to its unique structure conducive to Li-ion insertion. However, $Li_4Ti_5O_{12}$ has a low theoretical storage capacity of $175\,mAhg^{-1}$ vs. Li/Li^+ compared to that of graphite ($372\,mAh\,g^{-1}$) indicating scope for improvement. Research is currently being focused on Titanium dioxide, TiO_2, as a valid alternative to $Li_4Ti_5O_{12}$ due to its higher theoretical storage capacity ($335\,mAh\,g^{-1}$ vs. Li/Li^+) which is comparable to that of graphite

TiO_2 nanomaterials have found application in a wide range of common items such as paint pigment [349], sunscreen [350] and food colourings [351]. Similarly, TiO_2 nanomaterials have been employed as active materials in many technological processes such as water purification [352, 353], biomedicine [354] and photocatalysis. TiO_2's ability to act as a photocatalyst has sparked research into its application in photocells [355–357], photochemistry [358, 359] and more importantly, the photocatalytic degradation of pollutants [353, 360].

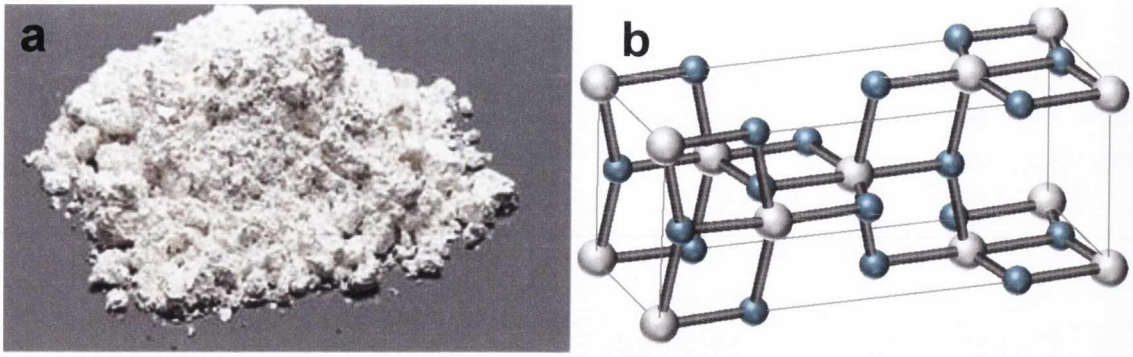


FIGURE 5.1: (a) optical image of the anatase TiO_2 powder (taken from [361]) and (b) The octahedral structure of tetragonal anatase TiO_2.

TiO_2 is a naturally occurring white powder, see Figure 5.1 (a), found in several minerals in many parts of the world [362]. Many different structural forms of TiO_2 exist, most notably the anatase, rutile, and brookite phases [363]. However, two further and much rarer naturally occurring polymorphs have been discovered namely Akaogiite and $TiO_2(II)$ [364, 365]. Several example of purely synthetic polymorphs exists, most notably that of monoclinic TiO_2 (B) produced by the hydrolysis of $K_2Ti_4O_9$ [366]. A vast majority of the world's TiO_2 is extracted directly from ilmenite ore ($FeTiO_2$) [367, 368]. The ilmenite ore is treated with concentrated sulphuric acid (H_2SO_4) at 100° C and TiO_2 is extracted from the product by a low temperature crystallization of the $TiOSO_4$.

$$FeTiO_3 + 2H_2SO_4 \rightleftharpoons FeSO_4 + TiOSO_4 + 2H_2O \tag{5.1}$$

$$TiOSO_4 + (n+1)H_2O \rightleftharpoons TiO_2nH_2O + H_2SO_4 \tag{5.2}$$

Temperatures exceeding 200° C are applied to remove the water of crystallization and depending on the final heating temperature either anatase of rutile is formed. However, a second more environmentally friendly method involves the direct treatment of rutile ore with chlorine at 1000° C in the presence of a coke catalyst.

$$TiO_2 + C + 2Cl_2 \rightleftharpoons TiCl_4 + CO + CO_2 \tag{5.3}$$

$$TiCl_4 + O_2 \rightleftharpoons TiO_2 + 2Cl_2 \tag{5.4}$$

Anatase and rutile are the most common natural forms of TiO_2, both crystallizing in a tetragonal crystal structure, however rutile is known to be the more stable polymorph. Similar to rutile, anatase has an octahedral structure consisting of bonded TiO_6 octahedrons, however, while rutile's octahedrons share two edges, anatase's share four edges and as a result have a four fold axis, see Figure 5.1 (b) [369].

The anatase, rutile and TiO_2 (B) phases have been widely studied in the past few decades as potential anode materials [84, 370, 371]. Due to its abundance, low cost structural stability and high potential (> 1.5 V vs. Li/Li^+), TiO_2 represents a suitable materials to meet modern demands for high energy Li-ion batteries [372]. Compared to current graphite based anodes, the formation of low potential SEI layers is severely reduced. However due to its semiconducting nature, TiO_2 suffers from a poor electrical conductivity. The Li-ion intercalation and deintercalation process into TiO_2 can be described as,

$$TiO_2 + xLi^+ + xe^- \rightleftharpoons Li_xTiO_2 \tag{5.5}$$

The theoretical capacity of TiO_2 is 335 $mAh\,g^{-1}$ for a single ion intercalation process.

The anatase phase of TiO_2 has received specific attention due its ability to transfer charge quickly through its wide channels. Much research is focused on the nanostructuring of the anatase TiO_2 to increase both its active surface area and improve Li-ion diffusion. Specifically, TiO_2 nanoparticles in which the (001) facet is exposed directly to Li-ions [59, 373]. Due to its lower surface energy, it is common for TiO_2 to crystallize with (101) terminations. The (001) facet possesses an energy barrier half that of the commonly observed (101) facet leading to improved charge transfer properties. Nanostructured TiO_2 exists in a wide variety of forms including nanotubes [374–377], nanowires [371, 378] and nanosheets [132, 379]. A wide range of nanostructuring methods have been used to synthesize TiO_2 including hydrothermal chemistry [375, 380, 381], atomic layer deposition [382, 383] and templating [384–386].

Despite falling short of its theoretical capacity, certain examples show how manipulation of anatase TiO_2 can produce high energy anodes. For example, Xiu *et al.* produced a highly mesoporous anatase nanoelectrode in which the initial charge storage capacity reached 300 $mAh\,g^{-1}$ at 0.1 C [373]. Similarly, Liu *et al.* synthesized a TiO_2/CNT composite exhibited storage capacities of 300 $mAh\,g^{-1}$ at 0.1 C with a 61% retention in capacity after 100 cycles [387]. As there is much scope for a high

capacity anatase based anode material, it is desirable to derive a facile, eco-friendly method to produce a high quality nanostructured TiO_2 anode. Herein, a TiO_2 colloid is synthesized *via* the sonication of commercial powder in H_2O. A series of exfoliation parameters were also studied along with stabilization mechanisms. The nanostructured TiO_2 particles are on the order of 100 - 200 nm with both exposed (001) and (101) facets. Large, flexible, binder free anodes were fabricated which display high storage capacities and impressive rate capabilities rivalling that from examples in literature.

5.2 Experimental

Synthesis - The TiO_2 nanoparticles were obtained *via* the liquid phase sonication of TiO_2 powder (Sigma Aldrich, 99.99 %, 325 mesh) in deionized H_2O. The dispersions ($0.2\,g\,L^{-1}$) were placed in a 50 ml centrifuge tube and sonicated for 3 h at 192 W, 80 kHz and kept at a temperature of 10° C by periodically changing the bath water (Fisherbrand P120 H, 240W). The resultant dispersion was centrifuged at a rate of 1000 rpm for 1 hr and the top 20 ml of supernatant was collected and kept in a 200 ml bottle for storage. The sonication process was repeated several times to provide adequate quantities for the succeeding experiments. The concentration of the TiO_2 nanoparticle dispersions were determined by vacuum filtration through an alumina filter membrane (Whatman, 0.02 μm pore diameter). The effects of initial concentration, and the sonication time, power and frequency on the resultant TiO_2 nanoparticle concentration were determined. In addition, the liquid phase sonication of TiO_2 powder in a range of different solvents such as NMP, benzyl alcohol, BB, ethanol, cyclohexanone, BA, methanol, dibutyl ether, acetone, IPA, formaldehyde, formamide, ethylene glycol, acetonitril, dichlorobenzene and DMF were also conducted. A separate dispersion of SWCNT was made by mixing 0.1 $mg\,ml^{-1}$ of P3-SWCNT (99.99%, Carbon Solutions Inc.) with 50 ml water and sonicated at 20 kHz for 1 hr.

Characterization - Scanning electron microscopy (SEM) was performed using a Zeiss Ultra Plus (Carl Zeiss, Germany). Transition electron microscopy (TEM), scanning transition electron microscopy (STEM) and energy dispersive x-ray spectroscopy (EDX) were performed using a Titan high-resolution TEM (HRTEM) at 300 kV (FEI, USA). The nanoparticle dispersion was drop-casted onto holey carbon grids (Agar Scientific, UK) and allowed to dry overnight. The nanoparticle dimensions were statistically analysed on TEM by measuring the longest axis of the nanoparticle and

assigning it as the length followed by measuring an axis perpendicular to this at its widest point and assigning it as the width. Optical spectroscopy was done using a Cary 6000i UV-Vis absorbance spectrometer (Agilent, USA). Each dispersion was diluted by a factor of ten with respect to the dispersing solvent to prevent over-scattering of the incident light beams. To further clarify the chemical compositions of the as-prepared TiO_2 nanoparticles, X-ray photoelectron spectroscopy (XPS) spectra (CLAM 4 MCD, VG Microtech, UK) was employed using a 200 W unmonochromated Mg X-ray excitation source (1253.6 eV) with samples supported on silicon substrates. All binding energies were referenced to that of aliphatic carbon at 284.8 eV. Crystal structures were studied on a X-ray diffraction (XRD) spectra (D5000 powder diffractometer, Bruker, USA) with a monochromatic Mo K radiation source (λ = 0.07107 nm) and a secondary monochromator. Brunauer-Emmett-Teller (BET) analysis was done using a Nova 4200e surface area analyser (Quantichrome, USA).

Electrode Preparation - TiO_2 thin film electrodes were fabricated by the ultrasonic spraying of the dispersed TiO_2 nanoparticles on copper foil ($20\,\mu m$, 18 mm diameter) pre-treated with an adhesive polyethyleneimine (PEI) layer (30%, Alfa Aesar). Typically, the TiO_2 nanoparticle dispersion was diluted down by a factor of five to allow for better flow and 30 ml of the diluted dispersion was placed in a syringe (100 ml) of the ultrasonic sprayer. During the spraying, the copper substrate was heated to 100°C to allow for H_2O evaporation. The resultant electrodes were then transferred to an Ar filled glove box after drying overnight at 100 ° C. The mass of the active material was determined by weighing the substrate before and after spraying. The same procedure was employed for the TiO_2/SWCNT composite electrode. For the TiO_2/SWCNT composite electrode, the TiO_2 nanoparticle dispersion was mixed with 0.1 $mg\,ml^{-1}$ of P3-SWCNT in a mass ratio of 95:5. The blended dispersion was then diluted down by a factor of five and allowed to mix for 1 hr using a magnetic stirring bar. The resulting electrodes were then transferred to the Ar glove box after subsequent drying and mass determination. As a control, a separate anode was fabricated from a slurry comprised to 80% unsonicated TiO_2 powder, 10% conductive C black and 10% PVDF as a polymer binder.

Electrochemical Characterization - The electrochemical behaviours of the electrodes were evaluated using the half-cell configuration with the active material as the working electrode, Li foil as the counter and reference electrodes and 1 M lithium perchloride ($LiClO_4$) dissolved in propylene carbonate (PC) (1 M $LiClO_4$/PC) as the electrolyte. Cyclic voltammetry (CV), galvanostatic cycling (GC), and electrochemical impedance spectroscopy (EIS) tests were performed on a VMP-300 potentiostat

(Bio-Logic, France). CV was recorded at 0.05 mVs^{-1} with a potential range 1-3 V (vs. Li/Li^+). GC were performed at different current density rates from 0.1 to 10 C within a potential range of 1 - 3 V (vs. Li/Li^+). EIS was measured at open-circuit potential (E_{OCP}) with a 10 mV amplitude and a frequency range of 1 mHz - 1 MHz. The cycling performance was conducted at a current density of 1 C for 100 cycles.

5.3 Results and Analysis

5.3.1 Synthesis of the Nanoparticle Colloid

Unlike V_2O_5 mentioned in Chapter 4, TiO_2 does not exhibit a natural layered structure. Therefore, applying sonic energy will not affect the TiO_2 in the manner exhibited by V_2O_5. Commercially acquired anatase powder (as seen in the TEM image in Figure 5.2 (a)) was added to deionized H_2O in a centrifuge tube and sonicated at 80 kHz for 3 hr. The powder itself exists as a series of weakly bonded particles in a matter similar to that exhibited by individual layers of a 2D material. The resulting dispersion was centrifuged at 1000 rpm for 1 hr and the supernatant was collected and herein named the "TiO_2 NP" dispersion. A sample was dropcast onto a holey carbon grid and subjected to TEM analysis.

A representative TEM image of a TiO_2 NP is shown in Figure 5.2 (b). The resultant TiO_2 NP appears to adopt a pseudo-3D structure with lateral dimensions on the order of 100 - 200 nm similar to that reported in literature for other methods [363, 388, 389]. The corresponding HRTEM images shown in Figure 5.2 (c) and (d) represent the edge and centre of an individual particle respectively. The {001} set of planes are clearly evident throughout the edge structure corresponding to an inter-planer spacing of 0.19 nm [59, 390]. The centre of the particles are dominated by the {101} set of planes relating to an inter-planer spacing of 0.35 nm [356]. The corresponding FFT pattern in Figure 5.2 (e) shows similar results. Both of these sets of planes are consistent with the anatase phase of TiO_2. An EDX spectrum was taken for a series of TiO_2 NP. Both Ti and O peaks are evident with an expected atomic ratio of 2 : 1. The Cu and C peaks can be attributed to the holey carbon grid.

To further elucidate the crystal structure of the resultant TiO_2 NP, XRD analysis was performed on a sample ultrasonically sprayed onto a Si substrate. As a control, an XRD spectrum was taken of the pure unsonicated anatase TiO_2 powder. Figure 5.3 (a) shows the corresponding XRD patterns. The unexfoliated powder exhibits a characteristic set of peaks centred at 11.57°, 17.13°, 21.59°, 24.06°, 24.56 and 27.68°.

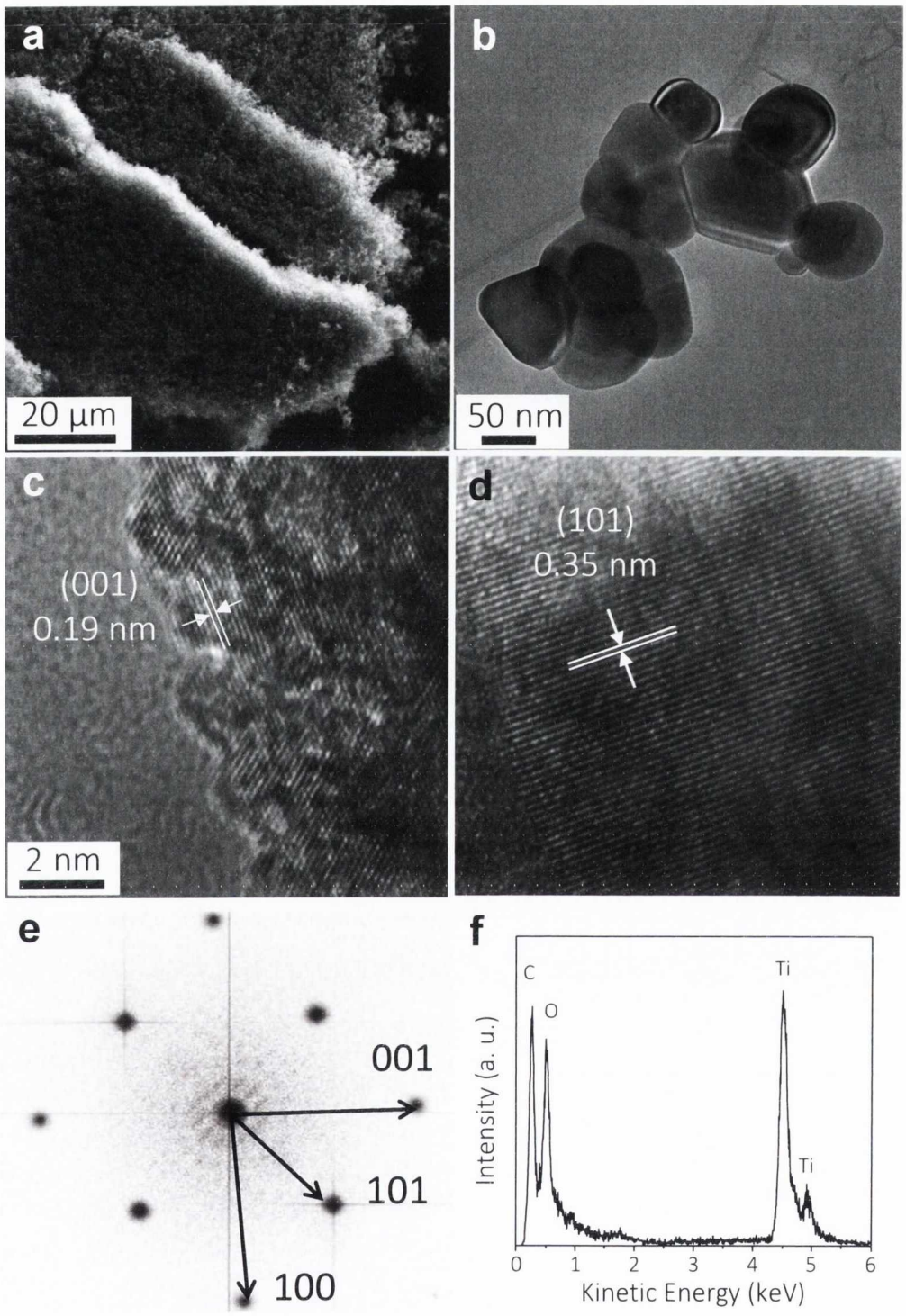


FIGURE 5.2: TEM images of the precursor (a) anatase TiO_2 powder and (b) a single nanostructured TiO_2 NP. (c) - (d) HRTEM image indicating the crystal planes of the TiO_2 NP and (e) the corresponding FFT pattern. (f) The EDX spectrum showing the principal elemental transition.

These peaks refer to the {101}, {004}, {200}, {105}, {211} and {204} series of planes indexed to the anatase phases of TiO_2 (JCPDS files # 21-1272) [391]. However, sonication does not seem to alter the peak positions or the intensities indicating that the crystal structure of the material is maintained. The absence of other peaks indicates the purity of the TiO_2 NP, i.e. minute traces of rutile, brookite *etc.*. Analysis of the {101} peak indicates an inter-planer spacing of 0.32 nm corresponding with that determined from TEM analysis previously.

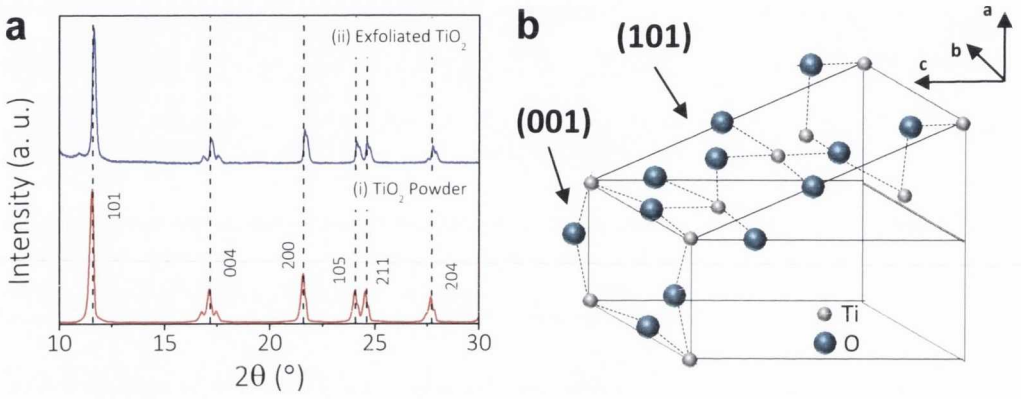


FIGURE 5.3: (a) XRD patterns of the TiO_2 and (b) the corresponding proposed NP structure.

As the XRD pattern remains relatively unchanged, it is assumed the sonication acts to separate the weakly bonded particles exposing the full surfaces to external influences. In general, TiO_2 tends to favour the formation of {101} terminations as it is more energetically favourable than that of the {001} termination [59, 372]. However, similar to reports elsewhere, a series of {001} planes are evident along the edges of the particles. As these {001} have higher surface energy, it is possible the particles in the powder were weakly bonded along these planes to minimize the resultant surface energy. The proposed structure of the resultant nanoparticles is shown in Figure 5.3 (b). The active surface area determined by N absorption analysis and BET theory of the TiO_2 NP was determined to be 21.4 $m^2\,g^{-1}$.

XPS was employed to further investigate the chemical structure of the TiO_2 NP ultrasonically sprayed onto a Si substrate. The deconvoluted TiO_2 spectrum is shown in Figure 5.4 (a). The peaks centred at binding energies of 458.6 eV and 464.4 eV can be attributed to the spin orbital splitting of the Ti 2p core level into 3/2 and 1/2 [392]. The separation of the spin orbital spitting was determined to be 5.7 eV with a peak ratio of 2 : 1 respectively which is consistent with that of stoichiometric TiO_2.

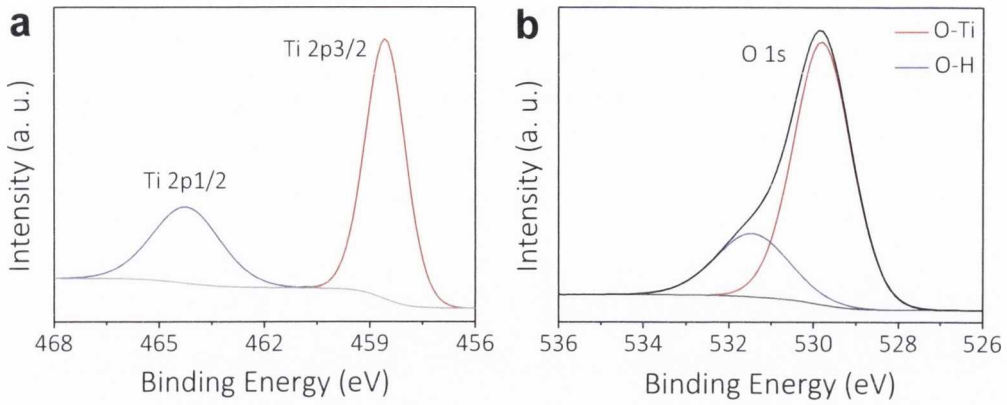


FIGURE 5.4: High resolution XPS spectra of (a) the Ti 2p and (b) O 1s core level peaks of the TiO_2 NP.

The major O 1s peak, in Figure 5.4 (b), can be located between binding energies of 527 - 535 eV. This peak can be further deconvoluted into a series of smaller peaks attributed to the binding states of the O. The peaks at 529.9 eV and 531.5 eV can be reasonably attributed to the binding of O to the Ti in the oxide and O - O bond of the water with the particles respectively. The total peak ratios between the Ti and the O are 2:5 with 81% of total O peak being attributed to the O - Ti bond. Therefore, the total atomic ratio between Ti and O is 1 : 2 in agreement with the EDX result shown earlier.

For quick and facile synthesis of TiO_2 anodes, it is advantageous optimize the resultant concentration of stable nanoparticles in solution [135]. This is achieved by tuning both the sonication parameters as well as the solvent medium. Previously, it was demonstrated in Chapter 4 how the Hildebrand solubility parameters could be employed to determine the range of solvents for which V_2O_5 NS formed a stable dispersion. As TiO_2 forms a three dimensional structure, the stabilization mechanism may differ. A similar array of solvents was chosen to represent a wide range of Hildebrand parameters. Figure 5.5 (a) shows the relative UV-vis spectra for a selected range of solvents.

The transition of electrons from the valence band to the conduction band of the TiO_2 is characterized by the apparent peak found 350 - 450 nm [393, 394]. This corresponds to a band gap E_g = 3.2 eV. It is evident from the figure that solvent choice has a huge effect on the resultant concentration of the TiO_2 NP dispersion. Solvents such as formaldehyde and NMP form more a concentrated dispersion similar to that exhibited by the V_2O_5 NS. Other solvents, such as H_2O or IPA, tend to reduce the resultant concentration drastically. Taking classical solubility theory into account, the

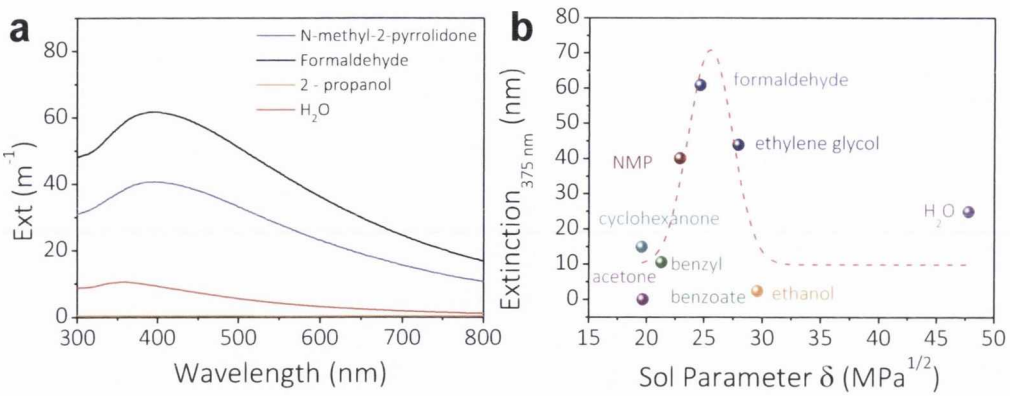


FIGURE 5.5: (a) Representative UV-vis spectra and (b) the extinction at 375 nm's dependence on the dispersing solvents Hildebrand solubility parameter of the TiO_2 NP dispersion

relative absorbance of each nanoparticle colloid was plotted against each solvents Hildebrand Parameter and illustrated in Figure 5.5 (b). The plot suggests a similar Guassian distribution as that demonstrated by the V_2O_5 NS, however, the region of stability lies between 23.0 - 27.5 $MPa^{0.5}$. This suggests that TiO_2 may have a slightly higher surface energy than that of V_2O_5. The stabilization process for TiO_2 in H_2O does not follow the same trends as the other solvents. The Hildebrand parameter is 47.8 $MPa^{0.5}$ falling well outside the optimum range yet still creates a relatively concentrated colloid. According to the XPS analysis mentioned previously, H_2O molecules can be detected after being sprayed. This may suggest the formation of hydrogen bonds with the TiO_2 along the terminal Os. This may form stable hydration sheaths despite having unfavourable surface energies.

Taking H_2O as the dispersing solvent, a series of sonication parameters were investigated in order to optimize the resultant dispersion concentration. A basic recipe of 2 $mg\,ml^{-1}$, 80 kHz and 192 W for 3 hr for chosen and each individual parameter was varied around that. A range of UV-vis spectra were taken for each dispersion and the resultant extinctions at 375 nm were plotted as a function of frequency, sonication power, sonication time and initial concentration of the TiO_2 powder as shown in Figure 5.6. No immediate trend may be observed when the resultant extinctions were plotted against frequency or power. As the powder consists of weakly bonded particles, it is understandable these two parameters may not have an effect on the resultant concentration as in both cases enough energy is being supplied to separate all the particles in the dispersion. Plotting the resultant extinctions dependence on time shows a clear exponential of the inverse time ($C_j \propto t^{0.5}$). During the initial 30 mins of sonication not enough energy is being provided to the powder dispersion to

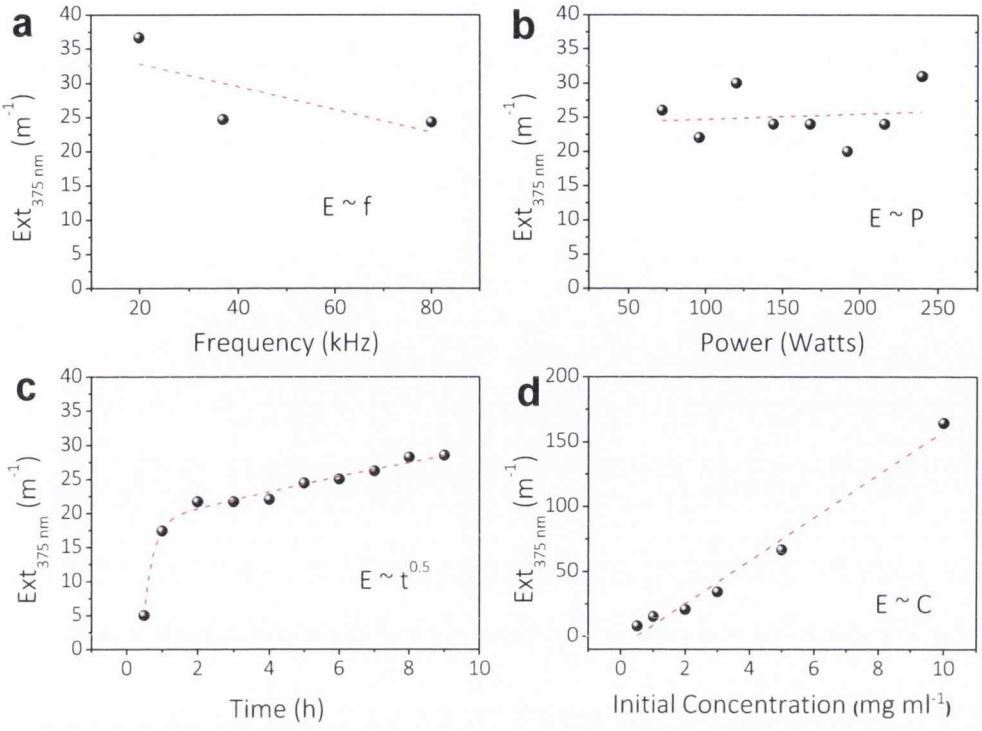


FIGURE 5.6: The Extinctions of the TiO_2 NP dispersion as a function of (a) sonication frequency, (b) sonication power, (c) sonication time and (d) initial concentration.

separate the particles, however, as the time reaches 1 hr, most of the particles have been separated which would explain the almost horizontal slope. Finally, the initial concentration of the TiO_2 powder also has a significant effect on the resultant concentration. There is a direct linear response increasing as the initial concentration increases.

A similar graph was plotted for the resultant dispersions dependence on centrifugation rate. Figure 5.7 (a) shows how the TiO_2 NP concentration decreases as the centrifugation rate increases. As centrifugation separates particles based on their size, unexfoliated particles sink to the bottom of the vessel while lighter particles remain dispersed. As the centrifugation rate increases particles of increasing mass tend to sink to the bottom leaving a less concentrated and lighter solution. Despite lower centrifugation rates having higher concentrations, the resultant particle sizes would be larger. Therefore all further centrifugations were done at 1000 rpm.

For future processing, an optimized stock dispersion was synthesized. To keep the process facile and cost effect but still yielding a highly concentrated dispersion, the chosen parameters were: an initial concentration of 2 $mg\,ml^{-1}$, a sonication frequency of 80 kHz and a power of 192 W for 3 hr. A sample of the resultant dispersion

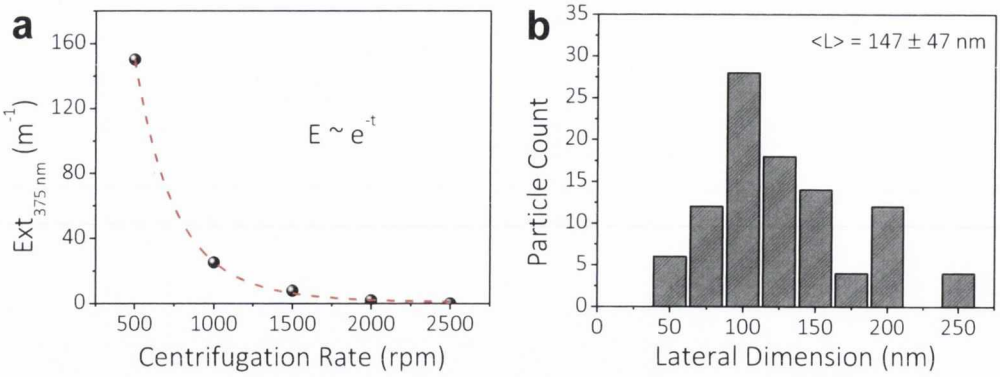


FIGURE 5.7: (a) The Extinctions of the TiO_2 NP dispersion as a function of centrifugation rate and (b) the particle size distribution histogram based on the optimized dispersion.

was dropcast onto a holey carbon grid and underwent statistical analysis from the TEM. A series of 100 TiO_2 NP were chosen and their longest lengths determined. Figure 5.7 (b) shows a histogram with the relative counts over a series of 100 TiO_2 NP. Most particles fall in the range of 75 nm - 150 nm. The average length determined was 147 $\pm$ 47 nm.

5.3.2 Anode Fabrication

A series of TiO_2 NP anodes were ultrasonically sprayed onto Cu current collectors pretreated with PEI adhesive from the optimized dispersion. [337]. The TiO_2 NP/SWCNT anodes were similarly fabricated. A separate dispersion of SWCNTs was dispersed in H_2O using a 20 kHz sonic horn. A 5% weight of SWCNT was added to the TiO_2 NP and allowed to mix overnight. Samples of both cathodes were also sprayed onto Si substrates for SEM analysis. Figures 5.8 (a) and (b) show low magnification images of the TiO_2 NP and TiO_2 NP/SWCNT. The porous structure of both anodes represent an efficient Li-ion diffusion system required for Li-ion energy storage. The corresponding higher magnification images are shown in Figures 5.8 (c) and (d). Compared to the TiO_2 NP anode, the TiO_2 NP/SWCNT anode exhibits a slightly higher porosity. The efficient mixing of both the NP and the SWCNT further benefit the charge transfer processes present in the anode.

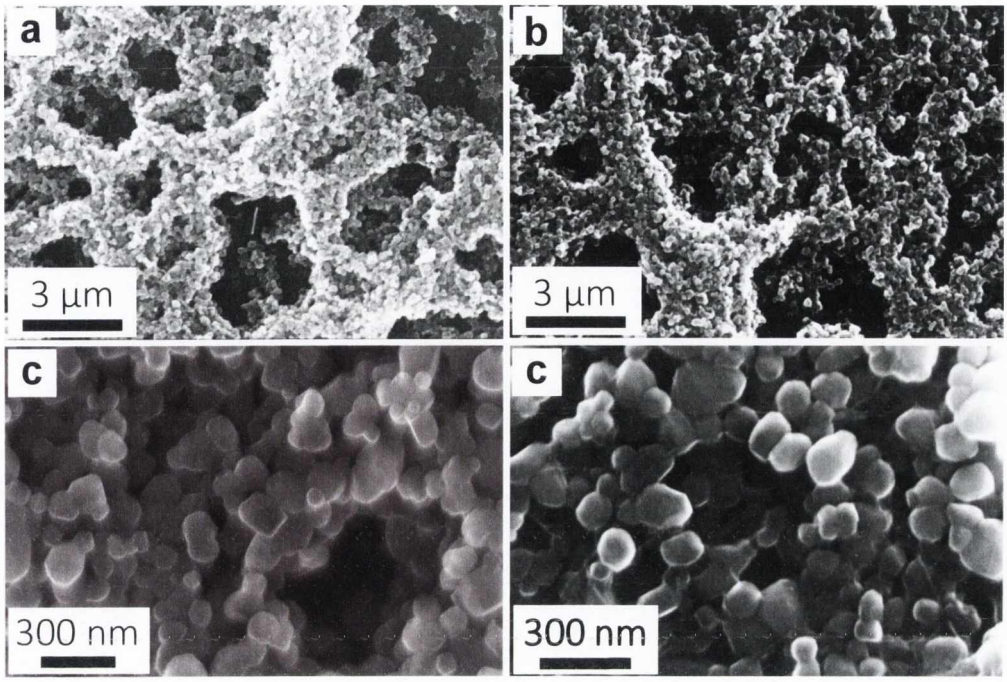


FIGURE 5.8: SEM images of (a) TiO_2 NP anode and (b) TiO_2 NP/SWCNT anode. High magnification SEM images of the (c) TiO_2 NP anode and (d) TiO_2 NP/SWCNT anode

5.3.3 Electrochemical Characterization

The electrochemical properties of both the TiO_2 NP and anodes were determined by a series of CV, GC and EIS measurements. Traditionally, this employs a potential window spanning 1 V to 3 V vs. Li/Li^+ to account for the principal insertion mechanism [48]. Initially the insertion and extraction processes were characterized by CV. Figure 5.9 (a) depicts the first and fifth CV curves for the TiO_2 NP anode at a scan rate of 0.1 $mV\ s^{-1}$. The peak centred at a potential of 2.2 V refers to the insertion of Li-ion into the TiO_2 lattice with the corresponding extraction peak centred at of 1.7 V [387, 395]. For the first cycle, a small extraction peak is also evident at a potential of 1.2 V may correspond to a side reaction with H_2O or an impurity as it does not feature in the fifth cycle. As the fifth cycle is completed, the extraction peak remains relatively unchanged, however the insertion peak has a shift in potential to 2.1 V indicating a gradual increase in the energy needed for insertion. This is perhaps due to Li-ion trapping after subsequent cycles. The over all shape of the curves reflects the typical insertion behaviour of TiO_2.

Similarly, Figure 5.9 (b) depicts the first and fifth CV curves for the TiO_2 NP/

SWCNT anode at a similar scan rate. The potential values of the peaks remain relatively unchanged, however, the increase in pseudocapacitive behaviour is clearly evident by the pseudo-rectangular shape of the CV profile. This would be a contribution from the capacitive charging of the SWCNTs at lower potentials coupled with the reduced charge transfer properties and increased diffusion properties provided by the SWCNTs at higher [339, 340, 387].

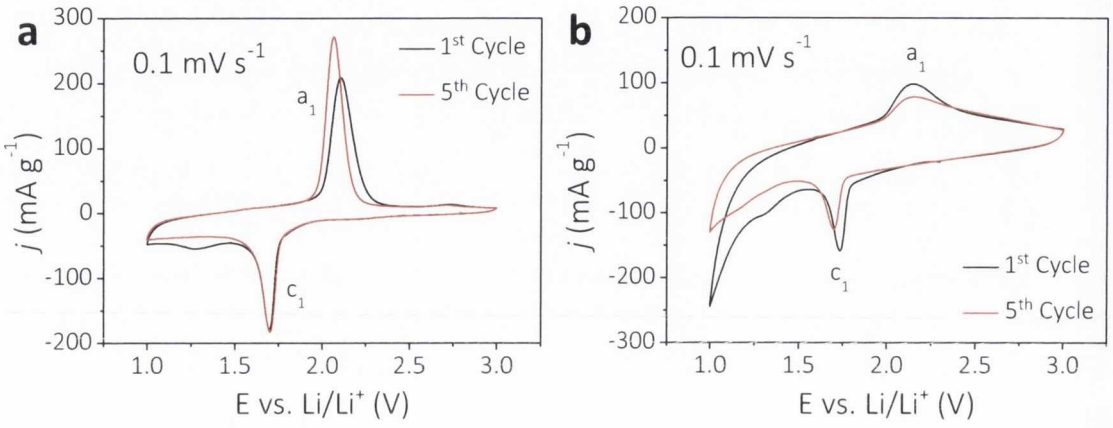


FIGURE 5.9: CVs of both the (a) TiO_2 NP and (b) TiO_2 NP/SWCNT anodes at a scan rate of 0.1 mVs^{-1}

The charge storage capacities of the TiO_2 NP and TiO_2 NP/SWCNT anodes were determined by GC methods. As a control, a separate anode was fabricated from a slurry comprising of 80% unexfoliated TiO_2 powder, 10% PVDF and, 10% conductive Super C65. All three cathodes were subjected to both charge and discharge cycles at a current density of 0.1 C between a potential window of 1 V - 3 V. Figure 5.10 compares the initial charge and discharge curves of all three anodes. Each anode shows a discharge plateau centred at a potential of about 1.7 V and a corresponding charge plateau at 2.0 V. Both these plateaus correspond to Li-ion insertion and extraction processes evident in the CV from Figure 5.9. Analysis of both the TiO_2 slurry and NP anodes reveals two major effects of the nanostructuring process. Firstly, the slurry anode exhibits a highly Faradaic charge storage mechanism due to the large potential drop below 1.7 V for the discharge process. This is commonly associated with the charge storage mechanisms in a battery. Nanostructuring the TiO_2 act to increase the pseudocapacitive properties of the anode due to the large increase in surface area [62]. This is evident with the reduced potential drop below 1.7 V. Secondly, as the surface area increases so does the resultant storage capacities. In terms of figures, the unexfoliated slurry anode exhibits an initial discharge capacity of 141.6 $mAh\,g^{-1}$ while the TiO_2 NP anode shows a capacity is 178.5 $mAh\,g^{-1}$. Due to structural constraints, TiO_2 tends to hold a maximum of 0.5

Li-ions per unit formula [372, 396]. The initial discharge capacities determined for the TiO_2 slurry and NP anode correspond to 0.42 ($Li_{0.42}TiO_2$) and 0.53 ($Li_{0.53}TiO_2$) Li-ions per unit formula in agreement with the literature values.

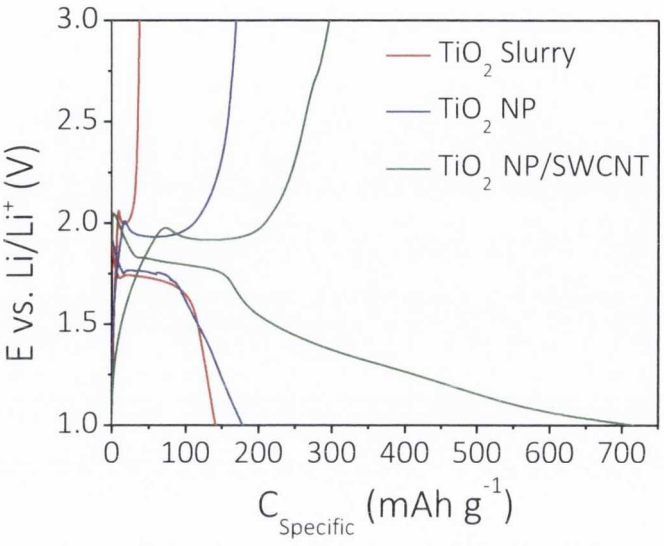


FIGURE 5.10: Initial GD curves of the TiO_2 slurry, NP and NP/SWCNT anodes

For TiO_2 to compete with contemporary graphite based anodes, work must be done to increase the quantity of Li-ion stored per unit formula to a value greater than 1. Anatase TiO_2 adopts a simple tetragonal structure with the Li-ions filling the centres of the octahedrons. However, as the quantity of Li-ions increases past 0.5 per unit formula the octahedral sites become filled and further storage occurs at the off centre sites. As such the TiO_2 adopts an orthorhombic arrangement [397, 398]. The amount of Li-ions per unit formula determined for the slurry and NP anodes show how this limit is reached despite the nanostructuring of the material. The potential drops further demonstrate the inability of the TiO_2 to accept more Li-ions. However, addition of the conductive SWCNTs acts to increase the pseudocapacitive properties of the TiO_2 NP and provides a larger storage capacity as shown in Figure 5.10. The initial discharge capacity of 716.6 $mAh\,g^{-1}$ indicates that 2.13 Li-ions are being inserted per unit formula. However, much of this may be attributed to the capacitive charge storage in the SWCNTs at lower potentials. As with the V_2O_5, the SWCNTs provide structural stability for the whole TiO_2 matrix. This structural stability coupled with the reduction in charge transfer resistance may facilitate the transition of TiO_2 from the tetragonal phase to the orthorhombic phase. In total, the large discharge capacity can be attributed to the nanostructuring of the material, the contribution in capacity from the SWCNT themselves, the general effect

the SWCNTs have on the TiO_2 and the presence of {001} terminations on the TiO_2 NP [59, 387]. The general discharge profile displays a highly pseudocapacitive tail compared to that of the pure TiO_2 NP anode indicating the extra contributions are mainly pseudocapacitive in nature [155] specifically at the SWCNTs at low potential. The corresponding charge storage process indicates a reduction in capacity to 296.16 $mAh\,g^{-1}$ corresponding to 0.88 Li-ion extracted per unit formula. This indicates a vast majority of Li-ion are being trapped in the anode and a possible formation of an SEI layer due to the SWCNTs after the first discharge as the potential reaches 1 V [355].

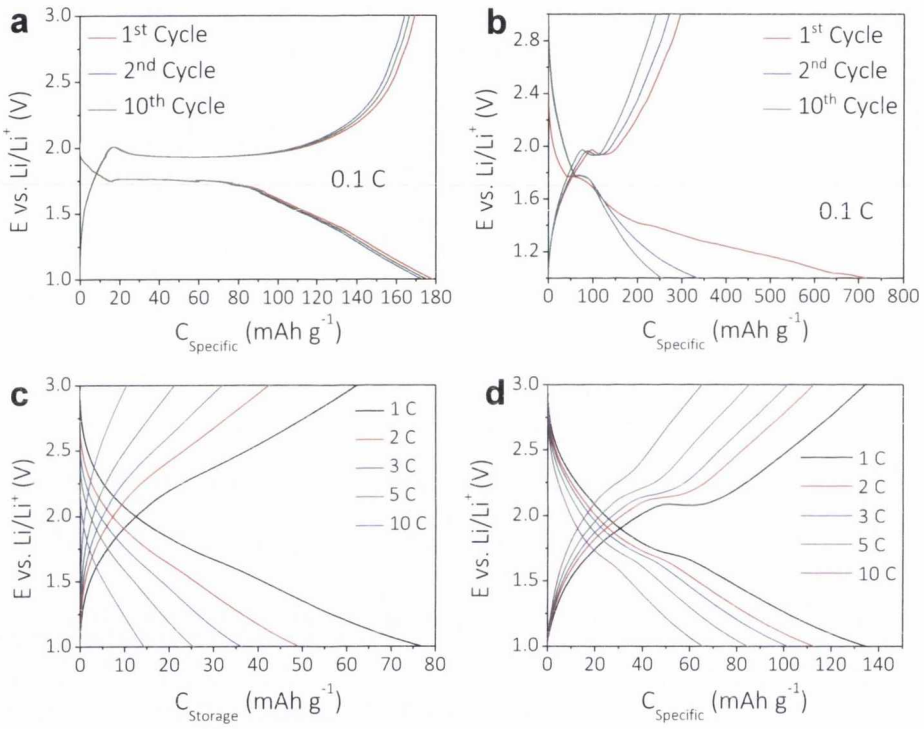


FIGURE 5.11: The first, second and tenth GC cycles for (a) the TiO_2 NP and (b) TiO_2 NP/SWCNT anodes. (c) TiO_2 NP and (d) TiO_2 NP/SWCNT anode current density ranges.

For both the TiO_2 NP and TiO_2 NP/SWCNT anodes, the first, second and tenth GC profiles were examined and compared. For the TiO_2 NP anode shown in Figure 5.11 (a), there is no major change in capacity by the second cycle compared to that of the first. By the tenth cycle the discharge capacity stabilizes off at 175.55 $mAh\,g^{-1}$. For the TiO_2 NP/SWCNT anode in Figure 5.11 (b), there is a much higher capacity decrease between the first and second cycled of about 379.97 $mAh\,g^{-1}$. As mentioned earlier this may be due to the reaction with residual hydrogen bonded H_2O molecules, or impurities, Li-ion trapping and the formation of an SEI layer around the SWCNTs. By the tenth cycle the capacity levels off at 254.63 $mAh\,g^{-1}$.

Figure 5.11 (c) and (d) shows the storage capacities determined for the current density range between 1 C and 10 C. For the TiO_2 NP anode, the discharge capacities determined were 76.67 $mAh\,g^{-1}$ at 1 C, 48.97 $mAh\,g^{-1}$ at 2 C, 36.29 $mAh\,g^{-1}$ at 3 C, 25.55 $mAh\,g^{-1}$ at 5 C and 14.48 $mAh\,g^{-1}$ at 10 C. For the TiO_2 NP/SWCNT anode, the discharge capacities determined were 134.13 $mAh\,g^{-1}$ at 1 C, 112.29 $mAh\,g^{-1}$ at 2 C, 101.36 $mAh\,g^{-1}$ at 3 C, 85.02 $mAh\,g^{-1}$ at 5 C and 65.07 $mAh\,g^{-1}$ at 10 C. In contrast the pure TiO_2 NP anode exhibits a relatively poor performance relative to the TiO_2 NP/SWCNT anode.

The long term effects of the Li-ions on the TiO_2 NP were investigated by determining their cycling and rate behaviours. Figure 5.12 (a) shows the cycling properties of both the TiO_2 NP and TiO_2 NP/SWCNTs for the first 100 cycles at 1 C. For the TiO_2 NP anode, the initial capacity decreases rapidly until the twentieth cycle after which the rate of decrease slows down. However, only the first two cycles of the TiO_2 NP/SWCNT anode show any sign of rapid decrease after which is a much slower decrease. After 100 consecutive cycles, the capacity retention of the TiO_2 NP is 21% its original value compared to that of the TiO_2 NP/SWCNT anode which is upwards of 59%. GC profiles shown previously indicate a larger capacity drop after the first cycle at 0.1 C than that at 1 C shown here. This is due to the Li-ions at 0.1 C having more access to the micropore structure and increasing the possibility to Li-ion trapping [155]. The increase in capacity retention at 1 C for the TiO_2 NP/SWCNT anode can be reasonably attributed to the increase in volume tolerance and capacitive properties provided by the SWCNTs.

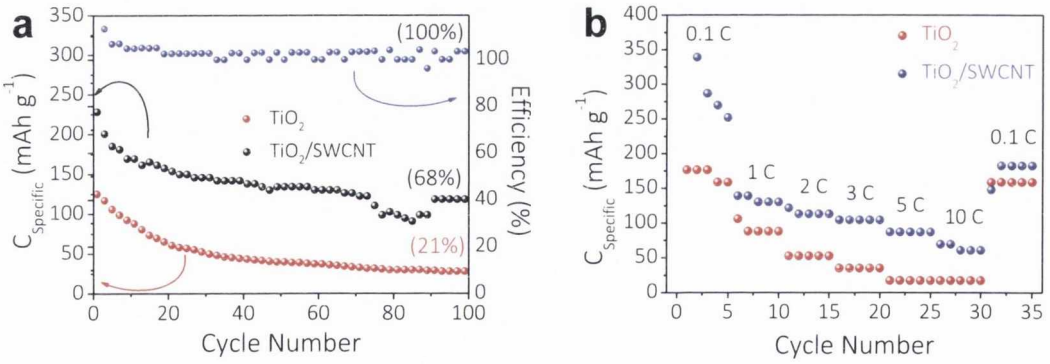


FIGURE 5.12: (a) The cycle performance and (b) of both the TiO_2 NP and NP/SWCNT anodes

The rate capabilities of both the TiO_2 NP and TiO_2 NP/SWCNT anodes are shown in Figure. 5.12 (b). Each of the anodes were tested at current densities of 0.1, 1, 2, 3, 5, 10 and 0.1 C for 5 cycles before changing. As expected, the TiO_2 NP/SWCNT anode shows a superior high rate capacity compared to that of the

TiO_2 NB anode. It is noteworthy that as the current density is switched back to its initial value of 0.1 C the discharge capacity 180 $mAh\,g^{-1}$ which corresponds to a value of x = 0.53.

To gain a better understanding of the processes at work in both the TiO_2 NP and TiO_2 NP/SWCNT anodes EIS was carried out on both. The spectra were taken an a sinusoidal potential of 10 mV between a frequency range of 1 mHz to 1 MHz. The resulting Nyquist plots are shown in Figure 5.13. As with the V_2O_5 cathode shown in 4, the TiO_2 anodes can be represented by a typical Randles equivalent circuit [242]. The series resistance, R_S for both anodes is 11 Ω as expected. Extrapolating the R_{CT}, shows that the addition of the conductive SWCNTs do reduce the value from 1390 Ω to 299 Ω reflecting the increased charge storage properties exhibited earlier. The Z_{CPE}'s exponent value increases from 0.77 to 0.80 reflecting the increased surface properties of the anode. This is reflected by the diminished semicircles evident in the spectra.

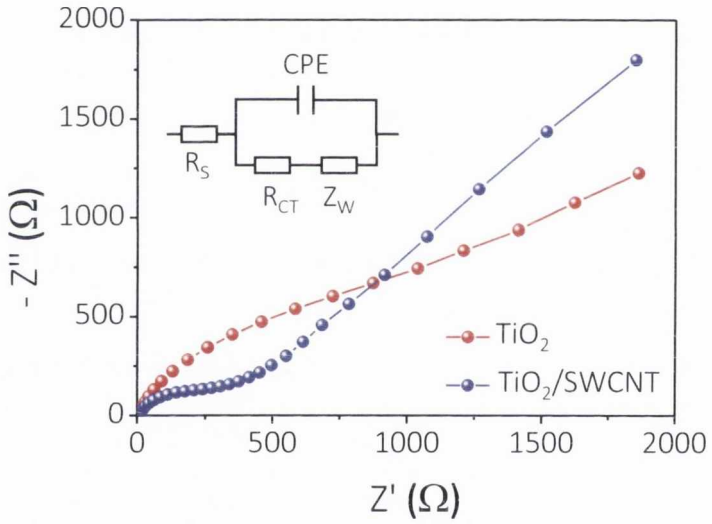


FIGURE 5.13: EIS spectrum of the TiO_2 NP anodes

5.3.4 Post Characterization

To assess the structure of the TiO_2 NP/SWCNT anode post cycling a series of SEM, EDX, XPS and XRD tests were carried out. After electrochemically cycling, the anode material for five cycles using CV, the anode was carefully removed from the cell and washed with IPA and Acetone to remove unwanted electrolyte. SEM images of the cycled TiO_2 NP/SWCNT anode are showed in Figure 5.14. The high

magnification SEM image in Figure 5.14 (b) shows the anode remains intact after cycling keeping its stable porous structure. The EDX maps in Figure 5.14 (c) shows the elemental distribution of C, Ti and O across the surface (see Figure 5.14 (a)). The SWCNTs and the TiO_2 NP remain relatively distributed throughout the anode.

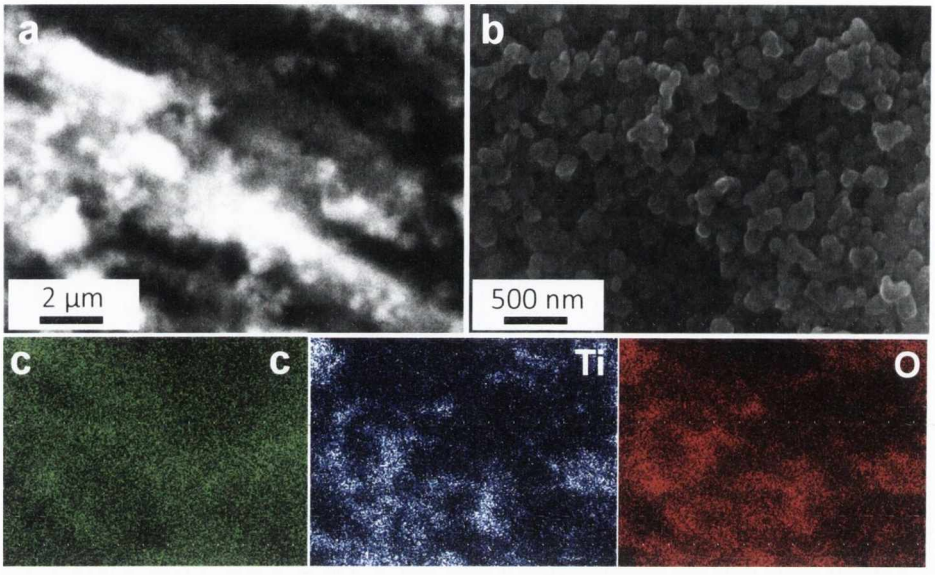


FIGURE 5.14: (a) Low magnification and (b) High magnification of the TiO_2 NP/SWCNT anode post cycling; and (c) the corresponding EDX maps.

Figure 5.15 (a) and (b) show the relative Ti 2p and O 1s core-level intensities for the electrochemically cycled TiO_2 NP/SWCNT anode. Similar to the fresh anode shown previously, the same 2:1 peak ratio of the Ti 2p 3/2 and 1/2 is present with an expected spin orbital splitting interval of 5.7 eV centred at binding energies of 458.6 eV and 464.4 eV. Also, the major O 1s peak is centred between 527 - 535 eV with the deconvoluted peaks corresponding to the chemical shifts associated with the bonding of O with the Ti, residual H_2O molecules and hydroxide groups. The peak ratio between the Ti and O remains at 1 : 2 in agreement with that expressed for the uncycled anode. However, the relative % of the O - Ti peak reduces from 76.6% to 67.8% from the total O 1s peak. This indicated contributions from other sources such as that from trapped ionic solvent species such as the $LiClO_4$ electrolyte or the formation of hydroxide based functional groups on the anode's surface. The corresponding XRD pattern shown in Figure 5.15 (c) shows a similar set of high intensity peaks centred at 11.6°, 17.1°, 21.6°, 24.1°, 24.6 and 27.7° referring to the {101}, {004}, {200}, {105}, {211} and {204} series of planes consistent with orthorhombic anatase phases of TiO_2 shown for the fresh anode (JCPDS files # 21-1272). An impedance spectrum of the electrochemically cycled TiO_2 NP/SWCNT anode was determined

at a potential of 10 mV between a frequency range of 1 mHz to 1 MHz. The relevant Nyquist plot shown in Figure 5.15 (d) shows a similar Randles profile as that shown in the fresh anode. However, the R_{CT} value increases from 298 (Ω) to 2500 (Ω) which reflects the initial decrease in capacity after the first cycle. This could possibly be attributed to the trapping of Li-ion reducing available intercalation sites at the SWCNTs.

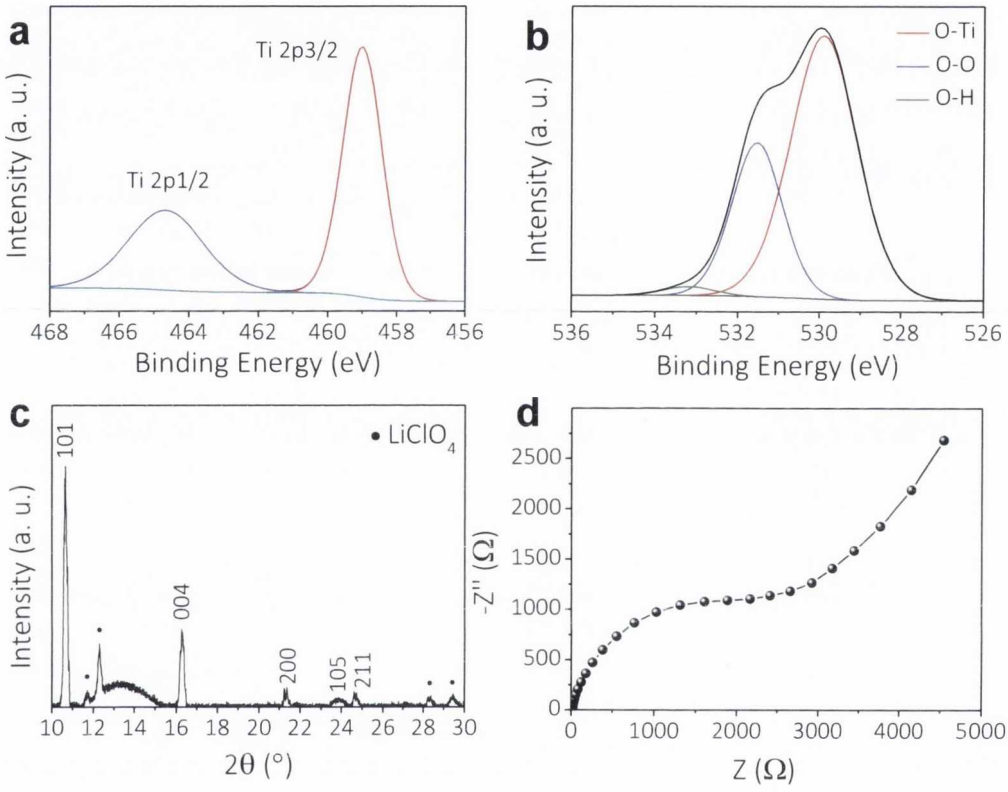


FIGURE 5.15: (a) Ti 2p and (b)) 1s core level XPS spectra, (c) XRD pattern and (D) Nyquist plot of the TiO_2 NP/SWCNT anode post electrochemical cycling.

5.4 Conclusion

In conclusion, a method was presented to produce a highly concentrated TiO_2 NP dispersion from commercially bought anatase TiO_2 powder in environmentally friendly solvents. These TiO_2 NP adopted a similar tetragonal structure than the of the unexfoliated power, however, the nanostructuring of the material had an overall positive effect on the properties of TiO_2. Furthermore, TEM, XPS and XRD analysis shows that the as-prepared TiO_2 NP showed high crystallinity, purity, a single Ti

oxidation state and lateral dimensions between 50 and 200 nm. Similar to the V_2O_5 NS demonstrated in Chapter 4, TiO_2 dispersions follow simple solution theory and have are most stable in solvents with Hildebrand solubility parameters between 23.0 - 27.5 $MPa^{0.5}$. However, the unexpected stability of H_2O based TiO_2 dispersions can be attributed to the hydrogen bonding of H_2O on specific sites on the TiO_2 particles. The complete retention in crystal structure suggests that the TiO_2 dispersion forms from the separation of individual particles from an agglomerate. To demonstrate the charge storage properties of the TiO_2 NP a series of Li-ion electrochemical experiments were carried out. A series of highly flexible, thin film anodes were fabricated by the ultrasonic spraying of the TiO_2 NP dispersion. Further addition of highly conductive SWCNTs worked to reduce the charge transfer resistance commonly exhibited by semiconducting TiO_2 as demonstrated by EIS analysis. CV showed a pair of well defined peaks for both the TiO_2 NP and TiO_2 NP/SWCNT anodes corresponding to the intercalation/deintercalation commonly exhibited by TiO_2. However, the shape of the whole TiO_2 NP/SWCNT anode indicated a more pseudocapacitive response as the SWCNTS act to increase the storage capacity and surface area. GC experiments show that while both the slurry and TiO_2 NP exhibit capacities corresponding to the intercalation of 0.5 Li per unit TiO_2 (147 $mAh\,g^{-1}$), the TiO_2 NP/SWCNT anode exhibits an initial discharge capacity upwards of 706.16 $mAh\,g^{-1}$ at 0.1 C. The TiO_2 NP/SWCNT anode also exhibited a 59% retention in capacity after 100 cycles. The improved electrochemical performance can be attributed to the nanostructuring of the TiO_2 coupled with the addition of SWCNTS conductive paths which increased both the surface Li^+ storage sites and electrical conductivity.

Chapter 6

Nanostructured Molybdenum Trioxide Composites

6.1 Introduction

Due to its impressive thermal and mechanical properties, the metallic element molybdenum is in widespread industrial use [399]. When used as an alloying element, it can enhance corrosion and wear resistance of the alloys [400]. This enhancement is due the formation of a thin layer of molybdenum oxide on the surface. Similar to other TMOs, the molybdenum oxides have a very interesting set of chemical and physical properties that have been successfully employed in applications such as gas sensing [401–404], catalysis [405–407], photochromism [408–411] and power storage [412, 413]. Specifically, the molybdenum oxides are showing huge promise in the future of pseudocapacitive devices [414]. The electrochemically active molybdenum oxide materials comprise of both MoO_2 and MoO_3, with MoO_3 proving to be the most desirable candidate. In addition to MoO_3's layered structure, the extended tunnels inside the MoO_6 octahedrons serve as highly conductive channels for mobile ion species. As a result, MoO_3 has shown to be both an effective material for rechargeable Li-ion batteries and supercapacitors coupled with its ability to act as either the active cathodic or anodic electrode.

Traditionally, MoO_3 is known to be able to intercalate a maximum of six Li-ions per unit formula giving it a theoretical capacity of 1117 $mAh\,g^{-1}$. As an anode material its experimental storage capacity can reach upwards of 1000 $mAh\,g^{-1}$ making it a suitable competitor for the modern graphite based anode device [415, 416]. However, as a cathode material, it reaches an average of 300 $mAh\,g^{-1}$ indicating much room for improvement if it is to become a competitor for the modern $LiCoO_2$ and $LiFePO_4$ based storage devices [417–419]. Much like other TMO materials, MoO_3

suffers from poor conductivities ($10^{-4} S\,cm^{-1}$) and cycling behaviour due to its inherent semiconducting nature and volume constraints. Therefore, it is necessary to improve the electrochemical properties of MoO_3 if it is to become a candidate for modern energy storage devices.

Of all the Molybdenum oxides, MoO_3 is the most widely produced on an industrial scale, sourced from molybdite ore [362] but more commonly synthesized from the roasting of molybdenum disulphide [420, 421],

$$2MoS_2 + 7O_2 \rightleftharpoons 2MoO_3 + 4SO_4 \tag{6.1}$$

It is commonly used in the manufacturing of pure Mo metal [421, 422]. MoO_3 has three basic polymorphs: $\alpha - MoO_3$ [344], $\beta - MoO_3$ [423] and $h - MoO_3$ [424] characterized by an orthorhombic, monoclinic and hexagonal structure respectively. Due to its thermodynamic stability, $\alpha - MoO_3$ has been selected as the strongest candidate over that of the other two phases. The orthorhombic structure consists of a series of two dimensional layers, each layer consisting of a pair of sub-layers, see Figure 6.1 [425]. These layers are formed by the corner sharing of the MoO_6 octahedrons along both the [100] and [001] directions with the pair of sub-layers bonded along the [010] direction. The layers themselves are then stacked along the [010] direction by means of weak van der Waal interactions giving an over all two dimensional layered structure. Much like V_2O_5, this layered structure is conducive to ion insertion and extraction allowing for application in energy storage and gas sensing.

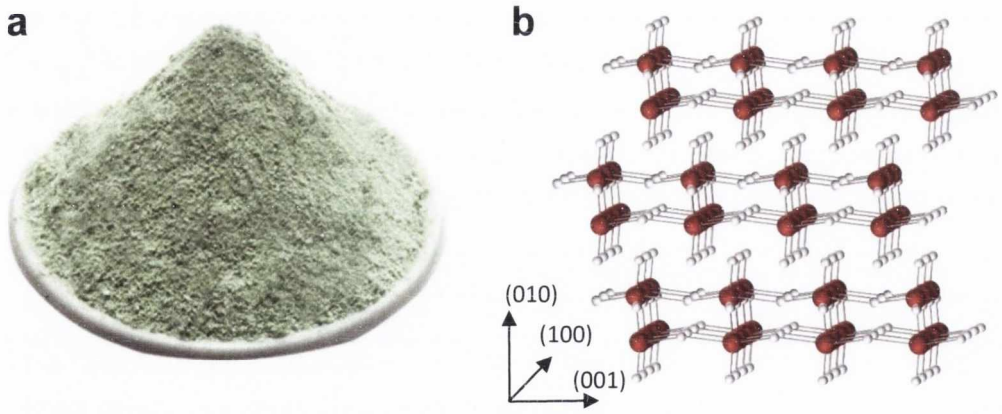


FIGURE 6.1: (a) Optical image showing unexfoliated MoO_3 powder (taken from [426]) and (b) schematic showing the corresponding layered structure.

As MoO_3 is layered, it is desirable to nanostructure the material as to exploit the potentially large surface areas and reduced diffusion lengths. Many methods to nanostructure MoO_3 have been reported in literature including hydrothermal synthesis [427–429], CVD [430, 431] and simple chemical methods [432–434] creating a wide range of different morphologies including nanotubes [435–437], nanorods [344, 424] and nanobelts [427, 428, 438]. However, much like V_2O_5, LPE is a highly advantageous method as it is both scalable and facile. It has been reported by Hanlon *et al.* that high quality MoO_3 nanobelts can be exfoliated and employed as a suitable thin film cathode material in commercial supercapacitors showing a capacitance upwards of 540 $F\,g^{-1}$ [210]. Other examples show how sonochemistry can be used to synthesize MoO_3 from pure Mo metal [439].

Similar to other layered compounds, MoO_3 undergoes a series of intercalation and deintercalation charge storage mechanisms. The Li^+ intercalation and deintercalation process into MoO_3 can be expressed by,

$$MoO_3 + xLi^+ + xe^- \rightleftharpoons Li_xMoO_3 \tag{6.2}$$

The theoretical capacity of Moo_3 is known to be 1117 $mAh\,g^{-1}$ corresponding to x = 6 per unit MoO_3. Like many other TMO materials MoO_3 suffers from poor conductivities and cycling properties and these need to be addressed.

To alleviate the semiconducting behaviour of a typical TMO material, it common to add conductive additives such as conductive polymers, nanotubes or graphene [440]. The work of Mendoza-Sanchez *et al.* showed how the addition of SWCNTs into layered $\alpha - MoO_3$ through vacuum filtration could improve the overall capacitance of the material [441]. The SWCNT act to provide a series of extra electronic states conducive to electron transfer across the electrode/electrolyte interface. Similarly, graphene has been shown provide the necessary electronic states to reduce the charge transfer resistance [442–444]. The work of Noerochim *et al.* showed how MoO_3/graphene free standing films could be fabricated by a rapid hydrothermal method [445]. These cathode materials exhibit a capacity of 291 $mAh\,g^{-1}$ at a current density of 100 $mA\,g^{-1}$ with a capacity retention of 59% after 100 cycles compared to that of a pure MoO_3 cathode (32%). Graphene, composed of a single layer of sp^2 hybridized carbon, has a continuous range of conductive bands with zero band gap making it an ideal composite material. It also benefits from a high chemical stability and a large surface area. As such, it is a highly versatile material having formed composites with a wide range of materials such as $LiFePO_4$ [446], SnO_2 [440] and NiO [447].

MoO_3 has been shown to form composites with a range of other non-carbon based materials. In particular, various sources have reported the electrochemical properties of mixed TMO composites such as that of MoO_3 with TiO_2 [448–450] or V_2O_5 [448, 451–453]. As shown previously, V_2O_5 shows a layered structure similar to that of MoO_3 conducive to Li-ion intercalation. V_2O_5 also has shown to produce cathodes with high capacity, enhanced cyclability and improved safety. The concept of a MoO_3/V_2O_5 composite material has been investigated as a possible Li-ion storage device. The work of Wei *et al.* has shown that V_2O_5 doped MoO_3 exhibited a storage capacity of 280.6 $mAh\,g^{-1}$ with a 60% retention in capacity after 50 cycles and a R_{CT} 1.6 times lower than that of pure MoO_3 [453]. Similarly, the work of Kim *et al.* used RF magnetron co-sputtered MoO_3 and V_2O_5 to produce thin film cathodes exhibiting a capacity retention of 69% after 70 cycles [452].

Herein, the LPE method is used to produce a series of MoO_3 composite materials. High quality MoO_3 nanobelts were synthesized showing both a thin structure and a moderate aspect ratio. Both a graphene and V_2O_5 based composite cathodes were fabricated and the resulting capacities were compared to that of pure MoO_3 nanobelts. Combining semiconducting MoO_3 with materials such as graphene or V_2O_5 worked to both improve the resulting storage capacities and increases the overall lifetime characteristics of the MoO_3.

6.2 Experimental

Synthesis - MoO_3 nanobelts were exfoliated by the method described by Hanlon *et al.* The dispersion consisted of 0.1 $mg\,ml^{-1}$ MoO_3 powder (99.99%, Sigma-Aldrich) in 50 ml IPA. The dispersion was then placed in a temperature controlled reaction vessel (10°C) and sonicated at 20 kHz using an ultrasonic horn (Fisherbrand) for 8 hr at 34 W. The resultant dispersion was then centrifuged (Heraeus Multifuge X1 centrifuge) at a rate of 1000 rpm for 1 hr and 40 ml of the supernatant was decanted and stored in a bottle. Similarly, the MoO_3/graphene nanocake dispersion was exfoliated by LPE using the ultrasonic horn. A dispersion of 0.2 $mg\,ml^{-1}$ graphite flakes and 0.04 $mg\,ml^{-1}$ MoO_3 powder was simultaneously sonicated at 20 kHz and 34 W for 8 hr with the temperature kept at a constant 10° C. The dispersion was then centrifuged at a rate of 3000 rpm for 1 hr and 40 ml of the supernatant was decanted and stored in a separate bottle. The resultant yields of MoO_3/graphene nanocakes as a function of initial concentrations of both graphite flakes (0.04 - 0.2 $mg\,ml^{-1}$) and MoO_3 powder (0.04 - 0.2 $mg\,ml^{-1}$) was also determined. The sonication process

was repeated several times to provide adequate quantities of each dispersion for the succeeding experiments. The concentration of the MoO_3 nanobelt and nanocake dispersions were determined by vacuum filtration through an alumina filter membrane (Whatman, 0.02 μm pore diameter). A separate dispersion of SWCNT was made by mixing 0.1 $mg\,ml^{-1}$ of P3-SWCNTs (99.99%, Carbon Solutions Inc.) with 50 ml IPA and sonicated at 20 kHz for 1 hr. Also, a dispersion of V_2O_5 NS was sonicated in water by the method described in chapter 5.

Characterization - Scanning electron microscopy (SEM) was performed using a Zeiss Ultra Plus (Carl Zeiss, Germany). Transition electron microscopy (TEM), scanning transition electron microscopy (STEM) and energy dispersive x-ray spectroscopy (EDX) were performed using a Titan high-resolution TEM (HRTEM) at 300 kV (FEI, USA). Both the MoO_3 nanobelt and nanocake dispersions were drop-cast onto holey carbon grids (Agar Scientific, UK) and allowed to dry overnight. The MoO_3 nanobelt and nanocake dimensions were statistically analysed on TEM by measuring the longest axis of the particle and assigning it as the length followed by measuring the axis perpendicular to this at its widest point and assigning it as the width. Optical spectroscopy was done using a Cary 6000i UV-Vis absorbance spectrometer (Agilent, USA). Each dispersion was diluted by a factor of ten with respect to the dispersing solvent to prevent over-scattering of the incident light beams. To further clarify the chemical compositions of the as-prepared MoO_3 nanobelt and nanocake, X-ray photoelectron spectroscopy (XPS) (CLAM 4 MCD, VG Microtech, UK) was employed using a 200 W unmonochromated Mo X-ray excitation source (1253.6 eV) with samples supported on silicon substrates. All binding energies were referenced to that of aliphatic carbon at 284.8 eV. Crystal structure of the MoO_3 nanobelt and nanocake materials were studied on a X-ray diffraction (XRD) spectra (D5000 powder diffractometer, Bruker, USA) with a monochromatic Mo K radiation source (λ = 0.07107 nm) and a secondary monochromator with samples supported on borosilicate glass slides. Brunauer-Emmett-Teller (BET) analysis was done using a Nova 4200e surface area analyser (Quantichrome, USA).

Electrode Preparation - MoO_3 nanobelt, nanocake and V_2O_5 composite thin film cathodes were fabricated by the ultrasonic spraying of the dispersed MoO_3 nanobelt, nanocake and V_2O_5 on aluminium foil (20 μm, 18 mm diameter) pre-treated with an adhesive polyethyleneimine (PEI) layer (30%, Alfa Aesar). Each MoO_3 dispersion was diluted by a factor of two to allow for better flow through the prism ultrasonic sprayer (Ultrasonic Systems Inc., USA) and 40 ml of the diluted dispersion was placed in the sprayers syringe (100 ml). During the spraying, the aluminium substrate was heated to 120° C to allow the H_2O and IPA to evaporate. The resultant

cathodes were then transferred to an argon filled glove box after drying overnight at 100° C. The mass of the active material was determined by weighing the substrate before and after spraying. For the MoO_3 nanocake cathode, the nanocake dispersion was further mixed with 0.1 $mg\,ml^{-1}$ SWCNTs in a mass ratio of 95 : 5. The blended dispersion was then diluted down by a factor of two and allowed to mix for one hour using a magnetic stirring bar. In the case of the MoO_3/V_2O_5 composite, three cathodes were fabricated using different weight % of V_2O_5 relative to the MoO_3, namely 25%, 50% and 75%. Each of these will be referred to as the MV25, MV50 and MV75 composite cathodes respectively.

Electrochemical Characterization - The electrochemical behaviours of the electrodes were evaluated using the half-cell configuration with the active material as the working electrode, Li foil as the counter and reference electrodes, and 1 M lithium perchlorate ($LiClO_4$) dissolved in propylene carbonate (PC) (1 M $LiClO_4$/PC) as the electrolyte. Cyclic voltammetry (CV), galvanostatic cycling (GC), and electrochemical impedance spectroscopy (EIS) tests were performed on a VMP-300 potentiostat (Bio-Logic, France). CV was recorded at 0.05 $mV\,s^{-1}$ with a potential range 1 V - 4 V (vs. Li/Li^+). GC were performed at different current densities from 20 to 1000 $mA\,g^{-1}$ within a potential window of 1 V - 4 V (vs, Li/Li^+). The cycling performance for each cathode was conducted at 100 $mA\,g^{-1}$ for 100 cycles. EIS was measured at E_{OCP} with a 10 mV amplitude and a frequency range of 1 mHz - 1 MHz.

6.3 Results

6.3.1 Molybdenum Trioxide Nanobelts

6.3.1.1 Synthesis of the Nanobelt Colloid

Unlike TiO_2 and V_2O_5, which form nanoparticles and nanosheets respectively, the LPE of MoO_3 tends to form a series of two dimensional nanobelts similar to that shown in literature [427, 428, 438]. These nanobelts possess a flat structure in which the longest axis along the basal plane tends to be much larger than that of the longest perpendicular width. As the purpose of this chapter is to determine the electrochemical properties of a series of MoO_3 composites, it is beneficial to determine the electrochemical properties of the pure MoO_3 nanobelts for comparative purposes.

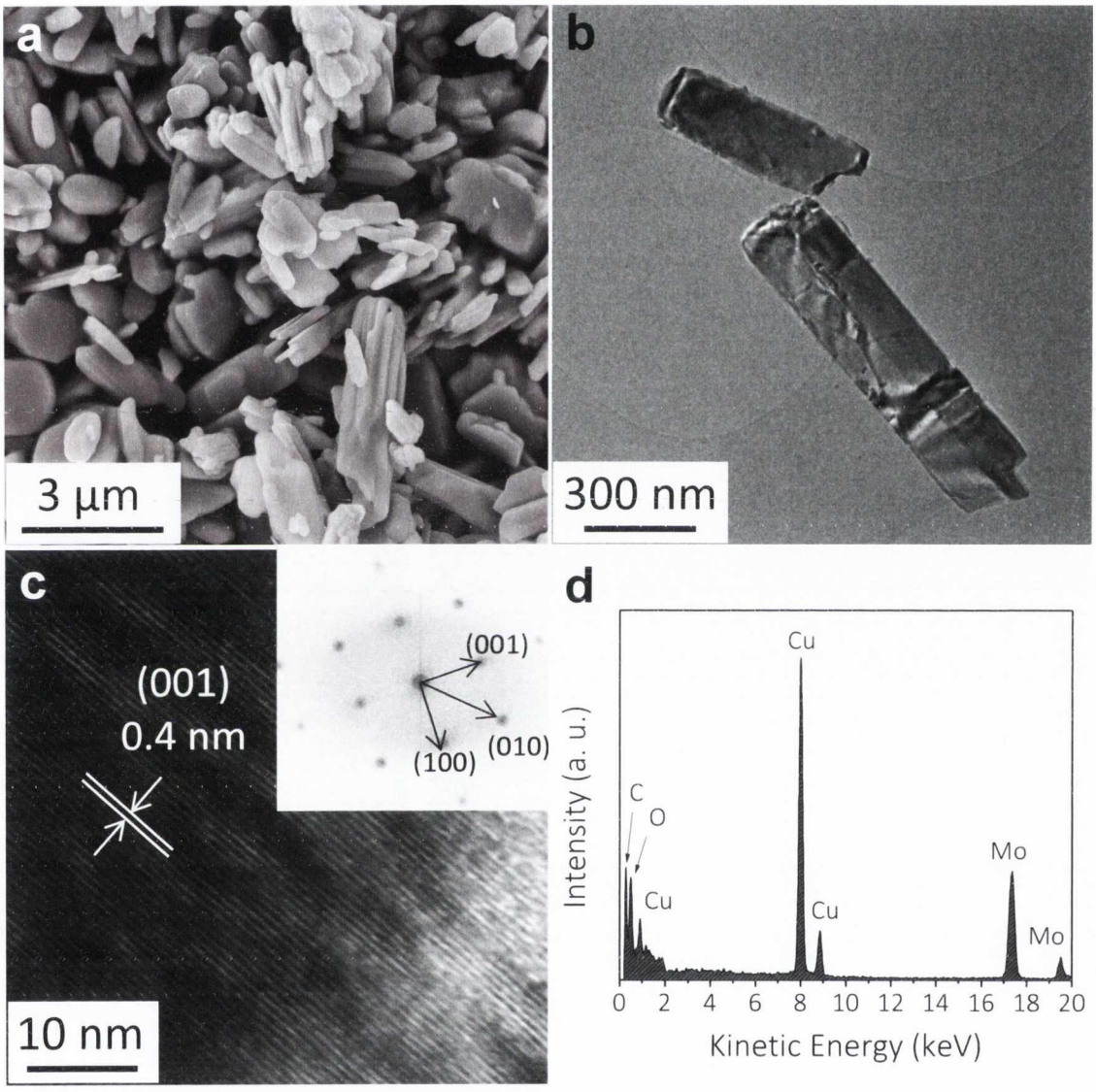


FIGURE 6.2: (a) TEM images of the (a) MoO_3 powder and (b) a representative pair of exfoliated MoO_3 NB; (c) HRTEM image and (inset) the corresponding FFT pattern showing the highly crystalline structure of MoO_3 NB. (d) MoO_3 NB EDX spectrum.

As mentioned earlier, the work of Hanlon *et al.* showed how MoO_3 nanobelts can be efficiently exfoliated in solvents possessing a Hildebrand solubility parameter in the region of 21 $MPa^{1/2}$ [210]. As this is consistent with classical solubility theory, it was decided that IPA would be the dispersing agent for MoO_3. IPA, as well as having a Hildebrand solubility parameter of 23.8 $MPa^{1/2}$, is environmentally benign, has a low boiling point and is relatively inert. MoO_3 powder consists of a series of large flakes on the order of 1 - 3 μm, as shown in Figure 6.2 (a). It is quite evident that these flakes are relatively thick and an efficient method of exfoliation is required to access as much of the layered surface area as possible. A predetermined concentration of pure MoO_3 powder was mixed with IPA and exfoliated using the ultrasonic horn at 20 kHz for 8 hr. The process is kept at a constant power of 34 W at 10° C using a circulation cooling system. Similar to other two dimensional materials, applying the high frequency sonic energy will cause cavitations to exist between the individual sheets separating them and forming a series of thin nanobelts. The resultant dispersion was then centrifuged at 1000 rpm for 1 hr to remove any unexfoliated flakes. The supernatant was collected and herein named "MoO_3 NB". To analyse the morphology of the MoO_3 NB, the dispersions were dropcast onto a holy carbon grid and underwent TEM analysis. A representative TEM image of a pair of MoO_3 NB is shown in Figure 6.2 (b). In general the flakes have lateral dimensions upwards of 1 μm with a perpendicular width several factors smaller.

Figure 6.2 (c) shows the HRTEM image of a MoO_3 NB with its corresponding FFT pattern in the inset. The HRTEM image clearly shows a series of crystalline fringes with a inter-planer distance of 0.40 nm referring to the {001} set of planes. Similarly, a bright spot representing the {001} set of planes is evident in the FFT pattern. Furthermore a bright spot 90° away from the {001} spot refers to the {100} set of planes exhibiting an inter-planer distance of 0.37 nm. Both of these sets of planes describe the sub-planer structure of an individual MoO_3 sheet. A third bright spot 45° relative to the other two can be indexed to the {010} set of planes. These set of planes have an inter-planer spacing of 0.25 nm and refers to the bilayer structure along the {010} direction. These values are consistent with that of the orthorhombic structure of the $\alpha - MoO_3$ [152]. Figure 6.2 (d) shows the corresponding EDX pattern. As expected, both the Mo and O peaks are present at a 1 : 3 atomic ratio. The Cu and C peaks can be attributed to the copper TEM grid.

XPS and ESCA were employed to further understand the chemical composition of the MoO_3 NB. The samples were prepared by ultrasonically spraying the dispersion onto clean, dry Si substrates. Figure 6.3 (a) shows the deconvoluted XPS spectra indicating the major Mo 3d peaks. As d peaks tend to undergo spin orbital splitting

in the presence of X-rays, the Mo 3d core level exhibits two split peaks at 236.1 eV and 233.0 eV [454]. These peaks are attributed to the binding energies of the Mo(VI) 3d 3/2 and 3d 5/2 core levels respectively. The integral areas calculated between the two doublets are in a 2 : 3 ratio with an energy interval, Δ_{so} = 3.15 eV consistent with Mo (VI) d orbital [233]. Traditionally, Mo metal has a binding energy in the region of 228.0 eV for the 3d 5/2 peak [455]. However, the chemical shift of the peak is indicative of $\tilde{3}$ electron transfer consistent with that of the oxide component of MoO_3.

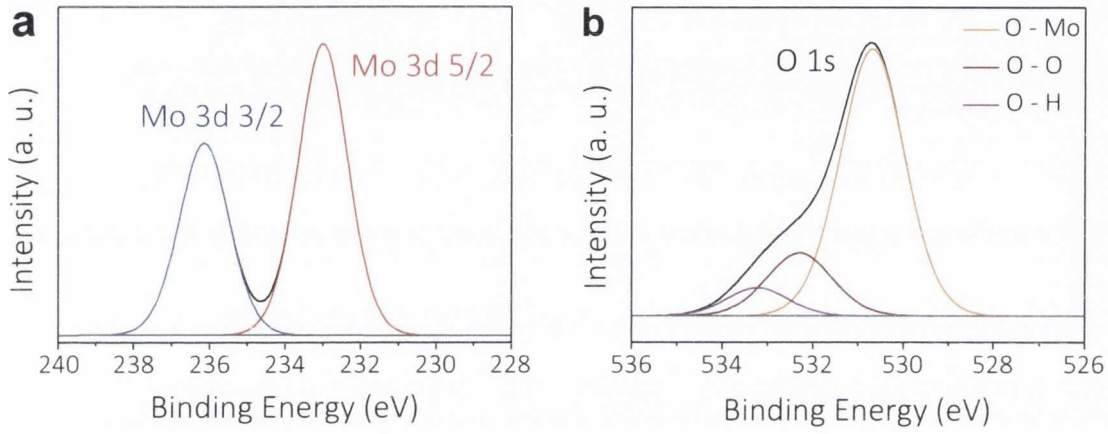


FIGURE 6.3: Deconvoluted XPS spectra of MoO_3 NB showing both the major (a) Mo 3d and (b) O 1s oxidation states.

Figure 6.3 (b) shows the deconvoluted O 1s peak situated between 528 eV and 535 eV. The strong intensity peak at 530.6 eV can be attributed to the binding between Mo and O in the metal oxide, agreeing with the chemical shift exhibited by the Mo 3d peaks shown previously. The remaining smaller peaks at 533.2 eV and 532.3 eV can be attributed residual water molecules bound to the MoO_3 NB due to hydrogen bonds and from possible hydroxyl groups respectively.

From the MoO_3 NB dispersion, the distribution of particle lengths was determined by statistical TEM analysis of a dropcast sample onto a holy carbon grid. Figure 6.4 (a) shows the distribution of the particle length of the longest axis over a series of 100 MoO_3 NB. Most particles are relatively long but the majority remain below 1 μm in length of the longest axis. The average length of a MoO_3 NB was determined to be 0.82 $\pm$ 0.47 μm. Taking the width of the MoO_3 NB as the longest width perpendicular to the longest length into account, the aspect ratio of the same 100 particles was determined and can be seen in Figure 6.4 (b). Most of the MoO_3 NB

have aspect ratios between 1.5 and 4 with a few reaching upwards of 10. The average aspect ratio was determined to be 3.54 ± 2.03 much smaller that that determined by other methods [344, 439]

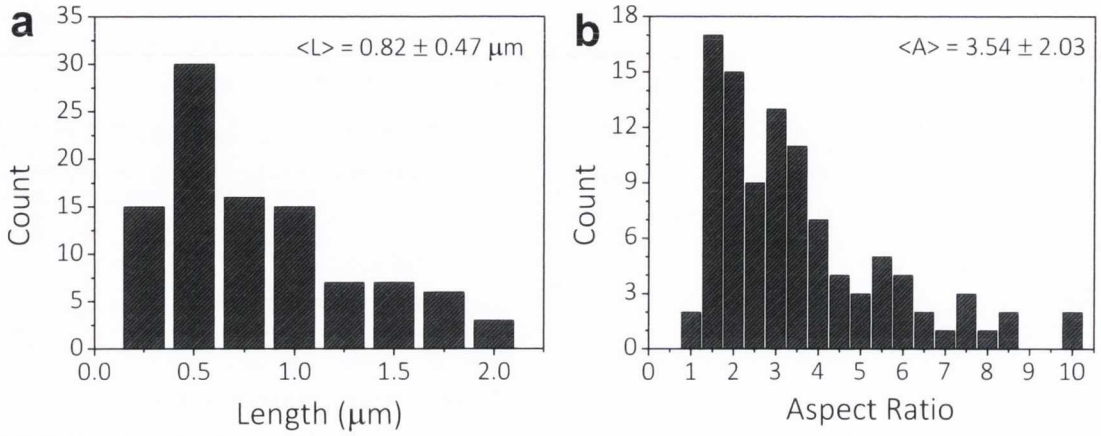


FIGURE 6.4: (a) Length and (b) aspect ratio histograms of the MoO_3 NB.

The MoO_3 NB dispersion was ultrasonically sprayed onto a machined glass substrate and underwent XRD analysis in order to ascertain the crystal structure of the NB. For comparative purposes, the XRD pattern of the commercial powder was also measured. Figure 6.5 shows the XRD patterns for both the pure MoO_3 powder and MoO_3 NB. Both samples conform to the orthorhombic phase of $\alpha - MoO_3$ for which the space group is Pbnm (JCPDS no. 05-0507) [344].

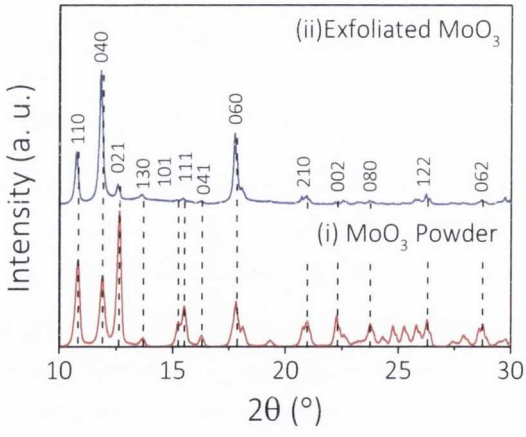


FIGURE 6.5: XRD of the MoO_3 NB cathode.

A series of {0k0} peaks are evident in both cathode materials where k = 2, 6, 8 centred at 11.8°, 17.7° and 25.4° respectively along with a series of non-{0k0} planes.

However, the exfoliated MoO_3 NB possess more intense {0k0} peaks than that of the non {0k0} ones. This indicates that the MoO_3 NB possess a strong crystalline structure and are preferentially stacked along the direction perpendicular to the basal planes. The lattice parameters calculated from the {0k0} peaks of the MoO_3 NB are a = 0.39 nm, b = 1.4 nm and c = 0.37 nm [456]. In order to determine how much surface area the MoO_3 NB has, a BET isotherm was measured for a sample of filtered MoO_3 NB. The surface area of the cathodic material was determined to be 200 $m^2\ g^{-1}$

6.3.1.2 Cathode Fabrication

Under optimized conditions set out by Hanlon, several hundred ml of MoO_3 NB dispersion was exfoliated in IPA and stored in a sealed bottle for the succeeding experiments [210]. A series of thin film cathodes were fabricated by ultrasonically spraying the dispersion directly onto thin Al substrates. The Al substrates were pretreated with adhesive PEI and kept at a constant temperature of 120 °C throughout the spraying procedure [337]. The dispersion was diluted by a factor of two with IPA before spraying to allow better flow of the material thought the ultrasonic spraying system. Simultaneously, a separate sample was sprayed onto a Si substrate, allowed to dry overnight at 100° C, and then were subjected to SEM and EDX analysis. Figure. 6.6 (a) shows a SEM image of a typical MoO_3 NB cathode surface. The MoO_3 NB form a stacked system with a highly porous structure exhibiting a large active surface area. The high magnification SEM image in Figure 6.6 (b) shows a specific mesopore on the order of 500 nm with a series of micropores on its inner surface. Compared to that of traditional bulk unexfoliated MoO_3, the nanostructured electrode consists of many channels conducive to efficient Li-ion transport

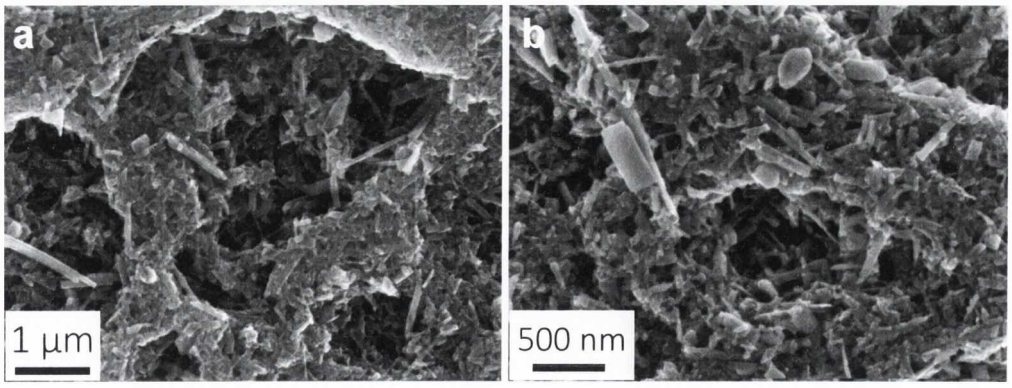


FIGURE 6.6: (a) Low and (b) high magnification SEM images of the MoO_3 NB cathode.

and diffusion.

6.3.1.3 Electrochemical Characterization

After the thin film MoO_3 NB cathodes were ultrasonically sprayed on Al substrates by the method described above, they were dried overnight at 100° C and transported to an Ar filled glove box. The electrochemical properties of the sprayed MoO_3 NB cathodes were evaluated as a half cell configuration using pure Li foil as both the counter and reference electrodes.

CV was initially employed to study the electrochemical properties of the $MoO3$ NB cathode. Figure 6.7 shows the first and tenth CV cycles of the MoO_3 NB cathode at a scan rate of 0.05 $mV\,s^{-1}$ with a potential window between 1 V and 4 V. The major cathodic peak located at a potential of 1.5 V during the first negative scan can correspond to the intercalation of the Li-ions into the MoO_3 NB. The reverse scan shows a minute peak at a potential of 2.0 V referring to the corresponding deintercalation process.

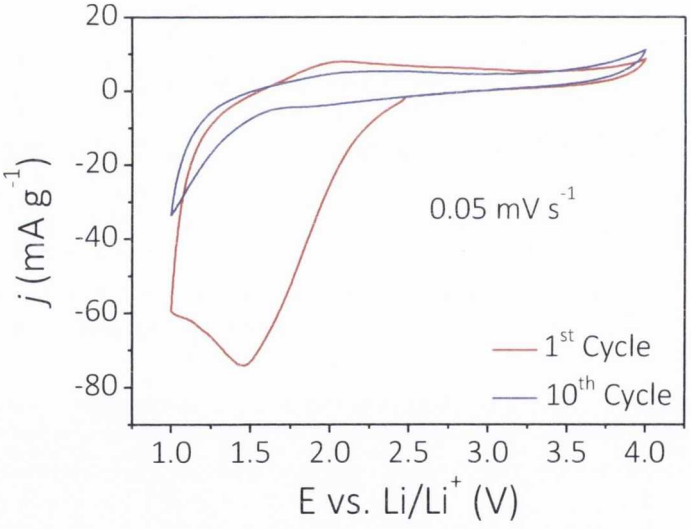


FIGURE 6.7: CV of the MoO_3 NB cathode at a scan rate of 0.05 $mV\,s^{-1}$.

It is reported in literature that not only can Li-ions intercalate between individual sheets but also into the MoO_6 octahedron intra-layers [152, 418]. The work of Li *et al.* suggests that a both intercalation and deintercalation processes should contain a pair of peaks corresponding to the intercalation into both the inter- and intra-layer spacings[418]. Li also suggests that the decrease in peak intensity for one

of the peaks can be reasonably attributed to the intercalation of Li-ions into the intra-layer spacings of the MoO_6 triggering an irreversible phase transition. Similarly, the reduction of the peaks after consecutive cycles further suggests this similar to Li. However, as the peaks present in Figure 6.7 are singular they can be reasonably be attributed to intercalation of Li-ions into the intra-layer spacings. As the amount of layers in each particle is reduced intercalation processes may be dominated by more surface sensitive possesses such as surface pseudocapacitance. The continued charge storage is a balance between intercalation into the thin layers coupled and the surface pseudocapacitance.

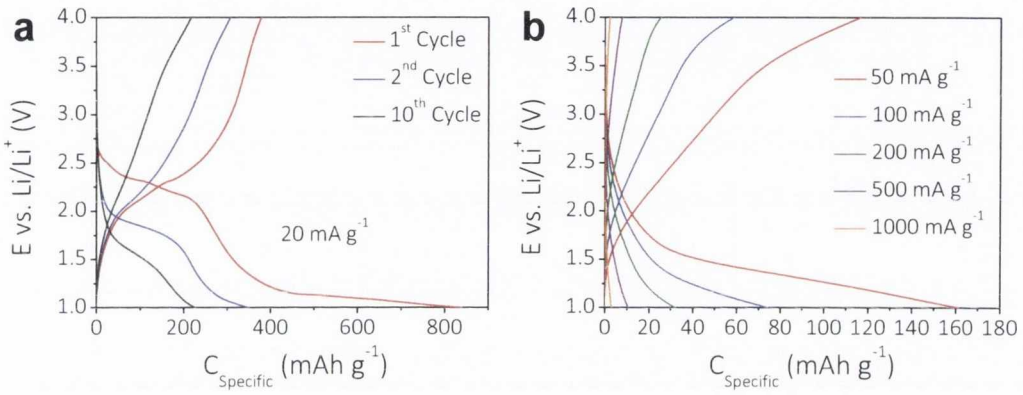


FIGURE 6.8: (a) First, second and tenth GC cycles at a current density of 20 $mA\,g^{-1}$ and (b) first GC cycles between the current density range of 50 $mA\,g^{-1}$ to 1000 $mA\,g^{-1}$ for the MoO_3 NB cathode.

To shed more light on the above electrochemical processes and to determine the capacities of the MoO_3 NB cathode, a series of GC measurements were carried between the potential windows of 1 V and 4 V. Figure 6.8 (a) shows the first, second and tenth GC curves for the MoO_3 NB cathode at a current density of 20 $mA\,g^{-1}$. A pair of partial plateau regions can be either observed at potentials of 2.25 V and 1.51 V in the first discharge profile, possibly referring to the intercalation of the Li-ions into the inter- and intra-layer spacings of the MoO_3 NB. These plateau regions seem to diminish as cycling continues. Specifically, the plateau at 1.5 V diminishes heavily, possibly indicating intercalation into the intra-layer spacings. However, succeeding cycling show a severely diminished capacity, highlighting the poor cycling properties of the MoO_3 NB as a result of its semiconducting behaviour and Li-ion trapping in the intra-layer spacings. The initial discharge capacity is 840.04 $mAh\,g^{-1}$, with the second and tenth cycles showing 350.35 $mAh\,g^{-1}$ and 227.76 $mAh\,g^{-1}$ respectively corresponding to x = 4.5, x = 1.86 and x = 1.20 from equation 6.2. Figure 6.8 (b) shows the relative storage capacities for the MoO_3 NB cathode at current densities between 50 $mA\,g^{-1}$ and 1000 $mA\,g^{-1}$. After initial activation, the capacities remain very low

with 162.67 $mAh\,g^{-1}$ at 50 $mA\,g^{-1}$, 57.42 $mAh\,g^{-1}$ at 100 $mA\,g^{-1}$, 23.49 $mAh\,g^{-1}$ at 200 $mA\,g^{-1}$, 9.57 $mAh\,g^{-1}$ at 500 $mA\,g^{-1}$ and 4.78 $mAh\,g^{-1}$ at 1000 $mA\,g^{-1}$. The lower capacities at higher current densities could indicate that most of the charge storage is pseudocapacitive in origin.

To investigate the long term cycling properties of the MoO_3 NB, fresh cathodes were subjected to rate capability and cycling profiles. The rate capability of the MoO_3 NB cathode was determined for a range of current densities between 20 $mA\,g^{-1}$ and 1000 $mA\,g^{-1}$ and the switched back to 20 $mA\,g^{-1}$, see Figure 6.9 (a). Similar to the GC profile shown previously, the initial discharge capacities reduce drastically at 20 $mA\,g^{-1}$ after successive cycles (hence the initial discharge is omitted for clarity). Increasing the current density above 20 $mA\,g^{-1}$ acts to reduce the capacities. After the current density is switched back to 20 $mA\,g^{-1}$, the capacity retains a low value at 138.7 $mAh\,g^{-1}$ compared to that of the stable 10th cycle (350.35 $mAh\,g^{-1}$) from the GC in Figure 6.8 (a).

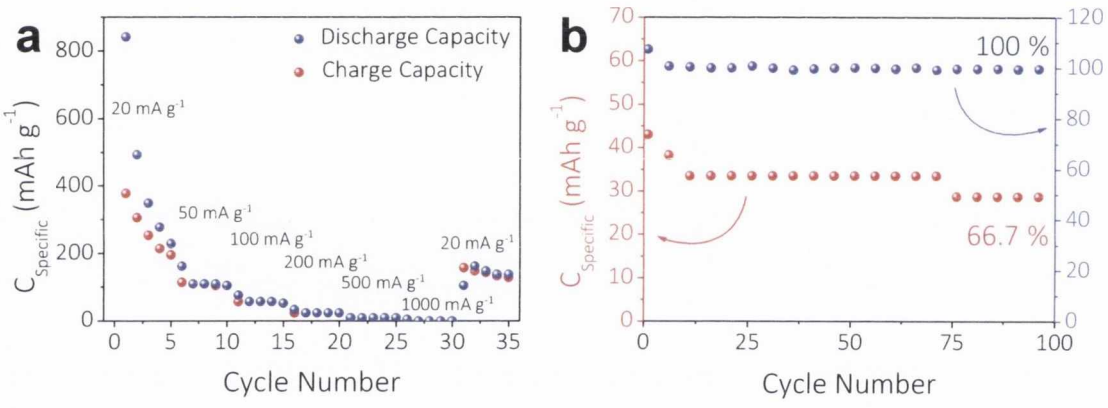


FIGURE 6.9: (a) The rate performance and (b) the cycle performance at at a current density of 100 $mA\,g^{-1}$ of the MoO_3 NB cathode.

Figure 6.9 (b) shows the cycling behaviour of the MoO_3 NB cathode at a current density of 100 $mA\,g^{-1}$. At a higher current density than that previously shown at 20 $mA\,g^{-1}$, the capacity retention was 24.5% its initial value after ten cycles due to the possible trapping of Li-ions in the intra-layer spacings of the MoO_3 NB matrix. However, repeated cycling at 100 $mA\,g^{-1}$ shows an over all decrease in capacity of about 66.7% after 100 cycles consistent with literature values [344, 418]. This could be due to the lack of energy required to intercalate inside the MoO_6 octahedrons. Consequently, the Coulombic efficiency of the MoO_3 NB cathode at 100 $mA\,g^{-1}$ is 100%.

EIS was used to further determine the kinetic properties of the MoO_3 NB at a potential of 10mV between 1 mHz and 1 MHz. Figure 6.10 shows the impedance spectrum of the MoO_3 NB cathode. As expected, the spectrum shows typical behaviour for that of a Randles circuit. The intercepts of the semicircle correspond to the series resistance, R_S, and the charge transfer resistance, R_{CT}, The value of R_S = 11 Ω consistent with the values obtained in previous experiments and the value of R_{CT} = 850 Ω reflects the poor conductive properties commonly associated with MoO_3. As expected for a highly porous electrode, the CPE exponent is 0.74 reflecting the non ideal capacitive behaviour of the cathode.

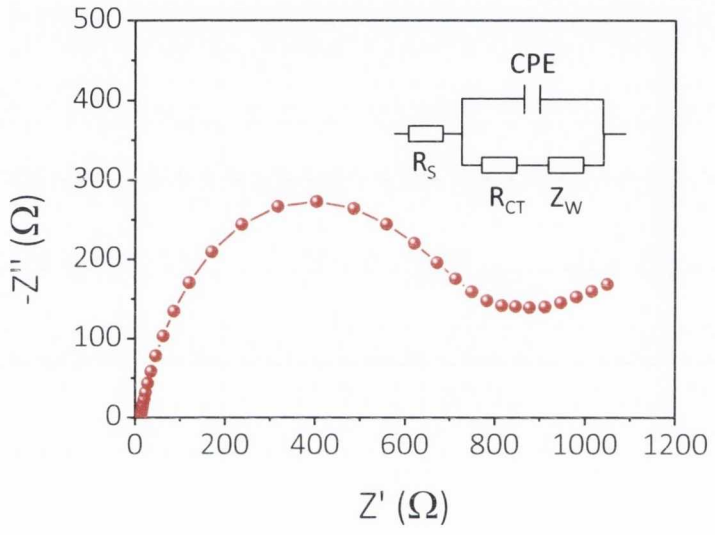


FIGURE 6.10: EIS of the MoO_3 NB cathode.

6.3.2 Molybdenum Trioxide/Graphene Nanocakes

6.3.2.1 Synthesis of the Nanocake Colloid

The fabrication of a composite electrode, such as that described in Chapters 4 and 5, involves the LPE of an individual material followed by mixing with a stable dispersion of SWCNTs. However, the synthesis of MoO_3/graphene nanocakes is unique in that both precursor materials underwent LPE in the same solvent simultaneously. In previous reports it has been shown that both MoO_3 and graphite can be efficiently exfoliated in IPA [210, 457]. In the previous section it was shown how MoO_3 formed a stable dispersion with IPA. Therefore this solvent remained as the solvent of choice for the synthesis of the MoO_3/graphene nanocakes. A pre-determined mass of both

graphite flakes and MoO_3 was added to IPA and sonicated at 20 kHz for 8 hr using an ultrasonic horn. As with the MoO_3 NB, the ultrasonic horn operated at 34 W and was kept at a constant temperature of 10° C using a circulation cooling system. After sonication the dispersion was centrifuged at 3000 rpm for 1 hr and the supernatant was decanted. The resultant nanocake dispersion was termed "MoO_3 NC". The dispersion remained stable against aggregation for a period of six months. The experiment was repeated several times to provide a large quantity for future processing. TEM was used to assess the morphological properties of the MoO_3 NC. The MoO_3 NC dispersion was dropcast onto holy carbon grids and allowed to dry overnight before undergoing analysis.

Figures 6.11 (a) and (b) shows a representative examples of MoO_3 NC. This unique structure is composed of a large sheet of multi-layered graphene, with a lateral dimension of about 1 μm, dotted with a series of small MoO_3 sheets with lateral dimensions below 50 nm. The appearance resembles that of a cake or chocolate chip cookie. It was seen in section 6.3.1 that the exfoliated MoO_3 NB had lateral dimensions between upwards of 1 μm. Therefore, simultaneous exfoliation with graphite works to decrease the resultant size of the MoO_3 sheets and hence may provide a larger surface area for Li-ion storage. It is also interesting to note that the particles are in sheet formation as opposed to the belt formation of the MoO_3 NB. A HRTEM image of a few MoO_3 nanosheets present on a graphene sheet is shown in Figure 6.11 (c). Crystal structure comparable to that exhibited by the MoO_3 NB in Figure 6.2 (c) is observable indicating that the MoO_3 retains its orthorhombic crystal structure in the NC. The corresponding FFT pattern is shown in the inset. As with the NB, both the {001} and the {100} set of planes are present corresponding to the inter-layer spacings of 0.40 nm and 0.37 nm of the basal plane. Similarly, the {010} peak present refers to the sub-inter-layer spacing of 0.26 nm [152, 445]. The EDX pattern shown in Figure 6.11 (d) shows the presence of both Mo and O peaks as expected. Investigation into the peak intensities determined the atomic ratio to be 1 : 3 as expected for MoO_3. The Cu and C peaks are in reference to the holey carbon grids. A representative HAADF STEM image if shown in Figure 6.11 (e). Similar to the bright field image shown above, the graphene and MoO_3 sheets can be clearly distinguished due to their relative brightnesses. However, slight variations in the brightness of the graphene sheets indicate a varying number of layers across the whole sheet itself. Figure 6.11 (f) similarly shows the elemental distribution of the Mo, O and C across an individual NC. As expected the whole sheet is covered with C from the graphene with high intensity points of Mo where the MoO_3 nanosheets are present. However, the O distribution is more widespread across the NC indicating that, not only is O present in MoO_3, it is also present on the surface of the

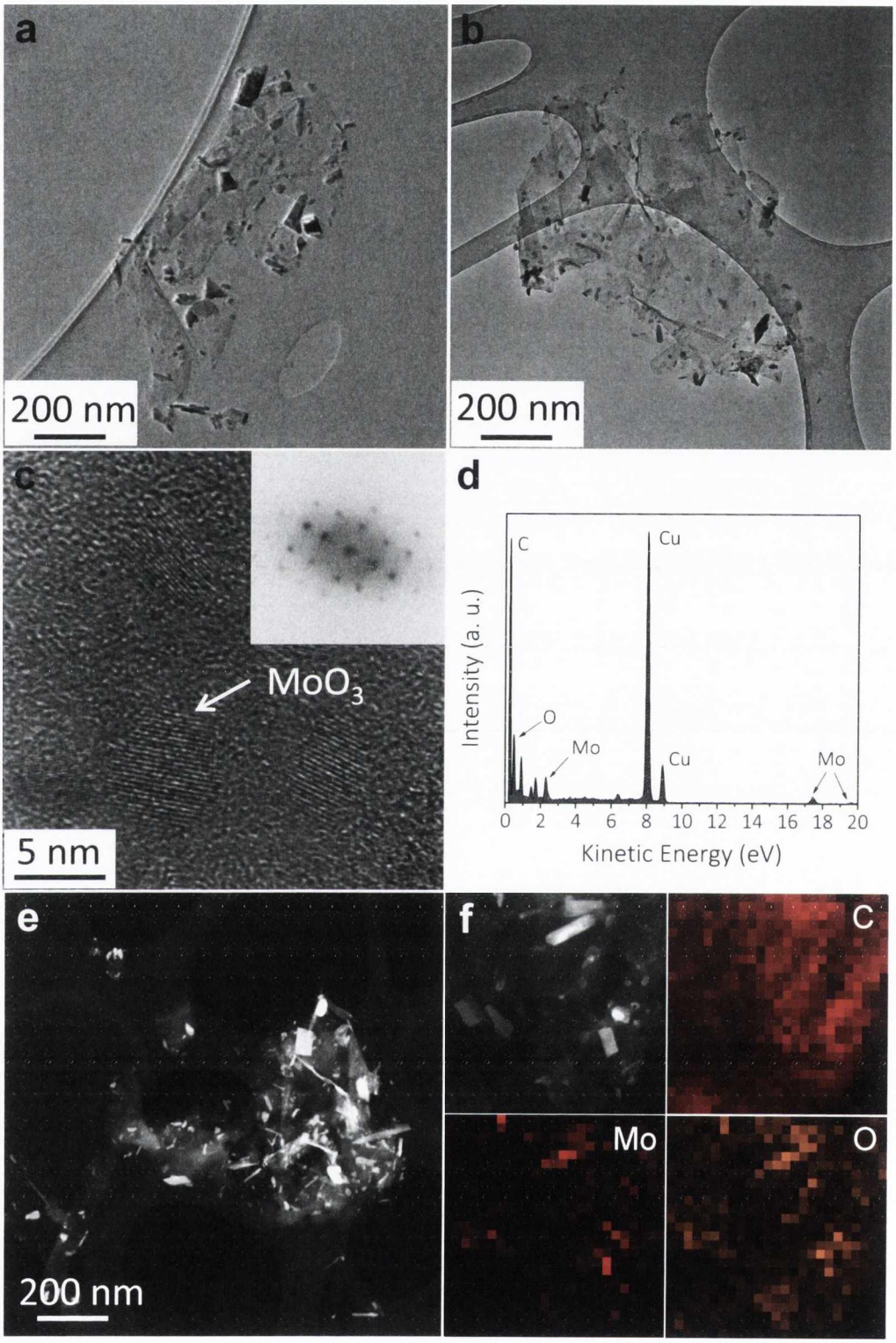


FIGURE 6.11: (a) and (b) Representative TEM image MoO_3 NC. (c) A HRTEM image and FFT pattern of the MoO_3 NC with (d) corresponding EDX pattern. (e) Representative HAADF STEM image showing relative thicknesses of the MoO_3 NC components and (f) the corresponding surface element profiles.

graphene possibly in the form of hydroxyl functional groups or impurities.

Further elemental analysis was carried out using XPS and ESCA. Samples were ultrasonically sprayed onto Si substrates and allowed to dry overnight before being subject to X-rays. Figure 6.12 (a) shows both the spin orbital split peaks of the the Mo 3d state consistent with that for MoO_3 in section 6.3.1. The O 1s peak shown in Figure 6.12 (b) centred at 352.1 eV can be deconvoluted into three separate peaks at 531.9 eV, 533.1 eV and 534.2 eV corresponding to the bonding of O with the Mo in the metal oxide, the C in graphene and the O in the residual H_2O molecules respectively.

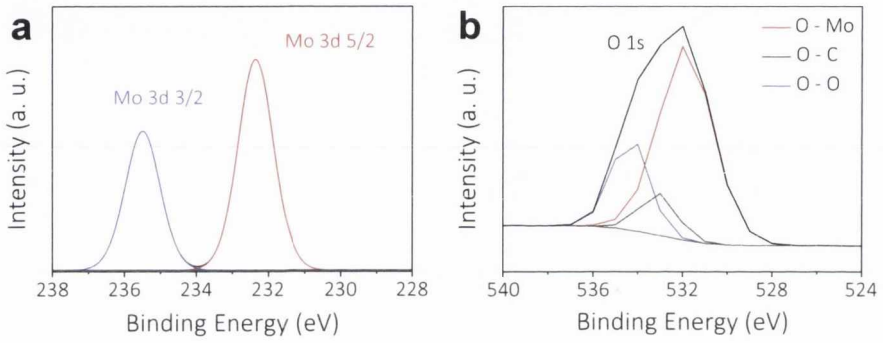


FIGURE 6.12: Deconvoluted XPS spectra of MoO_3 showing both the major (a) Mo 3d and (b) O 1s oxidation states.

Optimization of the dispersion concentration was achieved by investigating the dependence of final concentration on the initial concentration of each individual precursor material. UV-vis spectroscopy was employed to investigate the optimization of the MoO_3 NC colloid. The relative extinctions of each mixture was determined at 265 nm. Each samples was mixed with a predetermined weight of each precursor material. The samples are named based on the relative concentrations e.g. G2M2 contains an initial concentration of 2 $mg\,ml^{-1}$ graphite and 2 $mg\,ml^{-1}$ MoO_3 powder. There is no clear trend with initial concentrations as seen in Figure 6.13 (a). Dispersions that contain similar initial concentrations of both graphite and MoO_3 tended to show no resultant exfoliated flakes. However, the samples containing dissimilar amounts showed high yields of exfoliated MoO_3 NC. The sample containing initial concentrations of 10 $mg\,m^{-1}$ graphene and 2 $mg\,m^{-1}$ showed the largest yield. To further ascertain the composition of the resultant MoO_3 NC, thermogravimetric analysis (TGA) was employed. TGA was used to determine the relative weight percentage of MoO_3 to graphene in the dispersions acquired. Figure 6.13 (a) shows the TGA profile of the MoO_3 NC measured at 10° C s^{-1} from 0° C to 800° C. The initial losses up to 400° C can be attributed to the evaporation of residual solvents, trapped

water vapour and low boiling point functional groups on the graphene. The drop in mass between 430°C and 800° C can be attributed to the phase change of graphene. The relative quantities of MoO_3 determined was 50% weight overall.

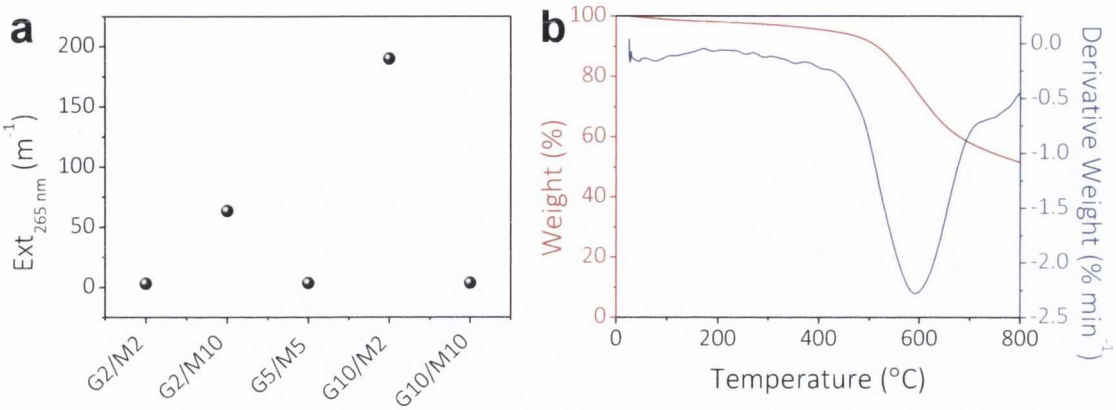


FIGURE 6.13: (a)Dependence of final concentration on the initial concentration of each individual precursor material and (b) TGA spectrum of the MoO_3 NC

XRD analysis was used to further ascertain the crystal structure of the MoO_3 NC. The XRD for pure graphene sheets were added for comparative purposes. For each dispersions, a machined glass slide was ultrasonically sprayed with a uniform coat and dried overnight at 100° C. The samples then underwent XRD from a Mo source X-ray target between a 2θ range of 2° - 30°. Figure 6.14 (a) shows the XRD patterns for both the graphene and MoO_3 NC cathodes. For the graphene in both samples, a major {002} peak is evident centred at 13.8 - 14.2° [458].

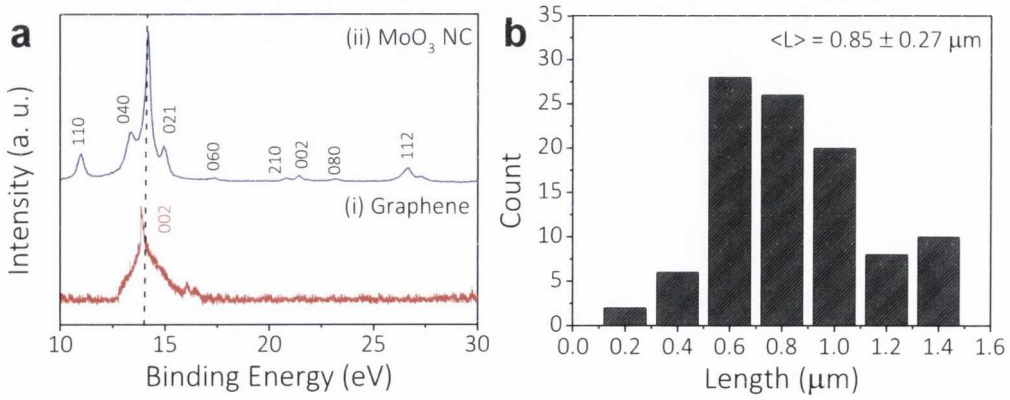


FIGURE 6.14: (a) XRD pattern and (b) lateral dimension count MoO_3 NC

However, the MoO_3 NC pattern shows an extra set of peaks coinciding with that of the MoO_3 NB shown in the previous section. The MoO_3 conforms to the

orthorhombic phase of $\alpha - MoO_3$ for which the space group is Pbnm (JCPDS no. 05-0507) [344]. Similarly, the presence of the {0k0} peaks indicate the preferential orientation to the individual MoO_3 nanosheets perpendicular to the substrate. The lattice parameters a and c are 0.4 nm and 0.37 nm respectively corresponding to {001} and {100} planes determined by TEM analysis earlier. The lattice parameter b = 0.14 nm corresponds to the distance between the layers along the {0k0} direction. A dispersion of optimized MoO_3 NC was vacuum filtered and dried overnight at 200° C and underwent BET analysis to determine the active surface area. The BET isotherm shown indicated that the cathode's surface area was 391.2 $m^2\,g^{-1}$.

The relative size distribution of the MoO_3 NC was determined by statistically analysing a series of 100 particles using TEM. A fresh sample was dropcast onto a holey carbon grid and the longest axis of each particles was measured. Figure 6.14 (b) shows the particle size distribution based on the size of the graphene sheets for a typical G10/M2 NC dispersion. A vast majority of the graphene sheets ranged between 0.5 μm and 1.1 μm in lateral dimension. The average particle length was determined to be $0.85 \pm 0.27\ \mu m$. It was also determined that the average amount of MoO_3 nanosheets found on the graphene was about 126 sheets per μm^2 of graphene.

6.3.2.2 Cathode Fabrication

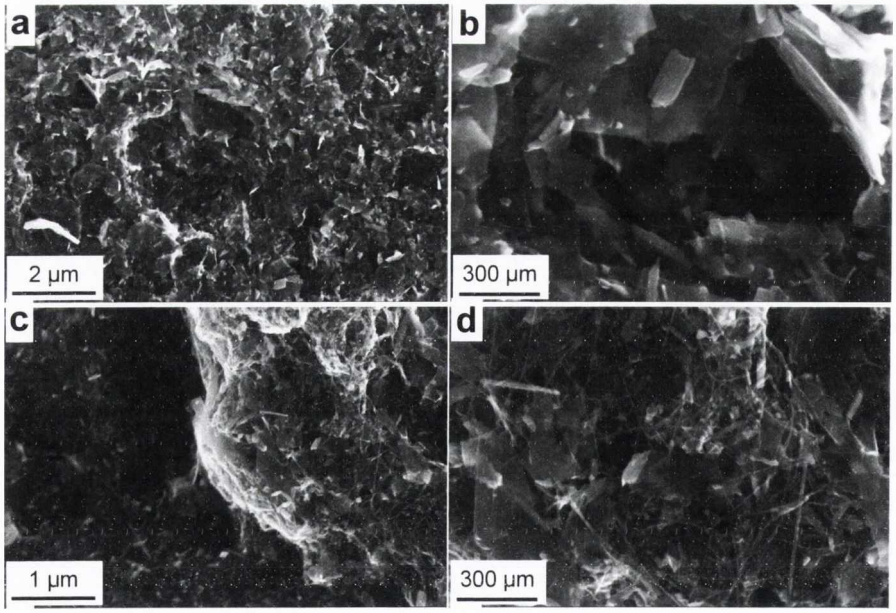


FIGURE 6.15: SEM and high magnification images of (a)-(b) MoO_3 NC and (c)-(d) MoO_3 NC/SWCNT cathodes.

Ultrathin, highly uniform MoO_3 NC cathodes were synthesized by ultrasonically spraying a controlled amount of dispersion on to Al substrate pre-treated with PEI [337]. Further cathodes were fabricated after mixing 5% weight of conductive SWCNTs dispersed in IPA. Figure 6.15 shows SEM images of both the MoO_3 NC and MoO_3 NC/SWCNT cathodes. Both cathodes show a series of stacked NC of varying sizes. Micropores are evident across the surfaces of both cathodes indicating channels useful for Li-ion intercalation. The higher magnified images show a more clear porous structure with evidence of the MoO_3 present on the large graphene sheets. The MoO_3 NC/SWCNT cathodes shown in Figures 6.15 (c) and (d) show how well dispersed the SWCNTs are throughout the NC matrix. This opens up more electronic conductive pathways required for more efficient transfer and transport of charge.

6.3.2.3 Electrochemical Characterization

As mentioned earlier, the addition of graphene has been shown to increase the conductive properties of the MoO_3 and improve the overall cycling performance [340]. As a result, the electrochemical performance of the MoO_3 NC was characterized by a series of techniques in a potential window similar to that of the MoO_3 NB (1 V - 4 V). Initially, CV was used to determine the intercalation properties of the MoO_3 NC cathode at a scan rate of 0.05 $mV\ s^{-1}$. Figure 6.16 (a) shows the first and tenth CV cycles for the MoO_3 NC cathode. A series of well defined intercalation peaks can be observed between potentials of 2 V and 2.5 V for the first cycle. This can be attributed to the insertion of Li-ions into the intralayer spacing of the MoO_3 nanosheets. The corresponding deintercalation process reveals no major peaks indicating initial trapping of the Li-ions as previously shown. As the tenth cycle reveals a severely diminished peak it reasonable to attribute this peak to the intra-layer intercalation process. The large pseudo-rectangular region at low potentials can be attributed to charge storage at specific graphene sites. At higher potentials the pseudocapacitive response is lessened due to the contribution only from MoO_3. Figure 6.16 (b) shows similar results with the presence of 5% weight SWCNTs. The major intercalation peak is centred at a potential of 1.96 V. This drop in potential could indicate the SWCNTs allow for easier intercalation into the intra-layer spacings. However, similar irreversible transformations are evident. In both cases, the low potential drops in current may be attributed to the start of formation of passivation layers as these generally happen below 1 V.

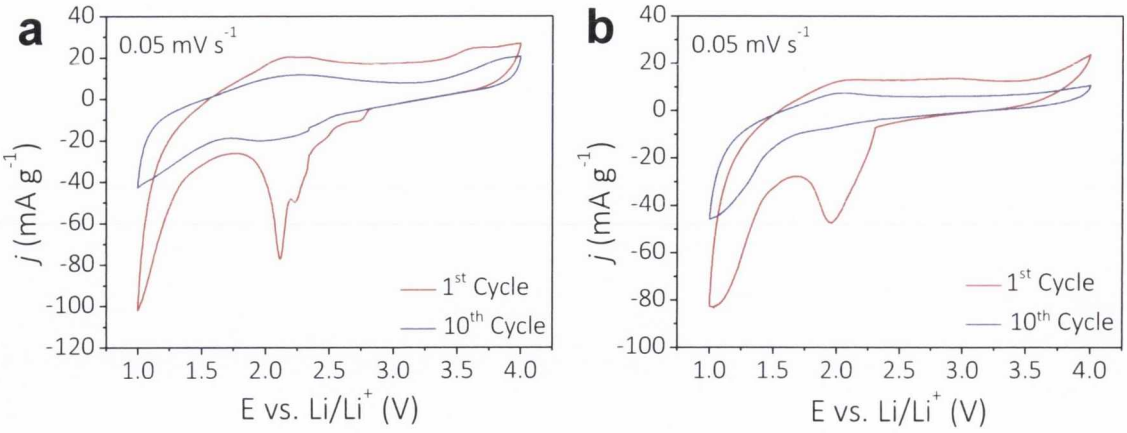


FIGURE 6.16: CVs of both the (a) MoO_3 NC and (b) the NC/SWCNT composite electrode at a scan rate of 0.05 mV s^{-1}

To further investigate the charge storage properties and to determine the relevant capacities of each composite cathodes, a series of GC measurements were carried out over a current density range of 20 to 1000 $mA\,g^{-1}$ in a potential window of 1 to 4 V. Figure 6.17 (a) shows the first, second and tenth GC cycles of the NC cathode at a current density of 20 $mA\,g^{-1}$. The pseudocapacitive response is quite evident due to the lack of well defined plateaus coupled long pseudocapacitive tails. However, for the first discharge cycle a plateau can be observed around a potential 2.1 V corresponding to the intercalation peak shown in Figure 6.16 (a). As expected, the corresponding cycles contain no plateaus suggesting a similar irreversible processes exhibited for the corresponding CV. The initial discharge cycle shows a capacity reaching 763.2 $mAh\,g^{-1}$ with the second cycle reaching only 283.9 $mAh\,g^{-1}$. This large drop in capacity can be attributed to the irreversible transformation after the intercalation into the intra-layer spacings coupled with the possible formation of a SEI layer along the graphene. After the 10th cycle the cathode reaches a stable capacity of 244.7 $mAh\,g^{-1}$. A similar result is acquired for the MoO_3 NC/SWCNT cathode showing similar pseudocapacitive and irreversible behaviour as shown in Figure 6.16 (b).

The respective discharge capacities are 1023.6 $mAh\,g^{-1}$, 373.9 $mAh\,g^{-1}$ and 363.8 $mAh\,g^{-1}$. Figures 6.16 (c) and (d) show the relevant capacities for current density ranges for both the MoO_3 NC and MoO_3 NC/SWCNT cathodes respectively. The MoO_3 NC cathode shows a discharge capacity of 164.7 $mAh\,g^{-1}$ at 50 $mA\,g^{-1}$, 104.2 $mAh\,g^{-1}$ at 100 $mA\,g^{-1}$, 72.0 $mAh\,g^{-1}$ at 200 $mA\,g^{-1}$, 56.1 $mAh\,g^{-1}$ at 300 $mA\,g^{-1}$, 47.8 $mAh\,g^{-1}$ at 400 $mA\,g^{-1}$, 41.2 $mAh\,g^{-1}$ at 500 $mA\,g^{-1}$ and 31.9 $mAh\,g^{-1}$ at 1000 $mA\,g^{-1}$. The MoO_3 NC/SWCNT cathode shows a discharge capacity of 247.6

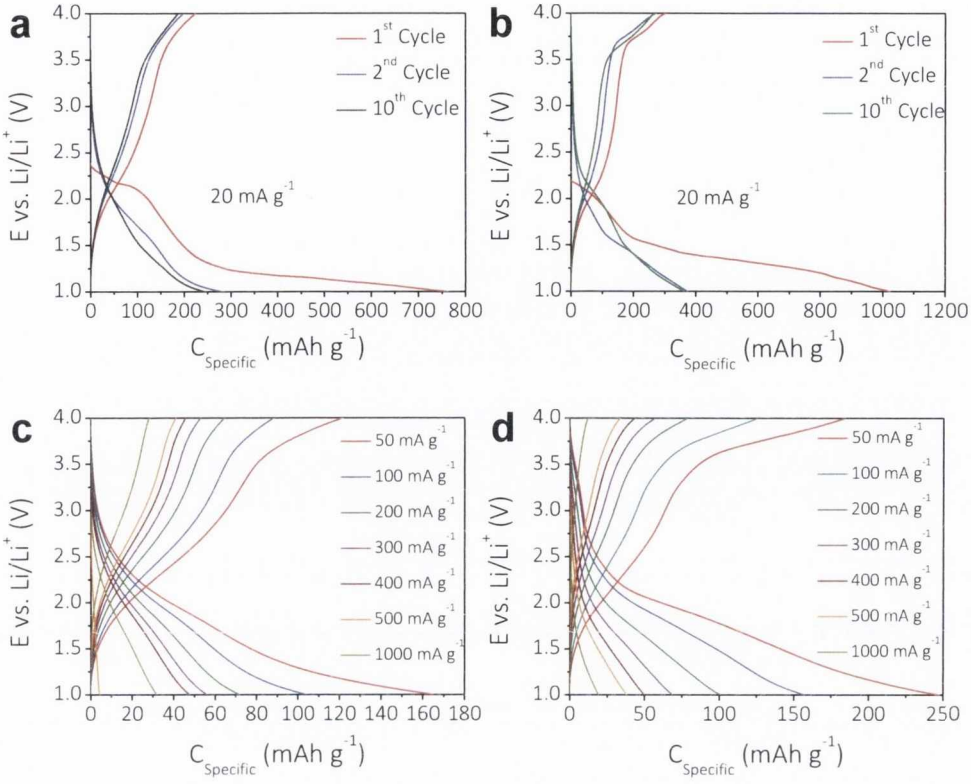


FIGURE 6.17: GCs of both the (a) MoO_3 NC and (b) the NC/SWCNT composite electrode at a current density of 20 $mA\,s^{-1}$. Relative capacities of the (a) MoO_3 NC and (b) the NC/SWCNT composite electrode for a range of current densities between 50 and 1000 $mAh\,s^{-1}$.

$mAh\,g^{-1}$ at 50 $mA\,g^{-1}$, 157.3 $mAh\,g^{-1}$ at 100 $mA\,g^{-1}$, 100.9 $mAh\,g^{-1}$ at 200 $mA\,g^{-1}$, 68.7 $mAh\,g^{-1}$ at 300 $mA\,g^{-1}$, 50.0 $mAh\,g^{-1}$ at 400 $mA\,g^{-1}$, 38.2 $mAh\,g^{-1}$ at 500 $mA\,g^{-1}$ and 19.2 $mAh\,g^{-1}$ at 1000 $mA\,g^{-1}$.

As graphene works to improve the cycling properties of MoO_3, a series of rate profiles and cyclability tests were carried out on the MoO_3 NC cathodes. A MoO_3 NC cathode underwent a GC test over a range of current densities from 20 $mA\,g^{-1}$ to 1000 $mA\,g^{-1}$ and back to 20 $mA\,g^{-1}$ in order to determine its rate capabilities. Both the MoO_3 NC and NC/SWCNT cathodes exhibit similar behaviour over the whole range with the NC/SWCNT cathode showing higher discharge capacities at smaller current densities as shown in Figure 6.18 (a). As the current density increases, the discharge capacities approach the same values. However, after current density is brought back to its initial value the discharge capacities both have shown to decrease by about 50 $mA\,g^{-1}$ for both cathodes. At higher charge densities the charge storage is preferentially attributed to the capacitive build up on the graphene.

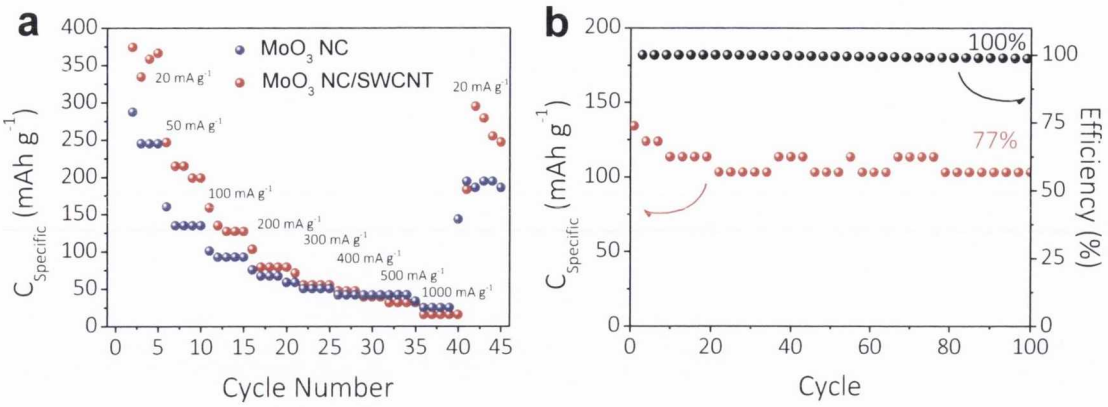


FIGURE 6.18: (a) The rate performance and (b) the cycle performance at at a current density of 100 $mA\,g^{-1}$ for the MoO_3 NC cathodes.

Similarly, a separate MoO_3 NC/SWCNT cathodes underwent GC tests at 100 $mA\,g^{-1}$ for 100 cycles. Figure 6.18 (b) shows the respective cycling behaviour and Coulombic efficiencies. After 100 cycles there is a 77% capacity retention for the MoO_3 NC/SWCNT cathode, an increase compared to that of the pure MoO_3 NB.

To gain an insight on how the addition of graphene and SWCNTs a series of EIS measurements were done to compare the relative conductivities of each cathode. The EIS measurements were performed at a potential of 10 mV between the frequency limits of 1 mHz an 1 MHz. The relevant Nyquist plots of both the MoO_3 NC and MoO_3 NC/SWCNT cathode are shown in Figure 6.19. The inset shows a close up version of the MoO_3 NC/SWCNT cathode spectrum.

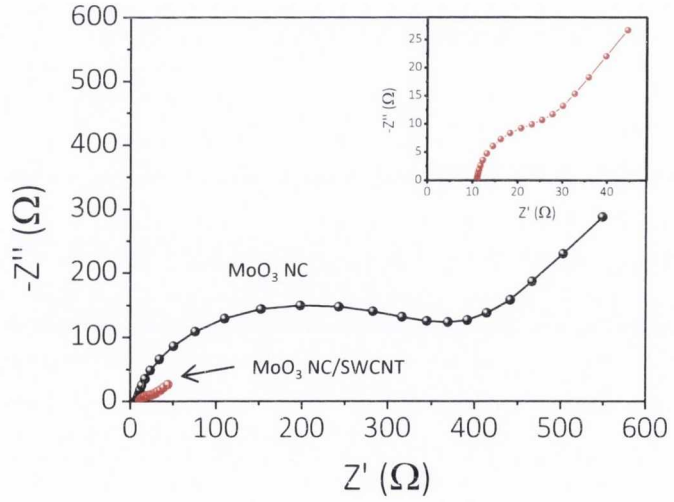


FIGURE 6.19: EIS for both the MoO_3 NC and MoO_3 NC/SWCNT cathodes.

The general shape of the impedance spectra follows that of the Randles circuit. The high frequency semicircle intercepts the real axis at two points, corresponding to the series R_S and the R_{CT}. Both cathodes exhibit an R_S of 11 Ω indicating a constant conductivity of the electrolyte in both cells. The values for R_{CT} are 340.0 Ω and 11.5 Ω for the MoO_3 NC and MoO_3 NC/SWCNT cathode respectively. This large decrease in R_{CT} can be reasonable attributed to the presence of highly conducting SWCNTs as they provide charge carrying paths for the liberated electrons. This agrees with the results shown previously as the addition of SWCNTs worked to increase the relative capacities of the NC cathodes. It is worth comparing the R_{CT} of the MoO_3 NC to that of the MoO_3 NB. The relatively high value of R_{CT} = 850 Ω for the NB is decreased upon addition of the graphene indicating the tendency of graphene to provide electronic states for more efficient charge transfer. In total, addition of both graphene and SWCNTs reduces the charge transfer resistance by a factor of 78.

6.3.2.4 Post Characterization

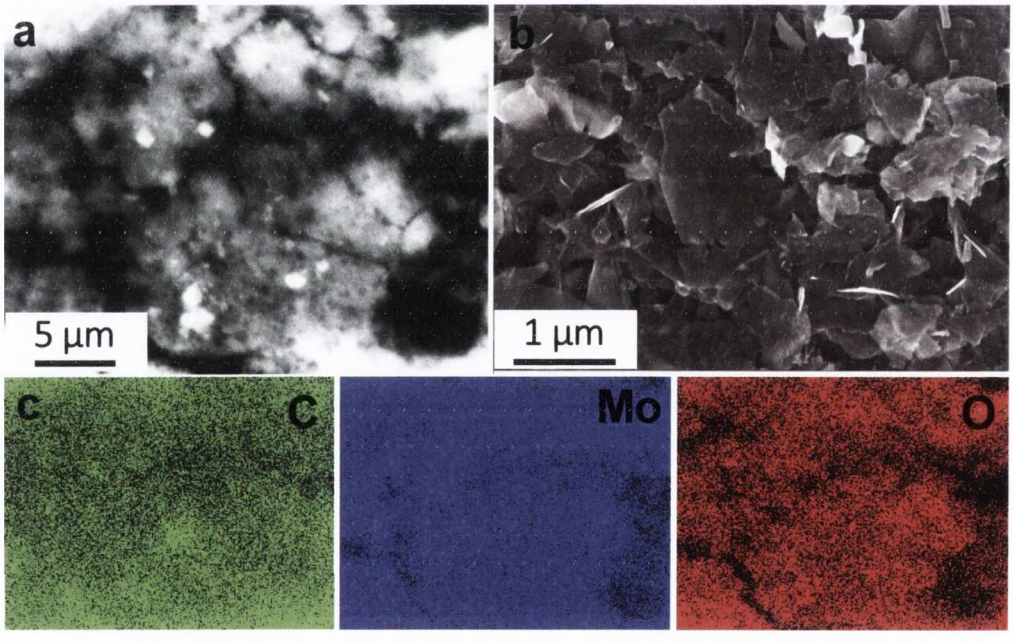


FIGURE 6.20: (a) Low resolution and (b) High resolution SEM images of the MoO_3 NC | SWCNT cathode post electrochemistry. (c) Corresponding EDX maps

After the MoO_3 NC/SWCNT cathode underwent five CV cycles at 0.05 $mV\ s^{-1}$, it was removed from the cell and carefully treated with acetone to remove the $LiClO_4$ electrolyte. The cathode was then dried overnight at 100°C and subject to SEM and

EDX analysis. Figure 6.20 (a) and (b) shows the SEM image of the cathode surface after cycling. The surface retains its structural integrity indicating that the intercalation and deintercalation processes do not act to pulverize the cathode. The general structure of the NC also remain intact with the MoO_3 nanosheets still present on the graphene surface. Also, the EDX maps shown in Figure 6.20 (c) indicate that the SWCNTs and the MoO_3 nanosheets remain relatively dispersed throughout the cathode.

Further analysis was done using XPS, XRD and EIS. Figure 6.21 (a) shows the XPS spectra of the Mo 3d peaks respectively. The Mo 3d peaks show no relative shift in binding energy compared to that of the pre cycled cathode (236.1 eV and 233.0 eV. for the 5/2 and 3/2 core level peaks respectively). This indicates that there is no major change in oxidation state of the MoO_3 nanosheets. The XRD pattern in Figure 6.21 (b) also suggests that the cathode has retained its crystal structure. The {002} peak associated with graphene and the series of {0k0} peaks (k = 2, 4, 6, 8) keep their initial positions as that shown for the uncycled cathode.

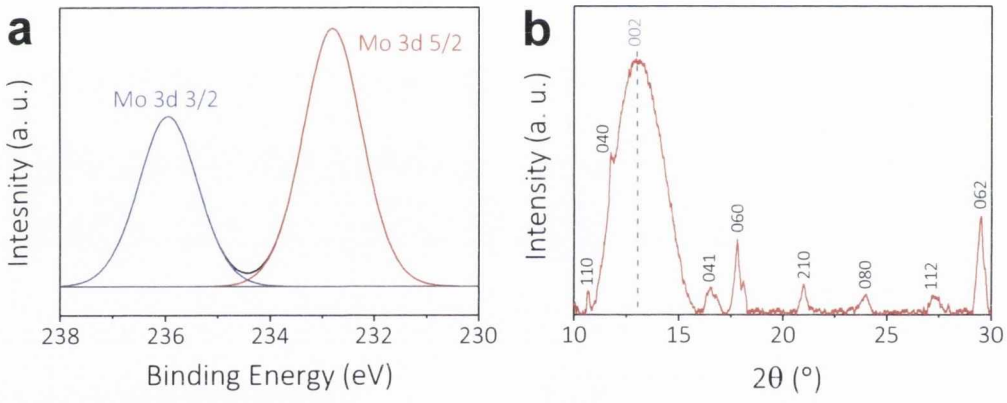


FIGURE 6.21: (a) XPS Mo 3d peak and (c) XRD pattern of the MoO_3 NC cathodes post electrochemistry

6.3.3 Molybdenum trioxide/Vanadium Pentoxide Nanocomposite

6.3.3.1 Cathode Fabrication

When fabricating a MoO_3/V_2O_5 nanocomposite, optimized dispersions of both V_2O_5 NS and MoO_3 NB were synthesized by ultrasonic exfoliation described in Chapter 4 and Section 6.3.2.1 respectively. The concentrations of both dispersions were determined accurately by vacuum filtration and subsequent drying over night at 100° C. As both MoO_3 and V_2O_5 are optimized in different solvents it was necessary to

determine how stable the resultant dispersions would be after mixing. It was determined that the mixed dispersions retained adequate stability for a period of one week without any noticeable flocculation of aggregation.

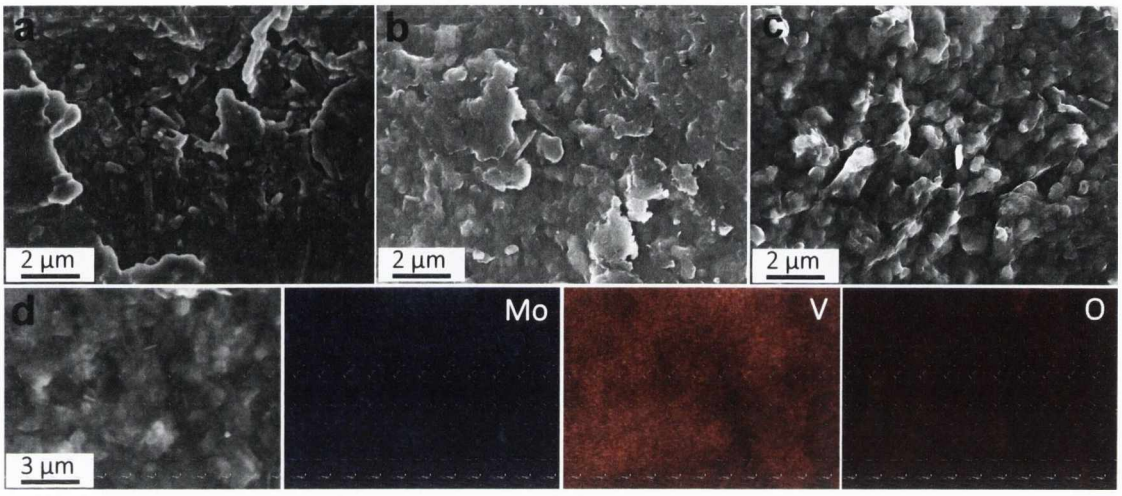


FIGURE 6.22: SEM images of the (a) MV25, (b) MV50 and (c) MV75 nanocomposite cathodes. (d) EDX mapping of the MV25 nanocomposite cathode.

A series of MoO_3/V_2O_5 nanocomposites were fabricated by mixing different % weight of both the optimized MoO_3 NB and V_2O_5 NS dispersions. The mixtures were defined by the relative % weight of V_2O_5 NS compared to that of the MoO_3 NB. A total of three different nanocomposite dispersions were mixed, namely 25%, 50% and 75%. The three dispersions were allowed to mix overnight until a homogeneous dispersion was achieved and subsequently named MV25, MV50 and MV75 respectively. Each resultant dispersion was then subject to ultrasonic spraying onto Al substrates pretreated with adhesive PEI to produce a series of thin film cathodes. Each dispersion was also ultrasonically sprayed onto a pre-cleaned Si substrate and subjected to SEM analysis. Figures 6.22 (a), (b) and (c) shows the SEM images of the surfaces of the MV25, MV50 and MV75 cathodes respectively. Each surface exhibits both MoO_3 NB and V_2O_5 NS with the amount of visible MoO_3 NB decreasing as the V_2O_5 NS content increases. The EDX surface profiles shown in figure 6.22 (d) indicate the uniform distribution of the MoO_3 NB and V_2O_5 NS across the whole surface for the MV25 cathode.

To further study the chemical composition of the three nanocomposites, a sample of each was ultrasonically sprayed onto a Si substrate and subject to XPS analysis. High resolution spectra for the principal MoO_3 and V_2O_5 peaks are shown in Figure 6.23. A similar set of Mo 3d peaks are shown in Figure 6.23 (a) as that shown

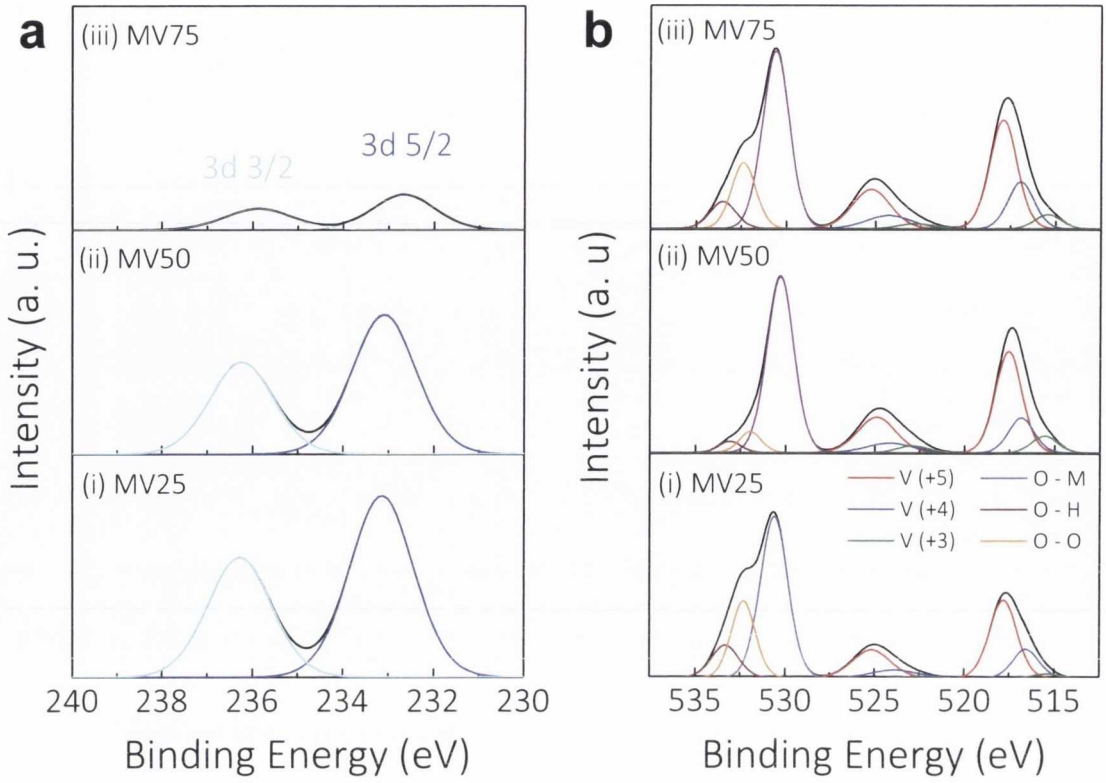


FIGURE 6.23: The major (a) Mo 3d and, (b) V 2p and O 1s core level peaks for the (i) MV25 (ii) MV50, and (iii) MV75 nanocomposite cathodes.

for the MoO_3 NB in section 6.3.2.1 for the (i) MV25, (ii) MV 50 and (iii) MV75 cathodes [454]. The spin orbital split peaks at binding energies of 236.1 eV and 233.0 eV correspond to the 3d 3/2 and 3d 5/2 core levels of the Mo(VI) oxidation state respectively. This similarity in binding energies indicates that the presence of the V_2O_5 NS do not alter the electronic state of the MoO_3 NB [233]. For each of the three cathodes, the relative intensity of each varies proportionally with the % weight of the MoO_3 NB. Similarly, in 6.23 (b), the V 2p 3/2 and 1/2 core peaks centred at 517.2 eV and 524.2 eV respectively show little deviation from the binding energies determined for that of the V_2O_5 NS in chapter 4 [319, 320]. However, the relative intensities of the oxidation peaks differ, see table 6.1. Compared to that of the pure V_2O_5 NS, all three of the composite cathodes contain much less the V (+5) oxidation state with values decreasing as the percentage of V_2O_5 increases relative to the MoO_3 NB. Therefore it can be reasonable assumed that the MoO_3 does alter the electronic states of the V_2O_5 NS leading to other morphologies. Also, unlike the pure V_2O_5 NS, a series minute peaks centred at 523.5 eV and 515.4 eV correspond to an extra V (+3) oxidation state not shown in chapter 4.

TABLE 6.1: Relative quantities of various V_2O_5 oxidation states for different composite cathodes.

O.S.	MV25	MV50	MV75	V_2O_5
V (+3)	3.82	10.63	8.08	0
V (+4)	24.90	22.12	26.61	4.76
V (+5)	71.29	67.24	65.03	95.24

The O 1s peak situated at between 528 eV and 532 eV can be further into three separate peaks referring to three different O bonds in the each cathode [322]. The strong intensity peak located at 530.00 eV can be attributed to the covalent bonding of the O atoms to the transition metals in both TMOs. The remaining smaller peaks at 531.33 eV and 532.79 eV can be attributed to hydrogen bonded water molecules trapped between adjacent layers of the NS and NB and the presence of hydroxyl groups respectively.

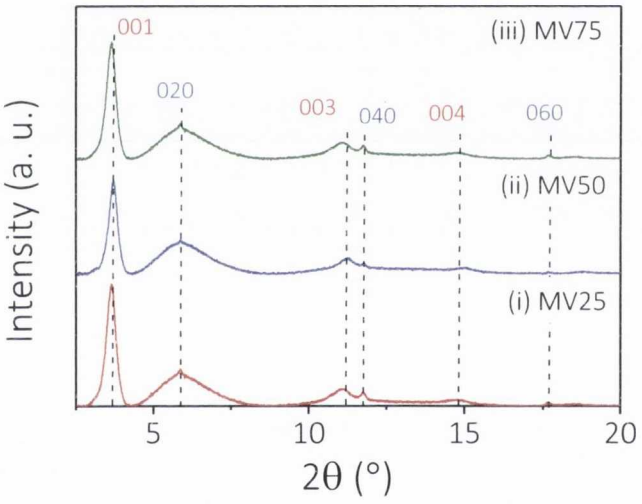


FIGURE 6.24: The XRD patterns for the (i) MV25, (ii) MV50, and (iii) MV75 nanocomposite cathodes. The blue labels indicate MoO_3 and the red labels indicate V_2O_5.

The relative crystal structures of each nanocomposite cathode was investigated using XRD. Samples sprayed on the glass slides were subject to a Mo source diffractometer with a 2θ range of 2 ° - 30 °. The XRD patterns of each nanocomposite are compared in Figure 6.24. The peaks centred at 5.9 °, 11.7 ° and 17.7 ° correspond to the {020}, {040} and {060}peaks associated with the orthorhombic phase of MoO_3 (JCPDS no. 05-0507), indicating MoO_3 retains its crystal structure. Therefore, similar to the results obtained in the XPS, the V_2O_5 does not change the crystal structure of the MoO_3 NB. Similarly, the peaks found at 3.5°, 10.6° and 14.0° correspond to the

{001}, {003} and {004} diffraction peaks similar to that determined for the hydrated V_2O_5 in Chapter 4 (JCPDS No. 40-1296) [326, 327]. As before the presence of the {00k} peaks indicates the one-dimensional turbostratic stacking of the layers perpendicular to the substrate. Even though the presence of MoO_3 alters the oxidation states of the V_2O_5, all the XRD peaks present in each cathode correspond to the V +5 oxidation state of V_2O_5. As the relative % weight of the V_2O_5 increases there is no change in the angle of 2θ indicating constant inter-planer spacings.

6.3.3.2 Electrochemical Characterization

A series of electrochemical tests were carried out on all three of the composite cathodes to determine their applicability in efficient Li-ion storage devices. Tests were carried out in a half cell configuration with both the reference and the counter electrodes as pure Li metal. A potential window of 1 V - 4 V was employed as it is the general potential window used for both the V_2O_5 NS in Chapter 4 and the MoO_3NB in section 6.3.1.3.

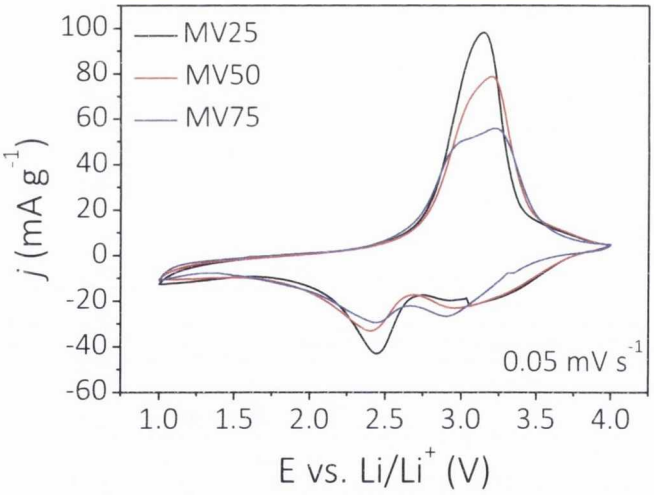


FIGURE 6.25: CV of the MoO_3/V_2O_5 nanocomposite cathodes at scan rates of $0.05mVs^{-1}$.

The initial CV curves of each cathode are shown in Figure 6.25 at a scan rate of 0.05 mVs^{-1}. A major intercalation peak can be observed between potentials of 2.2 and 2.7 V vs. Li/Li^+ for the cathodic process. The corresponding deintercalation process is demonstrated by the anodic polarization peak in the potential range of 2.8 V - 3.4 V. A second intercalation peak can be observed for the MV75 cathode. This extra peak is assumed to be an artefact of the V_2O_5 NS as it is not as prominent

in the cathodes containing less V_2O_5. The general shape of the CV is similar to that of the V_2O_5 NS cathode shown in chapter 4. The lack of a well defined MoO_3 peak as shown in section 6.3.1.3 indicates that the Li-ions are pseudocapacitively stored on the surfaces of the MoO_3 and to a lesser extent, in the interlayer spacings. Due to the apparent peaks corresponding to V_2O_5, charge storage may also occur in the interlayer spacing of the V_2O_5. The lack of a well defined MoO_3 intra-layer peak may be attributed to the preferential stoage in the V_2O_5.

As the peaks can be attributed directly to V_2O_5, it is reasonable to assume that the MoO_3 contributed a more pseudocapacitive contribution to the overall process. The relative intensity of each intercalation and deintercalation peak tends to decrease As the % weight of V_2O_5 increases. The XPS results in the previous section indicated that, as the relative % weight of the V_2O_5 increases, the amount of the V (+5) oxidation state decreases. It is possible that the V(+4) and V(+3) oxidation states increase the conductivity of the material leading to this peak height decrease.

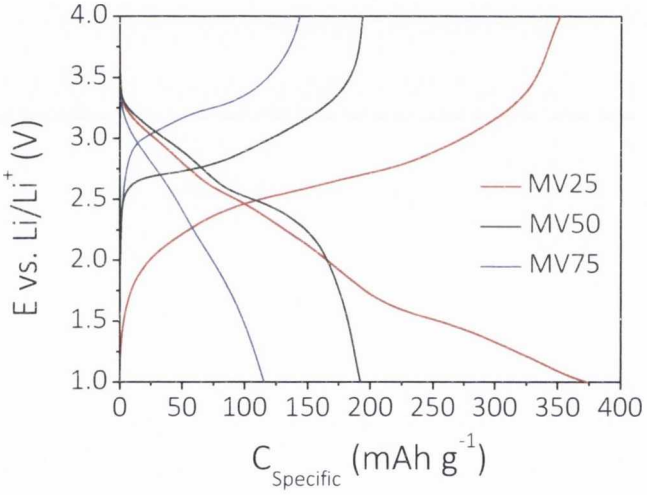


FIGURE 6.26: GC curves of the MoO_3/V_2O_5 nanocomposite cathodes at a current density of $20mAg^{-1}$.

To determine the relative storage capacities of each nanocomposite, GC curves were measured current density of 20 $mA\,g^{-1}$, see Figure 6.26. MV25 showed the highest discharge capacity at 374.2 $mAh\,g^{-1}$, greatly exceed that of MV50 (192.3 $mAh\,g^{-1}$), and MV75 (143.5 $mAh\,g^{-1}$). MV25 also exhibited the most pseudocapacitive tail indicating the heavy contribution from the highly pseudocapacitive MoO_3. As both MV50 and MV75 contained more V_2O_5, their plateaus are more well defined.

As MV25 showed the most impressive storage capacity of the three cathodes, a further series of electrochemical tests were carried out on it. Figure 6.27 (a) shows the first, second and tenth GC curves at 20 mAg^{-1} of MV25. The discharge capacities determined were 374.2 $mAh\,g^{-1}$, 353.4 $mAh\,g^{-1}$ and 349.5 $mAh\,g^{-1}$ respectively. The initial drop of 20.8 $mAh\,g^{-1}$ after the first cycle may entirely be attributed to the irreversible intercalation process between $\alpha - V_2O_5$ and $\delta - V_2O_5$ [269]. As this diminished capacity loss after the first cycle was not observed for either the pure MoO_3 NB or V_2O_5 NS cathodes, it is reasonable to assume the V_2O_5 alleviates the semiconducting behaviour of the MoO_3 NB. As explained earlier the presence of V_2O_5 reduces the intra-layer intercalation process while contributing to the overall capacity. By the tenth cycle, the capacity remains relatively unchanged indicating possible long time charge capacity retention.

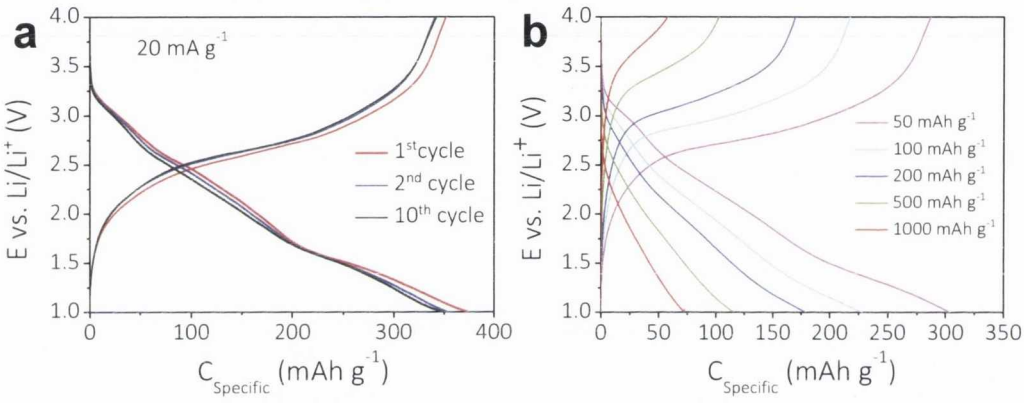


FIGURE 6.27: GC curves of the (a) first, second and tenth cycle at 20 mAg^{-1} and (b) first cycles at a current density range between 50 and 1000 mAg^{-1} for the MV25 nanocomposite cathodes.

In the previous situations, the addition such as SWCNTs in V_2O_5 or graphene in MoO_3 reduced the cycling deficiencies of the semiconducting TMOs [340, 442–444]. However, in the case of MoO_3, the addition of graphene still caused a massive decrease in capacity after the first cycle coupled with the formation of an SEI layer [459]. Despite graphene containing ample charge storage states to alleviate the semiconducting properties of MoO_3, the capacities and cycling properties desired were unreachable. Both V_2O_5 and MoO_3 are semiconducting materials, however, the addition of defects in the V_2O_5 may increase the overall conductivity of the composite facilitating more efficient charge transfer reactions.

Figure 6.27 (b) shows the GC curves for a serious of current densities between 50 and 1000 mAg^{-1}. The initial discharge capacities determined were 304.4 $mAh\,g^{-1}$ at 50 $mA\,g^{-1}$, 228.2 $mAh\,g^{-1}$ at 100 $mA\,g^{-1}$, 179.3 $mAh\,g^{-1}$ at 200 $mA\,g^{-1}$, 115.8 $mAh\,g^{-1}$

at 500 $mA\,g^{-1}$ and 72.4 $mAh\,g^{-1}$ at 1000 $mA\,g^{-1}$. Therefore, even at high current densities, the storage capacities of the MV25 cathode compete with that of modern $LiCoO_2$ devices [41].

Further electrochemical testing was done to examine the rate capabilities and long terms cycling properties of the MV25 nanocomposite. Figure 6.28 (a) shows the rate profile after initial activation at 20 $mA\,g^{-1}$ cycling up to 1000 $mA\,g^{-1}$ and then back to 20 $mA\,g^{-1}$. The MV25 composite cathode retains its initial capacity after it is switched back to 20 $mA\,g^{-1}$. This shows how resistant the cathode material is to changes in current density. Figure 6.28 (b) shows the first 100 cycles of the MV25 nanocomposite cathode at 100 $mA\,g^{-1}$ along with the corresponding Coulombic efficiency. After 100 cycles the storage capacity retains 90% of it's initial capacity with a 100% Coulombic efficiency.

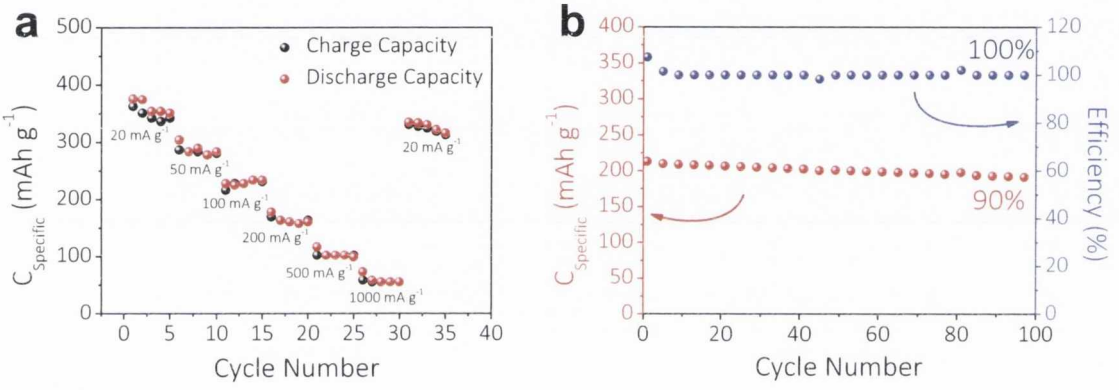


FIGURE 6.28: (a) The rate performance and (b) the cycle performance at a current density of 100 $mA\,g^{-1}$ for the MV25 nanocomposite cathode.

As MoO_3 and V_2O_5 are both semiconducting materials, an EIS spectrum was measured to compare to the MV25 nanocomposite cathode. The EIS measurements were performed at a potential of 10 mV between the frequency limits of 1 mHz an 1 MHz. The Nyquist plot calculated from the measurements is shown in Figure 6.29 along with the corresponding Randles circuit. The high frequency intercepts of the semicircle on the x-axis corresponding to the R_S and R_{CT} are 11 Ω and 400 Ω respectively. As expected, the value for R_S matches that of the previously shown cathodes. Compared to both the MoO_3 NB cathode (850 Ω) and the V_2O_5 NS cathode (1100 Ω), the MV25 cathode has a much lower R_{CT} value. This lower value supports the improved performance exhibited by the composite cathode.

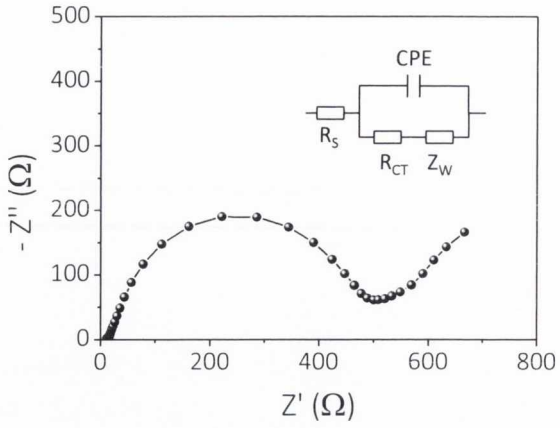


FIGURE 6.29: EIS for the MV25 nanocomposite cathode.

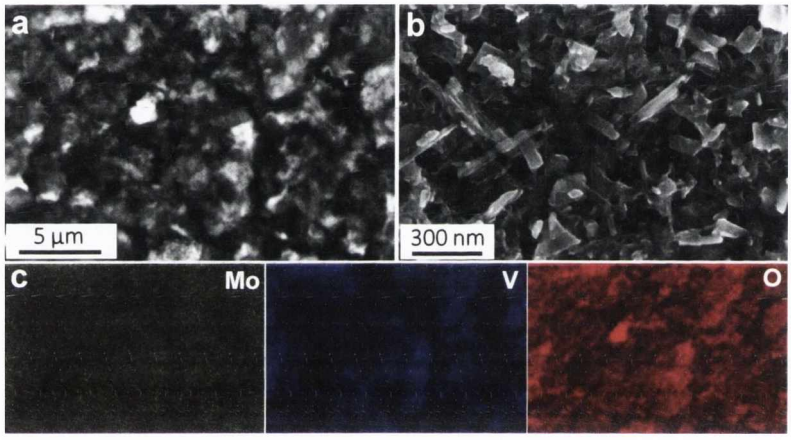


FIGURE 6.30: (a) Low and (b) high magnification SEM images of the MV25 nanocomposite cathode post electrochemical cycling. (c) The corresponding low magnification EDX pattern.

6.3.3.3 Post Characterization

After the MV25 cathode underwent five CV cycles at 0.05 $mV\ s^{-1}$, it was carefully removed from the electrochemical cell and treated with acetone to remove the remaining $LiClO_4$ electrolyte. The cathode was then dried overnight at 100°C and subject to SEM, EDX, XRD and XPS. Figure 6.30 (a) shows a low magnification SEM image of the cycled cathode. The cathodes structure remains relatively intact with little or no cracking. Figure 6.30 (a) shows a higher magnified image. It is clear that the even after cycling the cathode still retains its highly porous structure which may be a reason for the improved cyclability. Figure 6.21 (c) shows the even distribution of Mo, V and O across the cathode surface further indicating the stability of the cathode after repeated cycling.

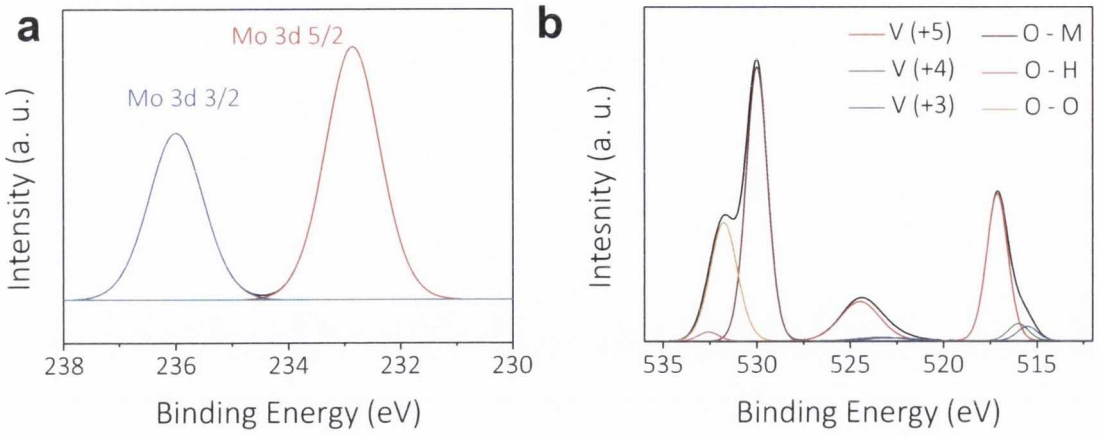


FIGURE 6.31: (a) Mo (IV), (b) V 2p and O 1s core level XPS spectra of the MV25 nanocomposite cathode post electrochemical cycling.

The XPS spectra showed no overall change in relative position compared to that of the pre-cycled cathode. The Mo 3d 5/2 and 3/2 can be found at 236.1 and 233.0 eV in Figure 6.31 (a). Figure 6.31 (b) shows the V 2p 3/2 and 1/2 core peaks centred at 517.2 eV and 524.2 eV respectively. There seems to be an overall increase in the V (+3) oxidation state indicating the larger and more diverse phase changes than that of the pure V_2O_5 NS in chapter 4. The O 1s peaks between 528 and 532 eV can be attributed to the bonding of O with the metal oxide, residual H_2O molecules and hydroxide groups. Similarly, the XRD pattern indicates that the crystal structure of the cathode remains unchanged post cycling, as can be seen in Figure 6.31 (c). The peaks centred at 5.9 °, 11.7 ° and 17.7 ° correspond to the {0k0} set of peaks associated with the orthorhombic phase of MoO_3 and the peaks found at 3.5°, 10.6° correspond to {00l} set of peaks of the hydrated phase of V_2O_5. This also indicates that both the MoO_3 NB and V_2O_5 retains their one dimensional stacking structure similar to that exhibited by the uncycled samples.

6.4 Conclusion

In conclusion, a series of MoO_3 NB, NC and a composite MoO_3 NB/V_2O_5 NS were prepared by the LPE of commercially acquired powders without the use of hazardous solvents. TEM analysis indicated the MoO_3 NB possessed a thin belt like structure commonly observed among MoO_3 nanomaterials with an average lateral dimension of 0.82 μm and an average aspect ratio of 3. X-ray analysis indicated that, after nanostructuring, the MoO_3 retained its crystal structure and oxidation states.

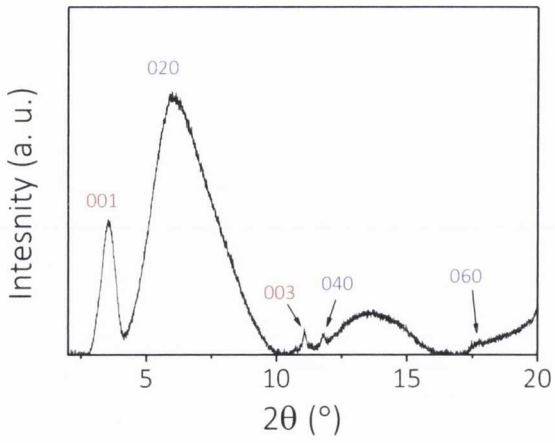


FIGURE 6.32: XRD pattern fo the MV25 nanocomposite cathode post electrochemical cycling. The blue labels indicate MoO_3 and the red labels indicate V_2O_5.

Similarly, LPE provides a method to co-exfoliate MoO_3 and graphite to form a MoO_3 NC. These MoO_3 NC consist of a graphene nanosheet on the order of 1 μm dotted with small MoO_3 sheets on the order of 20 nm. Further X-ray analysis indicated the graphene does not alter the structure of the MoO_3. A series of highly flexible thin film cathodes were prepared based on the different MoO_3 composites using a facile ultrasonic spraying method. As MoO_3 demonstrates semiconducting behaviour, the composite materials acted to alleviate this by providing extras charge transfer states which in all cases was confirmed by EIS analysis. For comparative purposes a thin film cathode was fabricated consisting solely of MoO_3 NB forming a porous surface structure as confirmed by SEM. Initial discharging demonstrated a storage capacity of 840.04 $mAh\,g^{-1}$ at 20 $mA\,g^{-1}$ falling short of the expected theoretical capacity of 1117 $mAh\,g^{-1}$. The cathodes showed a capacity retention of 66.7% after 100 cycles at 100 $mA\,g^{-1}$ as expected for a poorly conducting material. The MoO_3 NC cathodes demonstrated a relatively porous structure especially when conductive SWCNTs were added. Similarly, the series of MoO_3 NC/V_2O_5 NS showed a highly dispersed mixture specifically in the case of MV25. The addition of graphene and SWCNTs increased the overall discharge capacity to 1023.6 $mAh\,g^{-1}$ while addition of V_2O_5 decreased the over all capacity to 374.2 $mAh\,g^{-1}$ for the MV25 cathode at 20 $mA\,g^{-1}$. However, there is a clear improvement in cyclability of the MV25 cathode demonstrating a 90% retention in capacity after 100 cycles. This value is a serious improvement over that of commercial MoO_3, nanostructured MoO_3, MoO_3 NC (%) and the V_2O_5 NS exhibited in chapter 4. Post analysis of both composite materials demonstrated that, after electrochemical cycling, both cathodes remained relatively stable and maintained highly distributed and porous structures.

Chapter 7

Conclusion and Future Work

The scope of this thesis was to investigate the electrochemical properties of a series of nanostructured TMO materials. These nanostructured materials were synthesized by a facile, economic and scalable LPE technique employing high frequency ultrasonic energy. LPE has shown to be an efficient technique to nanostructure a wide array of TMO materials with specific application in high power energy storage devices such as MnO_2 [460], however, this thesis focused specifically on V_2O_5 [151], TiO_2 and MoO_3 [210].

Initially a series of LPE parameters were investigated on the TMOs in question, however, MoO_3 was omitted as this work was previously completed by Hanlon *et al.* A series of V_2O_5 and TiO_2 colloids were investigated by comparison of their extinction spectra as a function of Hildebrand parameters. Results indicate that the LPE of both materials demonstrate a general Guassian distribution centred at a region of δ_t = 24 - 26 $MPa^{0.5}$. This relative position indicates that solvents such as NMP and formaldehyde are ideal solvents for the efficient sonication of TMO materials and is typically observed for a series of other materials such as graphene [207] or TMDs [461]. However, to address the environmental concerns of large scale synthesis of TMO colloids, these solvents were not used due to their relative toxicity and high boiling points. As such, for both materials H_2O was chosen as the solvent for future processing due to its low boiling point and environmental inertness. In both cases H_2O demonstrated a relatively high yield of nanoparticles in their respective colloids, however, IPA was chosen for MoO_3 due to the previous work of Hanlon. TEM analysis indicated that LPE in H_2O yielded a series of V_2O_5 NS, TiO_2 NP and MoO_3 NB. Both the V_2O_5 NS and MoO_3 NB demonstrated relatively flat crystalline structures with lateral dimensions generally less than 1 μm. XPS and XRD analysis indicated that that V_2O_5 NS exhibited a bilayer xerogel structure orientated along the [00l] direction in which the LPE molecules intercalated between the individual layers forming hydrogen bonds with terminal Os expanding the interlayer spacing

from 0.43 nm to 1.15 nm. The array of MoO_3 NB demonstrated an average aspect ratio of 3.05 with XRD analysis suggesting a highly crystalline structure aligned along the [0k0] direction. However, TEM analysis suggests TiO_2 yields a series of pseudo-zero dimensional particles on the order of 200 nm. This is due TiO_2 not possessing the layered structure associated with V_2O_5 and MoO_3. A MoO_3/graphene composite was also synthesized using similar methods. TEM demonstrated how the resultant structures of the MoO_3 NC comprised of a thin graphene sheet with a lateral dimension of 1 μm covered with a series of MoO_3 sheets on the order of 20 nm. XRD analysis indicated how the MoO_3 retained their crystal structure after LPE.

A series of electrodes were fabricated from the optimized TMO colloids described previously using an facile and controllable ultrasonic spraying technique. In general, TMO materials exhibit low conductivities due to their semiconducting behaviour. As such, a separate colloid of conductive SWCNT was prepared using similar sonication methods as used as a conductive additive and binder for both the V_2O_5 NS and TiO_2 NP. SEM analysis indicated that both the pure V_2O_5 NS and TiO_2 NP electrodes exhibited a highly porous surface structure. The addition of SWCNT demonstrated similar porous structures with efficient distributions of SWCNTs throughout the TMO matrices. In the case of MoO_3, the graphene acted as the conductive additive for the MoO_3 NC. SEM analysis indicated that both the MoO_3 NC and MoO_3 NC/SWCNT electrodes possessed a porous structure with efficient distributions. Finally, a V_2O_5 NS/MoO_3 NB electrode was fabricated by mixing both the V_2O_5 NS and MoO_3 NB colloids with a controlled mass %. Similarly, the resultant electrodes possessed a highly porous and efficiently distributed structure.

The nanostructuring and the subsequent addition of SWCNTs demonstrated a vast improvement of the electrochemical properties of the normally semiconducting TMO materials. Surface area analysis indicated that for all three TMO materials, nanostructuring increased the relative surface areas leading to an increase in active sites for resultant charge storage. EIS analysis indicated how the addition of conductive additives such as SWCNTs or graphene decreased the charge transfer resistance of each TMO. GITT analysis indicated how the nanostructuring improved the diffusion coefficient of V_2O_5 by a factor of 14.5. As such a series of electrochemical experiments were carried out to determine the relative capacities of each material. Initial capacities of 372 $mAh\,g^{-1}$ were demonstrated for the V_2O_5 NS/SWCNT composite cathode, greatly bypassing that of its theoretical capacity (294 $mAh\,g^{-1}$)

and previously determined experimental capacities (300 $mAh\,g^{-1}$) at 0.05C. A capacity retention of 81% was achieved after 100 cycles at 1 C indicated a vast improvement from commercial acquired V_2O_5 material. Similarly, an initial storage capacity of 716 $mAh\,g^{-1}$ was determined for the TiO_2 NP/ SWCNT composite anode at 0.1 C, demonstrating an improvement over previous experimental capacities (300 $mAh\,g^{-1}$). However, a capacity retention of 59% at 1 C after 100 cycles suggests further improvements need to be carried out. Investigation into MoO_3 composites indicated that the MoO_3 NC/SWCNT and the MV25 cathodes demonstrated initial storage capacities 1024 $mAh\,g^{-1}$ and 374 $mAh\,g^{-1}$ at 20 $mA\,g^{-1}$ respectively. The MoO_3 NC/SWCNT shows a vast improvement in storage capacity compared to that of the pure MoO_3 NB (840 $mAh\,g^{-1}$), almost matching that of the theoretical capacity for MoO_3 (1117 $mAh\,g^{-1}$). However, the relatively low capacity of the MV25 cathode still demonstrates a superiority over contemporary Li-ion cathodes e.g. $LiCoO_2$. Despite the low storage capacity value, the relative cyclability at 100 $mA\,g^{-1}$ demonstrates a 90% retention at 100 $mA\,g^{-1}$, a serous improvement over that of commonly observed MoO_3 or V_2O_5 values. In comparison, the MoO_3 NC cathode demonstrates a % retention in capacity after 100 cycles.

Figure 7.1 demonstrates the energy and power densities position of the three studied TMO materials relative to conventional Li-ion battery materials, SC materials, electrolytic capacitors and typical combustion fuels. In general, each material demonstrates energy densities reaching upwards of 1,000 $Whkg^{-1}$ rivalling that of traditional combustion fuels. However, the general power densities exhibit values slightly higher than that exhibited by typical battery materials. Specifically for high powered application, the materials tend to exhibit energy densities on the order of 1000 Wkg^{-1} for a 3600 s (6 min) discharge process. This was reflected in Chapter 4 when it was demonstrated that, at 10 C (corresponding to a 6 min discharge), the V_2O_5 NS demonstrated a discharge capacity rivalling that of a typical low powered $LiCoO_2$ cathode. For a typical charging process commonly exhibited by Li-ion batteries (between 1 hr - 10 hr), the TMO materials exhibited energy densities of 200 - 1000 $Whkg^{-1}$ and power densities between 400 Wkg^{-1} and 1000 Wkg^{-1}.

Morphological analysis post electrochemical cycling indicated how the formation of TMO composites such as the addition of SWCNTS or graphene, increased the over all physical strength of the electrodes specifically in the case of V_2O_5. XRD and XPS analysis indicated how the TMO materials retained their crystal structure and oxidation stated while SEM analysis indicated the continued structural integrity of the electrodes.

In conclusion, this thesis presented a cost-effective and environmentally friendly

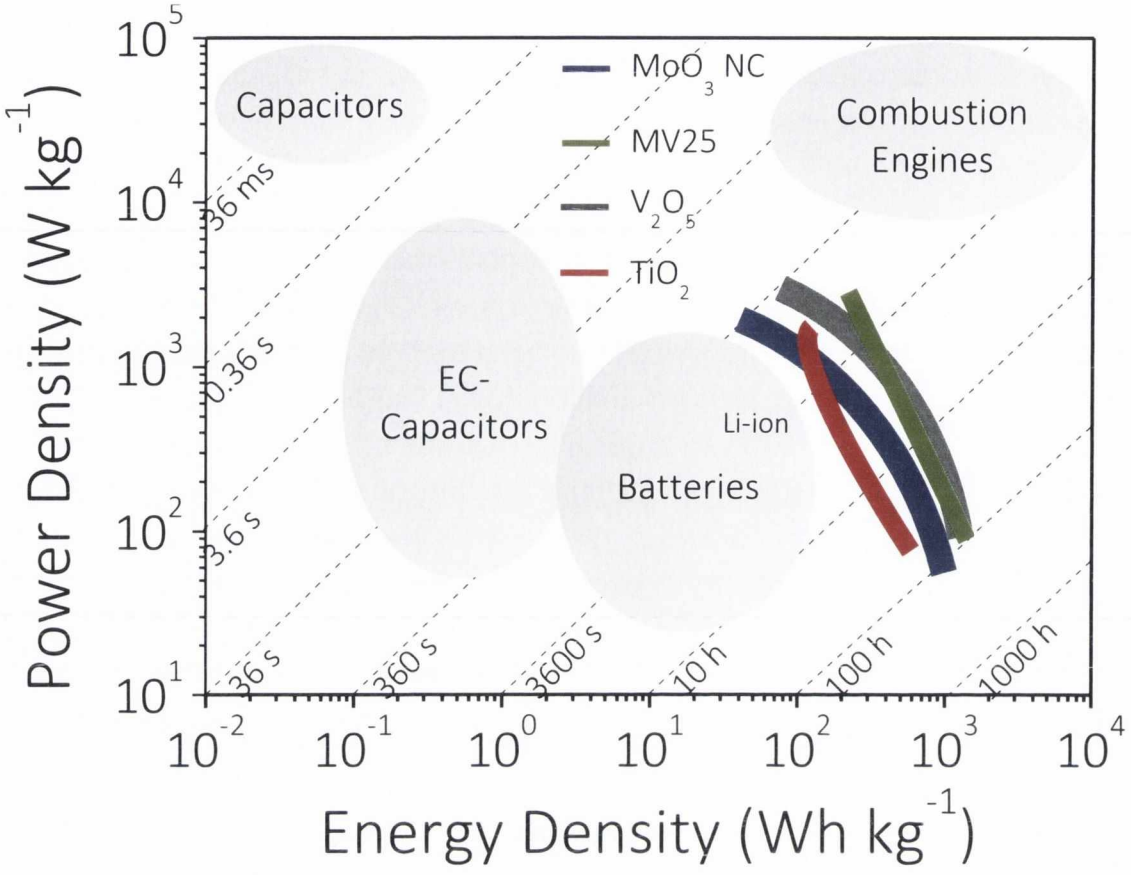


FIGURE 7.1: Ragone plot indicating the energy and power densities of the studied materials relative to conventional energy storage devices.

method to synthesize nanostructured TMO materials using facile LPE techniques. Similarly, ultrasonic spraying methods were employed to fabricate flexible, composite, thin film electrodes demonstrating superior energy and power densities rivalling that of contemporary Li-ion battery and SC materials.

7.1 Outlook

As these ultrasonic synthesis and fabrication techniques are facile and transferable, it may be possible to apply them to a series of electrochemically active nanostructurable materials. The LPE of common Li-ion battery materials such as layered $LiCoO_2$ may increase the relative surface area leading to more pseudocapacitive processes. As such the capacities may exceed the 140 $mAhg^{-1}$. However, as the respective quantity of layers decrease, the amount of interstitial Li-ions already present

in the CoO_2 lattice will decrease due to surface termination. Similarly, the nanostructuring of materials such as $LiFePO_4$ or $LiMn_2O_4$ would act to open diffusion pathways to intercalatable sites.

Further work can be done to understand the stable formation of TMOs in H_2O despite having unfavourable surface tensions. As the Hildebrand parameter is relatively crude, analysis of the Hansen parameters were initially analysed. However, while the dispersion and polar parameters are accurate, the hydrogen bonding parameters that actually encompass all interactions that don't include dispersion and polar are inaccurate. Therefore, it is an inaccurate value which may need further deconvolution to fully explain the interaction parameters, specifically along the lines of surface tensions. A combination of techniques such as contact angle measurements and FTIR may further provide information on the bonding parameters.

Electrochemical analysis of V_2O_5 cathodes synthesised from a wider array of solvents may provide interesting results. Already, an initial test indicated that if V_2O_5 is exfoliated in IPA and subject to electrochemical analysis, the resultant behaviours changes drastically compared to that of H_2O. The discharge capacities remain relatively low, however, as opposed to capacities decreasing over successive cycles, they increase. This may be a result of the lack of interlayer expansion and the subsequent exfoliation of V_2O_5 due to the intercalation of the Li-ions. As a result, more intercalation sites may be accessible over time. This is similar to the ion insertion problem exhibited by graphite electrodes in common Li-ion batteries. Intercalation over time will cause swelling and the subsequent delamination of the graphene sheets reducing the structural integrity of the electrode as a whole. It would also be interesting to have a more practical examination of the xerogel V_2O_5 electrode by the fabrication of full cell devices and further investigation into the application of the high charging properties.

Finally, analysis into the stabilization mechanisms of the V_2O_5/MoO_3 would provide information into their excellent performance. Further electrochemical analysis would also provide information into such concepts as preferential storage sites and percolation thresholds, specifically for devices similar to the MV25 cathode.

Overall, there is much work to be done on these materials if they are ever to be realized as potential high energy replacements for modern energy storage devices.

Bibliography

[1] I. E. Agency, "Energy and climate change", World Energy Outlook Special Report (2015).

[2] P. M. Cox, R. A. Betts, C. D. Jones, S. A. Spall, and I. J. Totterdell, "Acceleration of global warming due to carbon-cycle feedbacks in a coupled climate model", Nature **408**, 184–187 (2000).

[3] M. Pehnt, "Dynamic life cycle assessment (LCa) of renewable energy technologies", Renew. Energ. **31**, 55–71 (2006).

[4] J. B. Goodenough, "Electrochemical energy storage in a sustainable modern society", Energy Environ. Sci. **7**, 14–18 (2014).

[5] M. S. Whittingham, "History, evolution, and future status of energy storage.", Proceedings of the IEEE **100**, 1518–1534 (2012).

[6] H. Chen, T. N. Cong, W. Yang, C. Tan, Y. Li, and Y Ding, "Progress in electrical energy storage system: a critical review", Prog. Nat. Sci. **19**, 291–312 (2009).

[7] T. Christen and M Carlen, "Theory of ragone plots", J. Power Sources **91**, 210–216 (2000).

[8] J. B. Heywood, *Internal combustion engine fundamentals* (New York, 1998).

[9] Q. Wu, Y. Xu, Z. Yao, A. Liu, and G Shi, "Supercapacitors based on flexible graphene/polyaniline nanofiber composite films", ACS Nano **4**, 1963–1970 (2010).

[10] M. Winter and R. J. Brodd, "What are batteries, fuel cells, and supercapacitors?", Chem. Rev. **104**, 4245–4270 (2004).

[11] M. Armand and J.-M. Tarascon, "Building better batteries", Nature **451**, 652–657 (2008).

[12] L. Situ, "Electric vehicle development: the past, present and future", Power Elect. Sys. and App., 1–3 (2009).

[13] A. Khaligh and Z. Li, "Battery, ultracapacitor, fuel cell, and hybrid energy storage systems for electric, hybrid electric, fuel cell, and plug-in hybrid electric vehicles: state of the art", IEEE Trans. Veh. Technol. **59**, 2806–2814 (2010).

[14] A. Burke, "Batteries and ultracapacitors for electric, hybrid, and fuel cell vehicles", Proc. IEEE **95**, 806–820 (2007).

[15] *Retrieved from http://www.climatetechwiki.org/technology/jiqweb-es-batt.*

[16]B. Dibner, *Alessandro volta and the electric battery* (Franklin Watts, 1964).

[17]F. Scholz, "From the leiden jar to the discovery of the glass electrode by max cremer", J. Solid State Electrochem. **15**, 5–14 (2011).

[18]M. E. Weeks, "The discovery of the elements. ix. three alkali metals: potassium, sodium, and lithium", J. Chem. Educ. **9**, 1035 (1932).

[19]G. F. Martins, "Why the daniell cell works!", J. Chem. Educ. **67**, 482 (1990).

[20]W. J. Hamer, *Standard cells: their construction, maintenance, and characteristics* (US Government Printing Office, 1965).

[21]G. Bird, *Report of the seventh meeting of the british society for the advancement of science*, Vol. 6, 45 (J. Murray, 1837).

[22]J. B. Calvert, "The electromagnetic telegraph", (2008).

[23]W. Ayrton, "Practical electricity. cassell and company", Cassell and Company, 183–185 (1911).

[24]U. S. P. Office, *Specifications and drawings of patents relating to electricity issued by the u. s.* (1886).

[25]D. N. C. H. F. McMurdie and G. W. Vinal, "A study of equilibrium reactions in the leclanché dry cell", Journey of the Electrochemical Society **90**, 509–528 (1946).

[26]K. Kordesch, *Rechargeable alkaline mno2-zinc cell*, US Patent 4,091,178, 1978.

[27]*Durocell alkaline-manganese dioxide technical bulletin* ().

[28]P Kurzweil, "Gaston plante and his invention of the lead-acid battery. the genesis of the first practical rechargeable battery", J. Power Sources **195**, 4424–4434 (2010).

[29]H. Bode, *Lead-acid batteries* (John Wiley and Sons Inc., New York, NY, 1977).

[30]D. A. J. Rand and R. Woods, *Batteries for electric vehicles* (1981).

[31]T. Eguro, "Ni-cadmium batteries", in *Encyclopedia of applied electrochemistry*, edited by G. Kreysa, K. Ota, and R. F. Savinell (Springer New York, New York, NY, 2014), pp. 1358–1363.

[32]*Enegizer: nickel metal hydride (nimh) handbook and application manual* ().

[33]T. Sakai, I. Uehara, and H. Ishikawa, "R&d on metal hydride materials and ni-mh batteries in Japan", J. Alloys Compd. **293-295**, 762–769 (1999).

[34]M. S. Whittingham, "Lithium batteries and cathode materials", Chem. Rev. **104**, 4271–4302 (2004).

[35]J.-M. Tarascon and M. Armand, "Issues and challenges facing rechargeable lithium batteries", Nature **414**, 359–367 (2001).

[36]M. S. Whittingham, "Electrical energy storage and intercalation chemistry", Science **192**, 1126–1127 (1976).

[37]J. Dahn, W. McKinnon, R. R. Haering, W. J. L. Buyers, and B. M. Powell, "Structure determination of lixtis2 by neutron diffraction", Can. J. Phys. **58**, 207–213 (1980).

[38]P. W. K. Mizushima P.C. Jones and J. Goodenough, "New cathode material for batteries of high energy density", Mat. Res. Bull. **15**, 783–78 (1980).

[39]J. B. Goodenough and K. Park, "The li-ion rechargeable battery: a perspective", J. Am. Chem. Soc. **135**, 1167–1176 (2013).

[40]M. Dresselhaus and G. Dresselhaus, "Intercalation compounds of graphite", Adv. Phys. **30**, 139–326 (1981).

[41]S. S. Zhang, K. Xu, and T. R. Jow, "Study of the charging process of a licoo2-based li-ion battery", J. Power Sources **160**, 1349–1354 (2006).

[42]S. Lany, "Semiconducting transition metal oxides", J. Phys.: Condens. Matter **27**, 283203 (2015).

[43]E. Takeuchi, R. Mead, and C. Post, *Process for making cathode components for use in electrochemical cells*, US Patent 5,435,874, 1995.

[44]W.-J. Zhang, "Structure and performance of lifepo4 cathode materials: a review", J. Power Sources **196**, 2962–2970 (2011).

[45]H. Li, Z. Wang, L. Chen, and X. Huang, "Research on advanced materials for li-ion batteries", Adv. Mater. **21**, 4593–4607 (2009).

[46]H. W. Lee, P. Muralidharan, R. Ruffo, C. M. Mari, Y Cui, and D. K. Kim, "Ultrathin spinel limn2o4 nanowires as high power cathode materials for li-ion batteries", Nano Letters **10**, 3852–3856 (2010).

[47]M. Pumera, Z. Sofer, and A. Ambrosi, "Layered transition metal dichalcogenides for electrochemical energy generation and storage", J. Mater. Chem. A **2**, 8981–8987 (2014).

[48]S. Goriparti, E. Miele, F. De Angelis, E Di Fabrizio, R. P. Zaccaria, and C Capiglia, "Review on recent progress of nanostructured anode materials for li-ion batteries", J. Power Sources **257**, 421–443 (2014).

[49]L. Ji, Z. Lin, M. Alcoutlabi, and X. Zhang, "Recent developments in nanostructured anode materials for rechargeable lithium-ion batteries", Energy Environ. Sci. **4**, 2682–2699 (2011).

[50]K. Amine, I. Belharouak, Z. Chen, T. Tran, H. Yumoto, N. Ota, S.-T. Myung, and Y.-K. Sun, "Nanostructured anode material for high-power battery system in electric vehicles", Adv. Mater. **22**, 3052–3057 (2010).

[51]V. Etacheri, R. Marom, R. Elazari, G. Salitra, and D. Aurbach, "Challenges in the development of advanced li-ion batteries: a review", Energy Environ. Sci. **4** (2011).

[52]F. Joho, P. Novak, and M. E. Spahr, "Safety aspects of graphite negative electrode materials for lithium-ion batteries", J. Electrochem. Soc. **149**, A1020–A1024 (2002).

[53]D. Aurbach, E. Zinigrad, Y. Cohen, and H. Teller, "A short review of failure mechanisms of lithium metal and lithiated graphite anodes in liquid electrolyte solutions", Solid State Ion. **148**, 405–416 (2002).

[54]S. Zhang, M. S. Ding, K. Xu, J. Allen, and T. R. Jow, "Understanding solid electrolyte interface film formation on graphite electrodes", Electrochem. Solid-State Lett. **4 (12)**, A206–A208 (2001).

[55]Z.-I. Takehara, "Future prospects of the lithium metal anode", Journal of Power Sources **68**, 82–86 (1997).

[56]J. Hou, Y. Shao, M. W. Ellis, R. B. Moore, and B. Yi, "Graphene-based electrochemical energy conversion and storage: fuel cells supercapacitors and lithium ion batteries", Phys. Chem. Chem. Phys. **13**, 15384–15402 (2011).

[57]M. Ge, J. Rong, X. Fang, and C. Zhou, "Porous doped silicon nanowires for lithium ion battery anode with long cycle life", Nano Lett. **12**, 2318–2323 (2012).

[58]J. Yang, Y. Takeda, N. Imanishi, C. Capiglia, J. Xie, and O. Yamamoto, "Sio x-based anodes for secondary lithium batteries", Solid State Ion **152**, 125–129 (2002).

[59]J. S. Chen, Y. Tan, C. M. Li, Y. L. Cheah, D. Luan, S. Madhavi, F. Y. C. Boey, L. A. Archer, and X. W. Lou, "Constructing hierarchical spheres from large ultrathin anatase tio2 nanosheets with nearly 100% exposed (001) facets for fast reversible lithium storage", J. Am. Chem. Soc. **132**, 6124–6130 (2010).

[60]A. Burke, "Ultracapacitors: why, how, and where is the technology", J. Power Sources **91**, 37–50 (2000).

[61]A. K. Shukla, A. Banerjee, M. K. Ravikumar, and A. Jalajakshi, "Electrochemical capacitors: technical challenges and prognosis for future markets", Electrochim. Acta **84**, 165–173 (2012).

[62]J. R. Miller and P. Simon, "Electrochemical capacitors for energy management", Science **321**, 651–652 (2008).

[63]R. Katz and M. Carlen, "Principles and applications of electrochemical capacitors", Electrochim. Acta **45**, 2483–2498 (2000).

[64]H. Becker, *Low voltage electrolytic capacitor*, US Patent 2,800,616, 1957.

[65]R. Rightmire, *Electrical energy storage apparatus*, US Patent 3,288,641, 1966.

[66]J. Mierlo, P. Bossche, and G. Maggetto, "Models of energy sources for EV and hev: fuel cells, batteries, ultracapacitors, flywheels and engine-generators", J. Power Sources **128**, 76–89 (2004).

[67]A Burke and M. Miller, "The power capability of ultracapacitors and lithium batteries for electric and hybrid vehicle applications", J. Power Sources **196**, 514–522 (2011).

[68]*Industryarc global supercapacitor market (2014-2020).*

[69]*Murata technical guide of electrical double layer capacitor* (2015).

[70]A. Pandolfo and A. Hollenkamp, "Carbon properties and their role in supercapacitors", J. Power Sources **157**, 11–27 (2006).

[71]B. Conway, Briss, and W. J., "The role and utilization of pseudocapacitance for energy storage by supercapacitors", J. Power Sources **66**, 1–14 (1997).

[72]B. E. Conway and W. G. Pell, "Double-layer and pseudocapacitance types of electrochemical capacitors and their applications to the development of hybrid devices", J. Solid State Electrochem. **7**, 637–644 (2003).

[73]P. Simon and Y. Gogotsi, "Materials for electrochemical capacitors", Nat. Mater. **7**, 845–854 (2008).

[74]M. D. Stoller, S. Park, Y. Zhu, J. An, and R. S. Ruoff, "Graphene-based ultracapacitors", Nano Lett. **8**, 3498–3502 (2008).

[75]A. Hirsch, "The era of carbon allotropes", Nat Mater **9**, 868–871 (2010).

[76]E. Frackowiak and F. Beguin, "Carbon materials for the electrochemical storage of energy in capacitors", Carbon **39**, 937–950 (2001).

[77]M. S. Dresselhaus, G. Dresselhaus, and P. Eklund, *Science of fullerenes and carbon nanotubes: their properties and applications.* (Academic press, 1996).

[78]A. Nikitin and Y. Gogotsi, *"nanostructured carbide-derived carbon." encyclopedia of nanoscience and nanotechnology 10* (2004).

[79]H. Shi, "Activated carbons and double layer capacitance", Electrochim. Acta **41**, 1633–1639 (1996).

[80]L. Dai, D. W. Chang, J.-B. Baek, and W. Lu, "Carbon nanomaterials for advanced energy conversion and storage", Small (2012).

[81]Y. Wang, Z. Shi, Y. Huang, Y. Ma, C. Wang, M. Chen, and Y. Chen, "Supercapacitor devices based on graphene materials", J. Phys. Chem. C **113**, 13103–13107 (2009).

[82]R. W. Pekala, J. C. Farmer, C. T. Alviso, T. D. Tran, S. T. Mayer, J. M. Miller, and B. Dunn, "Carbon aerogels for electrochemical applications", J. Non-Cryst. Solids **225**, 74–80 (1998).

[83]Y. Zhang, H. Feng, X. Wu, L. Wang, A. Zhang, T. Xia, H. Dong, X. Li, and L. Zhang, "Progress of electrochemical capacitor electrode materials: a review", Int. J. Hydrogen Energy **34**, 4889–4899 (2009).

[84]G. Wang, L. Zhang, and J. Zhang, "A review of electrode materials for electrochemical supercapacitors", Chem. Soc. Rev. **41**, 797–828 (2012).

[85]P. J. C. J. P. Zheng and T. R. Jow, "Hydrous ruthenium oxide as an electrode material for electrochemical capacitors", J. Electrochem. Soc. **142**, 2699–2703 (1995).

[86]C. Hu, K. Chang, M. Lin, and Y. Wu, "Design and tailoring of the nanotubular arrayed architecture of hydrous ruo2 for next generation supercapacitors", Nano Lett. **6**, 2690–2695 (2006).

[87]S. Chen, J. Zhu, X. Wu, Q. Han, and X Wang, "Graphene oxide/mno2 nanocomposites for supercapacitors", ACS Nano **4**, 2822–2830 (2010).

[88]M. Toupin, T. Brousse, and D. Balanger, "Charge storage mechanism of mno2 electrode used in aqueous electrochemical capacitor", Chem. Mater. **16**, 3184–3190 (2004).

[89]T. A. Skotheim, *Handbook of conducting polymers* (CRC press, 1997).

[90]P. Novak, K. Maller, and K. Santhanam, "Electrochemically active polymers for rechargeable batteries", Chem. Rev. **97**, 207–282 (1997).

[91]A. Rudge, J. Davey, I. Raistrick, S. Gottesfeld, and J. P. Ferraris, "Conducting polymers as active materials in electrochemical capacitors", J. Power Sources **47**, 89–107 (1994).

[92]S. R. K., A. C. Rastogi, and S. B. Desu, "Pulse polymerized polypyrrole electrodes for high energy density electrochemical supercapacitor", Electrochem. Commun. **10**, 268–272 (2008).

[93]K. S. Ryu, Y.-G. Lee, Y.-S. Hong, Y. J. Park, X. Wu, K. M. Kim, M. G. Kang, N.-G. Park, and S. H. Chang, "Poly(ethylenedioxythiophene) (pedot) as polymer electrode in redox supercapacitor", Electrochim. Acta **50**, 843–847 (2004).

[94]R. P Feynman, "Here's plenty of room at the bottom", Engineering and science **23**, 22–36 (1960).

[95]G. Whitesides, "Nanoscience, nanotechnology, and chemistry", Small **1**, 172–179 (2005).

[96]T. Braun, A. Schubert, and S. Zsindely, "Nanoscience and nanotecnology on the balance", Scientometrics **38**, 321–325 (1997).

[97]V. Nicolosi, M. Chhowalla, M. G. Kanatzidis, M. S. Strano, and J. N. Coleman, "Liquid exfoliation of layered materials", Science **340** (2013).

[98]S. Z. Butler, S. M. Hollen, L. Cao, Y. Cui, J. A. Gupta, H. Gutierrez, T. F. Heinz, S. S. Hong, J. Huang, A. F. Ismach, E. Johnston-Halperin, M. Kuno, V. V. Plashnitsa, R. D. Robinson, R. S. Ruoff, S. Salahuddin, J. Shan, L. Shi, M. Spencer, M. Terrones,

W. Windl, and J. E. Goldberger, "Progress, challenges, and opportunities in two-dimensional materials beyond graphene", ACS Nano **7**, 2898–2926 (2013).

[99]M. Xu, T. Liang, M. Shi, and H Chen, "Graphene-like two-dimensional materials", Chem. Rev. **113**, 3766–3798 (2013).

[100]A. P. Alivisatos, "Semiconductor clusters, nanocrystals, and quantum dots", Science **271**, 933 (1996).

[101]D. Loss and D. P. DiVincenzo, "Quantum computation with quantum dots", Phys. Rev. A **57**, 120–126 (1998).

[102]X. Michalet, F. F. Pinaud, L. A. Bentolila, J. M. Tsay, S. Doose, J. J. Li, G. Sundaresan, A. M. Wu, S. S. Gambhir, and S. Weiss, "Quantum dots for live cells, in vivo imaging, and diagnostics", Science **307**, 538–544 (2005).

[103]H. W. Kroto, J. Heath, S. C. O'Brien, R. F. Curl, and R. E. Smalley, "C 60: buckminsterfullerene", Nature **318**, 162–163 (1985).

[104]R. H. Baughman, A. A. Zakhidov, and W. A. Heer, "Carbon nanotubes–the route toward applications", Science **297**, 787–792 (2002).

[105]N. Chopra, R. J. Luyken, K Cherrey, and V. H. Crespi, "Boron nitride nanotubes", Science **269**, 966 (1995).

[106]Y. Xia, P. Yang, Y. Sun, Y. Wu, B. Mayers, B. Gates, Y. Yin, F. Kim, and H. Yan, "One-dimensional nanostructures: synthesis, characterization, and applications", Adv. Mater **15**, 353–389 (2003).

[107]A. McWilliams, *Nanotechnology: a realistic market assessment*, Markey Research (BCCResearch, 2014).

[108]*Retrieved from* $https://polymersandmonomers.wikispaces.com/?responsetoken=eae7607a5$
$0030919597cdaf236a701a9$.

[109]*Retrieved from https://www.tedpella.com/gold_html/gold-colloids-wcopy.jpg.*

[110]*Retrieved from http://i.imgur.com/hazupaj.jpg.*

[111]*Retrieved from http://www.gaia3d.co.uk/3d-models/3d-chemistry/large-molecule/.*

[112]*Retrieved from http://www.gaia3d.co.uk/3d-models/3d-chemistry/carbon-nanotube/.*

[113]*Retrieved from https://d.ibtimes.co.uk/en/full/1446721/quantum-dot.jpg.*

[114]*Retrieved from http://www.turbosquid.com/search/index.cfm?keyword=.*

[115]*Retrieved from http://eandt.theiet.org/news/2014/jun/graphene-in-cars.cfm.*

[116]S. Marchesan and M. Prato, "Nanomaterials for nanomedicine", ACS Med. Chem. Lett. **4**, 147–149 (2013).

[117]O. Salata, "Applications of nanoparticles in biology and medicine", J. Nanobiotechnology **2**, 1–6 (2004).

[118]M. De, P. S. Ghosh, and V. M. Rotello, "Applications of nanoparticles in biology", Adv. Mater. **20**, 4225–4241 (2008).

[119]P. G. Bruce, B. Scrosati, and J. M. Tarascon, "Nanomaterials for rechargeable lithium batteries", Angew. Chem. Int. Ed. **47**, 2930–2946 (2008).

[120]A. S. Arico, P. Bruce, B. Scrosati, J.-M. Tarascon, and W. Schalkwijk, "Nanostructured materials for advanced energy conversion and storage devices", Nat. Mater. **4**, 366–377 (2005).

[121]J. Ahn, H. Kim, K. Lee, S. Jeon, S. Kang, Y. Sun, R. G. Nuzzo, and J. A. Rogers, "Heterogeneous three-dimensional electronics by use of printed semiconductor nanomaterials", Science **314**, 1754–1757 (2006).

[122]R. R. Schaller, "Moores law past, present and future", IEEE Spectrum **34**, 52–59 (1997).

[123]S. J. Klaine, P. J. J. Alvarez, G. E. Batley, T. F. Fernandes, R. D. Handy, D. Y. Lyon, S. Mahendra, M. J. McLaughlin, and J. R. Lead, "Nanomaterials in the environment: behavior, fate, bioavailability, and effects", Environ. Toxicol. Chem. **27**, 1825–1851 (2008).

[124]V. L. Colvin, "The potential environmental impact of engineered nanomaterials", Nat. Biotech. **21**, 1166–1170 (2003).

[125]U. Leonhardt, "Invisibility cup", Nat. Photonics **1**, 207–208 (2007).

[126]F. E. Wagner, S. Haslbeck, L. Stievano, S. Calogero, Q. A. Pankhurst, and K. P. Martinek, "Before striking gold in gold-ruby glass", Nature **407**, 691–692 (2000).

[127]B. Song, R. Yang, N. Xi, K. C. Patterson, C. Qu, and K. W. C. Lai, "Cellular-level surgery using nano robots", J. Lab. Autom **17**, 425–434 (2012).

[128]A. S. Edelstein and R. C. Cammaratra, *Nanomaterials synthesis, properties and applications.* (CRC press, 1998).

[129]G. Eda, G. Fanchini, and M. Chhowalla, "Large-area ultrathin films of reduced graphene oxide as a transparent and flexible electronic material", Nat Nano **3**, 270–274 (2008).

[130]V. Wagner, A. Dullaart, A.-K. Bock, and A. Zweck, "The emerging nanomedicine landscape", Nat Biotech **24**, 1211–1217 (2006).

[131]J. Wang, "Nanomaterial-based electrochemical biosensors", Analyst **130**, 421–426 (2005).

[132]D. Liu and G. Cao, "Engineering nanostructured electrodes and fabrication of film electrodes for efficient lithium ion intercalation", Energy Environ. Sci. **3**, 1218–1237 (2010).

[133]P. Chen, H. Chen, J. Qiu, and C. Zhou, "Inkjet printing of single-walled carbon nanotube/ruo2 nanowire supercapacitors on cloth fabrics and flexible substrates", Nano Res. **3**, 594–603 (2010).

[134]F. Levy, *Intercalated layered materials*, Vol. 6 (Springer Science & Business Media, 2012).

[135]J. N. Coleman, M. Lotya, A. O'Neill, S. D. Bergin, P. J. King, U. Khan, K. Young, A. Gaucher, S. De, R. J. Smith, I. V. Shvets, S. K. Arora, G. Stanton, H. Kim, K. Lee, T. Kim, G. S. Duesberg, T. Hallam, J. J. Boland, J. J. Wang, J. F. Donegan, J. C. Grunlan, A. Moriarty G.and Shmeliov, R. J. Nicholls, J. M. Perkins, E. M. Grieveson, K. Theuwissen, D. W. McComb, P. D. Nellist, and V. Nicolosi, "Two-dimensional nanosheets produced by liquid exfoliation of layered materials", Science **331**, 568–571 (2011).

[136]K. S. Novoselov, A. K. Geim, S. V. Morozov, D. Jiang, Y. Zhang, S. V. Dubonos, I. V. Grigorieva, and A. A. Firsov, "Electric field effect in atomically thin carbon films", Science **306**, 666–669 (2004).

[137]F. Bonaccorso, L. Colombo, G. Yu, M. Stoller, V. Tozzini, A. C. Ferrari, R. S. Ruoff, and V. Pellegrini, "Graphene, related two-dimensional crystals, and hybrid systems for energy conversion and storage", Science **347** (2015).

[138]A. K. Geim and K. S. Novoselov, "The rise of graphene", Nat. Mater. **6**, 183–191 (2007).

[139]C. Lee, X. Wei, J. W. Kysar, and J. Hone, "Measurement of the elastic properties and intrinsic strength of monolayer graphene", Science **321**, 385–388 (2008).

[140]G. Xin, T. Yao, H. Sun, S. M. Scott, D. Shao, G. Wang, and J. Lian, "Highly thermally conductive and mechanically strong graphene fibers", Science **349**, 1083–1087 (2015).

[141]A. K. Geim, "Graphene: status and prospects", Science **324**, 1530–1534 (2009).

[142]L. H. Li, Y. Chen, G. Behan, H. Zhang, M. Petravic, and A. M. Glushenkov, "Large-scale mechanical peeling of boron nitride nanosheets by low-energy ball milling", J. Mater. Chem. **21**, 11862–11866 (2011).

[143]A. S. Golub, Y. V. Zubavichus, Y. L. Slovokhotov, and Y. N. Novikov, "Single-layer dispersions of transition metal dichalcogenides in the synthesis of intercalation compounds", Russ. Chem. Rev. **72**, 123–141 (2003).

[144]M. Losurdo, M. M. Giangregorio, P. Capezzuto, and G. Bruno, "Graphene cvd growth on copper and nickel: role of hydrogen in kinetics and structure", Phys. Chem. Chem. Phys. **13**, 20836–20843 (2011).

[145]S. Stankovich, D. A. Dikin, R. D. Piner, K. A. Kohlhaas, A. Kleinhammes, Y. Jia, Y. Wu, S. T. Nguyen, and R. S. Ruoff, "Synthesis of graphene-based nanosheets via chemical reduction of exfoliated graphite oxide", Carbon **45**, 1558–1565 (2007).

[146]K. R. Paton, E. Varrla, C. Backes, R. J. Smith, U. Khan, A. O'Neill, C. Boland, M. Lotya, O. M. Istrate, P. King, T. Higgins, S. Barwich, P. May, P. Puczkarski, I. Ahmed, M. Moebius, H. Pettersson, E. Long, J. Coelho, S. E. O'Brien, E. K. McGuire, G. S. Mendoza Sanchez B.and Duesberg, N. McEvoy, T. J. Pennycook, C. Downing, A. Crossley, V. Nicolosi, and J. N. Coleman, "Scalable production of large quantities of defect-free few-layer graphene by shear exfoliation in liquids", Nat. Mater. **13**, 624–630 (2014).

[147]Y. Hernandez, V. Nicolosi, M. Lotya, F. M. Blighe, Z. Sun, S. De, T. McGovern, B. Holland, M. Byrne, Y. K. Gun'Ko, J. J. Boland, P. Niraj, G. S. Duesberg, S. Krishnamurthy, R. Goodhue, J. Hutchison, V. Scardaci, A. C. Ferrari, and J. N. Coleman, "High-yield production of graphene by liquid-phase exfoliation of graphite", Nat Nano **3**, 563–568 (2008).

[148]C. Jiang, E. Hosono, and H Zhou, "Nanomaterials for lithium ion batteries", Nano Today **1**, 28–33 (2006).

[149]P. Poizot, S. Laruelle, S. Grugeon, L. Dupont, and J.-M. Tarascon, "Nano-sized transition-metal oxides as negative-electrode materials for lithium-ion batteries", Nature **407**, 496–499 (2000).

[150]J. Desilvestro and O. Haas, "Metal oxide cathode materials for electrochemical energy storage: a review", J. Electrochem. Soc. **137**, 5C–22C (1990).

[151]X. Rui, Z. Lu, H. Yu, D. Yang, H. H. Hng, T. M. Lim, and Q. Yan, "Ultrathin v2o5 nanosheet cathodes: realizing ultrafast reversible lithium storage", Nanoscale **5**, 556–560 (2013).

[152]L. Zhou, L. Yang, P. Yuan, J. Zou, Y. Wu, and C. Yu, "Alpha-moo3 nanobelts: a high performance cathode material for lithium ion batteries", J. Phys. Chem. C **114**, 21868–21872 (2010).

[153]R. E. White, *Electrochemical cell design* (Springer Science & Business Media, 2012).

[154]J. Arntzen, *Electrochemical cell design*, US Patent 4,110,517, 1978.

[155]M. Lu, F. Beguin, and E. Frackowiak, *Supercapacitors: materials, systems and applications* (John Wiley & Sons, 2013).

[156]D. Linden, *Handbook of batteries and fuel cells* (New York, McGraw-Hill Book Co., 1984).

[157]B. Andresen, R. S. Berry, A. Nitzan, and P. Salamon, "Thermodynamics in finite time. i. the step-carnot cycle", Phys. Rev. A **15**, 2086–2093 (1977).

[158]A. J. Bard, L. R. Faulkner, J. Leddy, and C. G. Zoski, *Electrochemical methods: fundamentals and applications*, Vol. 2 (Wiley New York, 1980).

[159]A. J. Bard, R. Parsons, and J. Jordan, *Standard potentials in aqueous solution*, Vol. 6 (CRC press, 1985).

[160]P. W. Atkins and J. A. Beran, *General chemistry* (Scientific americal books, 1992).

[161]G. Milazzo, S. Caroli, and R. D. Braun, "Tables of standard electrode potentials", J Electrochem Soc **125**, 261C–261C (1978).

[162]M. Park, X. Zhang, M. Chung, G. B. Less, and A. M. Sastry, "A review of conduction phenomena in li-ion batteries", J. Power Sources **195**, 7904–7929 (2010).

[163]D. J. G. Ives, G. J. Janz, and C. King, "Reference electrodes: theory and practice", J. Electrochem. Soc. **108**, 246C–247C (1961).

[164]R. G. Compton and G. Sanders, *Electrode potentials* (Oxford University Press, 1996).

[165]C. H. P. Lupis, "Chemical thermodynamics of materials", Elsevier Science Publishing Co., 581 (1983).

[166]R. G. Compton and C. E. Banks, *Understanding voltammetry* (World Scientific, 2007).

[167]G. Cook and R. Dickerson, "Understanding the chemical potential", Am. J. Phys **63**, 737–742 (1995).

[168]G Job and F. Herrmann, "Chemical potential: a quantity in search of recognition", Eur. J. Phys. **27**, 353 (2006).

[169]W Nernst, "Theory of reaction velocity in heterogenous systems", Zeit. physikal. Chem **47**, 52–55 (1904).

[170]P. Bruce, *Solid state electrochemistry*, Vol. 5 (Cambridge University Press, 1997).

[171]K. J. Vetter, *Electrochemical kinetics: theoretical aspects* (Elsevier, 2013).

[172]J. Bockris and S. Khan, *Quantum electrochemistry* (Springer Science & Business Media, 2012).

[173]S. Arrhenius, *Uber die dissociation der in wasser gelosten stoffe* (Verlag von Wilhelm Engelmann, 1887).

[174]J. A. V. Butler, "Studies in heterogeneous equilibria. part ii.-the kinetic interpretation of the nernst theory of electromotive force", Trans. Faraday Soc. **19**, 729–733 (1924).

[175]J. A. V. Butler, "Hydrogen overvoltage and the reversible hydrogen electrode", Proc. R. Soc. A **157**, 423–433 (1936).

[176]N. Sato, "Some concepts of corrosion fundamentals", Corros. Sci. **27**, 421–433 (1987).

[177]D. A. Proshlyakov, M. A. Pressler, C. DeMaso, J. F. Leykam, D. L. DeWitt, and G. T. Babcock, "Oxygen activation and reduction in respiration: involvement of redox-active tyrosine 244", Science **290**, 1588–1591 (2000).

[178]J. Ingenhousz, *Experiments upon vegetables: discovering their great power of purifying the common air in the sun-shine, and of injuring it in the shade and at night. to which is joined, a new method of examining the accurate degree of salubrity of the atmosphere* (Printed for Elmsly, P. and Payne, H., 1779).

[179]R. W. Erickson and D. Maksimovic, *Fundamentals of power electronics* (Springer Science & Business Media, 2007).

[180]R Taylor, H. Marsh, E. Heintz, and F. Rodriguez-Reinoso, *Introduction to carbon technologies* (ed. Marsh, H, 1997).

[181]D. Boos, *Electrolytic capacitor having carbon paste electrodes*, US Patent 3,536,963, 1970.

[182]B. E. Conway, *Electrochemical supercapacitors: scientific fundamentals and technological applications* (Springer Science & Business Media, 2013).

[183]H. Helmholtz, "Ueber einige gesetze der vertheilung elektrischer ströme in körperlichen leitern mit anwendung auf die thierisch-elektrischen versuche", Ann. Phys. **165**, 211–233 (1853).

[184]H. L. Helmholtz, Weid. Ann. **7**, 337 (1897).

[185]G Gouy, "Constitution of the electric charge at the surface of an electrolyte", J. phys **9**, 457–467 (1910).

[186]D. L. Chapman, "Li. a contribution to the theory of electrocapillarity", Philos. Mag. **25**, 475–481 (1913).

[187]O. Stern, "The theory of the electrolytic double-layer", Z. Elektrochem **30**, 1014–1020 (1924).

[188]D. C. Grahame, "The electrical double layer and the theory of electrocapillarity.", Chem. Rev. **41**, 441–501 (1947).

[189]J. O. M. Bockris, M. A. V. Devanathan, and K. Muller, "On the structure of charged interfaces", Proc. R. Soc. A **274**, 55–79 (1963).

[190]S. Srinivasan, *Fuel cells from fundamentals to applications* (Springer Science and Business media, 2006).

[191]V. Augustyn, P. Simon, and B. Dunn, "Pseudocapacitive oxide materials for high-rate electrochemical energy storage", Energy Environ. Sci. **7**, 1597–1614 (2014).

[192]J. Crank, *The mathematics of diffusion* (Oxford university press, 1979).

[193]J. Philibert, "One and a half century of diffusion: fick, Einstein, before and beyond", Diffusion Fundamentals **4**, 1–19 (2006).

[194]A. Fick, "V. on liquid diffusion", Philos. Mag. **10**, 30–39 (1855).

[195]D. J. DiMaria and J. H. Stathis, "Explanation for the oxide thickness dependence of breakdown characteristics of metal-oxide-semiconductor structures", Appl. Phys. Lett. **70**, 2708–2710 (1997).

[196]F. Cottrell, "Application of the cottrell equation to chronoamperometry", Z Physik Chem **42**, 385 (1902).

[197]W. B. Russel, D. A. Saville, and W. R. Schowalter, *Colloidal dispersions* (Cambridge university press, 1989).

[198]J. H. Hildebrand, "Solubility", (1924).

[199]J. H. Hildebrand et al., "Solubility of non-electrolytes", (1936).

[200]C. M. Hansen, "The universality of the solubility parameter", Ind. Eng. Chem. Res. **8**, 2–11 (1969).

[201]C. M. Hansen, *Hansen solubility parameters: a user's handbook* (CRC press, 2007).

[202]R Klein and P Meakin, "Universality in colloid aggregation", Nature **339** (1989).

[203]J.-W. Kim, D. Lee, H. C. Shum, and D. A. Weitz, "Colloid surfactants for emulsion stabilization", Adv. Mater. **20**, 3239–3243 (2008).

[204]B. V. Derjaguin, L. Landau, et al., "Theory of the stability of strongly charged lyophobic sols and of the adhesion of strongly charged particles in solutions of electrolytes", Acta physicochim. U.R.S.S. **14**, 633–662 (1941).

[205]E. Verwey and J. T. G. Overbeek, *Theory of lyophobic colloids*, 1948.

[206]H. Hamaker, "The london van der waals attraction between spherical particles", physica **4**, 1058–1072 (1937).

[207]M. Lotya, Y. Hernandez, P. J. King, R. J. Smith, V. Nicolosi, L. S. Karlsson, F. M. Blighe, S. De, Z. Wang, and I. McGovern, "Liquid phase production of graphene by exfoliation of graphite in surfactant/water solutions", J. Am. Chem. Soc. **131**, 3611–3620 (2009).

[208]C. E. Brennen, *Cavitation and bubble dynamics* (Cambridge University Press, 2013).

[209]A. Charles, "Theory of centrifugation", Ind. Eng. Chem. Res. **53**, 430–433 (1961).

[210]D. Hanlon, C. Backes, T. M. Hggins, M. Hughes, A. O'Neill, P. King, N. McEvoy, G. Duesberg, B Mendoza Sanchez, H. Pettersson, V. Nicolosi, and J. N. Coleman, "Production of molybdenum trioxide nanosheets by liquid exfoliation and their application in high-performance supercapacitors", Chem. Mater. **26**, 1751–1763 (2014).

[211]L. Bayvel, *Liquid atomization*, Vol. 1040, 2756 (CRC Press, 1993).

[212]J. Anthony, *Ultrasonic spraying device*, US Patent 4,815,661, 1989.

[213]J. Soth and J. Klemm, *Ultrasonic spray nozzle and method*, US Patent 4,659,014, 1987.

[214]H.-H. Perkampus, H.-C. Grinter, and T. Threlfall, *UV-vis spectroscopy and its applications* (Springer, 1992).

[215]P. Bouguer, *Essai d'optique sur la gradation de la lumiere* (Jombert, 1729).

[216]J. H. Lambert and D. L. DiLaura, *Photometry, or, on the measure and gradations of light, colors, and shade: translation from the latin of photometria, sive, de mensura et gradibus luminis, colorum et umbrae* (Illuminating Engineering Society of North America, 2001).

[217]A. Beer, "Determination of the absorption of red light in colored liquids", Ann. Phys. Chem **86**, 78–88 (1852).

[218]D. B. Williams and C. B. Carter, "The transmission electron microscope", in *Transmission electron microscopy* (Springer, 1996), pp. 3–17.

[219]J. Goldstein, D. E. Newbury, P. Echlin, D. C. Joy, A. D. Romig Jr, C. E. Lyman, C. Fiori, and E. Lifshin, *Scanning electron microscopy and x-ray microanalysis: a text for biologists, materials scientists, and geologists* (Springer Science & Business Media, 2012).

[220]L. Rayleigh, "Xxxi. investigations in optics, with special reference to the spectroscope", Philos. Mag. **8**, 261–274 (1879).

[221]L. Broglie, "Xxxv. a tentative theory of light quanta", Philos. Mag. **47**, 446–458 (1924).

[222]E. Ruska and M. Knoll, "The magnetic concentrating coil for fast electron beams", Z. techn. Physik **12**, 389–400 (1931).

[223]O. L. Krivanek, M. F. Chisholm, V. Nicolosi, T. J. Pennycook, G. J. Corbin, N. Dellby, M. F. Murfitt, C. S. Own, Z. S. Szilagyi, M. P. Oxley, S. T. Pantelides, and S. J. Pennycook, "Atom-by-atom structural and chemical analysis by annular dark-field electron microscopy", Nature **464**, 571–574 (2010).

[224]D. A. Muller, L. F. Kourkoutis, M. Murfitt, J. H. Song, H. Y. Hwang, J. Silcox, N. Dellby, and O. L. Krivanek, "Atomic-scale chemical imaging of composition and bonding by aberration-corrected microscopy", Science **319**, 1073–1076 (2008).

[225]R. F. Egerton, *Electron energy-loss spectroscopy in the electron microscope* (Springer Science & Business Media, 2011).

[226]D. Shindo and T. Oikawa, "Energy dispersive x-ray spectroscopy", in *Analytical electron microscopy for materials science* (Springer, 2002), pp. 81–102.

[227]S. Brunauer, P. Emmett, and E. Teller, "Adsorption of gases in multimolecular layers", J. Am. Chem. Soc. **60**, 309–319 (1938).

[228]K. Oura, V. Lifshits, A. Saranin, A. Zotov, and M Katayama, *Surface science: an introduction* (Springer Science & Business Media, 2013).

[229]I. Langmuir, "The adsorption of gases on plane surfaces of glass mica and platinum.", J. Am. Chem. Soc. **40**, 1361–1403 (1918).

[230]H. P. Klug, L. E. Alexander, et al., *X-ray diffraction procedures*, Vol. 2 (Wiley New York, 1954).

[231]W. H. Bragg and B. W. L., "The reflection of x-rays by crystals", Proc. R. Soc. A **88**, 428–438 (1913).

[232]E. Prince and A. J. C. Wilson, "International tables for crystallography", (2004).

[233]J. F. Watts and J. Wolstenholme, *An introduction to surface analysis by xps and AES* (Wiley-VCH, 2003).

[234]K. Siegbahn, *Esca: atomic, molecular and solid state structure studied by means of electron spectroscopy*, Vol. 20 (Almqvist & Wiksells, 1967).

[235]A. Einstein, "Ist die tragheit eines karpers von seinem energieinhalt abhangig?", Ann. Phys. **323**, 639–641 (1905).

[236]T. Carlson, *Photoelectron and auger spectroscopy* (Springer Science & Business Media, 2013).

[237]P. Kissinger and W. R. Heineman, *Laboratory techniques in electroanalytical chemistry, revised and expanded* (CRC press, 1996).

[238]P. Arora and Z. Zhang, "Battery separators", Chem. Rev. **104**, 4419–4462 (2004).

[239]R. S. Nicholson, "Theory and application of cyclic voltammetry for measurement of electrode reaction kinetics.", Anal. Chem. **37**, 1351–1355 (1965).

[240]X. H. Rui, N. Ding, J. Liu, C. Li, and C. Chen, "Analysis of the chemical diffusion coefficient of lithium ions in li3v2(po4)3 cathode material", Electrochim. Acta **55**, 2384–2390 (2010).

[241]M. E. Orazem and B. Tribollet, *Electrochemical impedance spectroscopy*, Vol. 48 (John Wiley and Sons, 2011).

[242]J. E. B. Randles, "Kinetics of rapid electrode reactions", Discuss. Faraday Soc. **1**, 11–19 (1947).

[243]B. G.J., A. Eeden, S.-R. M., and J. Sluyters, "The analysis of electrode impedances complicated by the presence of a constant phase element", J. Electroanal. Chem. Interfacial Electrochem. **176**, 275–295 (1984).

[244]U Rammelt and G. Rei, "On the applicability of a constant phase element (cpe) to the estimation of roughness of solid metal electrodes", Electrochim. Acta **35**, 1045–1049 (1990).

[245]S. R. Taylor and E Gileadi, "Physical interpretation of the warburg impedance", Corrosion **51**, 664–671 (1995).

[246]T. A. Chirayil, P. Y. Zavalij, and M. S. Whittingham, "A new vanadium dioxide cathode", J Electrochem Soc **143**, L193–L195 (1996).

[247]C. R. Walk and J. S. Gore, "Li/v205 secondary cell", J. Electrochem. Soc **122**, 68C (1975).

[248]J. Liu, H. Xia, D. Xue, and L. Lu, "Double-shelled nanocapsules of v2o5-based composites as high-performance anode and cathode materials for li ion batteries", J. Am. Chem. Soc. **131**, 12086–12087 (2009).

[249]A. Cao, J. Hu, H. Liang, and L. Wan, "Self-assembled vanadium pentoxide v2o5 hollow microspheres from nanorods and their application in lithium-ion batteries", Angew. Chem. Int. Ed. **44**, 4391–4395 (2005).

[250]D. Su and G. Wang, "Single-crystalline bilayered v2o5 nanobelts for high-capacity sodium-ion batteries", ACS Nano **7**, 11218–11226 (2013).

[251]S. Tepavcevic, H. Xiong, V. R. Stamenkovic, X. Zuo, M. Balasubramanian, V. B. Prakapenka, J. C. S., and T. Rajh, "Nanostructured bilayered vanadium oxide electrodes for rechargeable sodium-ion batteries", ACS Nano **6**, 530–538 (2012).

[252]V. Raju, J. Rains, C. Gates, W. Luo, X. Wang, W. F. Stickle, G. D. Stucky, and X Ji, "Superior cathode of sodium-ion batteries: orthorhombic v2o5 nanoparticles generated in nanoporous carbon by ambient hydrolysis deposition", Nano Lett. **14**, 4119–4124 (2014).

[253]Y. Shao, X. Wang, M. Engelhard, C. Wang, S. Dai, J. Liu, Z. Yang, and Y Lin, "Nitrogen-doped mesoporous carbon for energy storage in vanadium redox flow batteries", J. Power Sources **195**, 4375–4379 (2010).

[254]L. Joerissen, J. Garche, C. Fabjan, and G Tomazic, "Possible use of vanadium redox-flow batteries for energy storage in small grids and stand-alone photovoltaic systems", J. Power Sources **127**, 98–104 (2004).

[255]J. Liu, X. Wang, Q. Peng, and Y. Li, "Vanadium pentoxide nanobelts highly selective and stable ethanol sensor materials", Adv. Mater. **17**, 764–767 (2005).

[256]A. D. Raj, T. Pazhanivel, P. Kumar, M. D., D. Nataraj, and N. Ponpandian, "Self assembled v2o5 nanorods for gas sensors", Curr. Appl Phys. **10**, 531–537 (2010).

[257]H. Yin, K. Yu, H. Peng, Z. Zhang, R. Huang, J. Travas-Sejdic, and Z. Zhu, "Porous v 2 o 5 micro/nano-tubes: synthesis via a cvd route, single-tube-based humidity sensor and improved li-ion storage properties", J. Mater. Chem. **22**, 5013–5019 (2012).

[258]R. Y. Saleh, I. E. Wachs, S. S. Chan, and C. C. Chersich, "The interaction of v2o5 with ti02 (anatase): catalyst evolution with calcination temperature and o-xylene oxidation", J. Catal. **98**, 102–114 (1986).

[259]Y. Wang, Z. Liu, L. Zhan, Z. Huang, Q. Liu, and J. Ma, "Performance of an activated carbon honeycomb supported v2o5 catalyst in simultaneous so2 and no removal", Chem. Eng. Sci. **59**, 5283–5290 (2004).

[260]*Retrieved from http://vanmotech.com/v2o5-v2o3-v.*

[261]D. K. Louie, *Handbook of sulphuric acid manufacturing* (DKL Engineering, Inc., 2005).

[262]J. M. Hughes and L. W. Finger, "The crystal chemistry of shcherbinaite, naturally occurring v2o5", Am. Mineral **68**, 1220–1222 (1983).

[263]M. Taniguchi and T. R. Ingraham, "Mechanism of thermal decomposition of ammonium metavanadate", Can. J. Chem. **42**, 2467–2473 (1964).

[264]R. Enjalbert and J. Galy, "A refinement of the structure of v_2o_5", Acta Crystallographica Section C **42**, 1467–1469 (1986).

[265]J. Ketelaar, "Crystal structure and shape of colloidal particles of vanadium pentoxide", Nature **137**, 316 (1936).

[266]A. Bystrom, K. Wilhelmi, and O. Brotzen, "Vanadium pentoxide-a compound with five-coordinated vanadium atoms", Acta. Chem. Scand **4**, 1119 (1950).

[267]J. Cheng, B. Wang, H. L. Xin, G. Yang, H. Cai, F. Nie, and H. Huang, "Self-assembled v2o5 nanosheets/reduced graphene oxide hierarchical nanocomposite as a high-performance cathode material for lithium ion batteries", J. Mater. Chem. A **1**, 10814–10820 (2013).

[268]M. S. Whittingham, "The role of ternary phases in cathode reactions", J Electrochem Soc **123**, 315–320 (1976).

[269]C. K. Chan, H. Peng, R. D. Twesten, K. Jarausch, X. F. Zhang, and Y. Cui, "Fast, completely reversible li insertion in vanadium pentoxide nanoribbons", Nano Lett. **7**, 490–495 (2007).

[270]S. Hub, A. Tranchant, and R. Messina, "X-ray investigations on electroformed lixv2o5 bronzes", Electrochim. Acta **33**, 997 (1998).

[271]J. Pereira-Ramos, R. Messina, C. Piolet, and. DevyDunn, "A thermodynamic study of electrochemical lithium insertion into vanadium pentoxide", Electrochim. Acta **33**, 1003–1008 (1988).

[272]C. C. Zhu, J. Shu, X. Z. Wu, P. Li, and X. Li, "Electrospun v2o5 micro nanorods as cathode materials for lithium ion battery", J. Electroanal. Chem. **759**, 184–189 (2015).

[273]C. V. S. Reddy, S. A. Wicker, E. H. Walker, Q. L. Williams, and R. R. Kalluru, "Vanadium oxide nanorods for li-ion battery applications", J. Electrochem. Soc. **155**, A599–A602 (2008).

[274]D. V. Raj, V. Nandhinidevi, D. Mangalaraj, and C. Viswanathan, "Electrodeposition of v2o5 nanorods on current collector substrate", Solid State Physics, Pts 1 and 2 **1447**, 435–436 (2012).

[275]A. Q. Pan, J. G. Zhang, Z. M. Nie, G. Z. Cao, B. W. Arey, G. S. Li, S. Q. Liang, and J. Liu, "Facile synthesized nanorod structured vanadium pentoxide for high-rate lithium batteries", J. Mater. Chem. **20**, 9193–9199 (2010).

[276]S. D. Perera, B. Patel, J. Bonso, M. Grunewald, J. P. Ferraris, and K. J. Balkus, "Vanadium oxide nanotube spherical clusters prepared on carbon fabrics for energy storage applications", ACS Appl Mater Interfaces **3**, 4512–4517 (2011).

[277]S. Nordlinder, A. Augustsson, T. Schmitt, J. H. Guo, L. C. Duda, J. Nordgren, T. Gustafsson, and K. Edstrom, "Redox behavior of vanadium oxide nanotubes as studied by x-ray photoelectron spectroscopy and soft x-ray absorption spectroscopy", Chem. Mater. **15**, 3227–3232 (2003).

[278]V. M. Mohan, B. Hu, W. L. Qiu, and W. Chen, "Synthesis, structural, and electrochemical performance of v2o5 nanotubes as cathode material for lithium battery", J. Appl. Electrochem. **39**, 2001–2006 (2009).

[279]L. F. Jiao, H. T. Yuan, Y. J. Wang, H. S. Cao, and Y. M. Wang, "Mg intercalation properties into open-ended vanadium oxide nanotubes", Electrochem. Commun. **7**, 431–436 (2005).

[280]W. Chen, L. Q. Mai, Q. Xu, J. F. Peng, and Q. Y. Zhu, "Synthesis, structure and electrochemical performance of vanadium oxide nanotubes", Chem. J. Chinese. U. **25**, 904–907 (2004).

[281]F. Carn, M. Morcrette, B. Desport, and R. Backov, "Lithium-ion battery electrode prepared by confining carbon nanotubes v2o5 nanoribbons suspension in model air-liquid foams", Solid State Sci. **17**, 134–139 (2013).

[282]G. Nagaraju, P. Chithaiahb, S. Ashokac, and N. Mahadevaiah, "Vanadium pentoxide nanobelts one pot synthesis and its lithium storage behavior", Cryst. Res. Technol. **47**, 868–875 (2012).

[283]C. L. Niu, J. B. Li, H. B. Jin, H. L. Shi, Y. Q. Zhu, W. Z. Wang, and M. S. Cao, "Self-template processed hierarchical v2o5 nanobelts as cathode for high performance lithium ion battery", Electrochim. Acta **182**, 621–628 (2015).

[284]X. H. Rui, J. X. Zhu, W. L. Liu, H. T. Tan, D. H. Sim, C. Xu, H. Zhang, J. Ma, H. H. Hng, T. M. Lim, and Q. Y. Yan, "Facile preparation of hydrated vanadium pentoxide nanobelts based bulky paper as flexible binder-free cathodes for high-performance lithium ion batteries", RSC Adv. **1**, 117–122 (2011).

[285]D. A. Semenenko, A. Y. Kozmenkova, D. M. Itkis, E. A. Goodilin, T. L. Kulova, A. M. Skundin, and Y. D. Tretyakov, "Growth of thin vanadia nanobelts with improved lithium storage capacity in hydrothermally aged vanadia gels", CrystEngComm **14**, 1561–1567 (2012).

[286]J. X. Wang, C. J. Curtis, D. L. Schulz, and J. G. Zhang, "Influences of treatment temperature and water content on capacity and rechargeability of v2o5 xerogel films", J. Electrochem. Soc. **151**, A1–A7 (2004).

[287]A. L. Tipton, S. Passerini, B. B. Owens, and W. H. Smyrl, "Performance of lithium/v2o5 xerogel coin cells", J. Electrochem. Soc. **143**, 3473–3477 (1996).

[288]H. K. Park and W. H. Smyrl, "V2o5 xerogel films as intercalation hosts for lithium", J. Electrochem. Soc. **141**, L25–L26 (1994).

[289]S. Mege, Y. Levieux, F. Ansart, J. M. Savariault, and A. Rousset, "Electrochemical properties of a new v2o5 xerogel", J. Appl. Electrochem. **30**, 657–664 (2000).

[290]M. Giorgetti, W. S. Passerini S.and Smyrl, and M. Passerini, "Evidence of bilayer structure in v2o5 xerogel", Inorg. Chem. **39**, 1514–1517 (2000).

[291]E. C. Almeida, M. Abbate, and J. M. Rosolen, "Formation of li2o in a chemically li-intercalated v2o5 xerogel", Solid State Ion **140**, 241–248 (2001).

[292]H. Q. Song, C. P. Zhang, Y. G. Liu, C. F. Liu, X. H. Nan, and G. Z. Cao, "Facile synthesis of mesoporous v2o5 nanosheets with superior rate capability and excellent cycling stability for lithium ion batteries", J. Power Sources **294**, 1–7 (2015).

[293]X. Peng, X. M. Zhang, L. Wang, L. S. Hu, S. H. S. Cheng, C. Huang, B. A. Gao, F. Ma, K. F. Huo, and P. K. Chu, "Hydrogenated v2o5 nanosheets for superior lithium storage properties", Adv. Funct. Mater. **26**, 784–791 (2016).

[294]S. Q. Liang, M. L. Qin, Y. Tang, Q. Zhang, X. L. Li, X. P. Tan, and A. Q. Pan, "Facile synthesis of nanosheet-structured v2o5 with enhanced electrochemical performance for high energy lithium-ion batteries", Met. Mater. Int. **20**, 983–988 (2014).

[295]S. Q. Liang, Y. Hu, Z. W. Nie, H. Huang, T. Chen, A. Q. Pan, and G. Z. Cao, "Template-free synthesis of ultra-large v2o5 nanosheets with exceptional small thickness for high-performance lithium-ion batteries", Nano Energy **13**, 58–66 (2015).

[296]J. F. Huang, X. N. Qiao, Z. W. Xu, L. Y. Cao, H. B. Ouyang, J. Y. Li, and R. Y. Wang, "V2o5 self-assembled nanosheets as high stable cathodes for lithium-ion batteries", Electrochim. Acta **191**, 158–164 (2016).

[297]Q. Y. An, Q. L. Wei, L. Q. Mai, J. Y. Fei, X. Xu, Y. L. Zhao, M. Y. Yan, P. F. Zhanga, and S. Z. Huanga, "Supercritically exfoliated ultrathin vanadium pentoxide nanosheets

with high rate capability for lithium batteries", Phys. Chem. Chem. Phys. **15**, 16828–16833 (2013).

[298]K. Takahashi, S. J. Limmer, Y. Wang, and G. Cao, "Synthesis and electrochemical properties of single-crystal v2o5 nanorod arrays by template-based electrodeposition", J. Phys. Chem. B **108**, 9795–9800 (2004).

[299]E. Armstrong, D. McNulty, H. Geaney, and C. O'Dwyer, "Electrodeposited structurally stable v2o5 inverse opal networks as high performance thin film lithium batteries", ACS Appl. Mater. Interfaces **7**, 27006–27015 (2015).

[300]J. K. Lee, G. P. Kim, I. K. Song, and S. H. Baeck, "Electrodeposition of mesoporous v2o5 with enhanced lithium-ion intercalation property", Electrochem. Commun. **11**, 1571–1574 (2009).

[301]K. H. Kim, D. K. Roh, I. K. Song, B. C. Lee, and S. H. Baeck, "Enhanced performance as a lithium-ion battery cathode of electrodeposited v2o5 thin films by e-beam irradiation", J. Solid State Electrochem. **14**, 1801–1805 (2010).

[302]I. Mjejri, N. Etteyeb, and F. Sediri, "Vanadium oxides nanostructures: hydrothermal synthesis and electrochemical properties", Mater. Res. Bull. **60**, 97–104 (2014).

[303]I. Mjejri, N. Etteyeb, and F. Sediri, "Mesoporous vanadium oxide nanostructures: hydrothermal synthesis, optical and electrochemical properties", Ceram. Int. **40**, 1387–1397 (2014).

[304]D. M. Minic and V. A. Blagojevic, "Hydrothermal synthesis and controlled growth of vanadium oxide nanocrystals", CrystEngComm **15**, 6617–6624 (2013).

[305]J. X. Wang, W. J. Yu, S. Xu, S. Y. Dai, J. D. Wang, C. X. Wang, W. Zeng, and P. S. Cao, "A study on the precursor of vanadium pentoxide by the hydrothermal method", Ceram. Int. **40**, 317–321 (2014).

[306]A. D. Raj, P. S. Kumar, Q. Yang, and D. Mangalaraj, "Synthesis and gas sensors behavior of surfactants free v2o5 nanostructure by using a simple precipitation method", Phys. E. **44**, 1490–1494 (2012).

[307]S. H. Ng, S. Y. Chew, J. Wang, D. Wexler, Y. Tournayre, K. Konstantinov, and H. K. Liu, "Synthesis and electrochemical properties of v2o5 nanostructures prepared via a precipitation process for lithium-ion battery cathodes", J. Power Sources **174**, 1032–1035 (2007).

[308]C. Piccirillo, R. Binions, and I. P. Parkin, "Synthesis and functional properties of vanadium oxides: v2o3, vo2, and v2o5 deposited on glass by aerosol-assisted cvd", Chem. Vap. Deposition **13**, 145–151 (2007).

[309]A. Mantoux, H. Groult, E. Balnois, P. Doppelt, and L. Gueroudji, "Vanadium oxide films synthesized by cvd and used as positive electrodes in secondary lithium batteries", J. Electrochem. Soc. **151**, A368–A373 (2004).

[310]H. H. Yin, K. Yu, H. Peng, Z. L. Zhang, R. Huang, J. Travas-Sejdic, and Z. Q. Zhu, "Porous v2o5 micro/nano-tubes: synthesis via a cvd route, single-tube-based humidity sensor and improved li-ion storage properties", J. Mater. Chem. **22**, 5013–5019 (2012).

[311]H. Nakazawa, K. Sano, and M. Baba, "Fabrication by using a sputtering method and charge-discharge properties of large-sized and thin-filmed lithium ion rechargeable batteries", J. Power Sources **146**, 758–761 (2005).

[312]Y. J. Park, K. S. Ryu, K. M. Kim, N. G. Park, M. G. Kang, and S. H. Chang, "Electrochemical properties of vanadium oxide thin film deposited by RF sputtering", Solid State Ion. **154**, 229–235 (2002).

[313]Z. Wang, D. Xu, L. Wang, and X. Zhang, "Facile and low-cost synthesis of large-area pure v2o5 nanosheets for high-capacity and high-rate lithium storage over a wide temperature range", ChemPlusChem **77**, 124–128 (2012).

[314]Y. W. Li, J. H. Yao, E. Uchaker, J. W. Yang, Y. X. Huang, M. Zhang, and G. Z. Cao, "Leaf-like v2o5 nanosheets fabricated by a facile green approach as high energy cathode material for lithium-ion batteries", Adv. Energy Mater. **3**, 1171–1175 (2013).

[315]F. Coustier, S. Passerini, and W. Smyrl, "A 400 mAh/g aerogel-like v 2 o 5 cathode for rechargeable lithium batteries", J. Electrochem. Soc. **145**, L73–L74 (1998).

[316]A. ONeill, U. Khan, and J. N. Coleman, "Preparation of high concentration dispersions of exfoliated mos2 with increased flake size", Chem. Mater. **24**, 2414–2421 (2012).

[317]D. Pan, Z. Shuyuan, Y. Chen, and J. Hou, "Hydrothermal preparation of long nanowires of vanadium oxide", J. Mater. Res. **17**, 1981–1984 (2002).

[318]D. Su, M. Wieske, E. Beckmann, A. Blume, G. Mestl, and R. Schlogl, "Electron beam induced reduction of v2o5 studied by analytical electron microscopy", Catal. Lett. **75**, 81–86 (2001).

[319]T. Kim, J. Shin, T. S. You, H. Lee, and J. Kim, "Thermally controlled v2o5 nanoparticles as cathode materials for lithium-ion batteries with enhanced rate capability", Electrochim. Acta **164**, 227–234 (2015).

[320]M Demeter, M Neumann, and W Reichelt, "Mixed-valence vanadium oxides studied by xps", Surf. Sci. **454**, 41–44 (2000).

[321]D. Briggs and M. P. Seah, *Practical surface analysis by auger and x-ray photoelectron spectroscopy* (John Wiley & Sons, 1983).

[322]V Bondarenka, S Kaciulis, Z Martunas, A Reddy C. V. S.za, G. Babonas, and A Revivkevivius, "Xps and optical properties of sol-gel processed vanadium pentoxide films", Lith. J. Phys. **48** (2015).

[323]A. Jin, W. Chen, Q. Zhu, Y. Yang, V. L. Volkov, and G. Zakharova, "Structural and electrochromic properties of molybdenum doped vanadium pentoxide thin films by sol–gel and hydrothermal synthesis", Thin Solid Films **517**, 2023–2028 (2009).

[324]J Livage and D Ganguli, "Solar gel electrochromic coatings and devices: a review", Sol. Energy Mater. Sol. Cells **68**, 365–381 (2001).

[325]H. Yan, S. Sokolov, J. C. Lytle, A. Stein, F. Zhang, and W. H. Smyrl, "Colloidal-crystal-templated synthesis of ordered macroporous electrode materials for lithium secondary batteries", J. Electrochem. Soc. **150**, A1102–A1107 (2003).

[326]G. N. Barbosa, C. F. Graeff, and H. P. Oliveira, "Thermal annealing effects on vanadium pentoxide xerogel films", en, Eclet. Qu **30**, 7–15 (2005).

[327]H. H. Kristoffersen and H. Metiu, "Structure of v2o5nh2o xerogels", J. Phys. Chem. C. **120**, 3986–3992 (2016).

[328]E. J. M. Hensen and B. Smit, "Why clays swell", J. Phys. Chem. B **106**, 12664–12667 (2002).

[329]V. Petkov, P. Trikalitis, T. Billinge S. V. T.and Vogt, and M. G. Kanat, "Structure of v2o5nh2o xerogel solved by the atomic pair distribution function technique", J. Am. Chem. Soc. **124**, 10157–10162 (2002).

[330]C ODwyer, V Lavayen, M. Santa Ana, E Benavente, G Gonzalez, and C. Sotomayor Torres, "Anisotropic vanadium oxide nanostructured host matrices for lithium ion intercalation", Adv. Phys. Chem. (2007).

[331]G. Teran-Escobar, J. Pampel, J. M. Caicedo, and M. Lira-Cantu, "Low-temperature, solution-processed, layered v 2 o 5 hydrate as the hole-transport layer for stable organic solar cells", Energy Environ. Sci. **6**, 3088–3098 (2013).

[332]A. T. Raj, K. Ramanujan, S. Thangavel, S. Gopalakrishan, N. Raghavan, and G. Venugopal, "Facile synthesis of vanadium-pentoxide nanoparticles and study on their electrochemical, photocatalytic properties", J. Nanosci. Nanotechnol. **15**, 3802–3808 (2015).

[333]F. Huguenin and R. M. Torresi, "Electrochemical behavior and structural changes of v2o5 xerogel", en, J. Braz. Chem. Soc. **14**, 536–543 (2003).

[334]A. E. Del-Rio-Castillo, C. Merino, E. Diez-Barra, and E. Vazquez, "Selective suspension of single layer graphene mechanochemically exfoliated from carbon nanofibres", Nano Res. **7**, 963–972 (2014).

[335]T. F. Tadros, *Solid-liquid dispersions* (Academic Press, 1987).

[336]W. Ma, C. Zhang, C. Liu, X. Nan, H. Fu, and G. Cao, "Impacts of surface energy on lithium ion intercalation properties of v2o5", ACS App. Mats. Int. (2016).

[337]A. Miller, *Polyethylenimine adhesive*, US Patent 3,909,469, 1975.

[338]C. Liu, E. I. Gillette, X. Chen, A. J. Pearse, A. C. Kozen, M. A. Schroeder, K. E. Gregorczyk, S. B. Lee, and G. W. Rubloff, "An all-in-one nanopore battery array", Nat. nanotech. **9**, 1031–1039 (2014).

[339]B. J. Landi, M. J. Ganter, C. D. Cress, R. A. DiLeo, and R. P. Raffaelle, "Carbon nanotubes for lithium ion batteries", Energy Environ. Sci. **2**, 638–654 (2009).

[340]G. Wang, H. Li, Q. Zhang, Z. Yu, and M. Qu, "The study of carbon nanotubes as conductive additives of cathode in lithium ion batteries", J. Solid State Electrochem. **15**, 759–764 (2011).

[341]Z. Wang, Q. Su, and H. Deng, "Single-layered v2o5 a promising cathode material for rechargeable li and mg ion batteries: an ab initio study", Phys. Chem. Chem. Phys. **15**, 8705–8709 (2013).

[342]X.-M. Liu, Z.-D. Huang, S. Oh, B. Zhang, B.-C. Ma, M. Yuen, and J.-K. Kim, "Carbon nanotube based composites as electrode material for rechargeable li-ion batteries a review", Compos. Sci. Technol. **72**, 121–144 (2012).

[343]L. Q. Mai, B. Hu, W. Chen, Y. Qi, C. Lao, R. Yang, Y. Dai, and Z. L. Wang, "Lithiated moo3 nanobelts with greatly improved performance for lithium batteries", Adv. Mater. **19**, 3712–3716 (2007).

[344]J. S. Chen, Y. L. Cheah, S. Madhavi, and X. W. Lou, "Fast synthesis of α-moo3 nanorods with controlled aspect ratios and their enhanced lithium storage capabilities", J. Phys. Chem. C **114**, 8675–8678 (2010).

[345]X. D. Yan, Z. H. Wang, M. He, Z. H. Hou, T. Xia, G. Liu, and X. B. Chen, "Tio2 nanomaterials as anode materials for lithium-ion rechargeable batteries", Energy Technol. **3**, 801–814 (2015).

[346]Y. Liu and Y. Yang, "Recent progress of tio 2-based anodes for li ion batteries", Journal of Nanomaterials **2016**, 2 (2016).

[347]B. Zhao, R. Ran, M. Liu, and Z. Shao, "A comprehensive review of li4ti5o12-based electrodes for lithium-ion batteries: the latest advancements and future perspectives", Mater. Sci. Eng. R-Rep. **98**, 1–71 (2015).

[348]X. Sun, P. V. Radovanovic, and B. Cui, "Advances in spinel li4ti5o12 anode materials for lithium-ion batteries", New J. Chem. **39**, 38–63 (2015).

[349]E. M. Ceresa, L. Burlamacchi, and M. Visca, "An esr study on the photoreactivity of tio2 pigments", J. Mater. Sci. **18**, 289–294 (1983).

[350]A. Jaroenworaluck, W. Sunsaneeyametha, N. Kosachan, and R. Stevens, "Characteristics of silica-coated tio2 and its UV absorption for sunscreen cosmetic applications", Surf. Interface Anal. **38**, 473–477 (2006).

[351]A. Weir, P. Westerhoff, L. Fabricius, K. Hristovski, and N. Goetz, "Titanium dioxide nanoparticles in food and personal care products", Environ. Sci. Technol. **46**, 2242–2250 (2012).

[352]X. B. Chen, "Tio2 nanomaterials as an efficient adsorbent and photocatalyst for environmental aqueous pollution removal", J. Am. Chem. Soc. **247** (2014).

[353]D. Bamba, M. Coulibaly, C. I. Fort, C. L. Cotet, Z. Pap, K. Vajda, E. G. Zoro, N. A. Yao, V. Danciu, and D. Robert, "Synthesis and characterization of tio2/c nanomaterials: applications in water treatment", Phys. Status Solidi B **252**, 2503–2511 (2015).

[354]Z. F. Yin, L. Wu, H. G. Yang, and Y. H. Su, "Recent progress in biomedical applications of titanium dioxide", Phys. Chem. Chem. Phys. **15**, 4844–4858 (2013).

[355]G. H. Liu, N. Hoivik, K. Y. Wang, and H. Jakobsen, "Engineering tio2 nanomaterials for CO2 conversion/solar fuels", Sol. Energy Mater. Sol. Cells **105**, 53–68 (2012).

[356]W.-Q. Wu, H.-S. Rao, Y.-F. Xu, Y.-F. Wang, C.-Y. Su, and D.-B. Kuang, "Hierarchical oriented anatase tio2 nanostructure arrays on flexible substrate for efficient dye-sensitized solar cells", Sci. Rep. **3**, 1892– (2013).

[357]X. X. Wang, M. Xi, H. Fong, and Z. T. Zhu, "Electrospun tio2 nanomaterials for dye-sensitized solar cell", J. Am. Chem. Soc. **248** (2014).

[358]H. Cheng, J. Y. Wang, Y. Z. Zhao, and X. J. Han, "Effect of phase composition, morphology, and specific surface area on the photocatalytic activity of tio2 nanomaterials", RSC Adv. **4**, 47031–47038 (2014).

[359]A. Al-Ahmed, B. Mukhtar, S. Hossain, S. M. J. Zaidi, and S. U. Rahman, "Application of titanium dioxide (tio2) based photocatalytic nanomaterials in solar and hydrogen energy: a short review", Photoc. Mats. Surf. Env. Cleanup **712**, 25–47 (2012).

[360]A. M. Mohamed, A. S. Aljaber, S. Y. AlQaradawi, and N. K. Allam, "Tio2 nanotubes with ultrathin walls for enhanced water splitting", Chem. Commun. **51**, 12617–20 (2015).

[361] *Retrieved from http://faculty.virginia.edu/metals/images/tio2%20powder.jpg.*

[362] J. Anthony, *Handbook of mineralogy, elements, sulfides and sulfosalts* (2005).

[363] D. Reyes-Coronado, A. Rodraguez-Gattorno, M.-E. Espinosa-Pesqueira, and C. Cab, "Phase-pure tio 2 nanoparticles: anatase, brookite and rutile", Nanotechnology **19**, 145605 (2008).

[364] A. Goresy, L. Dubrovinsky, P. Gillet, G. Graup, and M. Chen, "Letter. akaogiite: an ultra-dense polymorph of tio2 with the baddeleyite-type structure, in shocked garnet gneiss from the ries crater, Germany", Am. Mineral. **95**, 892–895 (2010).

[365] P. Simons and F. Dachille, "The structure of tio2(ii), a high-pressure phase of tio2", Acta Crystallogr. **23**, 334–336 (1967).

[366] R. Marchand, L. Brohan, and M. Tournoux, "Tio2(b) a new form of titanium dioxide and the potassium octatitanate k2ti8o17", Mater. Res. Bull. **15**, 1129–1133 (1980).

[367] C Alt, *Ullmann's encyclopedia of industrial chemistry*, 2006.

[368] G. McNulty, "Production of titanium dioxide", in Proceedings of norm v international conference, seville, spain (Citeseer, 2007), pp. 169–189.

[369] D. Hanaor and C. C. Sorrell, "Review of the anatase to rutile phase transformation", J. Mater. Sci. **46**, 855–874 (2011).

[370] M Pfanzelt, P Kubiak, M Fleischhammer, and M Wohlfahrt-Mehrens, "Tio 2 rutilean alternative anode material for safe lithium-ion batteries", J. Power Sources **196**, 6815–6821 (2011).

[371] A. Armstrong, G. Armstrong, J. Canales, R. Garcia, and P. Bruce, "Lithium-ion intercalation into tio2-b nanowires", Adv. Mater. **17**, 862–865 (2005).

[372] T. Song and U. Paik, "Tio 2 as an active or supplemental material for lithium batteries", J. Mater. Chem.A **4**, 14–31 (2016).

[373] Z. Xiu, M. H. Alfaruqi, J. Gim, J. Song, S. Kim, T. V. Thi, P. T. Duong, J. P. Baboo, V. Mathew, and J. Kim, "Hierarchical porous anatase tio2 derived from a titanium metal-organic framework as a superior anode material for lithium ion batteries", Chem. Commun. **51**, 12274–12277 (2015).

[374] A. Apolinario, C. T. Sousa, J. Ventura, J. D. Costa, D. C. Leitao, J. M. Moreira, J. B. Sousa, L. Andrade, A. M. Mendes, and J. P. Araujo, "Highly ordered hexagonal arrays of tio2 nanotubes", Microsc. Microanal. **21 Suppl 5**, 5–6 (2015).

[375] M. G. Choi, Y. G. Lee, S. W. Song, and K. M. Kim, "Lithium-ion battery anode properties of tio2 nanotubes prepared by the hydrothermal synthesis of mixed (anatase and rutile) particles", Electrochim. Acta **55**, 5975–5983 (2010).

[376]J. Kim and J. Cho, "Rate characteristics of anatase tio2 nanotubes and nanorods for lithium battery anode materials at room temperature", J. Electrochem. Soc. **154**, A542–A546 (2007).

[377]J. W. Xu, C. H. Ha, B. Cao, and W. F. Zhang, "Electrochemical properties of anatase tio2 nanotubes as an anode material for lithium-ion batteries", Electrochim. Acta **52**, 8044–8047 (2007).

[378]F. X. Wu, X. H. Li, Z. X. Wang, H. J. Guo, L. Wu, X. H. Xiong, and X. J. Wang, "A novel method to synthesize anatase tio2 nanowires as an anode material for lithium-ion batteries", J. Alloys Compd. **509**, 3711–3715 (2011).

[379]H. G. Yang, G. Liu, S. Z. Qiao, C. H. Sun, Y. G. Jin, S. C. Smith, J. Zou, H. M. Cheng, and G. Q. Lu, "Solvothermal synthesis and photoreactivity of anatase tio2 nanosheets with dominant {001} facets", J. Am. Chem. Soc. **131**, 4078–4083 (2009).

[380]W. Q. Wu, B. X. Lei, H. S. Rao, Y. F. Xu, Y. F. Wang, C. Y. Su, and D. B. Kuang, "Hydrothermal fabrication of hierarchically anatase tio2 nanowire arrays on fto glass for dye-sensitized solar cells", Sci. Rep. **3**, 1352 (2013).

[381]S. W. Oh, S. H. Park, and Y. K. Sun, "Hydrothermal synthesis of nano-sized anatase tio2 powders for lithium secondary anode materials", J. Power Sources **161**, 1314–1318 (2006).

[382]C. Ban, M. Xie, X. Sun, J. J. Travis, G. Wang, H. Sun, A. C. Dillon, J. Lian, and S. M. George, "Atomic layer deposition of amorphous tio2 on graphene as an anode for li-ion batteries", Nanotechnology **24**, 424002 (2013).

[383]B. Choi, D. Jeong, S. Kim, C. Rohde, S. Choi, J. Oh, H. Kim, C. Hwang, K. Szot, R. Waser, et al., "Resistive switching mechanism of tio2 thin films grown by atomic-layer deposition", J. Appl. Phys. **98**, 033715 (2005).

[384]K. Aisu, T. S. Suzuki, E. Nakamura, H. Abe, and Y. Suzuki, "Aao-template assisted synthesis and size control of one-dimensional tio2 nanomaterials", J. Ceram. Soc. Jpn. **121**, 915–918 (2013).

[385]Y. F. Jiang, G. Chen, X. Xu, X. H. Chen, S. G. Deng, S. Smirnov, H. M. Luo, and G. F. Zou, "Direct growth of mesoporous anatase tio2 on nickel foam by soft template method as binder-free anode for lithium-ion batteries", RSC Adv. **4**, 48938–48942 (2014).

[386]Y. N. Li, J. Su, X. Y. Lv, Y. F. Long, and Y. X. Wen, "Yeast bio-template synthesis of porous anatase tio2 and potential application as an anode for sodium-ion batteries", Electrochim. Acta **182**, 596–603 (2015).

[387]J. Liu, H. Feng, J. Jiang, D. Qian, J. Li, S. Peng, and Y. Liu, "Anatase-tio 2/cnts nanocomposite as a superior high-rate anode material for lithium-ion batteries", J. Alloys Compd. **603**, 144–148 (2014).

[388]A. Hassanjani-Roshan, S. Adeh, M. R. Vaezi, and A. Shokuhfar, "Effect of sonication power on the sonochemical synthesis of titania nano particles.", J. Ceram. Process. Res. **12**, 299–303 (2011).

[389]M.-Y. Cho, S.-M. Park, K.-B. Kim, and K. C. Roh, "Synthesis of mesoporous spherical tio2 and its application in negative electrode of hybrid supercapacitor", Electron. Mater. Lett. **9**, 809–812 (2013).

[390]L. Shengwei, Y. Jiaguo, and J. Mietek, "Anatase tio2 with dominant high-energy (001) facets: synthesis, properties, and applications", Chemistry of Materials **23**, 4085–4093 (2011).

[391]X. Chen and S. S. Mao, "Titanium dioxide nanomaterials: synthesis, properties, modifications, and applications", Chem. Rev **107**, 2891–2959 (2007).

[392]B. Erdem, G. W. Hunsicker R. Aand Simmons, E. D. Sudol, V. L. Dimonie, and M. S. El-Aasser, "Xps and ftir surface characterization of tio2 particles used in polymer encapsulation", Langmuir **17**, 2664–2669 (2001).

[393]A. T. Vu, Q. T. Nguyen, T. H. L. Bui, M. C. Tran, T. P. Dang, and T. K. H. Tran, "Synthesis and characterization of tio2 photocatalyst doped by transition metal ions (fe3+, cr3+ and v5+)", Adv. Nat. Sci.: Nanosci. Nanotechnol. **1**, 015009 (2010).

[394]C. Dette, M. A. Perez-Osorio, C. S. Kley, P. Punke, C. E. Patrick, P. Jacobson, F. Giustino, S. J. Jung, and K. Kern, "Tio2 anatase with a bandgap in the visible region", Nano Lett. **14**, 6533–6538 (2014).

[395]P. Kubiak, T. Fraschl, N. Hesing, U. Harmann, U. Kaiser, R. Schiller, C. K. Weiss, K. Landfester, and M. Wohlfahrt-Mehrens, "Tio2 anatase nanoparticle networks: synthesis, structure, and electrochemical performance", Small **7**, 1690–1696 (2011).

[396]R. Cava, D. Murphy, S. Zahurak, A. Santoro, and R. Roth, "The crystal structures of the lithium-inserted metal oxides li0.5tio2 anatase, liti2o4 spinel, and li2ti2o4", Journal of Solid State Chemistry **53**, 64–75 (1984).

[397]K. Ozawa, *Lithium ion rechargeable batteries: materials, technology, and new applications* (John Wiley & Sons, 2012).

[398]M. V. Koudriachova and N. M. Harrison, "Li sites and phase stability in tio2-anatase and zr-doped tio2-anatase", J. Mater. Chem. **16**, 1973–1977 (2006).

[399]J. Shields, *Application of molybdenum and its alloys*, International Molybdenum Association (IMOA), London, UK, 2013.

[400]D. M. Considine and G. D. Considine, *Van nostrands scientific encyclopedia* (Springer Science & Business Media, 2013).

[401]M. M.Y. A. Alsaif, M. R. Field, B. J. Murdoch, T. Daeneke, K. Latham, A. F. Chrimes, A. S. Zoolfakar, S. P. Russo, J. Z. Ou, and K. Kalantar-zadeh, "Substoichiometric two-dimensional molybdenum oxide flakes: a plasmonic gas sensing platform", Nanoscale **6**, 12780–12791 (2014).

[402]D. Manno, M. Di Giulio, A. Serra, T. Siciliano, and G. Micocci, "Physical properties of sputtered molybdenum oxide thin films suitable for gas sensing applications", J. Phys. D: Appl. Phys **35**, 228–233 (2002).

[403]C. Oros, A. Wisitsoraat, D. Phokharatkul, P. Limsuwan, and A. Tuantranont, "Fabrication and gas-sensing characterization of molybdenum oxide nanostructure by reactive rf sputtering", Adv. Mat. Res. **213**, 98–102 (2011).

[404]A. M. Taurino, A. Forleo, L. Francioso, P. Siciliano, M. Stalder, and R. Nesper, "Synthesis, electrical characterization, and gas sensing properties of molybdenum oxide nanorods", Appl. Phys. Lett. **88** (2006).

[405]M. Bertotti and D. Pletcher, "Catalysis of the bromate reduction at a molybdenum oxide modified electrode.", Qu Nova **21**, 167–171 (1998).

[406]C. Brookes, P. P. Wells, G. Cibin, N. Dimitratos, W. Jones, D. J. Morgan, and M. Bowker, "Molybdenum oxide on fe2o3 core-shell catalysts: probing the nature of the structural motifs responsible for methanol oxidation catalysis", ACS Catal. **4**, 243–250 (2014).

[407]Y. S. Zhou, L. B. Qin, C. Yu, T. Xiong, L. J. Zhang, W. Ahmad, and H. Han, "Towards applications in catalysis: investigation on photocatalytic activities of a derivative family of the keplerate type molybdenum-oxide based polyoxometalates", RSC Adv. **5**, 17149–17149 (2015).

[408]J. Scarminio, A. Lourenco, and A. Gorenstein, "Electrochromism and photochromism in amorphous molybdenum oxide films", Thin Solid Films **302**, 66–70 (1997).

[409]M. Rouhani, S. Gorelik, J. Hobley, S. J. Wang, E. L. Williams, and Y. L. Foo, "Delayed onset of photochromism in molybdenum oxide films caused by photoinduced defect formation", Sci. Tech. Adv. Mater. **12** (2011).

[410]M. Rouhani, Y. L. Foo, J. Hobley, J. S. Pan, G. S. Subramanian, X. J. Yu, A. Rusydi, and S. Gorelik, "Photochromism of amorphous molybdenum oxide films with different initial mo5+ relative concentrations", Appl. Surf. Sci. **273**, 150–158 (2013).

[411]T. He and J. N. Yao, "Photochromism of molybdenum oxide", J. Photochem. Photobiol. **4**, 125–143 (2003).

[412]N. A. Chernova, M. Roppolo, A. C. Dillon, and M. S. Whittingham, "Layered vanadium and molybdenum oxides: batteries and electrochromics", J. Mater. Chem. **19**, 2526–2552 (2009).

[413]V. S Saji and C.-W. Lee, "Molybdenum, molybdenum oxides, and their electrochemistry", ChemSusChem **5**, 1146–1161 (2012).

[414]H. Farsi, F. Gobal, H. Raissi, and S. Moghiminia, "On the pseudocapacitive behavior of nanostructured molybdenum oxide", J. Solid State Electrochem. **14**, 643–650 (2010).

[415]E. P.M., P. Gurunathan, and K. Ramesha, "Self-assembled lamellar alpha-molybdenum trioxide as high performing anode material for lithium-ion batteries", J. Power Sources **278**, 630 –638 (2015).

[416]W. Ji, R. Shen, R. Yang, G. Yu, X. Guo, L. Peng, and W. Ding, "Partially nitrided molybdenum trioxide with promoted performance as an anode material for lithium-ion batteries", J. Mater. Chem. A **2**, 699–704 (2014).

[417]K. Dewangan, N. N. Sinha, P. K. Sharma, A. C. Pandey, N. Munichandraiah, and N. Gajbhiye, "Synthesis and characterization of single-crystalline α-moo3 nanofibers for enhanced li-ion intercalation applications", CrystEngComm **13**, 927–933 (2011).

[418]W. Li, F. Cheng, Z. Tao, and J. Chen, "Vapor-transportation preparation and reversible lithium intercalation/deintercalation of α-moo3 microrods", J. Phys. Chem. B **110**, 119–124 (2006).

[419]S.-H. Lee, Y.-H. Kim, R. Deshpande, P. A. Parilla, E. Whitney, D. T. Gillaspie, K. M. Jones, A. H. Mahan, S. Zhang, and A. C. Dillon, "Reversible lithium-ion insertion in molybdenum oxide nanoparticles", Adv. Mater. **20**, 3627–3632 (2008).

[420]W. Lu, G.-h. Zhang, D. Jie, and K.-C. Chou, "Oxidation roasting of molybdenite concentrate", Trans. Nonferrous Met. Soc. China **25**, 4167–4174 (2015).

[421]N Wiberg, *Holleman-wiberg lehrbuch der anorganischen chemie, 91–100 auflage*, 1985.

[422]W. V. Schulmeyer and H. M. Ortner, "Mechanisms of the hydrogen reduction of molybdenum oxides", Int. J. Refract Met. H. **20**, 261–269 (2002).

[423]D. Mariotti, H. Lindstrom, A. C. Bose, and K. K. Ostrikov, "Monoclinic β-moo3 nanosheets produced by atmospheric microplasma: application to lithium-ion batteries", Nanotechnology **19**, 495302 (2008).

[424]V. Atuchin, T. Gavrilova, V. Kostrovsky, L. Pokrovsky, and I. Troitskaia, "Morphology and structure of hexagonal moo3 nanorods", Inorg. Mater. **44**, 622–627 (2008).

[425]A. F. Wells, *Structural inorganic chemistry* (Oxford University Press, 2012).

[426]*Retrieved from https://www.asianproducts.com/hotproduct/manufacturer_nano-powder_1.htm.*

[427]L. N. Wang, X. Zhang, Y. Ma, M. Yang, and Y. X. Qi, "Rapid microwave-assisted hydrothermal synthesis of one-dimensional moo3 nanobelts", Mater. Lett. **164**, 623–626 (2016).

[428]A. Phuruangrat, U. Cheed-Im, T. Thongtem, and S. Thongtem, "High visible light photocatalytic activity of eu-doped moo3 nanobelts synthesized by hydrothermal method", Mater. Lett. **172**, 166–170 (2016).

[429]J. W. Li, Y. H. Ma, F. F. Gong, G. S. Zhang, L. J. Xu, and S. Z. Wei, "The preparation technique of nanometer molybdenum trioxide by hydrothermal synthesis", Mater. Comput. Mech. **117-119**, 807–810 (2012).

[430]A. Abdellaoui, L. Martin, and A. Donnadieu, "Structure and optical-properties of moo3 thin-films prepared by chemical vapor-deposition", Phys. Status Solidi **109**, 455–462 (1988).

[431]J. J. Chen, M. M. Wang, X. Liao, Z. X. Liu, J. D. Zhang, L. J. Ding, L. Gao, and Y. Li, "Large-scale synthesis of single-crystal molybdenum trioxide nanobelts by hot-wire chemical vapour deposition", J. Alloys Compd. **619**, 406–410 (2015).

[432]K. Sakaushi, J. Thomas, S. Kaskel, and J. Eckert, "Aqueous solution process for the synthesis and assembly of nanostructured one-dimensional alpha-moo3 electrode materials", Chem. Mater. **25**, 2557–2563 (2013).

[433]T. H. Chiang and H. C. Yeh, "The synthesis of alpha-moo3 by ethylene glycol", Materials **6**, 4609–4625 (2013).

[434]P. Chandra, D. S. Doke, S. B. Umbarkar, and A. V. Biradar, "One-pot synthesis of ultrasmall moo3 nanoparticles supported on sio2, tio2, and zro2 nanospheres: an efficient epoxidation catalyst", J. Mater. Chem. A **2**, 19060–19066 (2014).

[435]B. P. Bastakoti, M. Imura, Y. Nemotoa, and Y. Yamauchi, "Synthesis of moo3 nanotubes by thermal mesostructural transition of spherical triblock copolymer micelle templates", Chem. Commun. **48**, 12091–12093 (2012).

[436]S. Hu and X. Wang, "Single-walled moo3 nanotubes", J. Am. Chem. Soc. **130**, 8126 (2008).

[437]Y. B. Li and Y. S. Bando, "Quasi-aligned moo3 nanotubes grown on ta substrate", Chem. Phys. Lett. **364**, 484–488 (2002).

[438]O. Yayapao, A. Phuruangrat, T. Thongtem, and S. Thongtem, "Synthesis, characterization and electrochemical properties of alpha-moo3 nanobelts for li-ion batteries", Russ. J. Phys. Chem. A **90**, 1224–1230 (2016).

[439]C. V. Krishnan, J. Chen, C. Burger, and B. Chu, "Polymer-assisted growth of molybdenum oxide whiskers via a sonochemical process", J. Phys. Chem. B **110**, 20182–20188 (2006).

[440]H. B. Wu, J. S. Chen, H. H. Hng, and X. W. D. Lou, "Nanostructured metal oxide-based materials as advanced anodes for lithium-ion batteries", Nanoscale **4**, 2526–2542 (2012).

[441]B. Mendoza-Sanches, D. Hanlon, J. Coelho, S. O Brien, H. Pettersson, C. J. N., and V. Nicolosi, "An investigation of the energy storage properties of a 2d alpha-moo3-swcnt composite film", (2016).

[442]F.-Y. Su, C. You, Y.-B. He, W. Lv, W. Cui, F. Jin, B. Li, Q.-H. Y., and F. Kang, "Flexible and planar graphene conductive additives for lithium-ion batteries", J. Mater. Chem. **20**, 9644–9650 (2010).

[443]N. Zhu, W. Liu, M. Xue, Z. Xie, D. Zhao, M. Zhang, J. Chen, and T. Cao, "Graphene as a conductive additive to enhance the high-rate capabilities of electrospun li 4 ti 5 o 12 for lithium-ion batteries", Electrochim. Acta **55**, 5813–5818 (2010).

[444]J. Shojan, C. V. Rao, and R. S. Katiyar, "Graphene as a conductive additive to improve the performance of layered lini0. 66co0. 17mn0. 17o2 for lithium-ion batteries", ECS Transactions **50**, 39–46 (2013).

[445]L. Noerochim, J.-Z. Wang, D. Wexler, Z. Chao, and H.-K. Liu, "Rapid synthesis of free-standing moo 3/graphene films by the microwave hydrothermal method as cathode for bendable lithium batteries", Journal of Power Sources **228**, 198–205 (2013).

[446]Y Ding, Y Jiang, F Xu, J Yin, H Ren, Q Zhuo, Z Long, and P Zhang, "Preparation of nano-structured lifepo 4/graphene composites by co-precipitation method", Electrochem. Commun. **12**, 10–13 (2010).

[447]Y. Zou and Y. Wang, "Nio nanosheets grown on graphene nanosheets as superior anode materials for li-ion batteries", Nanoscale **3**, 2615–2620 (2011).

[448]T. Machej, J. Haber, A. M. Turek, and I. E. Wachs, "Monolayer v2o5/tio2 and moo3/tio2 catalysts prepared by different methods", Appl. Catal. **70**, 115–128 (1991).

[449]J.-H. Kang, H. J. Yeo, J. H. Jeong, S.-M. Paek, and J.-H. Choy, "Titania-pillared molybdenum oxide as a new nanoporous photocatalyst", J. Phys. Chem. Solids **73**, 1469–1472 (2012).

[450]D. Guan, J. Li, X. Gao, and C. Yuan, "Controllable synthesis of moo 3-deposited tio 2 nanotubes with enhanced lithium-ion intercalation performance", J. Power Sources **246**, 305–312 (2014).

[451]H. Y. Chuai, D. F. Zhou, X. F. Zhu, Z. H. Li, and W. P. Huang, "Characterization of v2o5/moo3 composite photocatalysts prepared via electrospinning and their photodegradation activity for dimethyl phthalate", Chinese J. Catal. **36**, 2194–2202 (2015).

[452]Y.-S. Kim, H.-J. Ahn, H.-S. Shim, and T.-Y. Seong, "Electrochemical and structural properties of moo 3–v 2 o 5 nanocomposite thin film electrodes for lithium rechargeable batteries", Solid State Ion. **177**, 1323–1326 (2006).

[453]X. Wei, L. Jiao, S. Liu, J. Sun, W. Peng, H. Gao, Y. Si, and H. Yuan, "Synthesis and electrochemical performance of v 2 o 5 doped moo 3 cathode materials", J. Alloys Compd. **486**, 672–676 (2009).

[454]J.-G. Choi and L. Thompson, "Xps study of as-prepared and reduced molybdenum oxides", Appl. Surf. Sci. **93**, 143–149 (1996).

[455]J. Chastain, R. C. King, and J. Moulder, *Handbook of x-ray photoelectron spectroscopy: a reference book of standard spectra for identification and interpretation of xps data* (Physical Electronics Eden Prairie, MN, 1995).

[456]C. Reddy, Z. Deng, Q. Zhu, Y. Dai, J. Zhou, W. Chen, and S.-I. Mho, "Characterization of moo3 nanobelt cathode for li-battery applications", Appl. Phys. A **89**, 995–999 (2007).

[457]A. F. Ahmad, F. H. A. Moin, H. M. K. Mohd, I. A. Rahman, F. Mohamed, C. C. Hua, S. Ramli, and S. Radiman, "Graphene colloidal dispersion in various organic solvents", Mlysn. J. Anal. Sc. **17**, 475–480 (2013).

[458]C.-F. Chang, Q. D. Truong, and J.-R. Chen, "Graphene as excellent support for rapid and efficient near infrared-assisted tryptic proteolysis", Colloids Surf., B **104**, 221–228 (2013).

[459]S. J. An, J. Li, C. Daniel, D. Mohanty, S. Nagpure, and D. L. Wood, "The state of understanding of the lithium-ion-battery graphite solid electrolyte interphase (sei) and its relationship to formation cycling", Carbon **105**, 52–76 (2016).

[460]B. Mendoza-Sanchez, J. Coelho, A. Pokle, and V. Nicolosi, "A 2d graphene-manganese oxide nanosheet hybrid synthesized by a single step liquid-phase co-exfoliation method for supercapacitor applications", Electrochim. Acta **174**, 696–705 (2015).

[461]R. J Smith, P. J. King, M. Lotya, C. Wirtz, U. Khan, S. De, A. O'Neill, G. S. Duesberg, J. C. Grunlan, G. Moriarty, et al., "Large-scale exfoliation of inorganic layered compounds in aqueous surfactant solutions", Adv. mater. **23**, 3944–3948 (2011).